STRUCTURE VIBRATION: VIBRATION MITIGATION MATERIALS AND STRUCTURES

EDITED BY: Zhao-Dong Xu, Pir Abid Ali Shah, Yong Lu and Shi-Dong Li
PUBLISHED IN: Frontiers in Materials

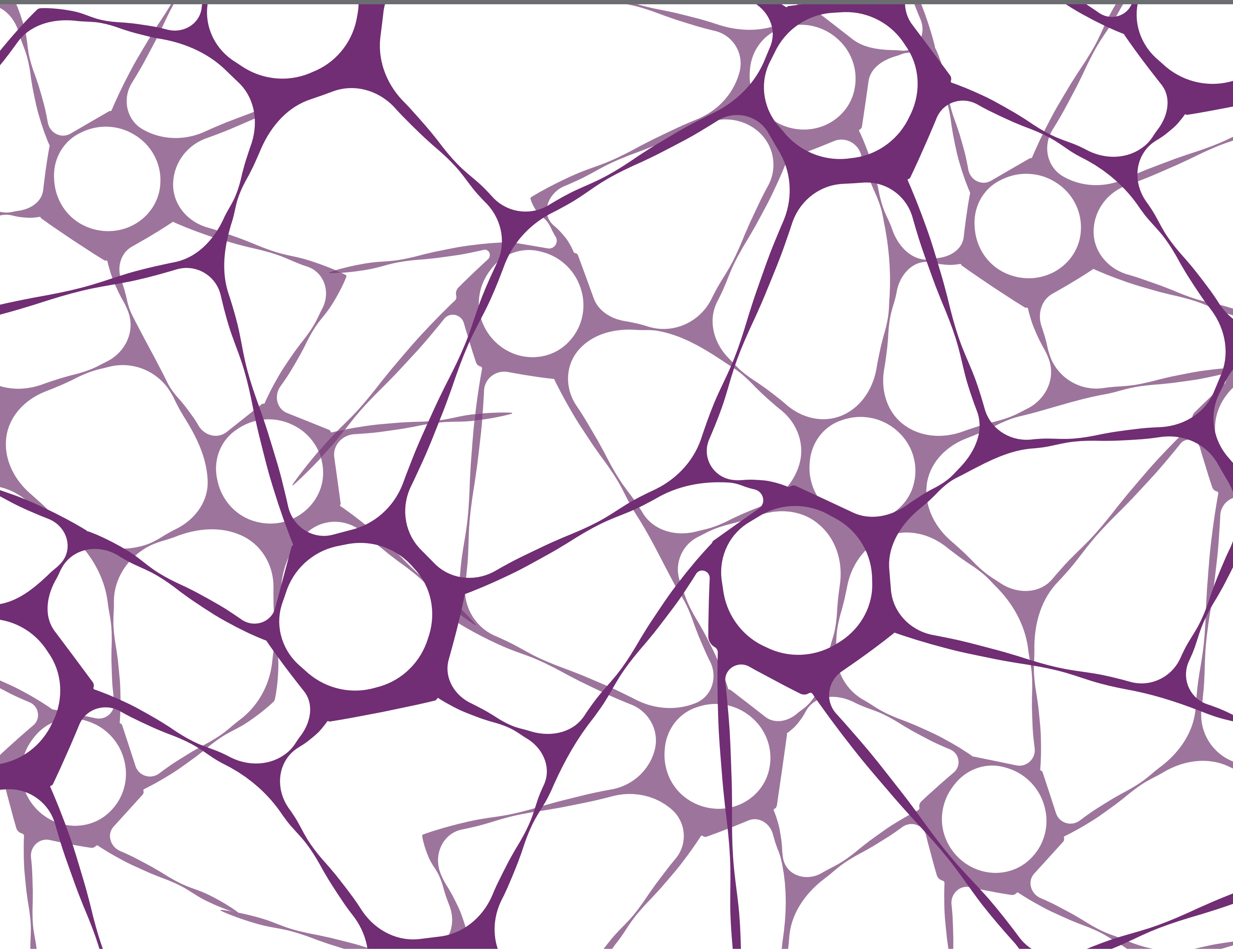

frontiers Research Topics

ISSN 1664-8714
ISBN 978-2-88963-212-1
DOI 10.3389/978-2-88963-212-1

About Frontiers

Frontiers is more than just an open-access publisher of scholarly articles: it is a pioneering approach to the world of academia, radically improving the way scholarly research is managed. The grand vision of Frontiers is a world where all people have an equal opportunity to seek, share and generate knowledge. Frontiers provides immediate and permanent online open access to all its publications, but this alone is not enough to realize our grand goals.

Frontiers Journal Series

The Frontiers Journal Series is a multi-tier and interdisciplinary set of open-access, online journals, promising a paradigm shift from the current review, selection and dissemination processes in academic publishing. All Frontiers journals are driven by researchers for researchers; therefore, they constitute a service to the scholarly community. At the same time, the Frontiers Journal Series operates on a revolutionary invention, the tiered publishing system, initially addressing specific communities of scholars, and gradually climbing up to broader public understanding, thus serving the interests of the lay society, too.

Dedication to Quality

Each Frontiers article is a landmark of the highest quality, thanks to genuinely collaborative interactions between authors and review editors, who include some of the world's best academicians. Research must be certified by peers before entering a stream of knowledge that may eventually reach the public - and shape society; therefore, Frontiers only applies the most rigorous and unbiased reviews.
Frontiers revolutionizes research publishing by freely delivering the most outstanding research, evaluated with no bias from both the academic and social point of view. By applying the most advanced information technologies, Frontiers is catapulting scholarly publishing into a new generation.

What are Frontiers Research Topics?

Frontiers Research Topics are very popular trademarks of the Frontiers Journals Series: they are collections of at least ten articles, all centered on a particular subject. With their unique mix of varied contributions from Original Research to Review Articles, Frontiers Research Topics unify the most influential researchers, the latest key findings and historical advances in a hot research area! Find out more on how to host your own Frontiers Research Topic or contribute to one as an author by contacting the Frontiers Editorial Office: researchtopics@frontiersin.org

STRUCTURE VIBRATION: VIBRATION MITIGATION MATERIALS AND STRUCTURES

Topic Editors:
Zhao-Dong Xu, Southeast University, China
Pir Abid Ali Shah, University of Science and Technology Bannu, Pakistan
Yong Lu, University of Edinburgh, United Kingdom
Shi-Dong Li, Southeast University, China

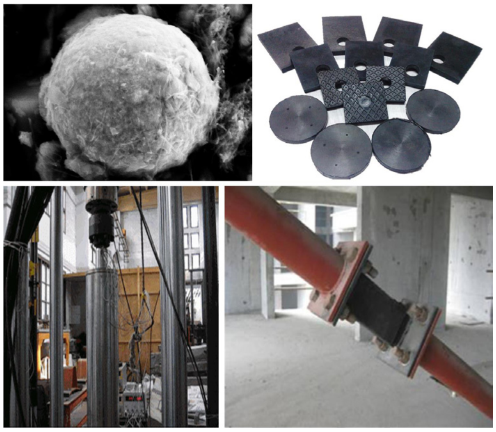

Image: Vibration Mitigation Materials and Structures
Original image created by Zhao-Dong Xu

Vibration is a common phenomenon when a structure is exposed to one or multiple mechanical or environmental actions, always at great cost to lives and to the economy. In order to reduce the adverse impact of vibration, vibration mitigation materials and structures have recently been at the center of attention. This book "Structure Vibration: Vibration Mitigation Materials and Structures" as the tip of the iceberg, provides a window to let people know about the flourishing of this young field. Twelve original research papers and one review paper have been included in this book to represent the recent development of vibration mitigation technology. The vibration mitigation material manufacture process, testing, analysis, and application have completely thoroughly studied. We wish more cutting-edge achievements will arise to benefit mankind and continually promote the development of vibration mitigation materials and structures.

Citation: Xu, Z.-D., Shah, P. A. A., Lu, Y., Li, S.-D., eds. (2019). Structure Vibration: Vibration Mitigation Materials and Structures. Lausanne: Frontiers Media.
doi: 10.3389/978-2-88963-212-1

Table of Contents

1. OVERVIEW

2. NEXT-GENERATION VIBRATION MITIGATION MATERIALS MANUFACTURING

3. MECHANICAL PROPERTIES TESTS OF VIBRATION MITIGATION MATERIALS

4. MECHANICAL MODELS OF VIBRATION MITIGATION MATERIALS

5. VIBRATION MITIGATION MATERIALS APPLICATION

5.1. NEW DAMPER DESIGN

5.2. MECHANICAL MODEL OF THE DAMPER

5.3. CONTROL OF THE DAMPER

6. NON-LINEAR DYNAMIC ANALYSIS OF A VIBRATION MITIGATION STRUCTURE

7. CONCLUSION AND PROSPECTS

frontiers in Materials

EDITORIAL
published: 19 September 2019
doi: 10.3389/fmats.2019.00229

Editorial: Vibration Mitigation Materials and Structures

Zhao-Dong Xu[1]*, *Shi-Dong Li*[1], *Pir Abid Ali Shah*[2] *and Yong Lu*[3]

[1] *Key Laboratory of C&PC Structures of the Ministry of Education, Southeast University, Nanjing, China,* [2] *Faculty of Engineering, University of Science and Technology Bannu, Bannu, Pakistan,* [3] *Institute for Infrastructure and Environment, School of Engineering, University of Edinburgh, Edinburgh, United Kingdom*

Keywords: vibration mitigation materials, material preparation, material mechanical properties, dampers, structural analysis

Editorial on the Research Topic

Vibration Mitigation Materials and Structures

For more than half a century, vibration mitigation technology has made significant contributions to social development and human progress. With the excellent hysteretic behavior and energy dissipation capability, vibration mitigation materials, and structures can effectively reduce the damage induced by harmful vibrations, and guarantee the safety of the equipment, infrastructure, environment, and human life. A lot of researchers have made substantial achievements in this field. New vibration mitigation materials successively spring up and continually update the traditional vibration mitigation structures. The new passive vibration mitigation materials (e.g., viscoelastic materials, rubber), new smart materials (e.g., magnetorheological fluid, magnetorheological elastomers, piezoelectric ceramics), new damper types, and new vibration mitigation structures have appeared in rapid succession, leading to the booming of this young field.

The Research Topic "Vibration Mitigation Materials and Structures," as the tip of the iceberg, provides a window to let people know about the flourishing of this young field. Twelve original research papers and one review paper have been included in this Research Topic to represent the recent development of vibration mitigation technology. The vibration mitigation material manufacture process, testing, analysis, and application have completely thoroughly studied. The articles in this topic are divided into five areas, namely (1) next-generation vibration mitigation materials manufacturing, (2) mechanical properties tests of vibration mitigation materials, (3) mechanical models of vibration mitigation materials, (4) vibration mitigation materials application, and (5) non-linear dynamic analysis of a structure reinforced by vibration mitigation materials.

The new generation vibration mitigation materials manufacture is the most interesting area. Liu and Han present a new kind of PVA-steel hybrid fiber reinforced cementitious composite (PVA-steel HyFRCC). The material mechanical properties of the material are discussed, together with the different fiber contents, fiber types, and fiber shapes. Due to the fiber hybridization, the material with a suitable fiber status can have excellent peak strain, compressive toughness, and post-peak ductility. PVA-steel HyFRCC, as a new generation vibration mitigation material, can enhance the energy dissipation and damage control capacity of vibration mitigation structures.

The study of the mechanical property tests of vibration mitigation materials is a multidisciplinary area. Guo et al., established the hybrid test system, which consists of upper computer and lower machine. The test system control method and hybrid test procedure are introduced. This hybrid test system is employed to test the dynamic performance of nominal viscoelastic material, which provided the robust operate program and benchmark index for research of viscoelastic material.

Edited and reviewed by:
John L. Provis,
University of Sheffield,
United Kingdom

****Correspondence:***
Zhao-Dong Xu
zhdxu@163.com

Specialty section:
This article was submitted to
Structural Materials,
a section of the journal
Frontiers in Materials

Received: *07 August 2019*
Accepted: *04 September 2019*
Published: *19 September 2019*

Citation:
Xu Z-D, Li S-D, Shah PAA and Lu Y
(2019) Editorial: Vibration Mitigation
Materials and Structures.
Front. Mater. 6:229.
doi: 10.3389/fmats.2019.00229

Establishing mathematical models to express material behavior is significant for vibration mitigation materials. Huang et al. transformed the Equivalent Standard Solid model into time domain by two-step approach and present the time domain oriented mathematical model to describe the behavior of the viscoelastic material. Sun et al. introduced the dynamic sandwich-type shear test for the viscous damping wall and presented the simplified method to calculate the velocity exponent, storage modulus and loss modulus of the polymer in viscous material. Based on the temperature-frequency equivalent principle, Xu et al. described the non-linear mechanical behavior of the viscoelastic material by modified the traditional seven parameters fractional derivative model. The influence of environment temperature and loading frequency was taken into account.

The application of vibration mitigation materials is a popular field in vibration mitigation technology. In reality, most vibration mitigation materials are designed as dampers to ensure the maximization of material efficiency. New damper design, mechanical model of the damper and control of the damper are three subareas of vibration mitigation materials application. Based on the vulcanizing-consolidating technology, Tu et al., designed a new leak-proof magnetorheological damper, and employed the correction factor of the pressure gradient to describe the energy dissipation and fluid-structure interaction property of the viscoelastic material. Jiang et al. designed a new combination damper based on the metallic vibration mitigation material and the viscoelastic vibration mitigation material. The damper has stable hysteretic behavior and excellent deformability, which is applied in the replaceable coupling beams. Wang et al. designed a new friction damper which was used in hybrid coupling beam, and established the thermal-mechanical model to describe the thermomechanical coupling effect of damping material existing in the friction damper. Zhou et al. investigated a new viscoelastic damper with hybrid non-linear properties and present the mechanical model to describe the multiple non-linear behavior. Guo et al. present the particle swarm optimization algorithm to change the mechanical behavior of magnetorheological damping material. The effective control and efficient utilization of smart vibration mitigation material was achieved.

Vibration mitigation materials will be used in practical projects after the procedures of manufacturing, testing, analyzing, and applying, which are combined with the traditional structures. The complete vibration mitigation structure system is then formed. The non-linear dynamic analysis and design of a structure reinforced by vibration mitigation materials and damper is the last step. He et al. introduced the design and analysis method of the vibration mitigation structural component taking a concrete filled steel tube structure as an example. Shi et al. present the design and analysis method of the vibration mitigation structural joint, taking the steel reinforced concrete structure as an example.

"Vibration mitigation materials and structures" is a broad and constructive topic. Recently, new passive vibration mitigation materials and new smart vibration mitigation materials appeared in a short time and are widely applied in civil engineering, mechanical engineering, and aerospace engineering. Viscous damping material, viscoelastic damping material, metallic material, magnetorheological elastomer, shape memory alloy, magneto strictive material, and piezoelectric ceramic material have been the focus of studies (Xu et al.). Although there are only 13 papers in this Research Topic, we still tried our best to present every aspect of vibration mitigation materials and structures in a complete way. It is expected that (1) wide temperature domain and wide frequency domain research of vibration mitigation materials, (2) new hybrid vibration mitigation materials manufacture, (3) new material mechanical models and (4) new application of vibration mitigation materials will continue to play a role in this young topic. We wish more cutting-edge achievements will arise to benefit mankind and continually promote the development of vibration mitigation materials and structures.

AUTHOR CONTRIBUTIONS

All authors listed have made a substantial, direct and intellectual contribution to the work, and approved it for publication.

ACKNOWLEDGMENTS

We would like to acknowledge all the authors, reviewers, editors, and publishers, who have supported this Research Topic. Furthermore, S-DL, as our assistant, had join our editorial group to help us to deal with the work of this Research Topic. The contribution of S-DL involves, but are not limited to, the preparation of the editorial article and the management of the Research Topic. Our editor group want to represent our thanks for his long-time help, and decide to add S-DL as our co-author into the author list for this editorial.

Conflict of Interest: The authors declare that the research was conducted in the absence of any commercial or financial relationships that could be construed as a potential conflict of interest.

frontiers in Materials

ORIGINAL RESEARCH
published: 10 May 2019
doi: 10.3389/fmats.2019.00108

Experimental Investigation on Compressive Toughness of the PVA-Steel Hybrid Fiber Reinforced Cementitious Composites

*Wenlin Liu and Jianping Han**

Key Laboratory of Disaster Prevention and Mitigation in Civil Engineering of Gansu Province, Lanzhou University of Technology, Lanzhou, China

In order to achieve the whole process control of crack formation of engineered cementitious composites (ECC) under loading and improve the mechanical properties of ECC, steel fibers are mixed into traditional ECC to get polyvinyl alcohol (PVA)-steel hybrid fiber reinforced cementitious composites (HyFRCC). And the key parameters to affect the HyFRCC performance are PVA fiber content, steel fiber content, and aspect ratio of steel fiber. In order to investigate the mechanical properties of PVA-steel HyFRCC such as the compressive toughness, 15 PVA-steel HyFRCC specimens with different volume fraction of steel fiber and PVA fiber, together with 1 non-fibrous cementitious composites specimen and 3 ECC specimens with PVA fibers only for comparison were designed and uniaxial compression tests were conducted. Furthermore, the effect of fiber content, fiber type and fiber geometrical characteristic on the compressive toughness of HyFRCC were analyzed. The results show that PVA fiber content, steel fiber content and aspect ratio of steel fiber have little impact on the uniaxial compressive strength of the PVA-steel HyFRCC, while the peak strain, compressive toughness and the post-peak ductility of PVA-steel HyFRCC are improved significantly due to fiber hybridization. The formation of large scale cracks of ECC specimens after post-peak loading is restrained effectively with the addition of steel fiber. The mixture of PVA and steel fiber has a remarkable effect on the improvement of ECC compression toughness and crack control. It indicates that the energy dissipation and damage control capacity of the structural component with PVA-steel HyFRCC under seismic loading will be enhanced.

Keywords: hybrid fiber, PVA fiber, steel fiber, engineered cementitious composite, compressive toughness, seismic performance improvement

Edited by:
Zhao-Dong Xu,
Southeast University, China

Reviewed by:
Yong Li,
University of Alberta, Canada
Wensheng Lu,
Tongji University, China

****Correspondence:***
Jianping Han
jphan1970@163.com

Specialty section:
This article was submitted to Structural Materials, a section of the journal Frontiers in Materials

Received: *28 February 2019*
Accepted: *24 April 2019*
Published: *10 May 2019*

Citation:
Liu W and Han J (2019) Experimental Investigation on Compressive Toughness of the PVA-Steel Hybrid Fiber Reinforced Cementitious Composites. Front. Mater. 6:108. doi: 10.3389/fmats.2019.00108

INTRODUCTION

The brittleness of ordinary concrete is an important factor that seriously restricts the workability and durability of concrete structures under complex loading conditions. Engineered cementitious composites (ECC) is a new civil engineering material proposed by Li with high crack resistance and damage resistance (Li and Leung, 1992; Li, 1993; Wang and Li, 2006). ECC material shows multiple cracking and strain-hardening behavior under tensile loading. The ultimate tensile strain of ECC can reach several hundred times that of ordinary concrete, which effectively overcomes the brittleness and improves the tensile ductility of ordinary concrete. The excellent mechanical and durability properties make ECC potential for resilient, durable, and sustainable civil infrastructures. A lot of research works on the properties of ECC material have been done which results in improving the traditional ECC material to get high performance ECCs such as the ultra-high ductile ECC that matches strength (Wang et al., 2015) and low drying shrinkage ECC (LSECC) (Zhang et al., 2009). At present, ECC has been widely used in many civil engineering fields such as bridge deck, pavement expansion joints and structural repair (Qian et al., 2009; Fan et al., 2017; Zhou et al., 2018).

It is necessary to fully understand the mechanical properties of the material when designing the structure and simulating the response of the structure and component. Most researches on the mechanical properties of ECC material mainly focus on the uniaxial tensile properties and the bending resistance. However, the basic uniaxial compression properties of ECC have not been widely concerned. Xu et al. (2009) and Cai and Xu (2011) investigated the uniaxial compression behavior of ECC materials using prismatic specimens and proposed the uniaxial compression constitutive model of ECC further. Deng et al. (2015) investigated the influence of different fiber content, water-binder ratio and fly ash content on ECC compressive toughness and obtained the relationship between fiber content and compressive toughness index of ECC. Zhou et al. (2015) tested the uniaxial compression of ECC with different strength and found that the compressive toughness of ECC decreases significantly with the increase of strength. Due to the higher pullout rate and the smaller dimension of PVA fiber, it is difficult to obtain full process control of crack formation simply via PVA fiber only. It was found that the mechanical properties of traditional ECC materials can be improved with the addition of high-modulus fibers such as steel fiber (Kawamata et al., 2003; Lawler et al., 2005; Maalej et al., 2005; Zhang et al., 2007). Soe et al. (2013) investigated the tensile characteristics and the rate dependence of the hybrid fiber reinforced ECC material with 1.75% PVA and 0.58% steel fiber, and it was found that the hybrid fiber reinforced ECC material exhibits improved strength, strain capability and impact resistance. Ali et al. (2017) investigated the impact resistance of an innovative hybrid fiber reinforced ECC incorporating short randomly dispersed shape memory alloy and PVA fibers using a drop weight impact test, and their results indicate that SMA fiber significantly enhances the tensile and impact performance of the ECC. The addition of steel fiber to the traditional ECC material is expected to achieve full crack control and high compressive toughness of ECC material.

In order to investigate the mechanical properties of PVA-steel HyFRCC such as the compressive toughness and the key parameters to affect HyFRCC performance, 15 PVA-steel HyFRCC specimens with different volume fraction of steel fiber and PVA fiber, together with 1 non-fibrous cementitious composites specimen and 3 ECC specimens with PVA fibers only were designed and uniaxial compression tests were conducted. And the effect of PVA fiber content, steel fiber content and aspect ratio of steel fiber on the mechanical properties of HyFRCC such as axial compressive strength, peak strain and compressive toughness were analyzed further.

EXPERIMENTAL PROGRAM

Material Composition and Mix Ratio

Ordinary Portland cement P.O 42.5, class II fly ash and standard sand for cement strength test were used to design the materials in this study. According to the recommendations for design and construction of ECC and the previous research results, the mix ratio of HyFRCC was designed. All of these mixtures that investigated in this study had the same cement, fly ash, sand, and water. The only difference was the type of used fibers and their combination. The quantity of each constituent of the material except fibers is given in **Table 1**.

Three types of steel fibers with different aspect ratios shown in **Table 2** were used. The PVA fibers used in this study is made by Kuraray and titled as *KURALON KII RECS15*. The properties of PVA fiber were shown in **Table 3**.

Specimens Design and Test Setup

Three parameters such as PVA fiber content, steel fiber content and aspect ratio of steel fiber were considered in this study. As shown in **Table 4**, 15 PVA-steel HyFRCC (A5-A19) with different volume fraction of steel fiber and PVA fiber, together with 1 non-fibrous cementitious composites (A1) and 3 ECC with PVA fiber only for comparison were investigated.

For each composite, three test cubes with the dimension of 150 × 150 × 150 mm and three test prisms with the dimension of 150 × 150 × 300 mm were cast in steel molds and compacted by vibration table. All specimens were demoulded 24 h after casting

TABLE 1 | Mixture design (kg/m^3).

Cement	Fly ash	Sand	Water
530	753	467	404.5

TABLE 2 | The mechanical and geometrical properties of steel fiber.

Fiber	Length (mm)	Diameter (mm)	Tensile strength (MPa)	Density (g/cm^3)	Type
S_a	24	0.6	≥600	7.8	Crimped steel
S_b	36				
S_c	48				

TABLE 3 | The mechanical and geometrical properties of PVA fiber.

Length (mm)	Diameter (μm)	Tensile strength (MPa)	Elongation (%)	Modulus (GPa)	Density (g/cm^3)
12	40	1,600	6	40	1.3

and stored in a standard curing room with 20 ± 2°C and 95% RH for additional 27 days.

Loading Device and Control Method

The compression tests were conducted by an electro-hydraulic servo compression machine with a load capacity of 300t. As shown in **Figure 1A**, cubes were tested to obtain the 28-day compressive strength and the tests were performed under a constant rate of 0.5 MPa/s. As shown in **Figure 1B**, prisms were tested to evaluate the full compressive loading-displacement response of the composites. A displacement control with 0.3 mm/min loading velocity was applied in the axial direction until ultimate failure occurred. Two grating displacement sensors were used to measure the vertical deformation in the gauge range of the specimens.

Test Phenomena

The axial compression resistance of non-fibrous cementitious composites is similar to that of ordinary concrete. After the peak load, a vertical main crack is formed through the prisms. The matrix on both side of the crack is obviously dislocated and the prisms lose the bearing capacity. The failure mode of the non-fibrous matrix is shown in **Figure 2A**.

There is a significant difference between the fiber reinforced cementitious composites and non-fibrous cementitious composites in the process of compression. The development of cracks is still in control after the peak load due to the addition of fibers and new cracks develop continuously. The residual loading capacity of the specimens is still maintained when they come to failure.

There is obvious difference between the ECC and HyFRCC prismatic specimens in the process of compression. At the initial stage of loading, the lateral deformation of the ECC and HyFRCC prismatic specimens is small, the specimens are in the linear elastic stage. When the vertical loads come up to 40∼60% of the peak load, the lateral deformation of the prismatic specimens is obviously increased. A number of fine cracks appear on the surface of the prisms. Due to the bridging of PVA fibers at the micro-crack, the generation and development of the micro-crack can well be inhibited and the specimens is still in the elastic stage approximately. When the vertical loads come up to more than 80% of the peak load, the lateral deformation of the prismatic specimens increases rapidly. The main vertical crack is formed and 45° oblique cracks are generated between the vertical cracks and the fizz sound that is produced by pulling out and snapping of PVA fibers can be clearly heard with the increase of the crack width. After peak load, the main vertical crack of the ECC prismatic specimens becomes wider suddenly and the

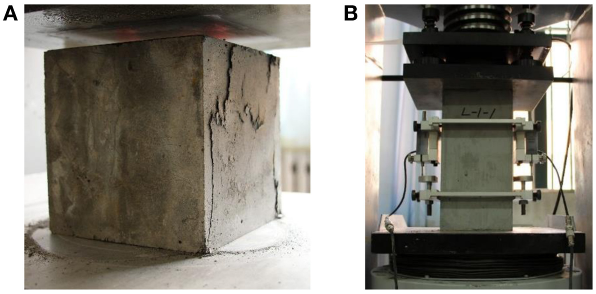

FIGURE 1 | Test specimens. **(A)** 150 mm cube. **(B)** 150 × 150 × 300 mm prism.

TABLE 4 | Test group and test results.

Specimen number	PVA fiber (% vol.)	Steel fiber (% vol.)	Aspect ratio of steel fiber	Peak loading (kN)	Peak deformation (mm)	Peak strain (μm/mm)
A1	–	–	–	1033.5	0.363	2,416
A2	0.5	–	–	918.00	0.565	3,764
A3	1.0	–	–	961.50	0.658	4,384
A4	1.5	–	–	996.00	0.745	4,964
A5	1.0	0.5	40	918.75	0.773	5,153
A6	1.0	1.0	40	923.25	0.788	5,253
A7	1.0	1.5	40	954.00	0.802	5,348
A8	1.0	0.5	80	938.25	0.776	5,171
A9	1.0	1.0	80	941.25	0.794	5,293
A10	1.0	1.5	80	951.00	0.811	5,404
A11	0.5	0.5	60	862.50	0.741	4,940
A12	0.5	1.0	60	885.00	0.777	5,180
A13	0.5	1.5	60	895.50	0.794	5,291
A14	1.0	0.5	60	918.75	0.845	5,633
A15	1.0	1.0	60	929.25	0.862	5,748
A16	1.0	1.5	60	945.75	0.879	5,860
A17	1.5	0.5	60	924.00	0.934	6,224
A18	1.5	1.0	60	964.50	0.950	6,335
A19	1.5	1.5	60	979.88	0.968	6,450

bearing capacity of the prisms drops sharply. Nevertheless, the existence of PVA fibers makes it still have some residual bearing capacity. For HyFRCC specimens, due to the presence of steel fiber, the main vertical crack width does not change abruptly after the peak load, and the development of the main crack can be controlled effectively during the decline of bearing capacity. In the meantime, new cracks are still formed in the prisms. Furthermore, the residual bearing capacity of the HyFRCC specimens is higher than that of the ECC specimens significantly. It indicates that HyFRCC is superior to the mono fiber reinforced cementitious composites in compressive toughness and crack control. The failure modes of the ECC specimens and the HyFRCC specimens are shown in **Figures 2B,C**.

TEST RESULTS AND ANALYSIS

Load-Deformation Curves

According to the test results, the axial compression load-deformation curves of the non-fibrous, the ECC and the HyFRCC prisms are shown in **Figure 3**. The peak load and peak deformation of each prism are shown in **Table 4**.

As shown in **Figure 3** and **Table 4**, the axial compressive strength of the fiber reinforced cementitious composites is smaller than that of the non-fibrous cementitious composites. The axial compressive strength of the ECC is about 10% lower than that of the non-fibrous cementitious composites, which is similar to the test results by Zhou et al. (2015) and

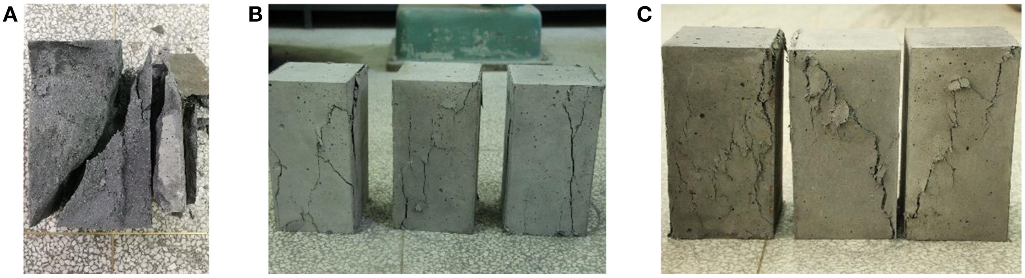

FIGURE 2 | Failure modes of tested prisms. **(A)** Non-fibrous. **(B)** ECC. **(C)** HyFRCC.

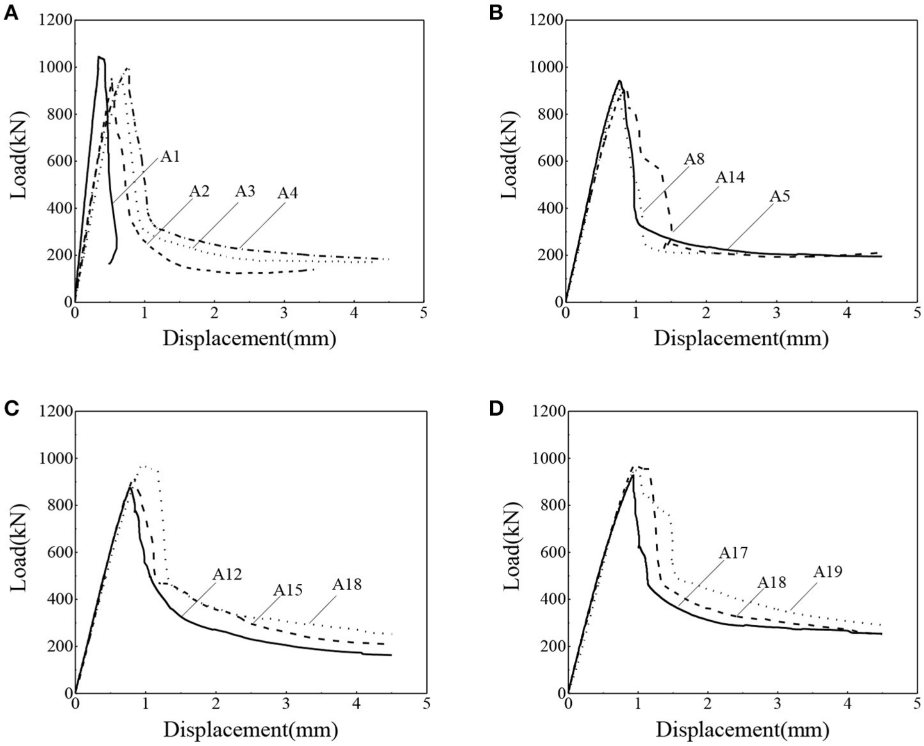

FIGURE 3 | The uniaxial compressive load-deformation curves of test specimens. **(A)** Non-fibrous and ECC. **(B)** Hybrid mixtures with variable aspect ratios of steel fiber. **(C)** Hybrid mixtures with variable volume fraction of PVA fiber. **(D)** Hybrid mixtures with variable volume fraction of steel fiber.

Wang et al. (2018). The results of the preliminary mix ratio test show that the axial compressive strength of the mono steel fiber specimen is about 5% lower than that of the non-fibrous cementitious composites. The addition of fibers introduces more defects in the matrix during the mixing, which leads to the reduction of the axial compressive strength of the specimen. Since the size of the steel fiber is much larger than the PVA fiber, the defect introduced by steel fibers is less than that introduced by PVA fibers with the same volume fraction. Thus, the strength reduction caused by steel fibers is less than that caused by PVA fibers. The addition of PVA fiber and steel fiber mainly bridges the matrix at the crack and improve the ductility of the material.

It can be seen from **Figure 3** and **Table 4** that the peak strain of each mixture is in the range from 3,500 to 6,500 μm/mm, which is much higher than the peak strain of the non-fibrous specimen, 2,416 μm/mm. The peak strain of ECC and HyFRCC is increased by 55 ∼ 105% and 104 ∼ 167%, respectively, which indicates that the addition of steel fiber has a significant effect on improving the deformation capability of the material before peak load, and the peak strain of the prismatic specimens increases gradually with the increase of steel fiber content. The peak strain of the HyFRCC specimens increases first and then decreases with the increase of the aspect ratio of steel fiber while the PVA fiber content and steel fiber content remain constant. When the aspect ratio of steel fiber is 60, the peak strain is maximum.

Compressive Strength

For the tested specimens in this paper, the axial compressive strength of ECC and HyFRCC increases with the increase of fiber content. In order to accurately quantify the influence of fiber size and fiber content to the axial compressive strength of the material, the concept of fiber characteristic value was introduced as:

$$\begin{cases} \lambda_{\mathrm{pf}} = \rho_{\mathrm{pf}} l_{\mathrm{pf}} / d_{\mathrm{pf}} & 0.5\% \leq \rho_{\mathrm{pf}} \leq 1.5\% \\ \lambda_{\mathrm{sf}} = \rho_{\mathrm{sf}} l_{\mathrm{sf}} / d_{\mathrm{sf}} & 0.5\% \leq \rho_{\mathrm{sf}} \leq 1.5\% \end{cases} \tag{1}$$

where ρ_{pf} and ρ_{sf} are the content of PVA fiber and steel fiber of the matrix, respectively, $l_{\mathrm{sf}}/d_{\mathrm{sf}}$ and $l_{\mathrm{pf}}/d_{\mathrm{pf}}$ are the aspect ratio of steel fiber and PVA fiber, respectively.

As shown in **Figure 4**, the relationship between the fiber characteristic value and the axial compressive of the material based on the test results is obtained as:

$$f_{\mathrm{c}}{}' = f_{\mathrm{c}}\left(1 - 0.1628\lambda_{\mathrm{pf}}{}^{-1} - 0.0128\lambda_{\mathrm{sf}}{}^{-1}\right) \tag{2}$$

where f_{c} and $f_{\mathrm{c}}{}'$ are the axial compressive strength of non-fibrous and HyFRCC matrix, respectively. When the content of PVA fiber and steel fiber are equal to zero, $f_{\mathrm{c}}{}'$ is equal to f_{c}.

Compressive Toughness

The compressive toughness index is important for quantitative analysis of energy dissipating ability of materials. At present, the commonly used compressive toughness analysis methods include energy method, strength method, energy ratio method and feature point method (Liu et al., 2005). The equivalent compressive toughness method proposed by Deng et al. (2015) was used to analyze and evaluate the compressive toughness of each specimen in this paper, as shown in **Figure 5**.

The compressive toughness index is calculated using the following equation:

$$W_{\mathrm{c}}^{u} = \frac{\Omega_u}{Al} \tag{3}$$

where W_{c}^{u} represents the equivalent compressive toughness index, Ω_u is the area under the load–deformation curve at vertical deformation of Δ_u, Δ_u is the vertical deformation corresponding to the axial load while the axial load is reduced to u times peak

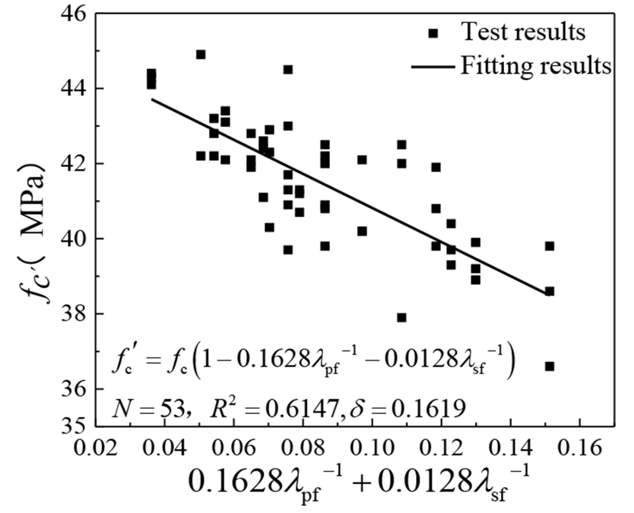

FIGURE 4 | Fitted curve of uniaxial compression strength of HyFRCC.

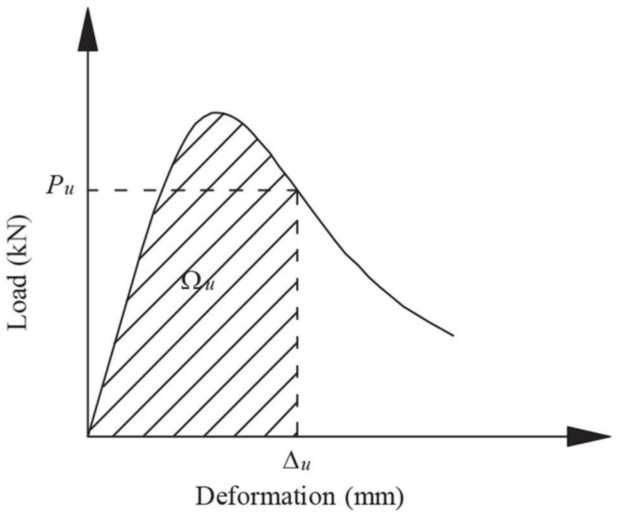

FIGURE 5 | The method of equivalent compressive toughness.

load, A is the uniaxial compression area of the test specimen, l is the axial height of the test specimen.

As shown in **Table 5**, the equivalent compressive toughness index of each specimen when u is 1.00, 0.85 and 0.3 was calculated based on the test results, respectively. $W_c^{1.00}$ corresponds to the compressive toughness when the specimen reaches to the ultimate load, which can be used for the analysis of bearing capacity of structures in the normal service condition. $W_c^{0.85}$ corresponds to the compressive toughness when the load of the specimen declines to 0.85 times ultimate load, which can be used to evaluate the ductility and energy dissipation of structures. $W_c^{0.30}$ corresponds to the compressive toughness when the load of the specimen declines to 0.30 times ultimate load, which can be used for collapse resistance analysis of structures.

The matrix material is typically brittle, and its compressive toughness index is significantly smaller than that of fibrous material. The fibers distributed in cementitious composites can bridge the matrix on both side of cracks, limit the generation and development of internal cracks in the matrix, and improve the vertical deformation capacity and compressive toughness of the specimen. Comparing with the non-fibrous cementitious composites specimen, $W_c^{1.00}$, $W_c^{0.85}$, and $W_c^{0.30}$ values of fibrous specimens increase by 82.87, 69.16, and 135.32% on average, respectively.

The PVA fiber and steel fiber in fiber reinforced cementitious composites can effectively inhibit the formation and development of cracks. Among them, the PVA fiber with smaller scale mainly inhibits the formation and development of fine cracks, while the steel fiber with larger scale mainly controls the development of wider cracks. As shown in **Table 5**, due to the special pullout mechanism of PVA fiber, the compressive toughness of ECC that with PVA fiber only is not much higher than that of the non-fibrous cementitious composites specimen. $W_c^{1.00}$, $W_c^{0.85}$, and $W_c^{0.30}$ values of ECC specimens increase by 54.71, 24.92, and 58.90% on average, respectively. With the addition of steel fiber with larger scale, the uniaxial compressive toughness of HyFRCC is obviously improved, the $W_c^{1.00}$, $W_c^{0.85}$, and $W_c^{0.30}$ values of HyFRCC specimens increase by 88.50, 76.46, and 150.61% on average, respectively.

The Influence of Various Parameters on the Toughness Index

The relationship between the compressive toughness index of the material and the PVA fiber content, steel fiber content and aspect ratio of steel fiber are shown in **Figure 6**.

The influence of various parameters on the compressive toughness index are summarized as follows:

As shown in **Figures 6B,E,H**, the compressive toughness index values of the fiber reinforced cementitious composites specimens increases with the increase of volume fraction of PVA fiber. Due to the special pullout mechanism of PVA fiber, the compressive toughness of ECC specimens is significantly lower than that of HyFRCC specimens, as shown in **Figure 6H**.

Steel fiber can effectively inhibit the development of wide cracks. However, the addition of steel fiber will inevitably introduce defects into the matrix. The combination of the two causes weakens the improvement of the compressive toughness which was enhanced by steel fibers. As shown in **Figures 6D,G**, the compressive toughness index values of the HyFRCC specimens increase first and then decrease with the increase of the steel fiber content while the PVA

TABLE 5 | Calculated results of equivalent compressive toughness.

Specimen no.	$\Omega_{1.00}$	$\Omega_{0.85}$	$\Omega_{0.30}$	$W_c^{1.00}$	$W_c^{0.85}$	$W_c^{0.30}$
	$\times 10^5$ (N·mm)			$(\times 10^{-2})$		
A1	2.24	3.10	3.77	3.325	4.594	5.582
A2	2.87	3.21	4.93	4.252	4.759	7.310
A3	3.20	4.02	5.59	4.742	5.950	8.281
A4	4.35	5.12	7.44	6.438	7.579	11.019
A5	3.79	4.59	6.58	5.612	6.801	9.755
A6	4.08	5.69	10.37	6.040	8.433	15.360
A7	4.26	5.46	7.47	6.313	8.086	11.061
A8	3.99	4.83	6.87	5.919	7.152	10.178
A9	4.05	5.12	10.87	6.001	7.593	16.108
A10	4.21	5.00	8.06	6.243	7.400	11.936
A11	3.46	4.23	5.93	5.126	6.267	8.785
A12	3.54	4.59	7.78	5.242	6.802	11.532
A13	3.96	4.46	6.88	5.864	6.604	10.190
A14	4.44	5.42	8.49	6.580	8.036	12.587
A15	4.46	6.74	13.16	6.604	9.982	19.491
A16	4.46	6.01	10.15	6.613	8.908	15.031
A17	4.79	5.91	10.43	7.103	8.760	15.455
A18	4.82	7.22	15.53	7.142	10.693	23.002
A19	5.14	6.80	13.07	7.612	10.079	19.363

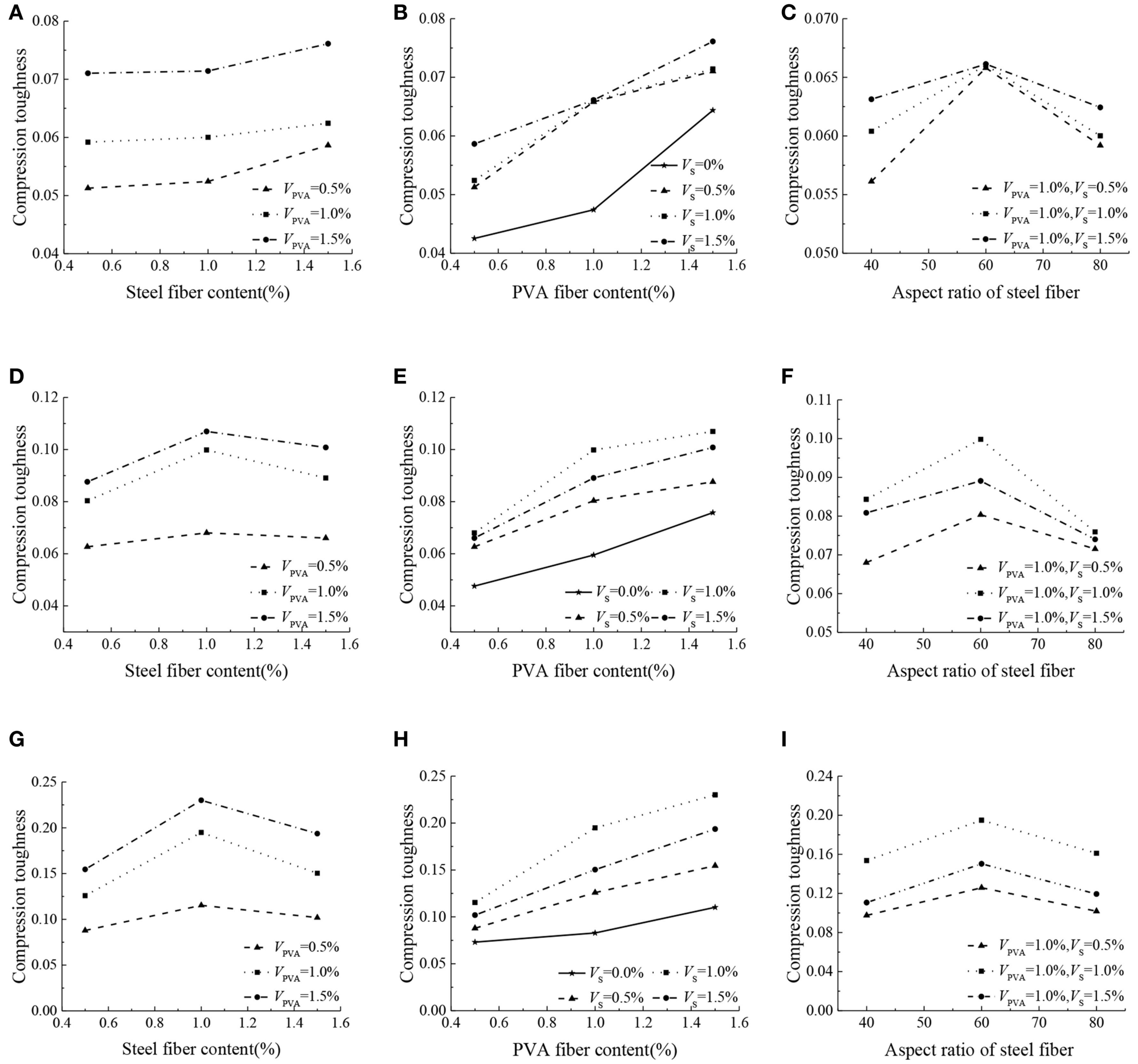

FIGURE 6 | The influence of various parameters for the compressive toughness. **(A)** Influence of steel fiber content on $\Omega_{1.00}$. **(B)** Influence of PVA fiber content on $\Omega_{1.00}$. **(C)** Influence of aspect ratio of steel fiber on $\Omega_{1.00}$. **(D)** Influence of steel fiber content on $\Omega_{0.85}$. **(E)** Influence of PVA fiber content on $\Omega_{0.85}$. **(F)** Influence of aspect ratio of steel fiber on $\Omega_{0.85}$. **(G)** Influence of steel fiber content on $\Omega_{0.30}$. **(H)** Influence of PVA fiber content on $\Omega_{0.30}$. **(I)** Influence of aspect ratio of steel fiber on $\Omega_{0.30}$.

fiber content remains constant. When the volume fraction of steel fiber is 1%, the compressive toughness index values are maximum. The negative fiber hybridization effect occurs when the volume fraction of steel fiber increases from 1.0 to 1.5%.

In HyFRCC, the total number of steel fibers decreases with the increase of the aspect ratio of steel fiber when the steel fiber content remains constant. Therefore, the number of steel fibers that bridging cracks will decrease. As shown in **Figures 6C,F,I**, with the increase of the aspect ratio of steel fiber, the compressive toughness of the HyFRCC specimens increases first and then decreases. When the aspect ratio of steel fiber is 60, the compressive toughness index values are maximum.

CONCLUSION

The fiber content and geometrical characteristics are the main factors affecting the axial compressive strength of HyFRCC material. The addition of fibers leads to the reduction of the axial compressive strength of the matrix material. The axial compressive strength of HyFRCC material increases with the increase of the PVA fiber and steel fiber content. The relationship between the axial compressive strength of HyFRCC and the fiber characteristic value is established according to the test results, which provides a reference for engineering application of HyFRCC.

The uniaxial compressive peak strain of HyFRCC significantly increases with the addition of fiber. The peak strain of ECC is

55 ∼ 105% higher than that of the non-fibrous cementitious composites. The peak strain of HyFRCC increases remarkably with the addition of steel fiber. And the peak strain of HyFRCC increases by 104∼167% when the volume fraction of steel fiber is 0.5 ∼ 1.5%. The deformation capability is significantly improved before reaching peak load.

Comparing with the non-fibrous cementitious composites, $W_{\mathrm{c}}^{0.85}$ and $W_{\mathrm{c}}^{0.30}$ values of ECC only increases by 24.92 and 58.90% on average, respectively. The crack control capability of HyFRCC is improved with the addition of steel fiber. The ductility and compressive toughness after peak load is also improved significantly. $W_{\mathrm{c}}^{0.85}$ and $W_{\mathrm{c}}^{0.30}$ values of HyFRCC increase by 76.46 and 150.61% on average, respectively.

The PVA fiber content, steel fiber content and aspect ratio of steel fiber have a significant effect on the compressive toughness of HyFRCC material. The compressive toughness of the HyFRCC is optimized when the PVA fiber content is 1.0%, the steel fiber content is 1.5%, and the aspect ratio of steel fiber is 60.

The compressive toughness, deformation and energy dissipation capacity of PVA-steel HyFRCC can be significantly improved. It is indicated that PVA-steel HyFRCC can be used for vibration isolation and mitigation of structures to improve the seismic performance of structures (Kasai et al., 1998; Xu et al., 2017, 2019).

DATA AVAILABILITY

The datasets generated for this study are available on request to the corresponding author.

AUTHOR CONTRIBUTIONS

WL and JH designed and prepared the specimens and conducted the test. Further analysis was performed by WL under the supervision of JH. All the authors collaborated on the writing of the manuscript.

REFERENCES

Ali, M. A., Soliman, A. M., and Nehdi, M. L. (2017). Hybrid-fiber reinforced engineered cementitious composite under tensile and impact loading. *Mater. Design* 117, 139–149. doi: 10.1016/j.matdes.2016.12.047

Cai, X., and Xu, S. (2011). Uniaxial compressive properties of ultra high toughness cementitious composite. *J. Wuhan Univ. Tech. Mater. Sci. Ed.* 26, 762–769. doi: 10.1007/s11595-011-0307-0

Deng, M., Liu, H., Qin, M., and Liang., X. (2015). Experimental research on compressive toughness of the high ductile fiber reinforced concrete. *J. Xi'an Univ. Arch. Tech.* 47, 660–665. doi: 10.15986/j.1006-7930.2015.05.009

Fan, J., Shi, Z., Gou, S., Nie, X., and Zhang, J. (2017). Experimental research on negative bending behavior of steel –ECC composite beams. *China Civil Eng. J.* 50, 64–72. doi: 10.15951/j.tmgcxb.2017.04.008

Kasai, K., Fu, Y., and Watanabe, A. (1998). Passive control systems for seismic damage mitigation. *J. Struc. Eng.* 124, 501–512. doi: 10.1061/(ASCE)0733-9445(1998)124:5(501)

Kawamata, A., Mihashi, H., and Fukuyama, H. (2003). Properties of hybrid fiber reinforced cement-based composites. *J. Adv. Concr. Technol.* 1, 283–290. doi: 10.3151/jact.1.283

Lawler, J. S., Zampini, D., and Shah, S. P. (2005). Microfiber and macro-fiber hybrid fiber reinforced concrete. *ASCE J. Mater. Civil Eng.* 17, 595–604. doi: 10.1061/(ASCE)0899-1561(2005)17:5(595)

Li, V. C. (1993). From micromechanics to structural engineering - the design of cementitous composites for civil engineering applications. *JSCE J. Struc. Mech. Earthq. Eng.* 471, 1–12. doi: 10.2208/jscej.1993.471_1

Li, V. C., and Leung, C. K. Y. (1992). Steady-state and multiple cracking of short random fiber composites. *J. Eng. Mech.* 118, 2246–2264. doi: 10.1061/(asce)0733-9399(1992)118:11(2246)

Liu, S., Huang, C., Wang, Q., and Zhao, G. (2005). Experimental investigation of uniaxial compressive characteristics of steel fiber improved high-strength concrete. *Indust. Constr.* 35, 78–80. doi: 10.13204/j.gyjz2005.11.023

Maalej, M., Quek, S. T., and Zhang, J. (2005). Behaviour of hybrid-fiber engineered cementitious composites subjected to dynamic tensile loading and projectile impact. *ASCE J. Mater. Civil Eng.* 17, 143–152. doi: 10.1061/(ASCE)0899-1561(2005)17:2(143)

Qian, S., Lepech, M. D., Kim, Y. Y., and Li, V. C. (2009). Introduction of transition zone design for bridge deck link slabs using ductile concrete. *ACI Struc. J.* 106, 96–105. doi: 10.14359/56288

Soe, K. T., Zhang, Y. X., and Zhang, L. C. (2013). Material properties of a new hybrid fibre-reinforced engineered cementitious composite. *Construc. Build. Mater.* 43, 399–407. doi: 10.1016/j.conbuildmat.2013.02.021

Wang, S., and Li, V. C. (2006). High-early-strength engineered cementitious composites. *ACI Mater. J.* 103, 3–12. doi: 10.14359/15260

Wang, Z., Zhang, J., Wang, J., and Shi, Z. (2015). Tensile performance of polyvinyl alcohol–steel hybrid fiber reinforced cementitious composite with impact of water to binder ratio. *J. Comp. Mater.* 49, 2169–2186. doi: 10.1177/0021998314542450

Wang, Z., Zuo, J., Zhang, J., Feng, L., and Jiang, G. (2018). Mechanical properties of hybrid fiber reinforced cementitious composites under uniaxial compression. *J. Build. Mater.* 21, 639–644. doi: 10.3969/j.issn.1007-9629.2018.04.018

Xu, S., Cai, X., and Zhang, Y. (2009). Experimental measurement and analysis of the axial compressive stress-strain curve of ultra high toughness cementitious composites. *China Civil Eng. J.* 42, 79–85. doi: 10.15951/j.tmgcxb.2009.11.009

Xu, Z., Huang, X., Xu, F., and Yuan, J. (2019). Parameters optimization of vibration isolation and mitigation system for precision platforms using non-dominated sorting genetic algorithm. *Mech. Syst. Signal Process.* 128, 191–201. doi: 10.1016/j.ymssp.2019.03.031

Xu, Z., Suo, S., Zhu, J., and Guo, Y. (2017). Performance tests and modeling on high damping magnetorheological elastomers based on bromobutyl rubber. *J. Intel. Mater. Syst. Struc.* 29, 1025–1037. doi: 10.1177/1045389X17730909

Zhang, J., Gong, C., Guo, Z., and Zhang, M. (2009). Engineered cementitious composite with characteristic of low drying shrinkage. *Cem. Concrete Res.* 39, 303–312. doi: 10.1016/j.cemconres.2008.11.012

Zhang, J., Maalej, M., and Quek, S. (2007). Performance of hybrid-fiber ECC blast/shelter panels subjected to drop weight impact. *ASCE J. Mater. Civil Eng.* 19, 855–863. doi: 10.1061/(ASCE)0899-1561(2007)19:10(855)

Zhou, J., Pan, J., and Leung, C. K. Y. (2015). Mechanical behavior of fiber-reinforced engineered cementitious composites in uniaxial compression. *J. Mater. Civil Eng.* 27:04014111. doi: 10.1061/(ASCE)MT.1943-5533.0001034

Zhou, T., Tian, P., Deng, M., Zhao, X., Zhang, H., and Liang, Z. (2018). Research on shaking table test of cavity-wall building strengthened with engineered cementitious composite. *J. Build. Struct.* 39, 147–152. doi: 10.14006/j.jzjgxb.2018.12.017

Conflict of Interest Statement: The authors declare that the research was conducted in the absence of any commercial or financial relationships that could be construed as a potential conflict of interest.

frontiers
in Materials

ORIGINAL RESEARCH
published: 05 June 2019
doi: 10.3389/fmats.2019.00116

Design on Hybrid Test System for Dynamic Performance of Viscoelastic Damping Material and Damper

Ying-Qing Guo[1]*, *Yang Li*[1], *Tian-Tian Yang*[1], *Xingjian Jing*[2], *Xiao Chen*[3] *and Ying Luo*[4]

[1] Mechanical and Electronic Engineering College, Nanjing Forestry University, Nanjing, China, [2] Department of Mechanical Engineering, The Hong Kong Polytechnic University, Hong Kong, China, [3] Nanjing Dongrui Damping Control Technology Co., Ltd, Nanjing, China, [4] Faculty of Civil Engineering and Mechanics, Jiangsu University, Zhenjiang, China

The viscoelastic material is one of most popular shock absorbing materials for mitigating vibrations of building structures due to earthquake. Its dynamic performance is affected by the temperature, the excitation frequency and the excitation amplitude. Therefore, in order to study the non-linear dynamic performance of the viscoelastic materials, a hybrid test system using the electric exciter is proposed, in which the electric exciter is the actuator, MATLAB is used for the simulation of the numerical substructure and the communication between the upper computer and the lower machine, and STM32 single-chip microcomputer is used to control the work state of the electric exciter. Based on the equivalent force control method and the incremental PID control algorithm, a controller is designed to make sure the electric exciter produces accurate control forces to the non-linear test component in the physical substructure. It can be shown from the test results that the developed whole hybrid test system is feasible and effective.

Keywords: viscoelastic damping material, hybrid test, electric exciter, equivalent force control, incremental PID

Edited and reviewed by:
Abid Ali Shah,
University of Science and Technology Bannu, Pakistan

Reviewed by:
Lihua Zhu,
Xi'an University of Architecture and Technology, China
Yanbin Shen,
Zhejiang University, China

****Correspondence:***
Ying-Qing Guo
gyingqing@126.com

Specialty section:
This article was submitted to Structural Materials, a section of the journal Frontiers in Materials

Received: *29 March 2019*
Accepted: *07 May 2019*
Published: *05 June 2019*

Citation:
Guo Y-Q, Li Y, Yang T-T, Jing X, Chen X and Luo Y (2019) Design on Hybrid Test System for Dynamic Performance of Viscoelastic Damping Material and Damper. Front. Mater. 6:116. doi: 10.3389/fmats.2019.00116

INTRODUCTION

In the process of the research of the structural dynamic performance induced by different earthquake, sometimes the core materials or components of the whole structure have very strong non-linearities and unknown properties, which accurate mathematical model cannot be obtained, at the same time, the structure is some kind of large-scale structures, so how to analysis the effect or functions of the core components and the whole structural dynamic performance? Hybrid Test, also called as on-line experiment (Hakuno et al., 1969; Takanashi et al., 1975) is an innovation experimental testing method. Hybrid Test mainly includes two parts: one part is the physical test for the core components of the whole structure; the other part is the numerical simulation for the rest of the whole structure. These two parts are be effectively combined to realize the evaluation of the dynamic performance of the structure and components.

Since the twenty-first century, with the advent of large-scale and complex structures, the hybrid test is developing in two directions: In the spatial domain, in order to integrate the experimental resources from different regions, the hybrid test is developed from local partial tests to network collaborative tests (Mosqueda et al., 2008); In the time domain, in order to test the velocity - dependent specimen, the hybrid test is developed from the rapid test in reality to the real-time test in the ideal (Nakashima, 2001). In 2004, Pearlman et al. (2004) arranged physical substructures and numerical substructures at the University of Colorado and the University of Illinois, respectively, the communication between the upper and lower machines relied on the network, which is a bold attempt to the division and location restrictions of physical substructures and numerical substructure of the hybrid test. In 2005, Pan et al. (2005) developed an Internet online test system which physical test and associated numerical analysis were different location, and the two locations communicate over the Internet. In 2006, Takahashi and Fenves (2006) developed an object-oriented software framework for distributed experimental-computational simulation of structural systems. And they carried out a distributed pseudo-dynamic test using a client-server approach, in which the server program controlled the test equipment in Japan and the client program performed the computational simulation in the United States. In 2009, Carrion et al. (2009) presented an approach for real-time hybrid simulation in which compensation for actuator dynamics was implemented using a model-based feed forward compensator. In 2012, Saouma et al. (2012) developed a specialized software written explicitly to perform, single site, hybrid simulation ranging from pseudo-dynamic to hard real time ones to improve the computational engine of the hybrid test. Chen et al. (2012) presented a real-time hybrid simulation system which included the hydraulic actuators, the IT control architecture, an integration algorithm, and actuator delay compensation. The integration algorithm provided a robust and accurate solution to the equations of motion, and the adaptive inverse compensation method ensured the accurate application of the command displacements to experimental substructure(s) by servo-hydraulic actuators. In 2013, Gao et al. (2013) proposed and validated an H loop shaping design for actuator motion control in real-time hybrid simulation to improve both the stability limit and test accuracy compared with several existing strategies. Furthermore, the feature of the strategy was its robust performance in terms of unmodeled dynamics and uncertainties. In 2016, Na and Kim (2016) developed a non-linear finite element analysis program for hybrid, in which the fixed number iteration method and parallel computational technique was used to shorten the computational time. And, in the real-time control system, the inter-communication between a substructure and an analysis program was simplified. In 2017, Fermandois and Spencer (2017) presented a framework for multi-axial real-time hybrid simulation, which consisted in prescribing multiple degrees-of-freedom at the interface between numerical and experimental substructures by using a multi-actuator loading assembly. The multi-axial real-time hybrid simulation was carried out for a single-story building structure. Xu et al. (2017) developed a hybrid dynamic test system based on electro dynamic fatigue test machine. In this hybrid test system, the electro dynamic fatigue test machine was used as the actuator, simulation program was made based on MATLAB which was easy to modify and debug in accordance with the real test's requirements; the high-performance STM32 single-chip microcomputer was used as the core control chip.

The viscoelastic material is one of most popular shock absorbing materials for mitigating vibrations of building structures due to earthquake (Xu et al., 2019). Its dynamic performance is affected by the temperature, the excitation frequency and the excitation amplitude. This paper presents a hybrid test system to study the non-linear dynamic performance of the viscoelastic materials. In the hybrid test system, the electric exciter is the actuator, MATLAB is used for the simulation of the numerical substructure and the communication between the upper computer and the lower machine, and STM32 single-chip microcomputer is used to control the work state of the electric exciter. Based on the equivalent force control method and the incremental PID control algorithm, a controller is designed to make sure the electric exciter produces accurate control forces to the non-linear test component in the physical substructure. The whole hybrid test system is tested, and the viscoelastic damper adopted as the non-linear test component. The test results show that the developed whole hybrid test system is feasible and effective.

DESIGN SCHEME OF HYBRID TEST SYSTEM

The hybrid test system using the electric exciter mainly includes two parts: the upper computer and the lower machine (that is the physical substructure), as shown in **Figure 1**. In the upper computer, MATLAB is used to write the numerical substructure program and the communication program between the upper computer and the lower machine. The numerical substructure program will realize the modeling and simulation of the numerical substructure. Through the communication program, the upper computer can send the command signals to the lower machine, and accept the displacement or the force signals transmitted by the lower machine. The lower machine, the physical substructure, mainly includes the non-linear test component, the controller, the electric exciter and sensors. The controller takes STM32 single-chip microcomputer as the main controller to write the serial communication program of the upper and the lower machine, the electric exciter control program and sensors data acquisition procedure.

Figure 2 shows the detail design scheme diagram of the hybrid test system. The electric exciter is as the actuator (that is, the power source of the whole system) to realize the loading of the vibration force of the non-linear test component. The STM32 single-chip microcomputer is as the core control chip to realize the data communication between the upper computer and the lower machine, the data collection of the sensors and the drive control of the exciter by using the PID controller. MATLAB is used to complete the modeling and simulation of the numerical substructure and the data communication of the upper computer and the lower machine. Serial communication mode is adopted to realize the real-time two-way communication between STM32 single-chip microcomputer and MATLAB in the upper computer, and to establish the relationship between the numerical substructure and the physical substructure.

DESIGN OF THE HYBRID TEST SYSTEM CONTROLLER

In this paper, the electric exciter is as the actuator, which works on the non-linear test component according to the control signal coming from the upper computer. Here the viscoelastic damper

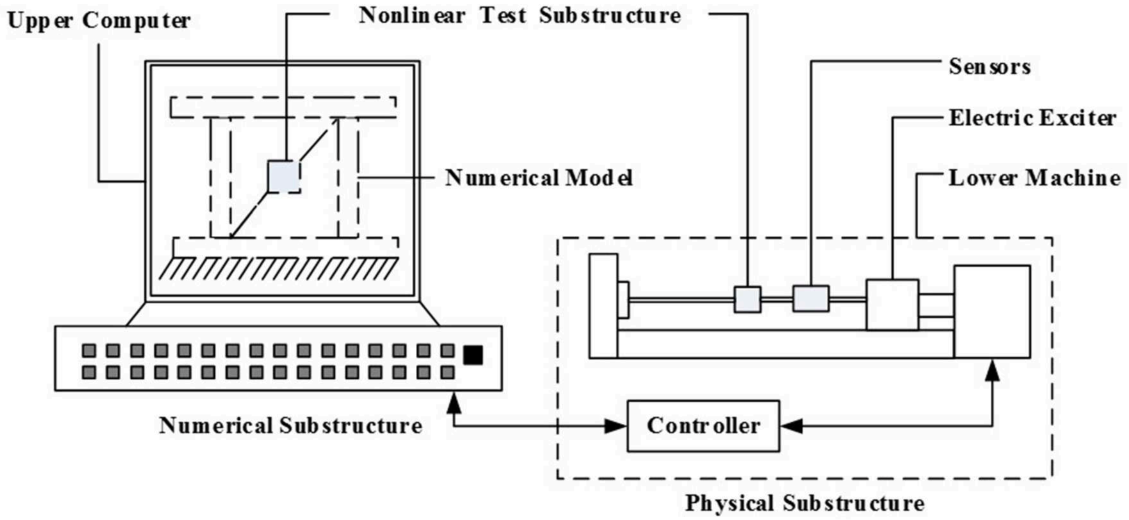

FIGURE 1 | The hybrid test system.

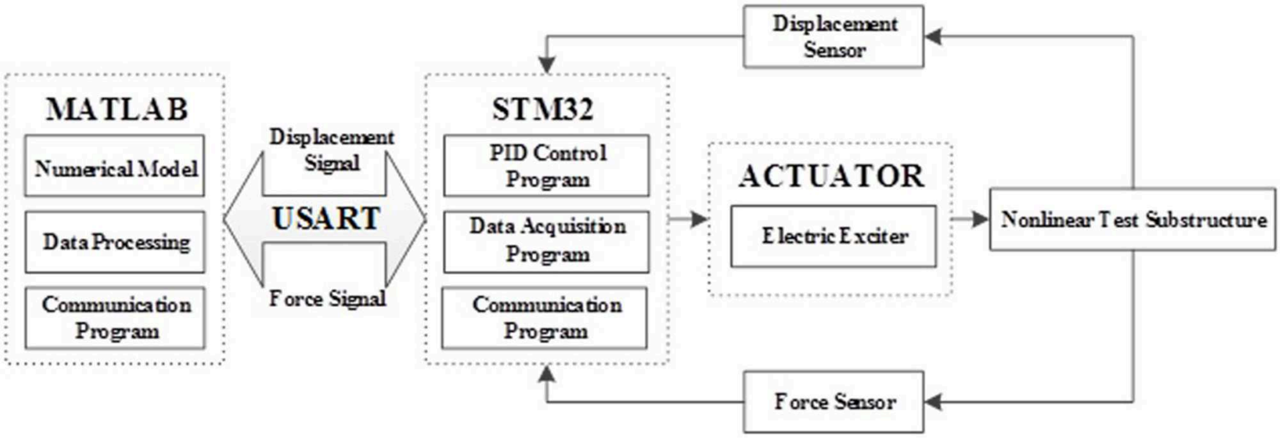

FIGURE 2 | The detail design scheme diagram of the hybrid test system.

is chosen as the non-linear test component. In order to make the electric exciter to produce accurate control forces, the equivalent force control method and the incremental PID control algorithm are used at the same time, as shown in **Figure 3**.

Equivalent Force Control Method

For the electric exciter, its control current is linear with the force it produces. While the test component is non-linear, the equivalent force control method (Wu et al., 2007; Bursi et al., 2008) is used to determine the control signal of the electric exciter. The equations of motion, the expressions of the displacement and the velocity in discrete time are as follows:

$$\mathbf{M}a_{i+1} + \mathbf{C}v_{i+1} + \mathbf{R}_N d_{i+1} + \mathbf{R}_E d_{i+1} = \mathbf{F}_{i+1} \tag{1}$$

$$d_{i+1} = d_i + \Delta t v_i + \frac{\Delta t^2}{4}(a_i + a_{i+1}) \tag{2}$$

$$v_{i+1} = v_i + \frac{\Delta t}{2}(a_i + a_{i+1}) \tag{3}$$

Where, **M** and **C** are the mass matrix and the damping matrix of the structure, respectively, which usually are constants; $\mathbf{R}_N$ is the reaction force vector of the numerical substructure; $\mathbf{R}_E$ is the reaction force vector of the non-linear test component; i is the time step; d_i, v_i, a_i are the displacement, the velocity and the acceleration, respectively; Δt is the integral time interval; **F** is the external load vector.

According to Equations (2, 3), the speed and the acceleration of step i+1 can be described as:

$$a_{i+1} = \frac{4}{\Delta t^2}(-d_i - \Delta t v_i - \frac{\Delta t^2}{4}a_i + d_{i+1}) \tag{4}$$

$$v_{i+1} = -\frac{2}{\Delta t}d_i - v_i + \frac{2}{\Delta t}d_{i+1} \tag{5}$$

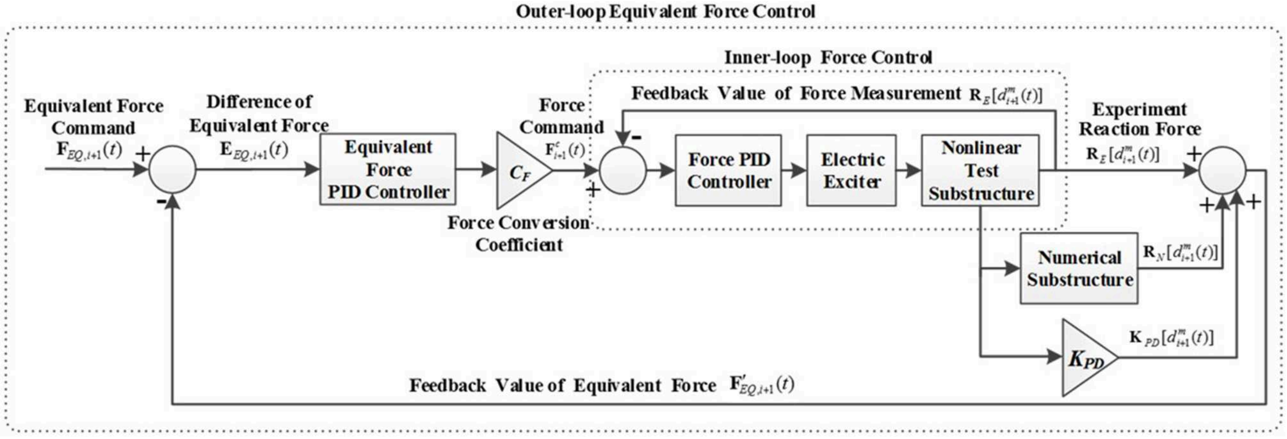

FIGURE 3 | Equivalent force control schematic diagram.

Substitute Equations (4, 5) into Equation (1):

$$\mathbf{R}_N d_{i+1} + \mathbf{K}_{PD} d_{i+1} + \mathbf{R}_E d_{i+1} = \mathbf{F}_{EQ,i+1} \tag{6}$$

$$\mathbf{K}_{PD} = \frac{4\mathbf{M}}{\Delta t^2} + \frac{2\mathbf{C}}{\Delta t} \tag{7}$$

$$\mathbf{F}_{EQ,i+1} = \mathbf{F}_{i+1} + \mathbf{M}a_i + (\frac{4\mathbf{M}}{\Delta t} + \mathbf{C})v_i + (\frac{4\mathbf{M}}{\Delta t^2} + \frac{2\mathbf{C}}{\Delta t})d_i \tag{8}$$

$\mathbf{K}_{PD}$ is a pseudo-stiffness matrix. $\mathbf{F}_{EQ,i+1}$ is the equivalent force for each load cycle, which consists of two parts, the external excitation force $\mathbf{F}_{i+1}$ in the current loading cycle and the pseudo-dynamic effect calculated according to the displacement response in this period. Equation (6) is a non-linear equation about the displacement variable d_{i+1}, which can also be regarded as an equilibrium equation about the equivalent force $\mathbf{F}_{EQ,i+1}$. Meanwhile it can be seen from Equation (6) that the left side of the equation is added by the damping force $\mathbf{R}_N d_{i+1}$ of the numerical substructure, the pseudo-dynamic $\mathbf{K}_{PD} d_{i+1}$ and the experimental reaction force $\mathbf{R}_{EQ} d_{i+1}$ of the non-linear test component,and the right side of the equation can be regarded as the equivalent external force $\mathbf{F}_{EQ,i+1}$. So the solution of the equation is the displacement d_{i+1} of the effect system under the influence of equivalent external force.

The equivalent force control method uses a closed-loop control system, that is, a feedback control method,the control method makes the feedback force [left side of Equation (6)] equal to the equivalent force [right side of Equation (6)]steadily and asymptotically, as shown in **Figure 3**. In each integral time interval Δt, with the equivalent force controller and the force conversion coefficient $\mathbf{C}_F$, the equivalent force difference $\mathbf{E}_{EQ,i+1}(t)$ between the equivalent force command $\mathbf{F}_{EQ,i+1}(t)$ and the equivalent force feedback value $\mathbf{F}'_{EQ,i+1}(t)$ obtain the next force command $\mathbf{F}^c_{i+1}(t)$. At the end of each loading cycle, when the equivalent force feedback value $\mathbf{F}'_{EQ,i+1}(t)$can infinitely approximate the equivalent force $\mathbf{F}_{EQ,i+1}(t)$ command in corresponding to the loading cycle, the actual displacement $d^m_{i+1}(t)$ will be infinitely close to the target displacement $d_{i+1}(t)$ and will become the solution of Equation (6). By the solution of Equation (6), the exciter outputs a corresponding displacement, which in turn produces equivalent force. Among them, $\mathbf{C}_F$ is the force distribution coefficient, its effect is equivalent to Newton iterative method in the Jacobian matrix, the value of the force distribution coefficient $\mathbf{C}_F$ is as follows:

$$\mathbf{C}_F = \frac{\mathbf{K}_E}{\mathbf{K}_{PD}+\mathbf{K}_N+\mathbf{K}_E} \tag{9}$$

Where, $\mathbf{K}_N$ and $\mathbf{K}_E$ are the initial stiffness matrices of the numerical substructure and the non-linear test component respectively.

Design of the Incremental PID Controller

The function of the controller is enabling the equivalent force feedback value track the equivalent force command accurately, the controller is divided into the inner-loop force controller and the outer-loop equivalent force controller. The outer-loop controller is equal-effect control to calculate the force loading command of the electric exciter by the force distribution coefficient. The inner-loop controller is the force control of the electric exciter, so that the electric exciter can accurately reach the force command. The PID controllers are adopted as these two controllers.

In the control system involving computer technology, most of the traditional analog PID cannot be used successfully, because the computer cannot perform integral or differential operation directly,computers can only be simulated infinitely to approach this mathematical calculation in other ways. On the other hand, in the single-chip microcomputer technology, the signal acquisition is also discrete, only can collect signal for feedback periodically through the signal acquisition module. Digital PID algorithm is divided into two kinds, the incremental PID algorithm and the position PID algorithm. The position PID algorithm directly produces the final output of the system in each control period, which is a relatively direct control method. But in this approach, each of the previous errors are accumulated, and the entire system is closely linked before and after each adjustment cycle. It can easily lead to excessive adjustment of the amplitude, and even cause serious control accidents. The incremental PID algorithm converts the analog signal into a digital signal, which is convenient for computer calculation and the single-chip acquisition. On the other hand, compared with the position PID algorithm, the incremental PID algorithm has a smaller calculation, which can guarantee the reliability and real-time performance of the system. Therefore, the incremental PID controller is chosen, and the discrete incremental PID algorithm is as follows:

$$u\left(k\right) = K_P\{e(k) + \frac{T}{T_i}\sum_{k=0}^{m} e(k) + \frac{T_d}{T}[e(k) - e(k-1)]\} \quad (10)$$

Where, $u\left(k\right)$ is the output of the k-th sampling period of the control system, and $e(k)$ is the input deviation of the k-th sampling period of the control system; K_P is the proportional coefficient of the control system; T_i is the integral time constant of the control system; T_d is the differential time constant of the control system; and T is the system sampling period. According Equation (10) the output value of the k-1-th sampling cycle is:

$$u\left(k-1\right) = K_P\{e(k-1) + \frac{T}{T_i}\sum_{k=0}^{m} e(k-1) + \frac{T_d}{T}[e(k-1) - e(k-2)]\} \quad (11)$$

The each adjustment cycle output of the incremental PID controller is the increment of adjustment on the basis of the first 2 times adjustment cycles, so by subtracting Equation (11) from Equation (10), the output equation of the incremental PID controller can be obtained:

$$\Delta u(k) = u(k) - u(k\text{-}1)\Delta u(k) = Ae(k) + Be(k\text{-}1) + Ce(k\text{-}2) \quad (12)$$

Where, $A = K_p(1 + \frac{T}{T_i} + \frac{T_d}{T})$; $B = K_p(1 + 2\frac{T_d}{T})$; $C = K_p\frac{T_d}{T}$.

Simulation Model of System

According to the above principle of equivalent force control, the Matlab/Simulink simulation model of the equivalent force control system of the hybrid test system is shown in **Figure 4**. In the hybrid test system there are two PID controllers, an inner-loop force PID controller and an outer-loop equivalent force PID controller. The "Subsystem" block includes the electric exciter model and the inner-loop force PID controller. The input of the inner-loop force PID controller is the difference between the target force and the actual force, and the output is the control value of the electric exciter. The function of the outer-loop equivalent force PID controller is "forcing" the motion Equation (6) of the hybrid test system to be established to ensure the stability and accuracy of the whole hybrid test system. And its input is the difference of equivalent force.

In the simulation model the viscoelastic damper is chosen as the non-linear test component, and its transfer function is:

$$Fs = \frac{1}{Ce \cdot s + Ke} \quad (13)$$

Where Ce is the equivalent damping of the viscoelastic damper and K_e is the equivalent stiffness of the viscoelastic damper. According to the basic theory of the viscoelastic damper, its parameters can be obtained. The shear modulus is:

$$G_1 = \frac{F_1 \times h}{n \times A \times u_0} \quad (14)$$

The loss factor is:

$$\eta = \frac{F_2}{F_1} \quad (15)$$

The loss modulus is:

$$G_2 = \eta G_1 \quad (16)$$

The equivalent stiffness is:

$$Ke = \frac{F_1}{u_0} = \frac{G_1 A}{h} \quad (17)$$

The equivalent damping is:

$$Ce = \frac{\eta K_E}{\omega} = \frac{G_2 A}{\omega h} \quad (18)$$

Where n is the number of layers of the viscoelastic damping material, A is the shear area of viscoelastic damping material layer, h is the thickness of the viscoelastic damping material layer; u_0 is the maximum displacement of the viscoelastic damper in horizontal direction; F_0 is the maximum damping force of the viscoelastic damper; F_1 is the damping force at the maximum displacement of the viscoelastic damper; F_2 is the damping force at zero displacement of the viscoelastic damper; ω is the loading circular frequency.

TEST ANALYSIS

The test device of the hybrid test system designed in this paper is shown in **Figure 5**. The physical substructure is mainly composed of the electric exciter, the force sensor, the displacement sensor, the viscoelastic damper and STM32 controller. The specific model of the electric exciter is KDJ100. Its maximum exciting force is 1,000 N, its maximum amplitude is ±15 mm and its maximum current is 30A. A plate viscoelastic damper is used as the non-linear component in the hybrid test system, which consists of an intermediate steel plate, two constrain steel plates and two pieces of viscoelastic material, as shown in **Figure 6**. For each piece of viscoelastic material, its area is 20 × 25mm, and its thickness is 8 mm. The thickness of all steel plates is 7 mm. The damping of the viscoelastic damper Ce=5KN·s/m, the stiffness of the viscoelastic damper Ke=200 KN/m. Three sets different sinusoidal signals are used to tests the physical substructure. El-Centro earthquake wave and Tianjin earthquake wave are used as the excitation signals of the whole hybrid test system.

Before testing the performance of the whole hybrid test system, the dynamic performance of the physical substructure is tested firstly. Three sets of sinusoidal signals with the same

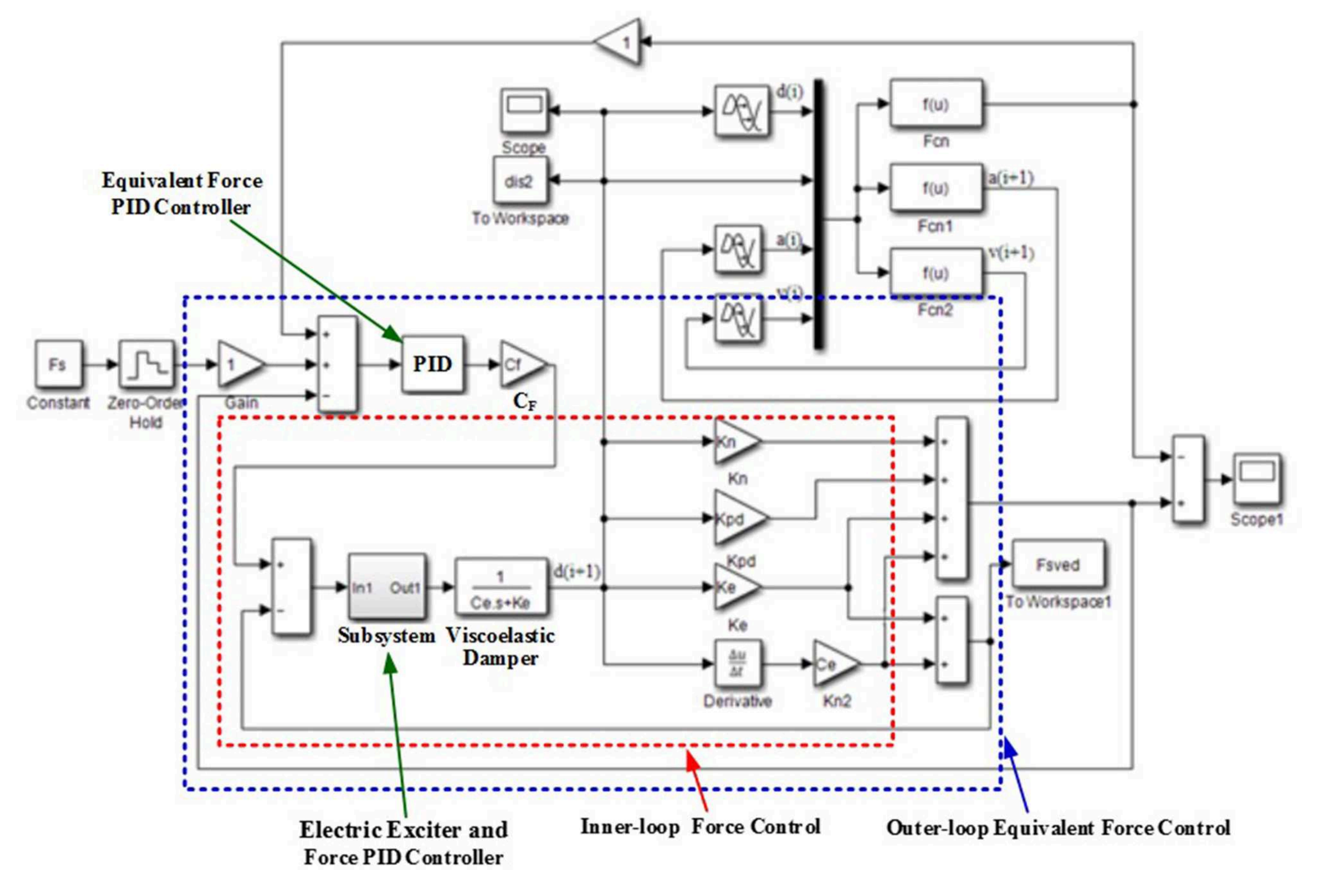

FIGURE 4 | Simulink simulation model of the equivalent control system.

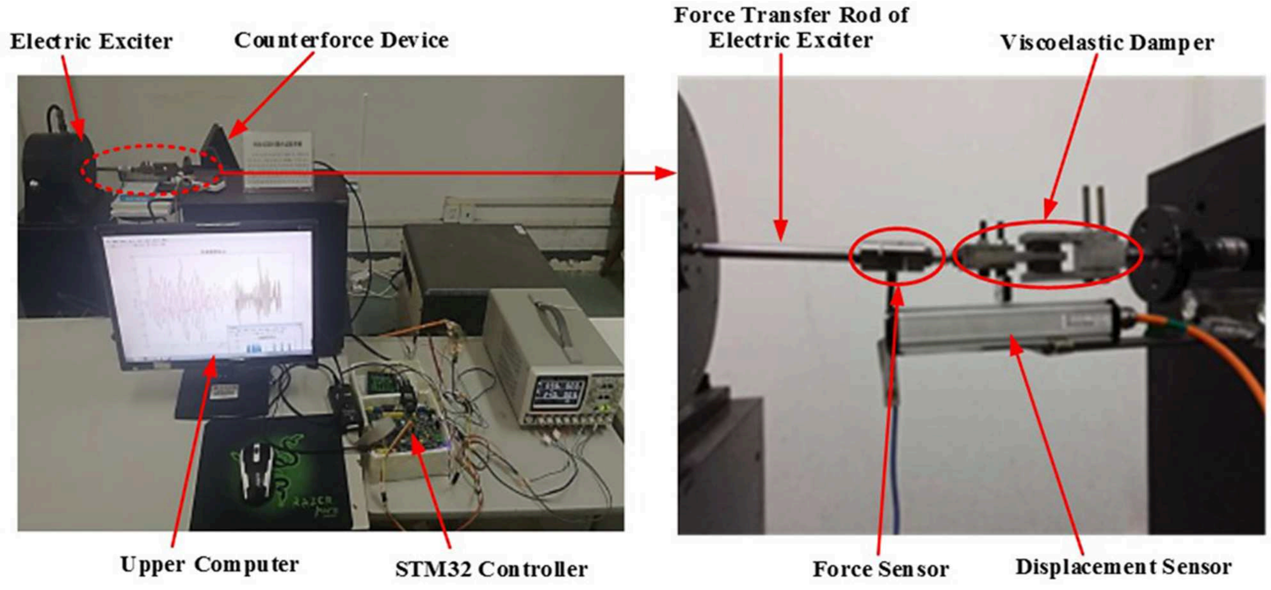

FIGURE 5 | The test device of the hybrid test system.

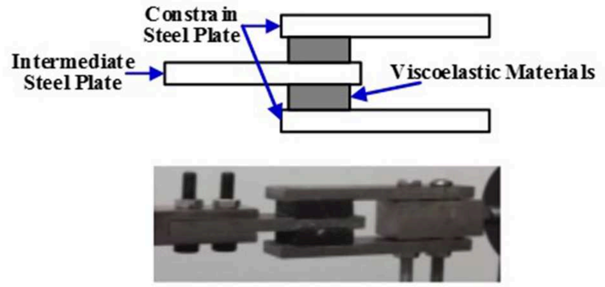

FIGURE 6 | The viscoelastic damper.

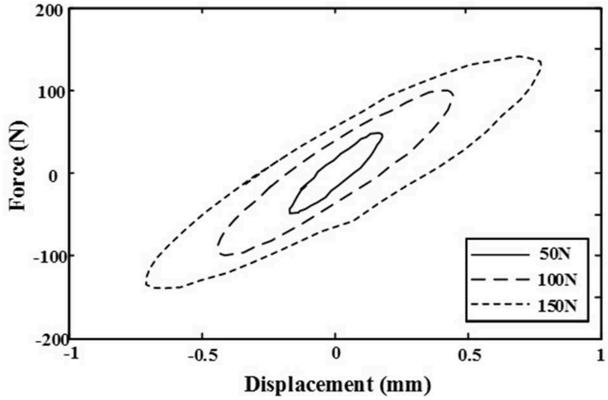

FIGURE 7 | Force-displacement hysteretic curve of the viscoelastic damper.

frequency and different amplitudes are used as the control signals of the electric exciter, which will make the electric exciter to produce the frequencies of the forces all are 5 Hz, and the amplitudes of the forces are 5, 100, and 150 N, respectively. Under these three sets of the forces the force-displacement relationship of the viscoelastic damper are detected by using the force sensor and the displacement sensor in the hybrid test system, and then the results are shown in **Figure 7**. It can be seen that at the same loading frequency, with the increase of the force amplitude, the inclination angle of hysteretic curves of the viscous damper decreases, the envelope area increases, that is, the equivalent stiffness of the viscoelastic damper decreases with the increase of the force amplitude, and the energy dissipation capacity increases with the increase of the force amplitude. Meanwhile, it can be obtained that the physical substructure of the hybrid test system can work normally, and the non-linear component, the viscoelastic damper, has strong non-linearity and good energy dissipation characteristics.

El-Centro earthquake wave and Tianjin earthquake wave are used as the excitation signals of the whole hybrid test system to test its performance. Under different earthquake wave excitation, the output forces of the electric exciter collected in real-time are compared with expected output forces, as shown **Figure 8**. It can be seen from **Figure 8** that whether under El-Centro earthquake wave or under Tianjin earthquake wave, the forces applied to the viscoelastic damper by the electric exciter is in good agreement with the expected forces of theoretical analysis, only there is a certain error at the individual point. Under El-Centro earthquake wave, the maximum force produced by the electric exciter is 191 N, the maximum expected value of the theoretical analysis is 200 N. The absolute error is 9 N and the relative error is 4.5%. The maximum error occurs at the 300th data point, where the experimental value is 141 N and the expected value is 160 N. And the absolute error is 19 N, the relative error is 11.9%. Under Tianjin earthquake wave, the maximum force produced by the electric exciter is 275 N, the maximum expected value of the theoretical analysis is 285 N. The absolute error is 10 N and the relative error is 3.5%. The maximum error appears at the 624th data point, the experimental value is 218 N and the expected value is 250 N. The absolute error is 32 N and the relative error is 12.8%. The main reason for these errors is that the viscoelastic damper is a kind of non-linear damping device, especially the viscoelastic material used in the device has strong non-linear characteristics which dynamic performance is affected by the temperature, the excitation frequency and the excitation amplitude (Xu et al., 2016). In the theoretical analysis, the model parameters of the viscoelastic damper are obtained by analyzing the data of its performance experiment. Within the allowable range of error, these model parameters of the viscoelastic damper can meet the requirements of most excitation frequency and excitation amplitude, but they are fixed values and cannot change with the change of the temperature, the excitation frequency and the excitation amplitude. However, the frequency and the amplitude of El-Centro earthquake wave and Tianjin earthquake wave used in the whole hybrid test system are changed at all times. This causes a certain error between the experimental value and the theoretical value at individual points. In addition, the parameters of the PID controller used in the entire hybrid test system are fixed during the whole test process, so that the control requirements under most excitation can be guaranteed. However, the parameters of the PID controller are not adjusted in real time with the change of the non-linear characteristics of the load, so that the optimal control effect cannot be achieved at individual points in the test process, and a certain error occurs.

CONCLUDING REMARKS

In this paper, a hybrid test system is proposed, in which MATLAB is used for the simulation of the numerical substructure and the communication between the upper computer and the physical substructure; the electric exciter is the actuator; STM32 single-chip microcomputer is used to control the work state of the electric exciter; the viscoelastic damper adopted as the non-linear test component; the force sensor and the displacement sensor are used to measure the force and the displacement of the non-linear test component. In order to make the electric exciter to produce accurate control forces to the non-linear test component in the physical substructure, the controller is designed based on the equivalent force control method and the incremental PID control algorithm. The dynamic performance of the physical substructure and the performance of the whole hybrid test system

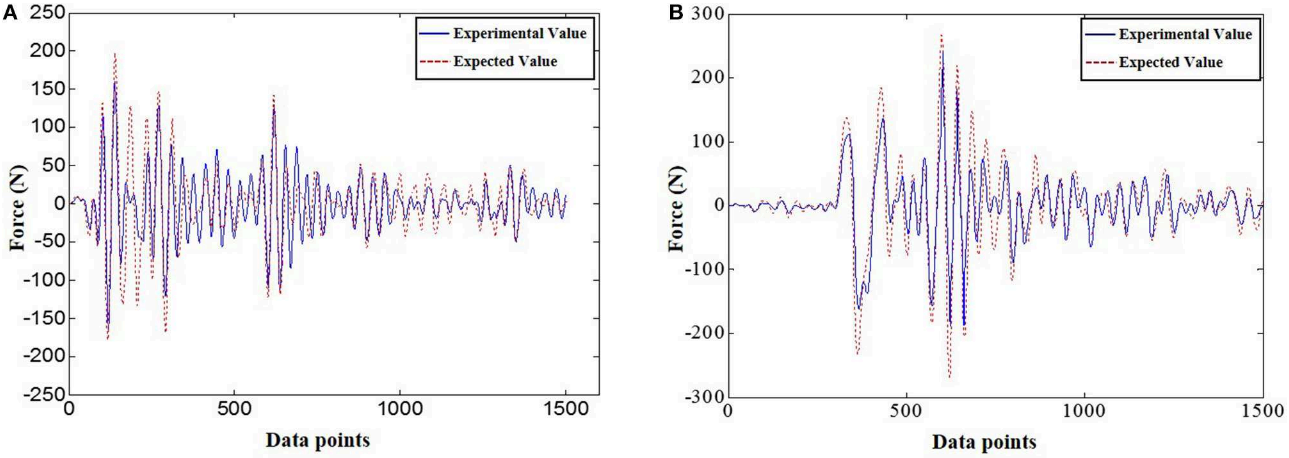

FIGURE 8 | Comparison between experimental value and expected value under different earthquake wave. **(A)** El-Centro earthquake wave. **(B)** Tianjin earthquake wave.

are tested. The test results show that the physical substructure can work normally; the viscoelastic damper has strong non-linearity and good energy dissipation characteristics; and the whole system is feasible and effective.

DATA AVAILABILITY

All datasets generated for this study are included in the manuscript and/or the supplementary files.

AUTHOR CONTRIBUTIONS

Y-QG proposed the idea of this paper. Under the guidance of Y-QG, YaL, XC, XJ, and YiL finish end the numerical analysis. YaL, T-TY, and XC finished the experiment of the hybrid test system. Y-QG, YaL, T-TY, and XJ jointly completed the writing of the article. YiL helped in proof reading of overall presentation and experimental data.

ACKNOWLEDGMENTS

The work was supported by The National Key R&D Programs of China with Grant Numbers (2016YFE0119700 and 2016YFE0200500), Jiangsu International Science and Technology Cooperation Program with Grant Number (BZ2018058), the Program of Chang Jiang Scholars of Ministry of Education, Ten Thousand Talent Program of Leading Scientists and the Program of Jiangsu Province Distinguished Professor.

REFERENCES

Bursi, O. S., Gonzalez-Buelga, A., and Vulcan, L. (2008). Novel coupling rosen brock-based algorithms for real-time dynamic substructure testing. *Earthqu. Eng. Struct. Dynam.* 37, 339–360. doi: 10.1002/eqe.757

Carrion, J. E., Spencer B. F. Jr., and Phillips, B. M. (2009). Real-time hybrid simulation for structural control performance assessment. *Earthqu. Eng. Eng. Vibrat.* 8, 481–492. doi: 10.1007/s11803-009-9122-4

Chen, C., Ricles, J. M., Karavasilis, T. L., Chae, Y., and Sause, R. (2012). Evaluation of a real-time hybrid simulation system for performance evaluation of structures with rate dependent devices subjected to seismic loading. *Eng. Struct.* 35, 71–82. doi: 10.1016/j.engstruct.2011.10.006

Fermandois, G., and Spencer, B. F. Jr. (2017). Model-based framework for multi-axial real-time hybrid simulation testing. *Earthqu. Eng. Eng. Vibrat.* 16, 671–691. doi: 10.1007/s11803-017-0407-8

Gao, X., Castaneda, N., and Dyke, S. J. (2013). Real time hybrid simulation: from dynamic system, motion control to experimental error. *Earthqu. Eng. Struct. Dynam.* 42, 815–832. doi: 10.1002/eqe.2246

Hakuno, M., Shidawara, M., and Hara, T. (1969). Dynamic destructive test of a cantilever beam, controlled by an analog-computer. *Trans. Jpn. Soc. Civil Eng.* 1969, 1–9. doi: 10.2208/jscej1969.1969.171_1

Mosqueda, G., Stojadinovic, B., Hanley, J., Sivaselvan, M. (2008). Hybrid seismic response simulation on a geographically distributed bridge model. *J. Struct. Eng.* 134, 535–543. doi: 10.1061/(ASCE)0733-9445(2008)134:4(535)

Na, O., and Kim, S. (2016). Multi-directional structural dynamic test using optimized real-time hybrid control system. *Exp. Techn.* 40, 441–452. doi: 10.1007/s40799-016-0047-3

Nakashima, M. (2001). Development, potential, and limitations of real-time online (pseudo-dynamic) testing. *Philos. Trans. R. Soc. A Math. Phys. Eng. Sci.* 359, 1851–1867. doi: 10.1098/rsta.2001.0876

Pan, P., Tada, M., and Nakashima, M. (2005). Online hybrid test by internet linkage of distributed test-analysis domains. *Earthqu. Eng. Struct. Dynam.* 34, 1407–25. doi: 10.1002/eqe.494

Pearlman, L., Kesselman, C., Gullapalli, S., Spencer, B. F Jr., Futrelle, J., Ricker, K., et al. (2004). "Distributed hybrid earthquake engineering experiments: experiences with a ground-shaking grid application," in *13th IEEE International Symposium on High Performance Distributed Computing, Proceedings* (Honolulu, HI), 14–23. doi: 10.1109/HPDC.2004.1323474

Saouma, V., Kang, D. H., and Haussmann, G. (2012). A computational finite-element program for hybrid simulation. *Earthqu. Eng. Struct. Dynam.* 41, 375–389. doi: 10.1002/eqe.1134

Takahashi, Y., and Fenves, G. L. (2006). Software framework for distributed experimental-computational simulation of structural systems. *Earthqu. Eng. Struct. Dynam.* 35, 267–291. doi: 10.1002/eqe.518

Takanashi, K., Udagawa, K., Seki, M., Okada, T., and Tanaka, H. (1975). Nonlinear earthquake response analysis of structures by a computer-actuator on-line system: part 1: details of the system. *Trans. Arch. Instit. Jpn*. 229, 77–83. doi: 10.3130/aijsaxx.229.0_77

Wu, B., Wang, Q., and Shing, P. B. (2007). Equivalent force control method for generalized real-time substructure testing with implicit integration. *Earthqu. Eng. Struct. Dynam.* 39, 1127–1149. doi: 10.1002/eqe.674

Xu, Z. D., Huang, X. H., Xu, F. H., and Yuan, J. (2019). Parameters optimization of vibration isolation and mitigation system for precision platforms using nondominated sorting genetic algorithm. *Mechan. Syst. Signal Process.* 128: 191–201. doi: 10.1016/j.ymssp.2019.03.031

Xu, Z. D., Liao, Y. X., Ge, T., and Xu, C. (2016). Experimental and theoretical study on viscoelastic dampers with different matrix rubbers. *J. Eng. Mechan. ASCE* 142:04016051. doi: 10.1061/(ASCE)EM.1943-7889.0001101

Xu, Z. D., Wang, K. Y., Guo, Y. Q., Wu, M. D., and Xu, M. (2017). Hybrid test on building structures using electrodynamic fatigue test machine. *Nondestruc. Test. Eval.* 32, 90–102. doi: 10.1080/10589759.2016.1149581

Conflict of Interest Statement: XC was employed by company Nanjing Dongrui Damping Control Technology Co., Ltd, Nanjing, China.

The remaining authors declare that the research was conducted in the absence of any commercial or financial relationships that could be construed as a potential conflict of interest.

frontiers in Materials

ORIGINAL RESEARCH
published: 14 May 2019
doi: 10.3389/fmats.2019.00109

A Two-Step Transformation Approach for ESS Model of Viscoelastic Material to Time Domain

Xing-Huai Huang[1]*, *Ze-Feng He*[2] *and Ye-Shou Xu*[1]

[1] *Key Laboratory of C&PC Structures of the Ministry of Education, Southeast University, Nanjing, China,* [2] *College of Civil Engineering, Xi'an University of Architecture and Technology, Xi'an, China*

ESS (Equivalent Standard solid) model is proofed to be accurate for describing the physical properties of viscoelastic material under different temperatures and excitation frequencies. However, the ESS model faces difficulties for calculating time history responses. Therefore, a two-step transformation approach for ESS model to time domain is proposed, which can obtain precise time history response of structural finite element models of with dampers made of viscoelastic materials. In the first step of the approach, ESS model is extended from frequency domain to complex frequency domain. In the second step, a high-precision numerical inverse Laplace transform method is chosen to transform the model from complex frequency domain to time domain. Experimental and numerical tests are conducted to verify the effectiveness of the two-step transformation approach under simple harmonic external excitation. The comparisons indicate that the approach is accurate under different temperatures and excitation frequencies. Finally, the time domain dynamic responses of the viscoelastic dampers are obtained under earthquake excitations. Comparing to the equivalent linearization method for ESS model, the proposed two-step transformation approach has absolute advantage to obtain accurate results under random excitation, such as earthquake excitations.

Keywords: viscoelastic material, ESS model, transformation approach, earthquake excitation, equivalent linearization method

Edited by:
Abid Ali Shah,
University of Science and Technology Bannu, Pakistan

Reviewed by:
Zheng Lu,
Tongji University, China
Antonio Caggiano,
Darmstadt University of Technology, Germany

***Correspondence:**
Xing-Huai Huang
hxh3956537@gmail.com

Specialty section:
This article was submitted to Structural Materials, a section of the journal Frontiers in Materials

Received: *27 February 2019*
Accepted: *25 April 2019*
Published: *14 May 2019*

Citation:
Huang X-H, He Z-F and Xu Y-S (2019) A Two-Step Transformation Approach for ESS Model of Viscoelastic Material to Time Domain. Front. Mater. 6:109. doi: 10.3389/fmats.2019.00109

INTRODUCTION

Viscoelastic material has strong energy dissipation capacity based on massive fillers within high molecular polymers, which exhibits physical properties of both viscous and elastic. When deformations occur under the reciprocating stress, the motion of the matrix molecular chain inside the material will fracture and recombination. In the meantime, mutual friction will occur between the fillers, or between the filler and the matrix. In such physical movement, a part of the energy is stored, and the other part of the energy is converted into thermal energy dissipated to the air (Trindade et al., 2000). The viscoelastic damper is a kind of energy dissipation device used in structural wind-resistant and seismic engineering, which is mainly composed of viscoelastic material and constrained steel plates. The dampers based on viscoelastic material has the characteristics of reliable performance, convenient installation, good damping effect and low cost of produce and maintenance (Park, 2001). However, the physical properties of viscoelastic material are affected significantly greatly by temperature and excitation frequency (Xu et al., 2019). As a result the viscoelastic dampers show strong non-linear characteristics in the working environment. And how to accurately calculate or simulate the mechanical properties of viscoelastic materials is a complex problem (Lewandowski and Chorazyczewski, 2010). A large number of scholars have studied viscoelastic materials and put forward a series of mechanical models, including Maxwell model, Kelvin model, standard solid model (Kim et al., 2003), ESS (equivalent standard solid) model (Xu, 2007; Xu et al., 2011), equivalent stiffness and equivalent damping model (Yoshida et al., 2002), fractional derivative model (Xu et al., 2015), Finite element model, complex stiffness model, Standard rheological model (Mould et al., 2011; Lee and Choi, 2018), fractional index model (Gonzalez et al., 2016; Chen et al., 2018), micro-oscillator model (Mctavish and Hughes, 1993), and so on. The ESS model is a new computational model based on temperature frequency equivalent principle and standard linear solid model, which can correctly describe the variation of viscoelastic damper with the change of temperature and frequency. Besides, the physical concept of the model is clear, and parameters of the ESS model can be quickly obtained through simple harmonic loading tests. As a result, it becomes one of the classical mechanical models of viscoelastic materials in the field of scientific research, and has been widely promoted and applied in engineering (Bhatti, 2013; Xu et al., 2014; Mehrabi et al., 2017; Xu Y. et al., 2017; Xu Z. et al., 2017).

However, the ESS model is the constitutive model based on frequency domain, which needs special mathematical strategy to obtain the time history response under forced vibration or free vibration determined by initial value problem. The most conventional mean current is to use the equivalent linearization method. By the equivalent linearization method, the viscoelastic material is expressed with two constant simplified parameters, i.e., equivalent stiffness and equivalent damping (Park et al., 2007). With the change of dynamic characteristics caused by variation of frequency and temperature, inestimable error will be introduced both in theory or practical application. So the ESS model lose its advantage, which is the high precision for describing the physical property of viscoelastic models. Aiming at the above problems, this paper presents a two-step transformation approach for ESS model of viscoelastic material to time domain, which can accurately obtain the time-domain dynamic response and avoid the establishment of differential equations. The approach directly starts from the frequency domain expressions of the ESS model, and then take two steps to solve the problem. The key innovation of the proposed method is making the ESS model suitable for random excitations. The standard theoretical tools in frequency domain, like the SS model and ESS model, are accurate and simple, but is not applicable in time domain. The standard models in time domain, like fractional derivative model and finite element model, are applicable in time domain, but they are complex in both mathematical formula and experimental tests. The presented model have the advantages in both frequency-domain and time domain, which is the main novel advances of this paper. As a result, the ESS model can be transferred to time domain and produce time history responses of viscoelastic dampers under earthquake excitations or any other stochastic excitations.

TWO-STEP TRANSFORM APPROACH OF ESS MODEL

The ESS model is suitable in frequency domain, which means it cannot be transformed to time domain directly. In the first step, the ESS model is extended to Laplace domain. In this step the key problem is the imaginary part will cause failure of the second step. As a result the imaginary unit j should be eliminated by certain substitution to prepare for the next step. In the second step, the Laplace expression is transformed to time domain. In this step the key problem is to simplify the formula to reduce the amount of calculation work.

STEP 1

ESS model is a mechanical model describing viscoelastic materials, which can not only describe the influence of performance change with frequency and temperature, but can also describe the relaxation and creep characteristics of viscoelastic dampers. Its expression is known as follows (Xu Y. et al., 2017):

$$\begin{aligned} G_1 &= \left(q_0 + p_1 q_1 \alpha_T^c \omega^c\right) / \left(1 + p_1^2 \alpha_T^c \omega^c\right) \\ \eta &= \left(q_1 - p_1 q_0\right) \alpha_T^d \omega^d / \left(q_0 + p_1 q_1 \alpha_T^{2d} \omega^{2d}\right) \end{aligned} \qquad (1)$$

In the equation, G_1 represents the energy storage modulus, η is loss factor, ω represents the circular frequency of the excitation load, p_1, q_0, q, c, d, T_0 are the material parameters of the ESS model respectively, which are generally obtained according to the performance test of the representative material. The dissipation modulus G_2 can be obtained from Equation (1):

$$G_2 = G_1 \eta = \frac{\left(q_0 + p_1 q_1 \alpha_T^c \omega^c\right)\left(q_1 - p_1 q_0\right) \alpha_T^d \omega^d}{\left(1 + p_1^2 \alpha_T^c \omega^c\right)\left(q_0 + p_1 q_1 \alpha_T^{2d} \omega^{2d}\right)} \qquad (2)$$

The frequency response function $H(\omega)$ of the system can be determined by the ESS model, as shown in equation (3):

$$H(\omega) = \frac{\tau(\omega)}{\gamma(\omega)} = G_1(\omega) + \mathrm{j} G_2(\omega) \qquad (3)$$

In the equation, τ is the shear stress of the material, γ is the shear strain of the material, and j indicates the unit imaginary number. Equation (3) belongs to the category of frequency domain, which is a specific form ($\sigma = 0$) of Laplace domain ($s = \sigma + \mathrm{j}\omega$), so it is necessary to transform the equivalent standard solid model of frequency category to Laplace domain. The frequency response function is transformed into system function $H(s)$, as shown in Equation (4):

$$\begin{aligned} H(s) = G_1(s) + \mathrm{j} G_2(s) \\ &= \frac{\left(q_0 + \mathrm{j}^{-c} p_1 q_1 \alpha_T^c s^c\right)\left(q_0 + \mathrm{j}^{-2d} p_1 q_1 \alpha_T^{2d} s^{2d}\right)}{\left(1 + \mathrm{j}^{-c} p_1^2 \alpha_T^c s^c\right)\left(q_0 + \mathrm{j}^{-2d} p_1 q_1 \alpha_T^{2d} s^{2d}\right)} \\ &+ \frac{j^{1-d}\left(q_0 + \mathrm{j}^{-c} p_1 q_1 \alpha_T^c s^c\right)\left(q_1 - p_1 q_0\right) \alpha_T^d s^d}{\left(1 + \mathrm{j}^{-c} p_1^2 \alpha_T^c s^c\right)\left(q_0 + \mathrm{j}^{-2d} p_1 q_1 \alpha_T^{2d} s^{2d}\right)} \end{aligned} \qquad (4)$$

Both real and imaginary parts exist in the system function as Equation. The transform methods of real part and imaginary part of system function are different, because the imaginary part cannot be transformed to the time domain directly. Some derivation and transformation have to be performed before final transformation. Firstly the real part and imaginary part has to be separated, so the imaginary term j^{--c} and j^{-2d} should be factorized as Equation (5):

$$\begin{aligned}\mathrm{j}^{-c} &= \left(e^{\mathrm{j}\pi/2}\right)^{-c} = e^{\mathrm{j}\pi c/2} = \cos(\pi c/2) - \mathrm{j}\sin(\pi c/2)\\ \mathrm{j}^{-2d} &= \left(e^{\mathrm{j}\pi/2}\right)^{-2d} = e^{-\mathrm{j}\pi 2d} = \cos\left(\pi d\right) - \mathrm{j}\sin\left(\pi d\right)\end{aligned} \quad (5)$$

After substituting Equation to Equation, the real and imaginary part of the system function will be separated as Equation (6)

$$H(s) = \mathrm{real}(H(s)) + \mathrm{jimag}(H(s)) = H_1(s) + \mathrm{j}H_2(s) \quad (6)$$

where $H_1(s)$ represents the real part, and $\mathrm{j}H_2(s)$ represents the imaginary parts of the system function. The physical meaning of Equation (6) is two systems connected in parallel. Because $s = \sigma + \mathrm{j}\omega$ and $\sigma = 0$, so $\mathrm{j} = \mathrm{s}/\omega$. As a result the imaginary part can be expressed in another form as Equation (7) to transform the imaginary part into time domain.

$$H(s) = H_1(s) + \frac{s}{\omega}H_2(s) \quad (7)$$

For the real part $H_1(s)$, the system function can be transformed to frequency response function $H_1(\mathrm{j}\omega)$ in frequency domain by letting $\sigma = 0$. The frequency response function $H_1(\mathrm{j}\omega)$ can be represented by Equation (8)

$$H_1\left(j\omega\right) = G_{1\_1} + jG_{1\_2} \quad (8)$$

where G_{1_1} is the storage modulus of the system $H_1(s)$, G_{1_2} is the loss modulus of $H_1(s)$. When sinusoidal excitation $u = u_0\sin(\omega t)$ applies on the system $H_1(s)$, the output of the system can be expressed as Equation (9)

$$f_1(t) = G_{1\_1}\sin(\omega t) + G_{1\_2}\cos(\omega t) \quad (9)$$

For the imaginary part $\mathrm{j}H_2(s)$, the system function cannot be converted to time domain directly. So at first, we transform $H_2(s)$ in to time domain. The frequency response function $H_2(\mathrm{j}\omega)$ can be represented by Equation (10)

$$H_2\left(j\omega\right) = G_{2\_1} + \mathrm{j}G_{2\_2} \quad (10)$$

where G_{2_1} is the storage modulus of the system $H_2(s)$, G_{2_2} is the loss modulus of $H_2(s)$. When sinusoidal excitation $u = u_0\sin(\omega t)$ applies on the system $H_2(s)$, the output of the system $g_2(t)$ can be expressed as Equation (11).

$$g(t) = G_{2\_1}\sin(\omega t) + G_{2\_2}\cos(\omega t) \quad (11)$$

As mentioned above, $\mathrm{s}H_2(s)/\omega$ is chosen to represent $\mathrm{j}H_2(s)$.When $g(t)$ is the original function of $H_2(s)$, the inverse Laplace transform of $\mathrm{s}H_2(s)$ is $f_2(t) = g^{'}(t)$, which means the derivative of the original function $g(t)$. So the output of the system can be expressed as Equation (12).

$$f_2(t) = \frac{g'(t)}{\omega} = -G_{2\_2}\sin(\omega t) + G_{2\_1}\cos(\omega t) \quad (12)$$

So the final system output $f(t)$ of the viscoelastic material in time domain can be expressed as Equation (13).

$$\begin{aligned}f(t) = f_1(t) + f_2(t) &= \left(G_{1\_1} - G_{2\_2}\right)\sin(\omega t)\\ &\quad + \left(G_{1\_2} + G_{2\_1}\right)\cos(\omega t)\end{aligned} \quad (13)$$

The above formula (13) shows the expression of the system output of the viscoelastic material under the harmonic excitation. However, the excitation in reality is often a non-harmonic random excitation. The derivation for the time domain response of the viscoelastic material under random displacement excitation is derived in the similar as the system in harmonic excitation. In Laplace domain, the output force of the system can be expressed as Equation (14).

$$\tau(s) = H(s)\cdot\gamma(s) = H_1(s)\cdot\gamma(s) + jH_2(s)\cdot\gamma(s) \quad (14)$$

where the input displacement γ can be decomposed into a superposition of multiple sinusoidal signals. The decomposition can be realize by Fourier transformation as Equation (15).

$$\gamma(t) = \sum_{n=1}^{\infty}\gamma_n(n\omega_0 t) = a_0 + \sum_{n=1}^{\infty}a_n\cos n\omega_0 t + b_n\sin n\omega_0 t \quad (15)$$

where n is the order of Fourier transformation, and ω_0 is the minimum circular frequency of the decomposed signals, and it is correlated with the sampling frequency of the original random signal $\gamma(t)$. a_0, a_n, b_n are the Fourier coefficients. Then Equation can be modified as Equation (16).

$$\tau(s) = H_1(s)\cdot\gamma(s) + H_2(s)\cdot\sum_{n=1}^{N}\frac{s\gamma_n(s)}{\omega_n} \quad (16)$$

where $\omega_\mathrm{n} = n\omega_0$, which means the circular frequency of the order n of the input signal. Then inverse Laplace transformation is performed on Equation. The following derivation will focus on the invers Laplace transformation of Equation (16).

STEP 2:

After the system function in Laplace domain is obtained, the numerical method of inverse Laplace transformation can be used to obtain the dynamic response in time domain. The direct inversion method is only suitable for simple function which can be decomposed into simple polynomial combination. As for the complexity of the system function of ESS model in Laplace domain, a numerical method is implemented to calculate the inverse transformation (Valsa and Brancik, 1998). The inverse Laplace transform expressions are as follows:

$$f(t) = L^{-1}\{F(s)\} = \frac{1}{2\pi\mathrm{j}}\int_{\sigma-\mathrm{j}\infty}^{\sigma+\mathrm{j}\infty}F(s)e^{st}\mathrm{d}s \quad (17)$$

Because the upper and lower limits of the integral of Equation (17) contain the positive and negative infinite amount in the imaginary part, it is not possible to integrate Equation (17) directly, so it is necessary to conduct mathematical substitution, if constant a>σt, then $|e^{-2a+2st}|<<1$, so:

$$\begin{aligned} e^{st} &= \frac{e^{st}}{1+e^{-2a+2st}} = \frac{e^{a}}{e^{a-st}+e^{-a+st}} \doteq \frac{e^{a}}{2\cosh(a-st)} \\ &= \pi e^{a}\sum_{n=0}^{\infty}\frac{(-1)^{n}(n+1/2)}{(n+1/2)^{2}\pi^{2}+(a-st)^{2}} \end{aligned} \tag{18}$$

The time domain results can be expressed as Equation (19):

$$f_c(t,a) = \frac{e^{a}}{2j}\int_{\sigma-j\infty}^{\sigma+j\infty}F(s)\sum_{n=0}^{\infty}\frac{(-1)^{n}(n+1/2)}{(n+1/2)^{2}\pi^{2}+(a-st)^{2}}\mathrm{d}s \tag{19}$$

Equation (19) can be simplified to:

$$f_c(t,a) = \frac{e^{a}}{2j}\sum_{n=0}^{\infty}(-1)^{n}(n+1/2)I_n \tag{20}$$

In which

$$\begin{aligned} I_n &= \int_{\sigma-j\infty}^{\sigma+j\infty}\frac{F(s)}{(n+1/2)^{2}\pi^{2}+z^{2}}\mathrm{d}s \\ &= \int_{\sigma-j\infty}^{\sigma+j\infty}\frac{F(s)}{G_n(s)}\mathrm{d}s = \int_{\sigma-j\infty}^{\sigma+j\infty}K_n(s)\,\mathrm{d}s \end{aligned} \tag{21}$$

In order to solve Equation (21), the original integral path can be regarded as the integral path of the semicircle of the right half plane radius of the coordinate system, so the system singularity points can be obtained as follows:

$$s_{1,2} = \frac{a \pm j(n+1/2)\pi}{t} \tag{22}$$

The integral along the contour is equal to the sum of the remaining digits of all singularities in the contour, so:

$$\begin{aligned} I_n &= -2\pi \mathrm{j}\left[\mathrm{res}_{s=s_1}K_n(s) + \mathrm{res}_{s=s_2}K_n(s)\right] \\ &= -2\pi \mathrm{j}\left[\frac{F(s_1)}{G'_n(s_1)} + \frac{F(s_2)}{G'_n(s_2)}\right] = \frac{F(s_2)-F(s_1)}{t(n+1/2)} \\ &= \frac{F\left[a-j(n+1/2)\pi\right] - F\left[a+j(n+1/2)\pi\right]}{t(n+1/2)} \end{aligned} \tag{23}$$

Finally, the time domain results are obtained:

$$\begin{aligned} f_c(t,a) &= \frac{e^{a}}{2j}\sum_{n=0}^{\infty}(-1)^{n}(n+1/2)\frac{F(s_2)-F(s_1)}{t(n+1/2)} \\ &= \frac{e^{a}}{2jt}\sum_{n=0}^{\infty}(-1)^{n}\left[F(s_2)-F(s_1)\right] \end{aligned} \tag{24}$$

The system function Equation (16) of the equivalent standard solid model is substituted into the Equation (15) to obtain the final result:

$$f_c(t,a) = \frac{e^{a}}{2jt}\sum_{n=0}^{\infty}(-1)^{n}\left[K(s_2)-K(s_1)\right] \tag{25}$$

According to Equation (16), the system function $H(s)$ in the complex frequency domain is transformed to the time domain. Under arbitrary input load, the response of the system at any time t can be directly solved by the above functions.

$$\tau_c(t,a) = \frac{e^{a}}{2jt}\sum_{n=0}^{\infty}(-1)^{n}\left[\tau(s_2)-\tau(s_1)\right] \tag{26}$$

Note that the inverse Laplace transformation on Equation (26) can be simplified. In Equation (16), because $\gamma(t)$is the original function of $\gamma(s)$, so the original function of $s\gamma(s)$ is $\gamma'(t)$, which means the derivative of $\gamma(t)$. As a result, the inverse transform only performed on $H_1(s)$ and $H_2(s)$, the remaining term only need to be derivation and convolution. So the final force output of the viscoelastic material under random displacement excitation can be expressed as Equation (27)

$$\tau(t) = L^{-1}\left[H_1(s)\right]*\gamma(t) + L^{-1}\left[H_2(s)\right]*\sum_{n=1}^{N}\frac{\gamma'_n(t)}{\omega_n} \tag{27}$$

Where L^{-1} means the inverse Laplace transform operator, * means the convolution operator.

VALIDATION UNDER HARMONIC LOAD

In order to verify the correctness of the above method, the preliminary test data of 9050A viscoelastic material in Wuxi Shock absorber Company are analyzed. The 9050A material is composed of high polymer, and is based on Nitrile Butadiene Rubber matrix and vulcanized at high temperature and pressure with variety of additives. The parameters of the material are also listed below. During the experimental test, the temperature is assumed to be uniform in the material, so only the temperature of the surface is measured. According to the test results of the material at different temperature and different frequency, the material parameters are determined by the ESS model, which are, $p_1 = 0.0240$, $q_0 = 2.8440 \times 10^6$, $q_1 = 5.940 \times 10^5$, $c = 1.5650$, d $= 0.7825$, $T_0 = 45.639^{\mathrm{o}}$C. The above parameters will determine the mechanical properties of viscoelastic materials.

The dynamic response of the viscoelastic damper of 9050A viscoelastic material under harmonic displacement excitation is calculated by equivalent linearization method and time domain extension method, respectively. The excitation frequency is 1 Hz, the excitation amplitude is 1 cm, and the force-time curve is shown in **Figure 1**, the force-displacement curve is shown in **Figure 2**.

As can be seen from **Figures 1**, **2**, the results are different at the initial moment between the proposed approach and equivalent linearization method. The force response obtained by

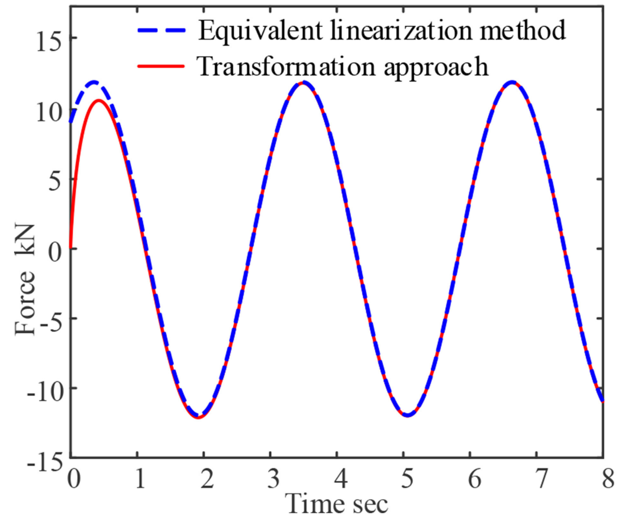

FIGURE 1 | Time history response of viscoelastic damper under harmonic load.

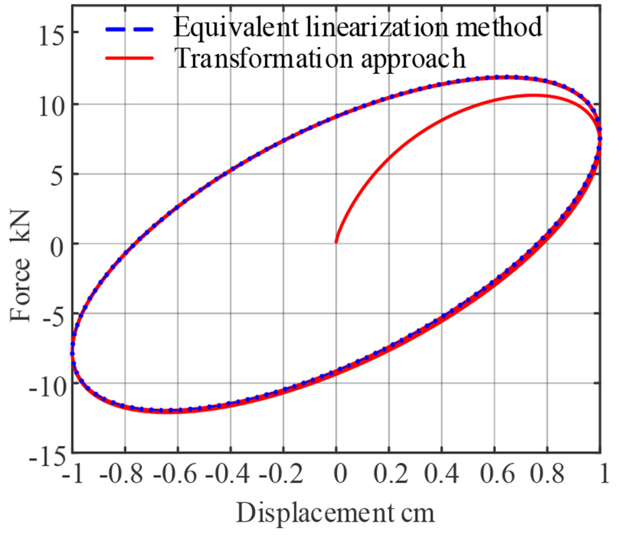

FIGURE 2 | Force-Displacement curve of viscoelastic resistance under harmonic load.

the proposed approach starts from the origin point, which reflects the relaxation characteristics of viscoelastic materials. The stress relaxation phenomenon is important in viscoelastic materials. When displacement is applied on a system with stress relaxation behavior, the output force of should start from 0, which is proved by Maxwell model. The Maxwell model is good at predicting the stress relaxation phenomenon by akin to a spring being in series with a dashpot. In contrast, the equivalent linearization model cannot reflect the relaxation response of viscoelastic materials. In addition, the results of the two methods tend to be equal after about 1 s, which indicates that the steady-state solution of the two-step transformation approach is correct.

The calculation formula of the storage modulus G_1 and the loss factor η from the force-displacement hysteresis curve is as follows:

$$G_1 = \frac{2E}{\gamma_0^2}$$
$$\eta = \frac{E_d \gamma_0^4}{2\pi E} \tag{28}$$

Where E_d represents the area surrounded by the force-displacement hysteresis curve, E represents the strain energy stored when the material produces the maximum strain γ_0, and γ_0 represents the maximum strain of the material. According to formula (17), in the case of the viscoelastic dampers at a temperature of -10°C, 0°C, 10°C, 20°C, under the input frequency for 0.1, 0.5, 1, 2 rad, the storage modulus and loss factor test and theoretical analysis of the results of the comparison can be calculated and as shown in **Table 1**. From the table, the comparison of the calculation results between the proposed approach and the equivalent linearization method, the maximum error of the energy storage modulus G_1 is 0.0054%, the maximum error of the loss Factor η is 0.2797%, and the error analysis indicates that the time domain extension method has sufficient precision for solving the solution. Note that the comparison is between the ESS model and the proposed two-step transformation approach. There are limitations of the ESS model that it cannot be used under earthquake excitations. So the two-step transformation approach is proposed to conquer this shortage. The comparison between ESS model and the proposed method indicates that the proposed method is indeed transferring the ESS model to time domain without bring much errors.

VALIDATION UNDER RANDOM EXCITATION

The two-step transformation approach adopts exactly the same mathematical strategy to process both harmonic and earthquake excitations. The comparisons under harmonic excitation indicate that not only the results under harmonic excitation is correct, but also the total mathematical strategy is accurate. So the results under earthquake excitation is also accurate, because it adopts the same accurate mathematical strategy. In other words, the mathematical formulas of the two-step transformation approach cannot tell the difference between harmonic signals and earthquake signals, which are both a series of different numbers. As a result, if the approach dealt with harmonic number correctly, they must dealt with earthquake signals correctly. Both El Centro and Taft earthquake waves are chosen as excitations to verify the applicability of the proposed method.

The equivalent linearization method is also adopted in the following comparisons because it is based on ESS model and is usually adopted to calculate the response of viscoelastic material. Although the equivalent linearization method will bring errors to the system, it is simple and practical. The comparisons can

TABLE 1 | Calculation results of 9050A models of viscoelastic materials.

T	*ω*	Test value		ESS model		Two-step approach		Error of two-step approach	
°C	**rad**	**G_1 Mpa**	η	**G_1 Mpa**	η	**G_1 Mpa**	η	**G_1 Mpa**	η
−10	1	5.8	1.39	4.7805	1.3008	4.7811	1.302	0.0126%	0.0923%
−10	2	10	1.4	7.7279	1.1799	7.7289	1.1807	0.0129%	0.0678%
0	0.1	2.5	0.4	2.8651	0.237	2.865	0.2383	0.0035%	0.5485%
0	0.5	3.3	0.9	3.1027	0.7627	3.1027	0.7641	0.0000%	0.1836%
0	1	3.8	1.1	3.592	1.1075	3.5922	1.109	0.0056%	0.1354%
10	1	3	0.71	3.1343	0.7993	3.1343	0.8007	0.0000%	0.1752%
10	2	3.4	0.92	3.6813	1.1409	3.6815	1.1423	0.0054%	0.1227%
20	1	2.7	0.4	2.9596	0.5362	2.9595	0.5377	0.0034%	0.2797%

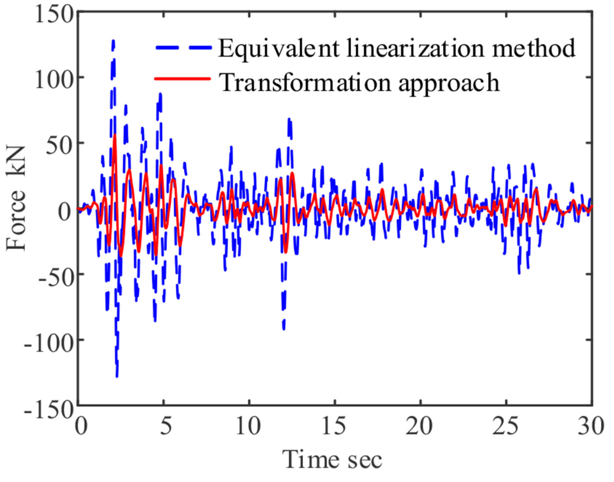

FIGURE 3 | Force-time curve of viscoelastic damper under seismic load (assuming working frequency is 0.2 Hz).

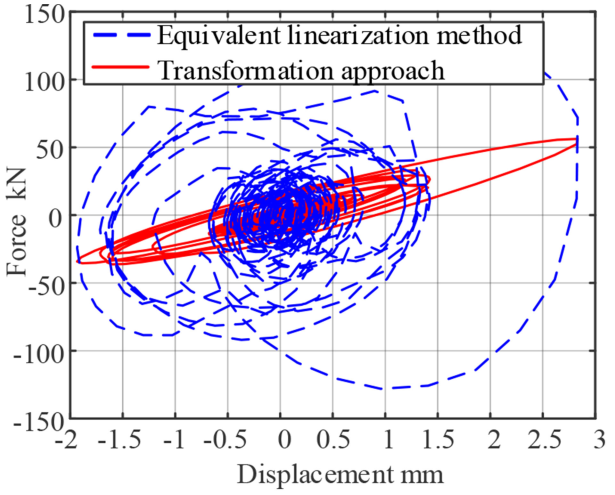

FIGURE 4 | Force-Displacement curve of viscoelastic resistance under seismic load (assuming working frequency is 0.2 Hz).

quantify the exact error that the equivalent linearization method brings to the system.

Validation Under El Centro Earthquake Wave

The two-step transformation approach is used to calculate the response of the Viscoelastic damper under the El-Centro earthquake excitation with 400 gal amplitude. The time history curve of force is shown in the red solid line in **Figure 3**. The force-displacement cure is shown in the red solid line in **Figure 4**. At the same time, equivalent linearization method is used to make approximate calculation on the viscoelastic system. The equivalent linearization method assumes that the system works under simple harmonic loads of fixed frequency, and the excitation frequency usually equals to the nature frequency of the system. In this working condition, the frequency of the equivalent linearization method assumes to be 0.2 and 5 Hz, respectively.

For example, when the assuming frequency is 0.2 Hz, the equivalent linearization method considers that the damper's operating frequency is $\omega = 2\pi f = 1.2566$ rad. So based on the assumptions, the storage modulus $G_1 = 5.5113 \times 10^6$ Pa, Loss factor $\eta = 1.2998$, and the time history curve of force and force-displacement curves of the damper are plotted as shown in the blue dashed lines of **Figures 3**, **4**.

Through comparisons, the maximum output of the system calculated by the two-step transformation approach is 56.2315 kN, and the maximum output of the damper calculated by the equivalent linearization method is 124.6607 kN, and the proposed method improve the system accuracy by 121.69%. The force-displacement curve can also be found that the hysteresis loop calculated by the equivalence method is extremely full, so the energy dissipation effect of the damper is overestimated, which is an unsafe behavior in engineering design.

When the working frequency of the viscoelastic system is assumed to be 5 Hz, the equivalent linearization method considers that the working frequency of the system is $\omega = 2\pi f = 31.4159$ rad, so it can be calculated based on the assumption that the storage modulus $G_1 = 23.7705 \times 10^6$ Pa, loss

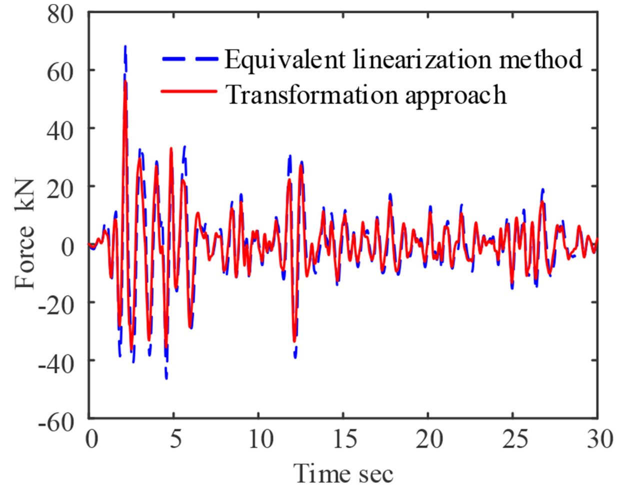

FIGURE 5 | Force time curve of viscoelastic damper under seismic load (assuming working frequency 5 Hz).

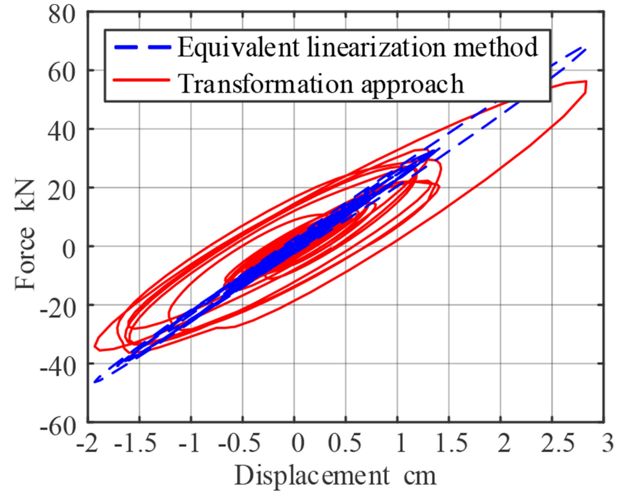

FIGURE 6 | Force-Displacement curve of viscoelastic resistance under seismic load (assuming working frequency 5 Hz).

factor $\eta = 0.1905$, The force-time curve and force-displacement curve of the viscoelastic system are shown in the blue dashed lines of **Figures 5**, **6**.

Through comparisons, it is concluded that the maximum output force of the damper calculated by the proposed approach is 56.2315 kN, and the maximum output force of the damper calculated by the equivalent linearization method is 68.7177 kN. The proposed method improve the system accuracy reaches 22.2%. The force-displacement curve can also concludes that the hysteresis loop of the equivalent linearization method is not full and the slope increases. It is shown that the equilibration method underestimates the energy consumption effect of the damper, and overestimates the stiffness of the damper, which is quite different from the real result.

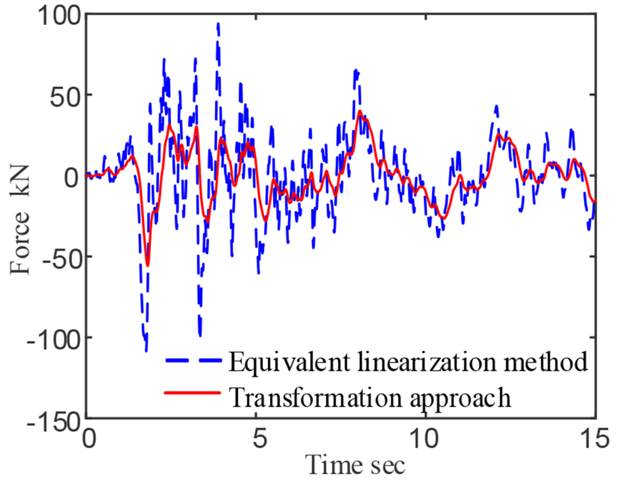

FIGURE 7 | Force-time curve of viscoelastic damper under seismic load (assuming working frequency is 0.2 Hz).

In addition, when the frequency is 0.2 Hz, it means the first frequency of the system is assumed to be 0.2 Hz for equivalent linearization method. This condition is usually suitable for the high rise building which is soft. On the other hand, 5 Hz means the period of the structure is 0.2 s which means the structure is low and stiff. For viscoelastic material, the loss factor decreases with increasing frequency, so the curve in high frequency is not as full as in low frequency.

Validation Under Taft Earthquake Wave

In order to verify the universality of the proposed two-step transformation approach. Taft earthquake excitation with 400 gal amplitude is chosen as the input excitation on the viscoelastic system. The force time history curve of the damping system is shown in the red solid line in **Figure 7**. The force-displacement cure is shown in the red solid line in **Figure 8**. At the same time, equivalent linearization method is used to make estimation of the response of the viscoelastic system. The working frequency of the approximate method is also assumed to be 0.2 and 5 Hz, respectively.

As mentioned before, when the assuming working frequency is 0.2 Hz, the equivalent linearization method considers that the damper's working frequency is $\omega = 2\pi f = 1.2566$ rad, and the calculated energy storage modulus $G_1 = 5.5113 \times 10^6$ Pa, Loss factor $\eta = 1.2998$, the time history curve of force and force-displacement curves of the damper are calculated as shown in the blue dotted lines of **Figures 7**, **8**.

Through comparison, the maximum output of the viscoelastic system calculated by the two-step transformation approach is 55.7772 kN, and the maximum output of the damper calculated by the equivalent linearization method is 108.7909 kN, and the proposed method improve the system accuracy reaches 95.05%. The same as El Centro earthquake, the force-displacement curve of Taft earthquake wave can also be found that the hysteresis loop calculated by the equivalence method is extremely full, and the

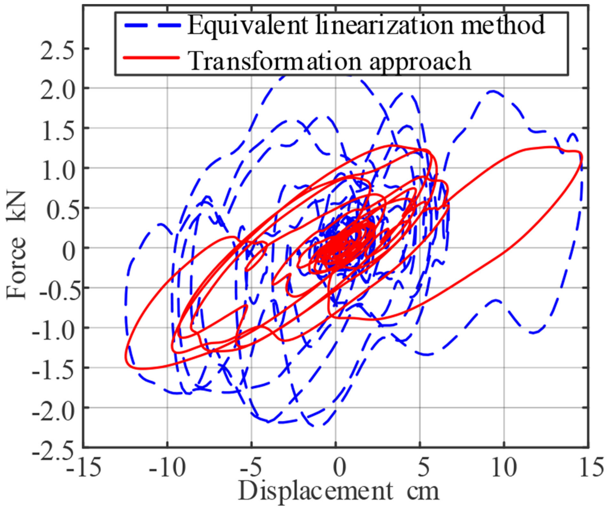

FIGURE 8 | Force-Displacement curve of viscoelastic resistance under seismic load (assuming working frequency is 0.2 Hz).

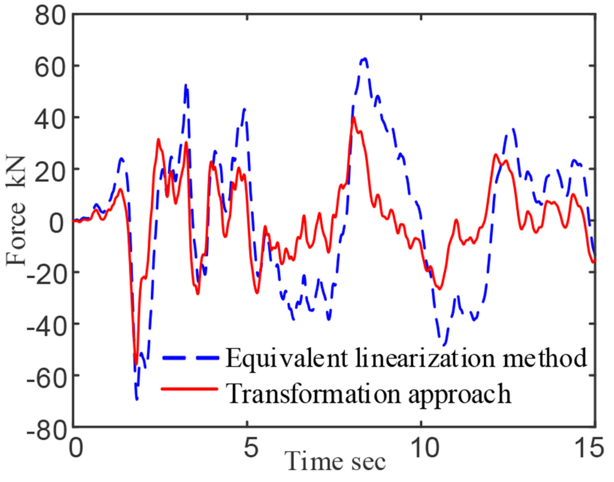

FIGURE 9 | Force time curve of viscoelastic damper under seismic load (assuming working frequency 5 Hz).

energy dissipation effect of the damper is overestimated, which is an unsafe behavior in engineering design.

When the operating frequency of the damper is assumed to be 5 Hz, the equivalent linearization method considers that the operating frequency of the damper is $\omega = 2\pi f = 31.4159$ rad, and the calculated storage modulus$G_1 = 23.7705 \times 10^6$ Pa, loss factor $\eta = 0.1905$, The force-time curve and force-displacement curve for calculating the damper are shown in the blue dashed lines of **Figures 9**, **10**.

Through comparison, it is concluded that the maximum output force of the damper calculated by the proposed approach is 55.7772 kN, and the maximum output force of the damper calculated by the equivalent linearization method is 69.3388 kN. The proposed method improve the system accuracy reaches 24.31%.

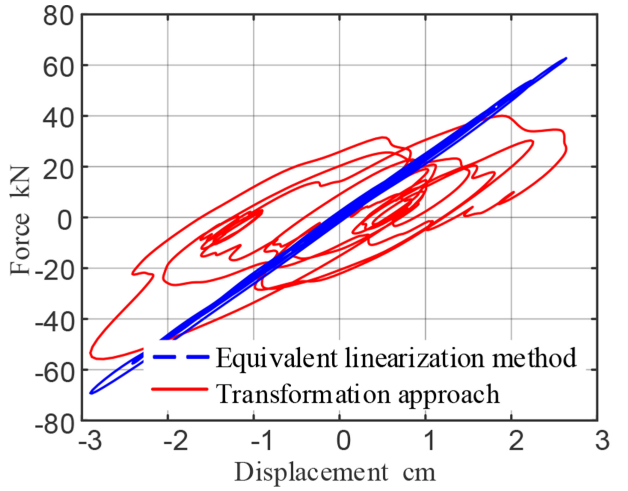

FIGURE 10 | Force-Displacement curve of viscoelastic resistance under seismic load (assuming working frequency 5 Hz).

Same as El Centro earthquake, the force-displacement curve under Taft earthquake can also be found that the hysteresis loop of the equivalent linearization method is not full, and the slope increases. It is also shown that the equilibration method underestimates the energy consumption effect of the damper, and overestimates the stiffness of the damper, which is quite different from the real result.

In addition, because the ESS model is only suitable for harmonic signal, so an equivalent linearization method is usually adopted to extend the ESS model to time domain. However, the equivalent linearization method is approximate, and the two-step transformation approach is more accurate. As a result, the difference is large when using earthquake excitation. The equivalent linear model can only deal with signals with one frequency, while the earthquake contain plenty of frequencies. So only one representative frequency of earthquake waves is choose to perform the calculation. That's the reason why the equivalent linearization method is approximate and inaccurate, and why the two-step transformation approach is proposed.

CONCLUSION AND PROSPECT

In this paper, a two-step transformation approach is used to calculate the response of the viscoelastic damper under the El-Centro earthquake excitation. The proposed approach avoids the establishment of complex time-domain differential equations, which can start directly from the frequency domain expression of the ESS model of viscoelastic materials, and calculate the time domain response of viscoelastic materials under harmonic excitation and seismic excitation.

The following conclusions are drawn by experimental tests and numerical solutions:

(1) The proposed method can accurately calculate the ESS model in the time domain range. The comparison calculation

results show that the error is small, the maximum error of the energy storage modulus G_1 0.0054%, and the maximum error of the loss Factor η 0.2797%.

(2) The traditional solution method with equivalent stiffness and equivalent damping will bring large errors, when it is assumed that ω is large, the hysteresis loop is very full calculated by the equivalence method, the energy dissipation effect of the damper is overestimated, and when the ω is assumed to be small, the energy dissipation effect of the damper is estimated low. On the other hand, the stiffness of the damper is over estimated. The engineers is encouraged to use the two-step transformation approach to evaluate and predict the mechanical properties of viscoelastic materials.

(3) In the current stage, the two-step transformation approach under random earthquakes is mainly verified by numerical results. The future research will focus on the experimental verification under random excitations. Also the accuracy of the models should be improved and the computation cost should be reduced in the following research.

DATA AVAILABILITY

The raw data supporting the conclusions of this manuscript will be made available by the authors, without undue reservation, to any qualified researcher.

AUTHOR CONTRIBUTIONS

All authors listed have made a substantial, direct and intellectual contribution to the work, and approved it for publication.

ACKNOWLEDGMENTS

Financial supports for this research are provided by National Natural Science Foundation of China (56237845), Natural Science Foundation of Jiangsu Province (BK20170684), National Key R&D Program Key Special Project (2016YFE0200500), National Key R&D Program Project Funding (2016YFE0119700), and Fundamental Research Funds for the Central Universities (2242017K40215). These supports are gratefully acknowledged.

REFERENCES

Bhatti, A. Q. (2013). Performance of viscoelastic dampers (VED) under various temperatures and application of magnetorheological dampers (MRD) for seismic control of structures. *Mech. Time-Depend. Mat.* 17, 275–284. doi: 10.1007/s11043-012-9180-2

Chen, S., Liu, F., Turner, I., and Hu, X. (2018). Numerical inversion of the fractional derivative index and surface thermal flux for an anomalous heat conduction model in a multi-layer medium. *Appl. Math. Model.* 59, 514–526. doi: 10.1016/j.apm.2018.01.045

Gonzalez, E. A., Castro, M. J. B., Presto, R. S., Radi, M., and Petras, I. (2016). "Fractional-order models in motor polarization index measurements," in *17th International Carpathian Control Conference (ICCC)*. (Tatranská Lomnica), 214–217. doi: 10.1109/CarpathianCC.2016.7501096

Kim, J., Choi, H., and Min, K. W. (2003). Performance-based design of added viscous dampers using capacity spectrum method. *J. Earthq. Eng.* 7, 1–24. doi: 10.1080/13632460309350439

Lee, D. K., and Choi, M. S. (2018). Standard reference materials for cement paste, part I: suggestion of constituent materials based on rheological analysis. *Materials* 11:1040624. doi: 10.3390/ma11040624

Lewandowski, R., and Chorazyczewski, B. (2010). Identification of the parameters of the Kelvin-Voigt and the Maxwell fractional models, used to modeling of viscoelastic dampers. *Comput. Struct.* 88, 1–17. doi: 10.1016/j.compstruc.2009.09.001

Mctavish, D. J., and Hughes, P. C. (1993). Modeling of linear viscoelastic space structures. *J. Vib. Acoust.* 115, 103–110. doi: 10.1115/1.2930302

Mehrabi, M. H., Suhatril, M., Ibrahim, Z., Ghodsi, S. S., and Khatibi, H. (2017). Modeling of a viscoelastic damper and its application in structural control. *PLoS ONE* 12:e0176480. doi: 10.1371/journal.pone.0176480

Mould S., Barbas J., Machado A.V., Nóbrega J.M., and Covas J.A. (2011). Measuring the rheological properties of polymer melts with on-line rotational rheometry. *Polym. Test.* 30, 602–610. doi: 10.1016/j.polymertesting.2011.05.002

Park, J., Min, K., Chung, L., Lee, S., Kim, H., and Moon, B. (2007). Equivalent linearization of a friction damper-brace system based on the probability distribution of the extremal displacement. *Eng. Struct.* 29, 1226–1237. doi: 10.1016/j.engstruct.2006.07.025

Park, S. W. (2001). Analytical modeling of viscoelastic dampers for structural and vibration control. *Int. J. Solids Struct.* 38, 8065–8092. doi: 10.1016/S0020-7683(01)00026-9

Trindade, M. A., Benjeddou, A., and Ohayon, R. (2000). Modeling of frequeney-dependent viscoelastic materials for active-passive vibration damping. *J. Vib. Acoust.* 122, 169–174. doi: 10.1115/1.568429

Valsa, J., and Brancik, L. (1998). Approximate formulae for numerical inversion of Laplace transforms. *Int. J. Numer. Model. El.* 11, 153–166. doi: 10.1002/(SICI)1099-1204(199805/06)11:3<153::AID-JNM299>3.0.CO;2-C

Xu, Y., Xu, Z., Ge, T., and Xu, C. (2017). Equivalent fractional order micro-structure standard linear solid model for viscoelastic materials. *Chin. J. Theor. Appl. Mech.* 49, 1059–1069. doi: 10.6052/0459-1879-17-134

Xu, Z. (2007). Earthquake mitigation study on viscoelastic dampers for reinforced concrete structures. *J. Vib. Control* 13, 29–43. doi: 10.1177/1077546306068058

Xu, Z., Gai, P., Zhao, H., Huang, X., and Lu, L. (2017). Experimental and theoretical study on a building structure controlled by multi-dimensional earthquake isolation and mitigation devices. *Nonlinear Dyn.* 89, 723–740. doi: 10.1007/s11071-017-3482-5

Xu, Z., Huang, X. H., Xu, F. H., and Yuan, J. (2019). Parameters optimization of vibration isolation and mitigation system for precision platforms using non-dominated sorting genetic algorithm, *Mech. Syst. Signal Process.* 128, 191–201. doi: 10.1016/j.ymssp.2019.03.031

Xu, Z., Wang, D., and Shi, C. (2011). Model, tests and application design for viscoelastic dampers. *J. Vib. Control* 17, 1359–1370. doi: 10.1177/1077546310373617

Xu, Z., Wang, S., and Xu, C. (2014). Experimental and numerical study on long-span reticulate structure with multidimensional high-damping earthquake isolation devices. *J. Sound Vib.* 333, 3044–3057. doi: 10.1016/j.jsv.2014.02.013

Xu, Z., Xu, C., and Hu, J. (2015). Equivalent fractional Kelvin model and experimental study on viscoelastic damper. *J. Vib. Control* 21, 2536–2552. doi: 10.1177/1077546313513604

Yoshida, N., Kobayashi, S., Suetomi, I., and Miura, K. (2002). Equivalent linear method considering frequency dependent characteristics of stiffness and damping. *Soil Dyn. Earthq. Eng.* 22, 205–222. doi: 10.1016/S0267-7261(02)00011-8

Conflict of Interest Statement: The authors declare that the research was conducted in the absence of any commercial or financial relationships that could be construed as a potential conflict of interest.

frontiers in Materials

ORIGINAL RESEARCH
published: 17 May 2019
doi: 10.3389/fmats.2019.00112

Dynamic Mechanical Property Experiment of Viscous Material for Viscous Damping Wall

Feifei Sun[1], **Jiaqi Yang**[2]* **and Tanye Wu**[2]

[1] State Key Laboratory of Disaster Reduction in Civil Engineering, Tongji University, Shanghai, China, [2] Department of Structure Engineering, College of Civil Engineering, Tongji University, Shanghai, China

Viscous damping wall (VDW) is an effective velocity-dependent damper, which can dissipate earthquake energy by shear strain of viscous material. The damping force equation of VDW can only be obtained from regression of VDW dynamic test results, as velocity exponent of power-law material can not be obtained from rheometers. In this study, a Dynamic Sandwich-Type Shear test was designed matching the design working conditions of VDW. A series of experiments with different frequencies and strain amplitudes were conducted. Simple data procession methods were proposed to calculate velocity exponent and storage/loss modulus of polymer from experimental data. Comparison with methods adapted from those for VDW formula validated that radial linear regression method was proper to separate stress components and pivotal point method was accurate to evaluate velocity exponent. The velocity exponents obtained varied from 0.8 to 1, with various loading frequency and strain amplitude. Finally, the differences between the results of storage/loss modulus in DSTS test and ARES test were compared. Due to the extrusion effect caused by engineering working condition, the storage and loss modulus obtained by DSTS test was larger than the modulus obtained by ARES test.

Keywords: polymer, dynamic mechanical property, velocity exponent, viscous damping wall, dynamic sandwich-type shear (DSTS) test

OPEN ACCESS

Edited by:
Yong Lu,
University of Edinburgh,
United Kingdom

Reviewed by:
Ionut Ovidiu Toma,
Gheorghe Asachi Technical University
of Iaşi, Romania
Antonio Caggiano,
Darmstadt University of
Technology, Germany

***Correspondence:**
Jiaqi Yang
yjqjarvis@tongji.edu.cn

Specialty section:
This article was submitted to
Structural Materials,
a section of the journal
Frontiers in Materials

Received: 26 February 2019
Accepted: 30 April 2019
Published: 17 May 2019

Citation:
Sun F, Yang J and Wu T (2019)
Dynamic Mechanical Property
Experiment of Viscous Material for
Viscous Damping Wall.
Front. Mater. 6:112.
doi: 10.3389/fmats.2019.00112

INTRODUCTION

One of the most challenging tasks for civil engineers in recent decades has been solving overwhelming earthquake problems, which may cause heavy casualties. Besides vibration isolation design (Xu et al., 2019), researchers have been focusing on seismic mitigation technologies using viscous damping components (Xu et al., 2003, 2004, 2016; Xu, 2007). Viscous damping wall (VDW) is a new type of wall-shaped energy absorber, which can be hidden in building walls and provides large energy absorbing capacity. The performance of VDW is largely dependent on its viscous material. However, the investigations on mechanical properties of such viscous materials are insufficient, causing a major obstacle for in-depth research on VDW.

Researchers have investigated the performance of VDW itself and damping force formula. Miyazaki et al. (1986) carried out a series of cyclic tests to investigate the performance of VDW itself and obtained a design formula. Ou et al. (2005a) proposed a VDW damping force model by regression method and conducted a series of dynamic experiments to study the dynamic performance of VDW with variable temperature, displacement amplitude, velocity, and vibration frequency. Sasaki et al. (2012) conducted a series of oscillation tests against large earthquakes to clarify the characteristics of VDW. A simplified design formula neglecting the influence of stiffness was proposed and compared with experimental curves. Experimental results showed that VDW can still dissipate energy of oscillations even though the damping force decreased over a long time. Sun et al. (2018) conducted a small-scale shaking table test and a large-scale dynamic actuator test to investigate the influence of loading frequency on VDW's performance, and proposed a unified model considering the influence of loading frequency by means of introducing the effect of loading history.

Viscous materials for VDW are mainly semi-solid material such as polymer having both elastic properties and viscous properties. In the field of civil engineering, the investigations of polymer's mechanical properties are insufficient. Ou et al. (2005b) investigated the stability under high temperatures, durability, chemical security and dynamic performance of a new type of viscous material for VDW. Bouix et al. (2009) investigated the compressive stress- strain behavior of Polypropylene over a wide range of engineering strain rates from 0.01 to 1,500 microstrain/s. Drozdov et al. (2010) conducted a uniaxial tensile test for polypropylene/polyethylene blends with constant strain rates, relaxation tests and creep tests at room temperature. Ardakani et al. (2012) studied the rheology of Polypropylene/polybutene-1 blend with low frequency and large shear rate.

Several kinds of testing methods have been used to measure the mechanical parameters of polymer. A cone-and-plate method was used to investigate the storage and loss modulus of viscous fluid (Makris et al., 1993). Several scholars used a non-linear ultrasound method called Dynamic Acoustoelastic Testing (DAET) to assess the non-linear mechanical properties of viscoelastic material. The DAET method is based on the interaction between a low-frequency acoustic wave to successively compress and expand the material, and ultrasound pulse to probe this medium. The Time of Flight Modulations (TOFM) of the ultrasound pluses are plotted as a function of the low-frequency pressure amplitude on DAET diagrams (Trarieux et al., 2013). The mechanical properties of silicone oils were investigated by DAET. An analytical model to describe non-linear viscoelastic properties of silicone oil was proposed and validated the accuracy by comparing analytical results with DAET results (Trarieux et al., 2012, 2013). However, DAET cannot measure the parameters of polymer under shear strain excitation. Rheometer is another technique to investigate the mechanical properties of polymer under shear strain. Dynamic Shear Rheometer (DSR) was used to investigated the effect of time and temperature on blending level between fresh and actual RAP blinders (Yousefi Rad et al., 2014). ARES system is a is an advanced strain controlled rheometer, which tests the polymer's modulus precisely. ARES test usually used to measure the linear mechanical property under shear strain of polymer. Polymers such as SBR and PEKK were investigated on the influences of frequencies, strain rates and strain amplitudes on modulus of polymers (Hu et al., 2008; Snijkers and Vlassopoulos, 2011; Dessi et al., 2016; Coulson et al., 2018). However, polymers are usually shear-thinning material and following the power-law whose velocity exponent is not equal to 1 (Fatkullin et al., 2011; Li et al., 2013), while rheometers assume that the velocity exponent is always equal to 1 during measuring process. Therefore, a method to measure the velocity exponent is needed.

Rheometers and other testing methods do not consider velocity exponent's effects and the working condition of viscous material in VDW. In order to solve these problems, a new DSTS (Dynamic Sandwich-Type Shear) test was designed and used in this research. Moreover, a processing method is proposed in order to measure the storage/loss modulus and velocity exponent of polymer. The influence of loading frequency and strain amplitude on storage, loss modulus and velocity exponent was also studied in this paper by DSTS test.

MATERIALS AND METHODS

In this experiment, Oppanol-B12-PIB supplied by BASF SE (BASF SE, Ludwigshafen, Germany) has been used. Oppanol-B12-PIB is a kind of polymer containing 200 mg/kg of hexane and 4 mg/kg of fluorine with viscose average molecular weight of 60,000 and specific gravity 0.92 g/cm^3. Viscosity of Oppanol-B12-PIB under 100 degree Celsius is 30,000 $mPa\cdot s$ and coefficient of expansion under 20 degree Celsius is $6.3 \cdot 10^{-4} k^{-1}$. The dissipation coefficient of Oppanol-B12-PIB under the loading frequency 50 Hz is $5 \cdot 10^{-4}$. The melting point of Oppanol-B12-PIB is −64 degree Celsius.

Storage Modulus and Loss Modulus

Consider an oscillatory shear flow between two parallel plates at a distance h apart, where the bottom plate is stationary and top plate is sinusoidal displaced by a small amount $\delta \sin(\omega t)$. According to Boltzmann's concept of fading memory (Phan-Thien, 2002), shear stress can be obtained as

$$\tau = G^{'}(\omega)\,\gamma\,(t) + \mu'(\omega)\,\dot{\gamma}(t) \tag{1}$$

where ω is angular frequency (rad/s), $\gamma\,(t)$ is the shear strain and $\gamma\,(t) = \frac{\delta}{h}\sin(\omega t)$, $\dot{\gamma}(t)$ is shear strain rate, and $\dot{\gamma}\,(t) = \frac{\delta}{h}\omega\cos(\omega t)$(microstrain/s). $G'(\omega)$ is the storage modulus (N/m^2), $\mu'(\omega)$ is the dynamic viscosity (N·s/m^2). The other two related quantities, the loss modulus $G''\,(\omega)$ (N/m^2), and the storage viscosity $\mu''\,(\omega)$ (N·s/m^2) are defined as

$$\mu''(\omega) = \frac{G'(\omega)}{\omega} \tag{2}$$

$$G''\,(\omega) = \omega\mu'(\omega) \tag{3}$$

Power Law

Polymers are usually Non-Newtonian material, and the velocity exponent α of Non-Newtonian fluid does not equal to 1. In the other words, the relationship between viscous stress and strain rate of polymers is non-linear, which is called power law.

The constitutive equation of power law is

$$\tau_V = \mu' \cdot \dot{\gamma}^{\alpha} \tag{4}$$

where α is velocity exponent, τ_V is viscous shear stress, $\dot{\gamma}$ is shear strain rate, μ' is viscosity.

Concept of DSTS Test

To investigate the mechanical properties of PIB under shear strain like VDW, and to obtain the velocity exponent, a Dynamic Sandwich-Type Shear test (DSTS test) is proposed with schematic diagram shown in **Figure 1**. As in the actual engineering condition in VDW, the shear plate is sandwiched in the polymers, and the PIB is bonding on the surface of shear plate. When the shear plate undergoes displacement, the shear plate drives PIB to move together, which causes shear strain of PIB. At the same time, the PIB provides corresponding shear stress on bonding surface of shear plate, and the resultant force of the shear stress is damping force. The shear force and displacement can be converted into shear stress and shear strain as:

$$\tau = \frac{Q}{A} \tag{5}$$

$$\gamma = \frac{S}{H} \tag{6}$$

Where Q is damping force, S is displacement of shear plate, and H is the gap between polymers A is the area of shear plate that inserted in the polymer, A = 2ab, a is the width of shear plate and b is the insertion depth, γ is shear strain τ is shear stress.

According to the material mechanic of viscoelastic material and power law, the constative equation can be written as:

$$\tau = \tau_V + \tau_E = \mu' \dot{\gamma}^{\alpha} + G'\gamma \tag{7}$$

where τ_V is viscous shear stress, τ_E is elastic shear stress. α is velocity exponent, $\dot{\gamma}$ is shear strain rate. γ is shear strain, μ' is viscosity, $G'$is storage modulus.

Methods for Data Processing

Radial Linear Regression for Stress Separation

As indicated in Equation (7), the measured shear stress is a direct sum of two components of τ_V and τ_E. Given the complexity due to the power of the first derivative combined with a linear term, it is not a straightforward issue to separate the stress components. Observing the symmetry of the hysteresis curve, radial linear regression is proposed to regress the linear term from the hysteretic curve, and the slope of the regression line is the storage modulus G' which is shown in **Figure 2A**. Thus, the viscous shear stress can be isolated from total shear stress as:

$$\tau_V = \tau - G'\gamma \tag{8}$$

Pivotal Point Method for Velocity Exponent

As there are two undetermined quantities in Equation (4), two conditions are needed to solve the velocity exponent and loss modulus. This paper used maximum strain rate point and 0.5 times maximum strain rate point to calculate the parameters, as the two pivotal points shown in **Figure 2B**.

The equations are expressed as:

$$\ln(\tau_{V_{\gamma max}}\omega) = \ln(G'') + \alpha \ln(\dot{\gamma}_{max}) \tag{9}$$

$$\ln(\tau_{V_{\gamma_{\frac{1}{2}max}}}\omega) = \ln(G'') + \alpha \ln(\dot{\gamma}_{\frac{1}{2}max}) \tag{10}$$

where $\dot{\gamma}_{max}$ is the maximum strain rate, $\dot{\gamma}_{\frac{1}{2}max} = \frac{1}{2}\dot{\gamma}_{max}$, $\tau_{V_{\gamma max}}$ is the stress at $\dot{\gamma} = \dot{\gamma}_{max}$, $\tau_{V_{\gamma_{\frac{1}{2}max}}}$ is the stress at $\dot{\gamma} = \dot{\gamma}_{\frac{1}{2}max}$.

Fitting Method for Strain Rate

The shear stain γ can be obtained from the measured displacement S by Equation (6). Regarding the shear strain rate $\dot{\gamma}$, as the pivotal point method is sensitive to its accuracy, it

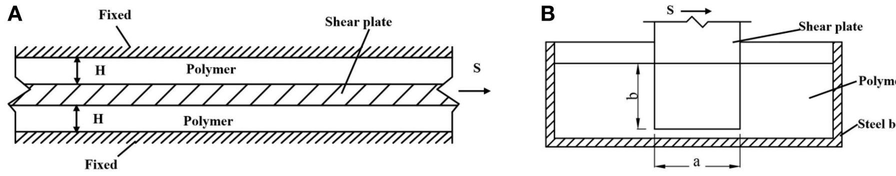

FIGURE 1 | Schematic diagram of Dynamic Sandwich-Type Shear test. **(A)** Top view **(B)** Front view.

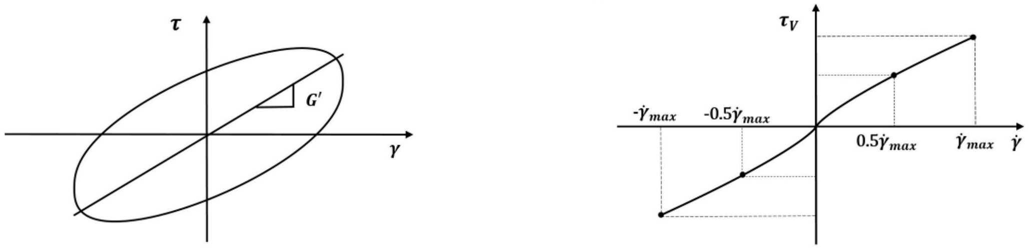

FIGURE 2 | Data procession. **(A)** Radial linear regression **(B)** Pivotal points.

is not appropriate to use numerical differences to calculate the first derivate of γ. Therefore, the strain curves were fitted by sinusoidal functions firstly, and then the strain rates were derived as the first derivate of the fitted sinusoidal functions, as illustrated later in sub-section Calculation Results.

Experimental Set-Up

As shown in **Figure 3A**, the test specimen is composed of a steel plate sandwiched by PIB filled in a steel box. The insertion depth of shear plate is 25 mm, and the gap distance between steel shear plate and steel box is 5 mm, which is shown in **Figure 3A**. The width of shear plate is 40 mm (shown in **Figure 3B**), and the overall dimensions of steel box are 138 ×22 × 49 mm (shown in **Figure 3C**).

The experiments were conducted at the Structural Laboratory of Tongji University. The Instrumentation schematic is shown in **Figure 4A** and the actual installation of DSTS test is shown in **Figure 4B**. The reaction frame is fixed and load cell is fixed on the end of the reaction frame. The shear plate is connected on the load cell rigidly, and the shear plate is inserted in the steel box which is filled with PIB. And the steel box is rigidly connected on the shake table.

During the experiment, the shake table is going to provide sinusoidal excitation and the steel box which is rigidly connected on shake table is going to move together, the load cell is going to receive reaction force signal and laser displacement meter is going to receive displacement signal.

A series of test cases were conducted and the test cases are shown in **Table 1**. In variable frequency test, the imposed displacement amplitude was 4 mm, while the angular frequencies of loading sine wave were 0.63, 1, 1.6, 2.5, 4, 6.3 rad/s, respectively. During variable frequency test, the excitation angular frequencies of ARES tests were 0.63, 1, 1.6, 2.5, 4, 6.3 rad/s, respectively which were set in the ARES's program and cannot be changed. In order to compare with the results of ARES test, this paper selected the same test cases as ARES test during DSTS test. In variable strain test, the imposed displacement amplitudes were 1.25, 2.5, 4, 6, 8, 10 mm, respectively, while the angular frequency of loading sine wave was 6.3 rad/s. In order to investigate the behavior of PIB under small and large shear strain, this paper selected small displacement amplitudes 1.25 and 2.5 mm, while the large displacement amplitudes were 4, 6, 8, 10 mm. Cycles of each testing case were 5. Sine wave used as excitation wave in the loading process according to the displacement control scheme. The displacement was measured by laser displacement meters with measurement period of 20 ms, and the force was measured by load cell with period of 20 ms.

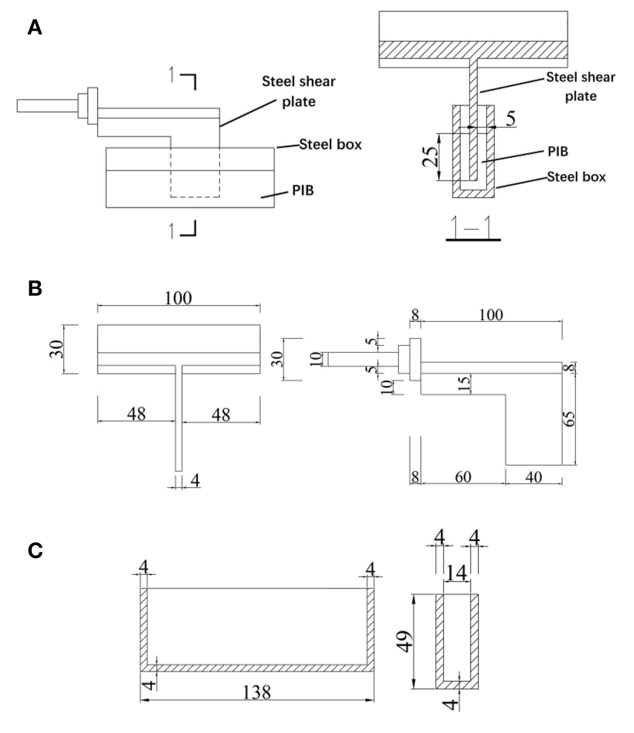

FIGURE 3 | Test specimen, shear plate and steel box (unit: mm). **(A)** Installed specimen **(B)** Steel plate **(C)**Steel box.

TABLE 1 | Test cases.

Number	Variable frequency test		Variable strain test	
	Frequency (rad/s)	Displacement (mm)	Frequency (rad/s)	Displacement (mm)
1	0.63	4	6.3	1.25
2	1	4	6.3	2.5
3	1.6	4	6.3	4
4	2.5	4	6.3	6
5	4	4	6.3	8
6	6.3	4	6.3	10

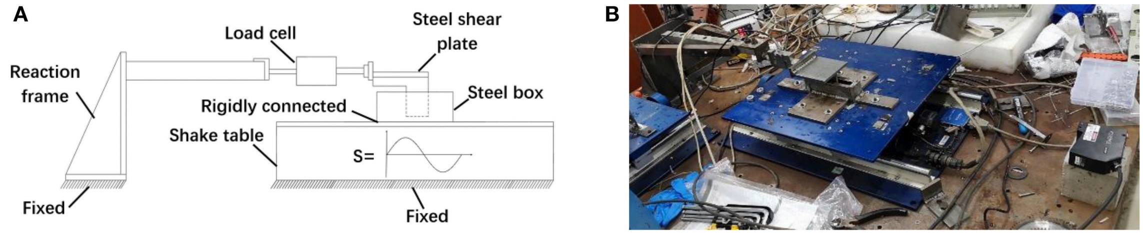

FIGURE 4 | Instrumentation schematic and Actual installation of DSTS test. **(A)** Instrumentation schematic **(B)** Actual Installation of DSTS test.

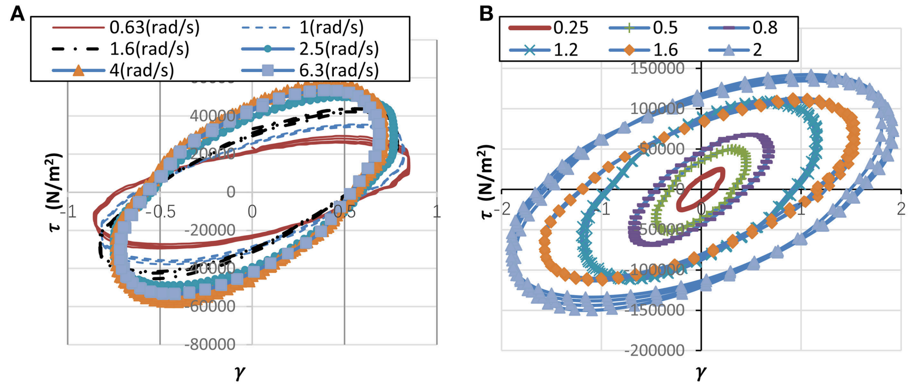

FIGURE 5 | Hysteretic curves of DSTS test. **(A)** Variable loading frequency **(B)** Variable loading strain.

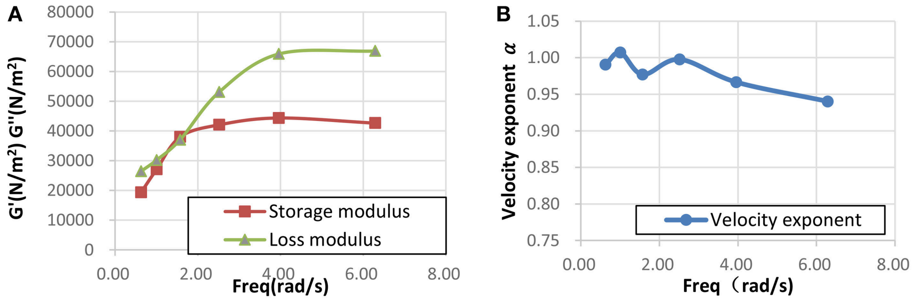

FIGURE 6 | Results of DSTS test (variable loading frequency test). **(A)** Storage/loss modulus **(B)** Velocity exponent.

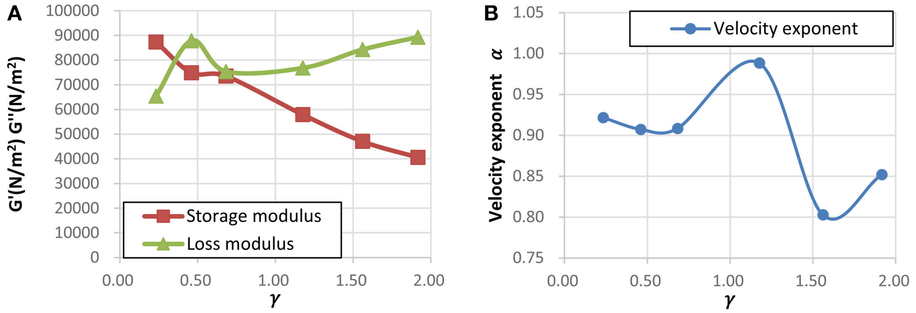

FIGURE 7 | Results of DSTS test (variable strain amplitude test). **(A)** Storage/loss modulus **(B)** Velocity exponent.

RESULTS

Hysteretic Curve

The hysteretic curves of variable loading frequency test are shown in **Figure 5A**. As the frequency increases, the peak stress increases, and the slope of the hysteretic curve increases gradually. The hysteretic curves under 4 and 6.3 rad/s are almost overlapping, indicating that PIB is insensitive to frequency variations over this frequency range.

The hysteretic curves of variable strain amplitude test are shown in **Figure 5B**. The displacement amplitudes were transformed into strain amplitudes by Equation (6) and strain amplitudes were shown in the legend of **Figure 5B**. As the strain amplitude increases, the area of hysteretic loop increases rapidly, the peak stress also increases and the slope of the hysteretic curve decreases.

Calculation Results

Taking the third cycle of hysteretic loop for calculation. The strain time history curves were fitted by sinusoidal functions. Taking the case at the frequency of 0.63 Hz and the strain amplitude of 0.8 as an example, the strain time history was fitted as $0.7293sin(3.958t + 0.6208)$, with a coefficient of regression of

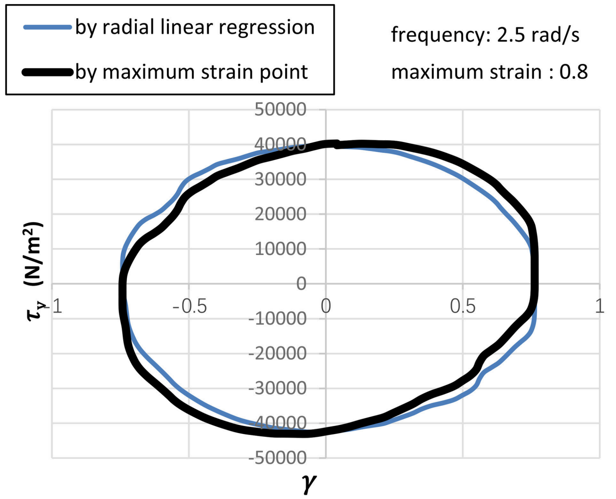

FIGURE 8 | Viscous stress hysteretic curve.

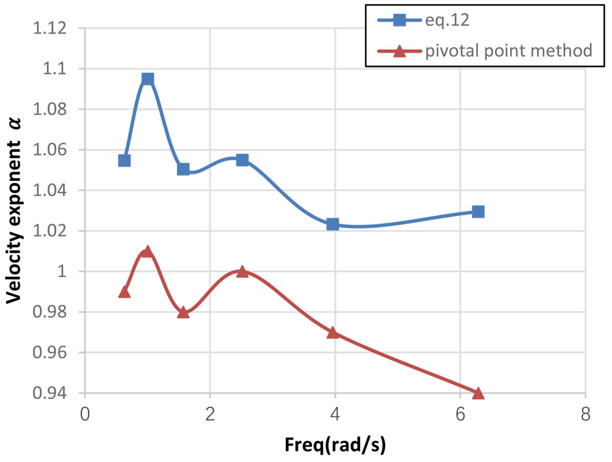

FIGURE 9 | Comparison between velocity exponent between pivotal point method and Equation (12).

$R^2 = 0.991$. The needed strain rates of the pivotal points were then calculated with the first derivative of the fitting function.

The relationship between frequency and mechanical parameters of PIB are shown in **Figure 6**. As the frequency increases, the storage modulus and loss modulus increase (shown in **Figure 6A**). And these phenomena are typical for polymer in the test results obtained in other investigations (Ardakani et al., 2012). As the frequency increases, velocity exponents decreases in the range of 0.94∼1.02 (shown in **Figure 6B**).

The relationship between strain amplitude and mechanical parameters of PIB are shown in **Figure 7**. As the amplitude increases, the storage modulus decreases, and the loss modulus increases (shown in **Figure 7A**). And these phenomena are typical for polymer in the test results obtained in other investigations (Ou et al., 2005b). Velocity exponent exhibits no clear trend with the frequency increase, and fluctuates within the range of 0.8∼1 (shown in **Figure 7B**).

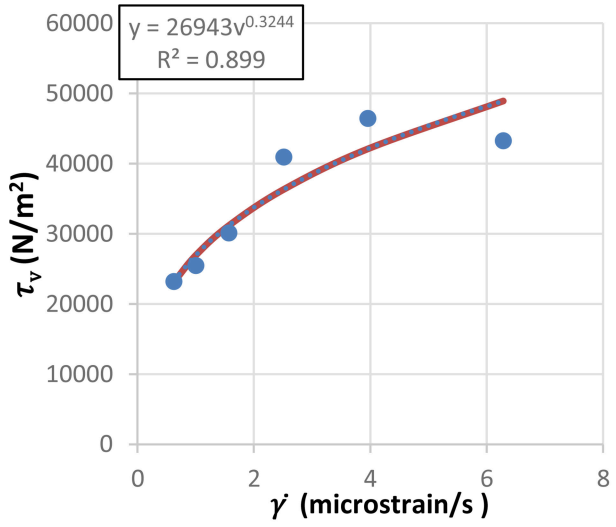

FIGURE 10 | Regression results of viscous stress amplitudes.

DISCUSSION

Validation of Stress Separation Method

In comparison with the radial linear regression method mentioned in sub-section Radical Linear Regression for Stress Separation, the maximum strain point, adapted from the approach often intuitively used for VDW, is also applied here to separate the stress components with the following equation.

$$G' = \frac{\tau_{\gamma max}}{\gamma_{max}} \tag{11}$$

where $\tau_{\gamma max}$ is stress at the maximum strain, γ_{max} is the maximum strain.

The test case with frequency 2.5 rad/s, strain 0.8 is taken as an example to illustrate effect of two different ways of stress separation. After calculating storage modulus, bringing storage modulus into Equation (8) can separate elastic stress and obtain viscosity hysteretic curve. **Figure 8** presents the comparison of viscous stress-strain hysteretic curves obtained by radial linear method and maximum strain point method. It can be seen from **Figure 8**, the curve obtained by the former method is symmetric while the other one is obviously asymmetric about horizontal axis, indicating that some elastic strain has not been taken out. Therefore, the radial linear method is more suitable to separate stress components.

Validation of Pivotal Point Method

Qualitative Validation

The following Equation (12) (Japan Society of Seismic Isolation, 2008) was adapted from the regressed energy formula of the relationship between dissipation energy and velocity power

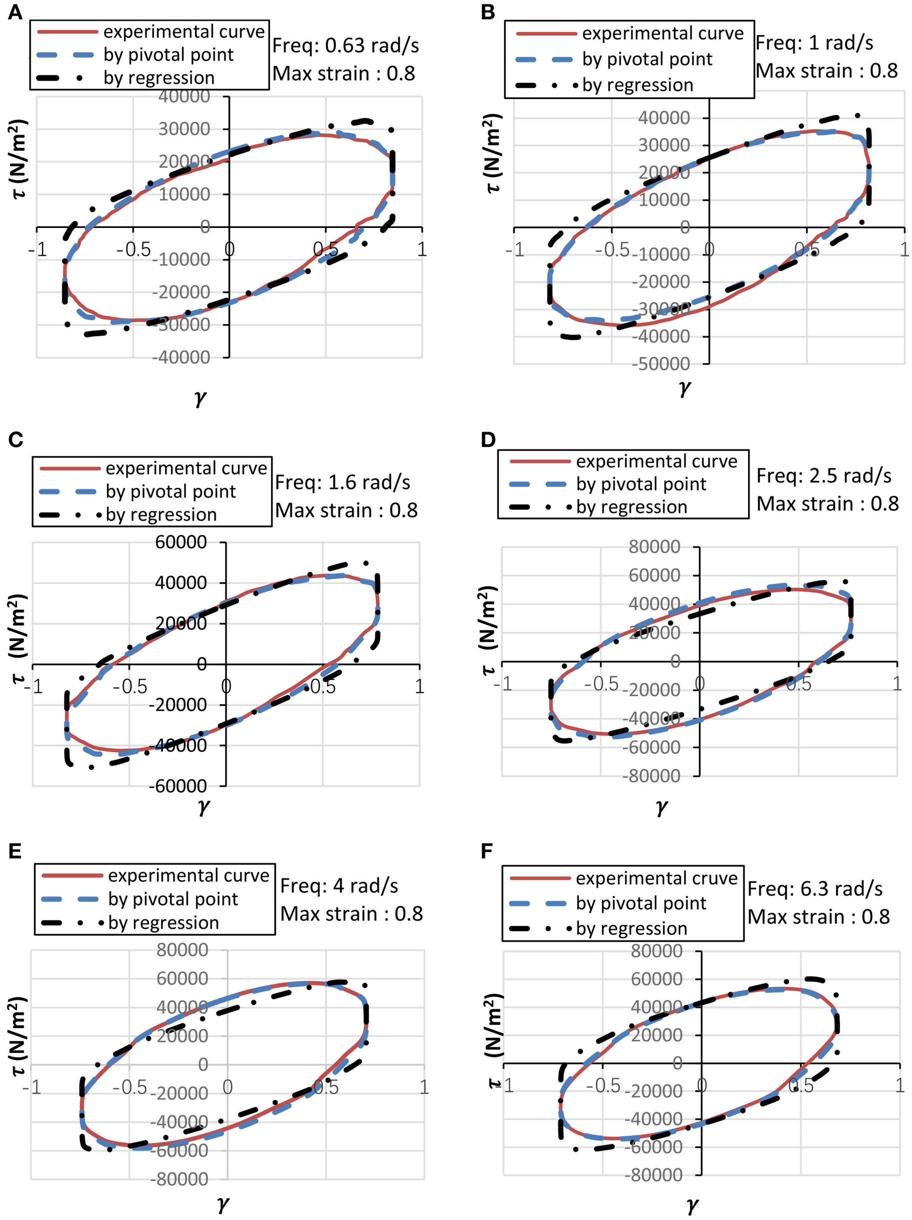

FIGURE 11 | Comparison of hysteretic curves between experimental results and simulated results with Equation (7).

exponent of VDW based on enormous amount of test data of VDWs.

$$E_d = 4e^{-0.24\alpha}\tau_{V\gamma,max}\gamma_{\gamma,max} \tag{12}$$

where E_d is the dissipated energy E_d equals to the area of hysteretic loop. α is velocity exponent, $\gamma_{\gamma,max}$ is the maximum strain, $\tau_{V\gamma,max}$ is the corresponding viscous shear stress when γ is the maximum strain.

The comparison of velocity exponents by pivotal point method and Equation (12) are presented in **Figure 9**. Under variable loading frequency test, the velocity exponent obtained from two methods both tend to decrease as the frequency increases. The velocity exponent obtained by Equation (12) is larger than 1, while the velocity exponent obtained by pivotal point method is smaller than 1. As the testing material in DSTS test is a kind of shear-thinning material for VDW, the results of pivotal point method are more acceptable.

Accuracy Validation

In practice, viscous damping force of VDW is expressed as a power function of stroke velocity, which can be regressed with measured data of viscous damping force amplitudes and

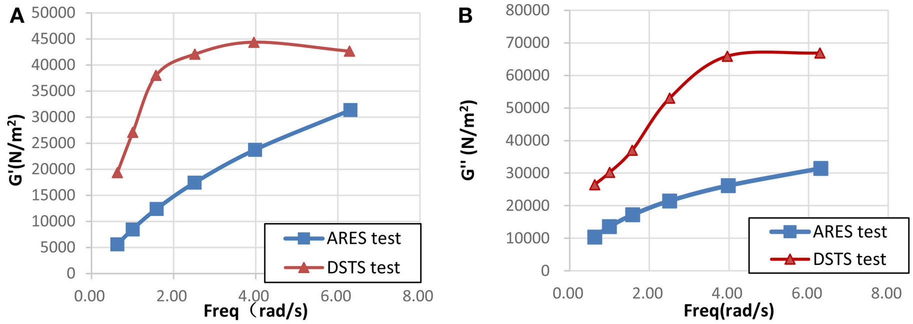

FIGURE 12 | Comparison of storage modulus and loss modulus between ARES test and DSTS test. **(A)** Storage modulus **(B)** Loss modulus.

velocity amplitudes of a series of test cases with different loading frequencies. The same regression approach was applied herein for the present data of viscous shear stress amplitudes and shear strain rate amplitudes under variable loading frequencies, which were separated by radial linear regression. As shown in **Figure 10**, the regression produces parameters value $G'' = 26942\mathrm{N/m^2}$ and $\alpha = 0.32$. In this way the obtained α is smaller than 1, and is far from the values in **Figure 6B**, which is qualitatively acceptable. This approach produces a single set of parameters over a range of loading frequency.

Figure 11 presents the comparison of hysteresis curve between experimental results and simulated results by Equation (7) with the parameters obtained by pivotal point method and the above regression approach. It can be seen that all the simulated curves obtained by the pivotal point method fit experimental curves well, while the other simulated curves depart significantly from experimental curve. Therefore, the pivotal point method is quite accurate and more reasonable to calculate velocity exponent.

Comparison of Modulus Between ARES Test and DSTS Test

ARES system is an advanced strain controlled rheometer, which tests the specimen's storage modulus and loss modulus precisely. This paper also conducted an ARES test on the same material and the results of ARES test and DSTS test are compared. In the ARES test, the diameter of plate is 25 mm, the gap between two plate is 1 mm and the frequency ranges from 0.63 to 6.3 rad/s.

The comparison of storage modulus between ARES test and DSTS test is shown in **Figure 12A**. It is shown that the storage modulus increases as the frequency increases in ARES test. The storage modulus obtained by DSTS test is 1.4∼3.5 times ARES's result. This phenomenon was caused by extrusion effect. When the shear plate was moving in the steel box, the moving path of shear plate and surface of polymer did not fit smoothly which can cause additional lateral compression, namely the extrusion effect, while the ARES test is pure shear test without the extrusion effect. The extrusion effect does unavoidably exist in the behavior of VDW, showing the necessity of DSTS test.

The comparison of loss modulus between ARES test and DSTS test is shown in **Figure 12B**. It is shown that the loss modulus increases as the frequency increases in ARES test. The loss modulus obtained by DSTS test is 2.1∼2.5 times ARES's result. This phenomenon was also caused by the extrusion effect. The comparison here above indicates that the DSTS test can capture dynamic mechanical properties of materials under engineering condition.

CONCLUSION

The influence of loading frequency and strain amplitude on mechanical properties of PIB has been investigated by DSTS test which was designed by considering the engineering working condition of PIB in VDW. The main conclusion can be summarized as follow:

1. Radial linear regression method was proposed to calculate storage modulus and pivotal point method was proposed to calculate loss modulus and velocity exponent. The radial linear regression method could accurately separate stress components The velocity exponent obtained by pivotal point method was both qualitatively reasonable and accurate to simulate the experimental curves.
2. The velocity exponent obtained was generally smaller than 1, and varied from 0.8 to 1. With strain amplitude in the range of "0.4∼2.4" and the angular frequency in the range of "0.63 ∼6.3 rad/s", the velocity exponent tends to decrease with the increase of frequency and strain.
3. The storage modulus of PIB decreases as the strain amplitude increases, while it increases as the frequency increases. The loss modulus of PIB increases as the strain amplitude and frequency increase.
4. Due to the extrusion effect caused by engineering working condition, Storage modulus obtained by DSTS test is 1.4∼3.5 times ARES's result, and loss modulus obtained by DSTS test is 2.1∼2.5 times ARES's result.

In the variable strain amplitude test cases, the modulus and velocity exponent of PIB exhibited obvious fluctuation with the increase of strain amplitude. This phenomenon will affect the performance of VDW, and it will be systematically studied in the future. The suitable viscous materials for VDW are rare, therefore only DSTS tests of one kind of PIB were conducted in this paper. In the future, DSTS test will be used to find more material that suitable for VDW.

DATA AVAILABILITY

All datasets generated for this study are included in the manuscript and/or the supplementary files.

ETHICS STATEMENT

The testing material and the parameters were supplied by the Chinese agent of BASF SE.

AUTHOR CONTRIBUTIONS

FS contributed experimental design, result discussion and data analysis. JY designed DSTS test, collected and analyzed data, interpreted results, and drafted the manuscript. TW conducted ARES test and collected data.

FUNDING

Financial support by the National Key Research and Development Program of China (Project No. 2016YFC0701203) and Financial support by National Natural Science Foundation of China (No. 51778488) are greatly acknowledged.

REFERENCES

Ardakani, F., Jahani, Y., and Morshedian, J. (2012). Dynamic viscoelastic behavior of polypropylene/polybutene-1 blends and its correlation with morphology. *J. Appl. Polym. Sci.* 125, 640–648. doi: 10.1002/app.36324

Bouix, R., Viot, P., and Lataillade, J. L. (2009). Polypropylene foam behaviour under dynamic loadings: strain rate, density and microstructure effects. *Int. J. Impact Eng.* 36, 329–342. doi: 10.1016/j.ijimpeng.2007.11.007

Coulson, M., Quiroga Cortés, L., Dantras, E., Lonjon, A., and Lacabanne, C. (2018). Dynamic rheological behavior of poly (ether ketone ketone) from solid state to melt state. *J. Appl. Polym. Sci.* 135:46456. doi: 10.1002/app.46456

Dessi, C., Tsibidis, G. D., Vlassopoulos, D., De Corato, M., Trofa, M., D' Avino, G., et al. (2016). Analysis of dynamic mechanical response in torsion. *J. Rheol.* 60, 275–287. doi: 10.1122/1.4941603

Drozdov, A. D., Christiansen, J. D., Klitkou, R., and Potarniche, C. G. (2010). Viscoelasticity and viscoplasticity of polypropylene/polyethylene blends. *Int. J. Solids Struct.* 47, 2498–2507. doi: 10.1016/j.ijsolstr.2010.05.010

Fatkullin, N., Mattea, C., and Stapf, S. (2011). A simple scaling derivation of the shear thinning power-law exponent in entangled polymer melts. *Polymer* 52, 3522–3525. doi: 10.1016 /j.polymer.2011.06.009

Hu, Y. T., Palla, C., and Lips, A. (2008). Comparison between shear banding and shear thinning in entangled micellar solutions. *J. Rheol.* 52:379. doi: 10.1122/1.2836937

Japan Society of Seismic Isolation (2008). *Passive Damping Structure Design and Construction Manual*. Translated by T. Jiang. Beijing: China Architecture & Building Press [in Chinese].

Li, J. J., Jiang, H. Q., and Liu, Y. (2013). The viscoelastic effect of polymer on tracer dispersion. *J. Dispers. Sci. Technol.* 34, 222–227. doi: 10.1080/01932691.2012.658318

Makris, N., Dargush, G. F., and Constantinou, M. C. (1993). Dynamic analysis of generalized viscoelastic fluids. *J. Eng. Mech.* 119, 1663–1679.

Miyazaki, M., Kitada, Y., Arima, F., and Hristov, I. (1986). "Earthquake response control design of buildings using viscous damping walls," in *Proceedings of the 1st East Asian Conference on Structural Engineering and Construction* (Bangkok), 1882–1891. doi: 10.1016/j.engstruct.2008.05.023

Ou, J., Liu, W. Q., and Zhang, Z. T. (2005a). Experimental study on dynamic performance of viscous damping wall [in Chinese]. *Earthq. Resist. Eng. Retrofit.* 27, 55–59. doi: 10.3969/j.issn.1002-8412.2005.06.011

Ou, J., Liu, W. Q., and Zhang, Z. T. (2005b). Experimental research on a new type of viscous damping material [in Chinese]. *J. Earthq. Eng. Eng. Vibr.* 25, 108–112. doi: 10.3969/j.issn.1000-1301.2005.01.019

Phan-Thien, N. (2002). *Understanding Viscoelasticity*. Berlin: Springer, 101–102. doi: 10.1007/978-3-642-32958-6

Rad, F., Sefidmazgi, N., and Bahia, H. (2014). Application of diffusion mechanism. *Transp. Res. Rec.* 2444, 71–77. doi: 10.3141/2444-08

Sasaki, K., Miyazaki, M., and Sawada, T. (2012). "Characteristics of viscous wall damper of intense oscillation test against large earthquakes," in *Proceedings of the 15th World Conference on Earthquake Engineering* (Lisbon), 1742–1750.

Snijkers, F., and Vlassopoulos, D. (2011). Cone-partitioned-plate geometry for the ARES rheometer with temperature control. *J. Rheol.* 55:1167. doi: 10.1122/1.3625559

Sun, F. F., Wu, T. Y., and Mo, G. (2018). Resistant force model of viscous damping wall considering influence of loading frequency. *Eng. Struct.* 161, 96–107. doi: 10.1016/j.engstruct.2018.01.071

Trarieux, C., Callé, S., Moreschi, H., Poulin, A., Tranchant, J. F., and Defontaine, M. (2013). "An analytical model to describe nonlinear viscoelastic properties of fluids measured by Dynamic Acoustoelastic Testing," in *Ultrasonics Symposium* (Glasgow: IEEE). doi: 10.1109/ULTSYM.2012.0182

Trarieux, C., Callé, S., Poulin, A., Tranchant, J. F., and Defontaine, M. (2012). Measurement of nonlinear viscoelastic properties of fluids using dynamic acoustoelastic testing. *IOP Conf. Ser. Mater. Sci. Eng.* 42:2026. doi: 10.1088/1757-899X/42/1/012026

Xu, Z. D. (2007). Earthquake mitigation study on viscoelastic dampers for reinforced concrete structures. *J. Vibr. Control* 13, 29–45. doi: 10.1177/1077546306068058

Xu, Z. D., Huang, X. H., Xu, F. D., and Yuan, J. (2019). Parameters optimization of vibration isolation and mitigation system for precision platforms using non-dominated sorting genetic algorithm. *Mech. Syst. Signal Process.* 128, 191–201. doi: 10.1016/j.ymssp.2019.03.031

Xu, Z. D., Liao, Y. X., Ge, T., and Xu, C. (2016). Experimental and theoretical study on viscoelastic dampers with different matrix rubbers. *J. Eng. Mech. ASCE* 142: 04016051.

Xu, Z. D., Shen, Y. P., and Zhao, H. T. (2003). A synthetic optimization analysis method on structures with viscoelastic dampers. *Soil Dyn. Earthq. Eng.* 23, 683–689. doi: 10.1016/j.soildyn.2003.07.003

Xu, Z. D., Zhao, H. T., and Li, A. Q. (2004). Optimal analysis and experimental study on structures with viscoelastic dampers. *J. Sound Vibr.* 273, 607–618. doi: 10.1016/s0022-460x(03)00522-4

Conflict of Interest Statement: The authors declare that the research was conducted in the absence of any commercial or financial relationships that could be construed as a potential conflict of interest.

frontiers in Materials

ORIGINAL RESEARCH
published: 09 August 2019
doi: 10.3389/fmats.2019.00194

Properties Tests and Mathematical Modeling of Viscoelastic Damper at Low Temperature With Fractional Order Derivative

Yeshou Xu [1,2], Yaorong Dong [1], Xinghuai Huang [1], Ying Luo [3] and Shiwei Zhao [2,4]*

[1] Key Laboratory of C&PC Structures of the Ministry of Education, Southeast University, Nanjing, China, [2] Department of Civil and Environmental Engineering, Northwestern University, Evanston, IL, United States, [3] Faculty of Civil Engineering and Mechanics, Jiangsu University, Zhenjiang, China, [4] School of Aeronautic Science and Engineering, Beihang University, Beijing, China

In the present paper, several dynamic properties tests of the viscoelastic damper at −5°C are conducted under different frequencies and displacements to investigate the dynamic behavior of the viscoelastic damper at low temperature. The seven-parameter fractional derivative model is modified with the temperature-frequency equivalent principle and utilized to describe the dynamic properties of the viscoelastic damper. The 9050A and ZN22 viscoelastic materials are used to verify the modified seven-parameter fractional derivative model. The experimental and numerical results show that the viscoelastic damper has perfect energy dissipation capacity at low temperature, and the modified seven-parameter fractional derivative model can well capture the dynamic behavior of viscoelastic materials and dampers.

Keywords: viscoelastic damper, properties tests, mathematical modeling, temperature-frequency equivalent principle, seven-parameter fractional derivative model

Edited by:
Abid Ali Shah,
University of Science and Technology Bannu, Pakistan

Reviewed by:
Antonio Caggiano,
Darmstadt University of Technology, Germany
Peng Pan,
Tsinghua University, China

***Correspondence:**
Yeshou Xu
xuyeshou@163.com

Specialty section:
This article was submitted to Structural Materials, a section of the journal Frontiers in Materials

***Received:** 25 February 2019*
***Accepted:** 29 July 2019*
***Published:** 09 August 2019*

Citation:
Xu Y, Dong Y, Huang X, Luo Y and Zhao S (2019) Properties Tests and Mathematical Modeling of Viscoelastic Damper at Low Temperature With Fractional Order Derivative. Front. Mater. 6:194. doi: 10.3389/fmats.2019.00194

INTRODUCTION

Viscoelastic materials and dampers are a kind of passive energy dissipation techniques, which are widely used for vibration isolation and suppression in the fields of aerospace, mechanical engineering, precision instruments, and civil engineering. Rao (2003) introduced the noise control and vibration isolation technology with special treated viscoelastic laminates and spray paints and its application in vehicles and commercial airplanes. Rashid and Nicolescu (2008) developed a tuned viscoelastic damper for the unwanted vibration control of a workpiece on a palletized workholding system in milling operations. The tuned viscoelastic damper has high damping performance over a wide range of excitation frequencies, and can effectively reducethe vibration amplitudes during the milling process. Xu Z. D. et al. (2019) utilized a new kind of vibration isolation and mitigation system with high damping viscoelastic materials for reducing dynamic responses of a platform structure. The simulation results show that the system can significantly reduce the dynamic responses of the platform. Xu (2007) and Tsai and Lee (1993) applied the viscoelastic dampers in civil engineering to control the seismic behaviors of the reinforced concrete frame structures and high-rise buildings, respectively. The mathematical models for viscoelastic materials are investigated, and the effectiveness of the viscoelastic dampers are verified with dynamic experiments.

In practical applications, viscoelastic dampers are always added to the building structures or equipment, and work together to reduce the vibration responses. The dynamic properties, structure design and applications of viscoelastic dampers have been extensively studied by scholars. Min et al. (2004) carried out the seismic experiments of a 5-story full-scale steel structure model with added viscoelastic dampers, and presented a design process of the viscoelastic dampers by using the modal strain energy method. Samali and Kwok (1995) summarized the usage of viscoelastic dampers in building structures, and identified the factors affecting the dynamic performance and design procedure of viscoelastic dampers. Matsagar and Jangid (2005) investigated the seismic behaviors of multi-storied base-isolated structures with various types of isolation systems. The structures were also connected to the adjacent base-isolated or base-fixed structures by using viscoelastic dampers. The governing equations of motions for the structures were derived and solved with the Newmark's step-by-step method. The viscoelastic damper connection is found to be effective and useful in upgrading the seismic performance of the combined structures. Xu et al. (2003, 2004) introduced the simplex method to optimize the design parameters and locations of viscoelastic dampers, and conducted shaking table tests about reinforced concrete structures with viscoelastic dampers to validate the efficiency of the simplex method.

Viscoelastic materials are the main components of the viscoelastic damper, and the mechanical properties of the viscoelastic damper are greatly affected by the damping performance of the viscoelastic materials. Therefore, it is necessary to study the dynamic properties of viscoelastic materials. The appropriate selection of mathematical models is the basis for the investigation of energy dissipation and material application of viscoelastic materials. The classical models, such as the Kelvin model, Maxwell model, generalized viscoelastic models et al. (Christensen, 1971), can well describe the dynamic properties of the viscoelastic materials with varying frequencies. Based on classical models, Payne (1963) found that the amplitude of loading displacement had a significant influence on the dynamic properties of viscoelastic materials and proposed the Krous model to capture the displacement effect. Drozdov and Dorfmann (2002) studied the fracture and reformation phenomenon of the polymer molecular chains and formulated the viscoelastic constitutive relations of the rubber polymers considering the temperature influence.

The theory of fractional derivative is a concept from mathematical field, which unifies and generalizes classical calculus for non-integer order of derivation. After the first introduction by Abel in the last decades of nineteenth century, the fractional derivative was successfully applied in many areas such as heat conduction, diffusion, viscoelasticity, and mechanics of solids, control theory, and electricity (Caputo, 1974; Bagley and Torvik, 1983; Koeller, 1984; Rossikhin and Shitikova, 1997). Pritz (2003) and Schiessel et al. (1995) utilized the fractional derivative to study the viscoelastic materials and obtained the five-parameter fractional derivative model and generalized fractional derivative mathematical model. Poojary and Gangadharan (2018) introduced fractional calculation to modify the traditional viscoelastic theories and used the fractional Maxwell model to describe the viscous behavior of magnetorheological elastomers. Liu and Xu (2006) adopt the higher-order fractional derivative model to discuss the rheological properties of human bones, and the test and numerical results show that the higher-order fractional derivative model is successful and efficient in describing the viscoelasticity of human tissues. Xu et al. (2014, 2015, 2016), Xu Y. S. et al. (2019) combined the fractional derivative mathematical models and the temperature-frequency equivalent theory to characterize the effects of ambient temperature and frequency on dynamic performance of viscoelastic dampers.

It can be seen that there are few studies on the dynamic properties of viscoelastic materials and dampers at extreme low temperature with fractional derivative. In the present paper, several dynamic properties tests of the viscoelastic damper at -5°C are conducted under different frequencies and displacements. The seven-parameter fractional derivative model is modified with the temperature-frequency equivalent principle and utilized to describe the dynamic behaviors of the viscoelastic damper. The 9050A and ZN22 viscoelastic materials are used to verify the modified seven-parameter fractional derivative model. The experimental and numerical results show that the viscoelastic damper has perfect energy dissipation at low temperature (-5°C), and the modified seven-parameter fractional derivative model can well capture the dynamic behavior of viscoelastic materials and dampers under different frequencies and temperatures.

PROPERTIES TESTS

To investigate the mechanical properties of the viscoelastic damper at low temperature, the dynamic properties tests under different excitation frequencies and displacement amplitudes with -5°C are carried out and analyzed. The results show that the viscoelastic damper has perfect energy dissipation capacity, and the dynamic properties are increasing with excitation frequency and reduces when the displacement amplitude increases.

Test Procedure

The viscoelastic damper used in this paper consists of two 10-mm thick parallel viscoelastic layers and three 7-mm thick steel plates, as seen in **Figure 1**. The viscoelastic material used for the viscoelastic layers is based on the nitrile butadiene rubber, which has been developed and tested in our previous research (Xu et al., 2016), and has high energy dissipation capacity. The viscoelastic layers and the steel plates are connected together by chemical bonding in vulcanization, and deform in the opposite direction. The viscoelastic layer of the viscoelastic damper undergoes almost pure shear deformation and the external energy can be transferred into heat during the loading process.

In order to study the influence of excitation frequency and displacement amplitude on mechanic properties of the viscoelastic damper, the performance tests are conducted with a 100 kN servo-hydraulic test machine in RC&PC Key Laboratory of Education Ministry, China, as shown in **Figure 2**. Each test is conducted with 10 cycles of sinusoidal displacement u_d =

FIGURE 1 | Photo of the viscoelastic damper.

TABLE 1 | Loading conditions for properties tests of the viscoelastic damper.

Temperature t (°C)	Displacement amplitude d (mm)	Frequency f (Hz)	Cycle number (cycles)
−5	0.2, 0.5, 1.0, 1.5, 2	0.1, 0.2, 0.5, 1.0	10

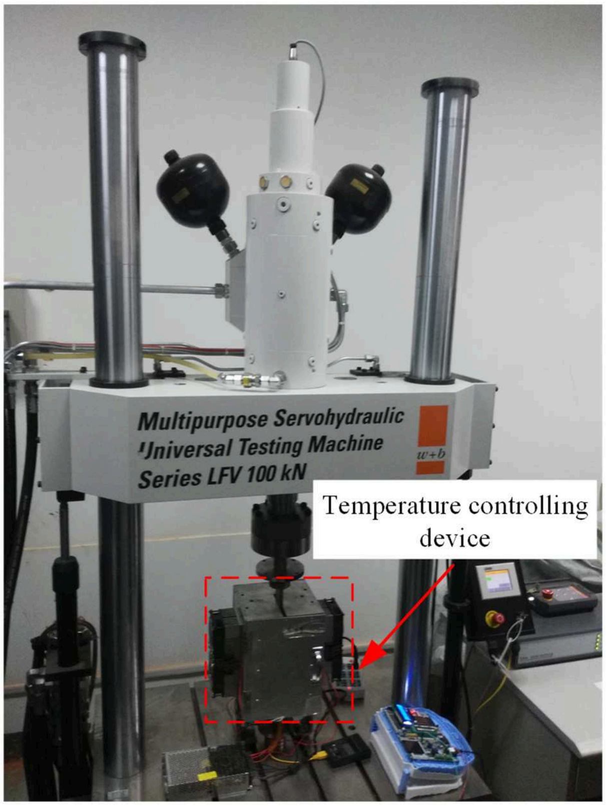

FIGURE 2 | Properties tests of the viscoelastic damper.

$u_0 \sin\left(2\pi f t\right)$, where u_0 is the maximum displacement during one loading circle, and f is the excitation frequency, the loading conditions are listed in **Table 1**. The environmental temperature of the viscoelastic damper is kept at $-5°C$ with a temperature controlling device during the whole test, as seen in **Figure 2**.

Test Results and Analysis

To obtain the dynamic properties of the viscoelastic damper, the force-displacement recording of the fifth loading circle at each test condition is picked up and vividly graphed. Additionally, the dynamic properties parameters of the viscoelastic damper at each test condition is obtained and analyzed.

The representative hysteresis curves of the viscoelastic damper are given in **Figure 3**. It can be seen that the hysteresis curves of the viscoelastic damper are almost full ellipse, which demonstrates that the viscoelastic damper has perfect energy dissipation (Tsai and Lee, 1993; Samali and Kwok, 1995; Min et al., 2004). It can be seen in **Figures 3A,B** that, the slope and area of the hysteresis curves increase when the frequency increases, meaning that the energy dissipation capacity and stiffness increase with increasing frequency. **Figures 3C,D** show that the area of the hysteresis curves increases with increasing displacement, while the slope of the hysteresis curves is slightly decreased. As the slope and area of the hysteresis curves are directly related to the energy dissipation and stiffness of the viscoelastic damper, it can be concluded that the energy dissipation increases with increasing displacement and the stiffness decreases.

According to the energy dissipation theory of viscoelastic dampers (Tsai and Lee, 1993; Samali and Kwok, 1995; Min et al., 2004), each single hysteresis curve of the viscoelastic damper with the sinusoidal excitation $u_d = u_0 \sin\left(2\pi f t\right)$ can be taken as a full ellipse as shown in **Figure 4**. The force-displacement relationship has the form

$$\left(\frac{F_d - K_e u_d}{\eta K_e u_0}\right)^2 + \left(\frac{u_d}{u_0}\right)^2 = 1 \tag{1}$$

where F_d and u_d is the damping force and displacement of the viscoelastic damper, respectively; K_e is the equivalent stiffness and $K_e = \frac{F_1}{u_0}$, and u_0 is the displacement amplitude, and F_1 is the damping force at the maximum displacement; F_2 is the corresponding force at the zero displacement, and F is the biggest damping force in the single hysteresis curve.

Then, the most important dynamic parameters, the storage modulus G_1 and loss factor η of the viscoelastic damper can be expressed as

$$G_1 = \frac{F_1 h_v}{n_v A_v u_0} \tag{2}$$

$$\eta = \frac{F_2}{F_1} \tag{3}$$

where n_v presents the number of viscoelastic material layers, A_v and h_v is the shear area and thickness of the viscoelastic material layer. For the viscoelastic damper used in this study, $n_v = 2$, $A_v = 3000\ \mathrm{mm}^2$ and $h_v = 10$ mm. Then, with Equations (2) and (3), the storage modulus G_1 and loss factor η of the viscoelastic damper at each test condition can be calculated and listed in **Table 2**.

To clearly reveal the dynamic properties and energy dissipation of the viscoelastic damper, the storage modulus G_1 and loss factor η at each test condition are pictured in **Figure 5**.

Figures 5A,B show the relationship of characteristic parameters and excitation frequency. It can be seen that the storage modulus and loss factor increase rapidly with increasing

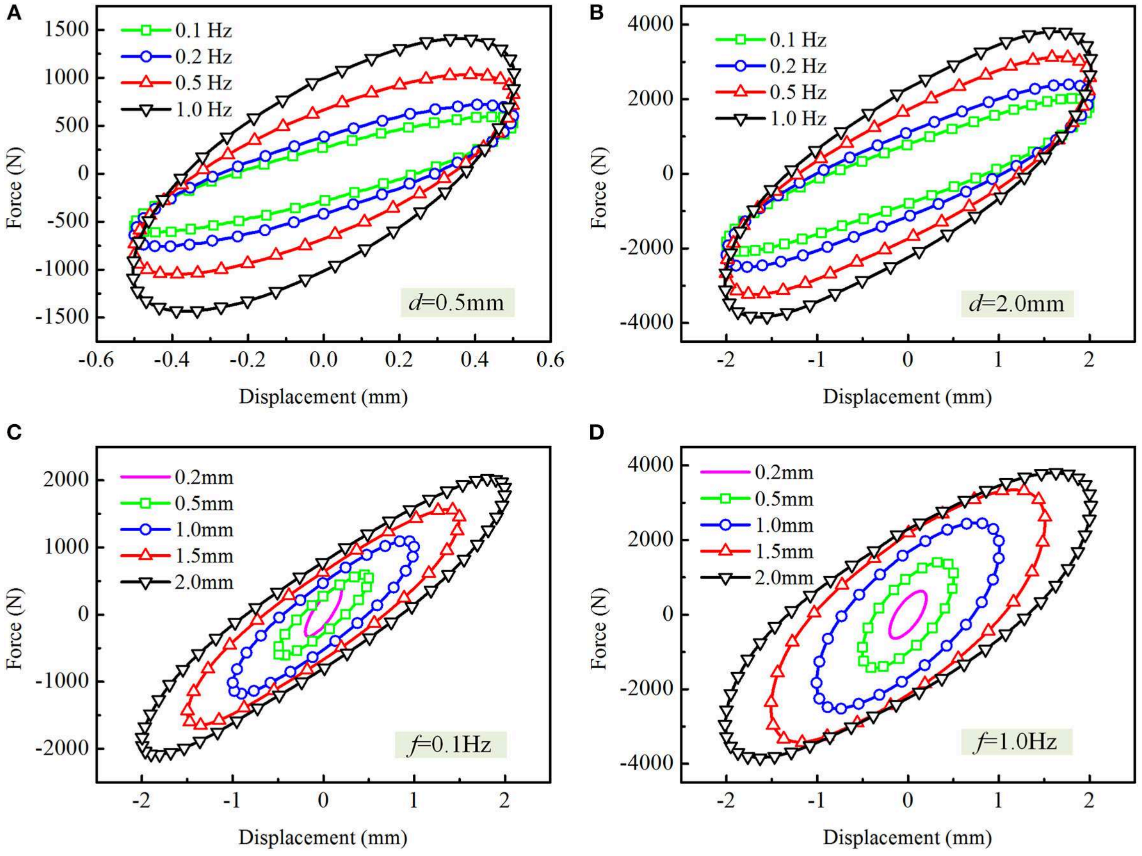

FIGURE 3 | The representative force-displacement hysteresis loops of the viscoelastic damper. **(A–D)** *d* = 0.5 mm, *d* = 2.0 mm, *f* = 0.1 Hz, and *f* = 1.0 Hz, respectively.

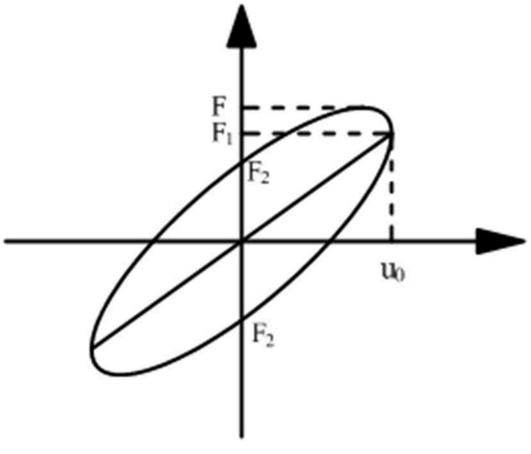

FIGURE 4 | Force-displacement hysteresis curve.

frequency. Take 1 mm as an example, the storage modulus is increased by 14.59% in the range of 0.1–0.2 Hz, increased by 32.03% in the range of 0.2–0.5 Hz, and increased by 19.52% in the range of 0.5–1.0 Hz. The loss factor is increased by 24.6% in the range of 0.1–0.2 Hz, increased by 24.63% in the range of 0.2–0.5 Hz and increased by 20.46% in the range of 0.5–1.0 Hz. In summary, the storage modulus and loss factor of the viscoelastic damper are greatly influenced by the excitation frequency.

Figures 5C,D give the relationships between the characteristic parameters and displacement amplitude. It can be seen that the storage modulus and loss factor decreases with increasing displacement amplitude. Taking the condition of 0.5 Hz as an example, the storage modulus is decreased by 9.52% in the range of 0.2–0.5 mm, decreased by 4.69% in the range of 0.5–1.0 mm, decreased by 9.07% in the range of 1.0–1.5 mm, and decreased by 8.4% in the range of 1.5–2.0 mm. The loss factor is decreased by 1.29% in the range of 0.2–0.5 mm, decreased by 8.48% in the range of 0.5–1.0 mm, decreased by 2.19% in the range of 1.0–1.5 mm and decreased by 8.45% in the range of 1.5–2.0 mm. It also should be noted that the storage modulus with frequency 0.1 Hz and displacement 0.2 mm are much larger than that with frequency 0.2 Hz and displacement 0.2 mm, this abnormal phenomenon may occur due to the test errors during the experimental process and the properties complexity of viscoelastic materials at low temperature situations. In summary, the displacement amplitude have important influence on the storage modulus and loss factor of the viscoelastic damper.

TABLE 2 | Characteristic parameters G_1, η of the viscoelastic damper.

Displacement ***d*** **(mm)**	**Frequency** ***f*** **(Hz)**	**Storage modulus** G_1 **(MPa)**	**Loss factor** η
0.2	0.1	2.5578	0.6942
	0.2	2.2325	0.8012
	0.5	2.9713	0.8442
	1.0	3.8817	0.9869
0.5	0.1	1.7238	0.5332
	0.2	2.0579	0.6507
	0.5	2.6885	0.8333
	1.0	3.6217	0.9282
1.0	0.1	1.6943	0.4911
	0.2	1.9408	0.6119
	0.5	2.5625	0.7626
	1.0	3.0626	0.9186
1.5	0.1	1.5822	0.4547
	0.2	1.8828	0.5825
	0.5	2.3300	0.7459
	1.0	2.7726	0.8716
2.0	0.1	1.5546	0.4254
	0.2	1.7681	0.5352
	0.5	2.1343	0.6829
	0.1	2.4470	0.7688

MODIFICATION OF THE SEVEN-PARAMETER FRACTIONAL DERIVATIVE MODEL

The seven-parameter fractional derivative model include three parallel elements, one Hook spring element and two fractional Maxwell models (Müller et al., 2011), as shown in **Figure 6**. The stress-strain relation of the Hook spring can be given as

$$\mu_0 \varepsilon_0 = \sigma_0 \tag{4}$$

where μ_0 presents the modulus of the Hook spring element. For the two fractional Maxwell models

$$\mu_i \varepsilon_{is} = \eta_i D^{\alpha_i} \varepsilon_{id} = \sigma_i \tag{5}$$

$$\varepsilon_{is} + \varepsilon_{id} = \varepsilon_i \tag{6}$$

where μ_i and η_i present the modulus of the spring and the damping coefficient of the fractional dashpot for the i-th fractional Maxwell model, respectively, $i = 1, 2$; D^{α_i} denotes the α_i-order fractional derivative, and $0 < \alpha_i < 1$; σ_i and ε_i denote the stress and strain of i-th fractional Maxwell model, respectively; ε_{is} andε_{id} present the strain of the spring and dashpot, respectively. Then we have

$$\varepsilon_0 = \varepsilon_1 = \varepsilon_2 = \varepsilon_t \tag{7}$$

$$\sigma_0 + \sigma_1 + \sigma_2 = \sigma_t \tag{8}$$

where σ_t and ε_t are the stress and strain of the seven-parameter fractional derivative model.

From Equations (5) and (6), we can obtain

$$\mu_i \eta_i D^{\alpha_i} \varepsilon_i = \left(\mu_i + \eta_i D^{\alpha_i}\right) \sigma_i \tag{9}$$

By performing the Fourier transform on Equation (9), we can get

$$\mu_i \eta_i (j\omega)^{\alpha_i} \varepsilon_i^* = \left(\mu_i + \eta_i (j\omega)^{\alpha_i}\right) \sigma_i^* \tag{10}$$

where ω is the angular frequency of the loading stress or strain; and j is the unit complex number; and the star symbol denotes that the strain and stress are in complex form. Then the modulus of each fractional Maxwell model in complex form, expressed in the frequency domain, can be obtained as

$$G_i^* = \frac{\mu_i \eta_i (j\omega)^{\alpha_i}}{\mu_i + \eta_i (j\omega)^{\alpha_i}} \tag{11}$$

Together with Equations (4), (7), (8), and (11), we can obtain the complex modulus of the seven-parameter fractional derivative model

$$G^* = \mu_0 + \sum_{i=1}^{2} \frac{\mu_i \eta_i (j\omega)^{\alpha_i}}{\mu_i + \eta_i (j\omega)^{\alpha_i}} \tag{12}$$

By applying the relation $j^{\alpha_i} = \cos\left(\frac{\alpha_i \pi}{2}\right) + \sin\left(\frac{\alpha_i \pi}{2}\right) j$ into Equation (12), the complex modulus can be decomposed into two parts, the real part and the imaginary part, which are defined as the storage modulus and loss modulus of viscoelastic materials, and the ratio of the loss modulus to the storage modulus is taken as the loss factor, then

$$G_1 = \mathrm{Re}\left(G^*\right) = \mu_0 + \sum_{i=1}^{2} \frac{\mu_i^2 \eta_i \omega^{\alpha_i} \cos\left(\frac{\alpha_i \pi}{2}\right) + \mu_i \eta_i^2 \omega^{2\alpha_i}}{\mu_i^2 + 2\mu_i \eta_i \omega^{\alpha_i} \cos\left(\frac{\alpha_i \pi}{2}\right) + \eta_i^2 \omega^{2\alpha_i}} \tag{13}$$

$$G_2 = \mathrm{Im}\left(G^*\right) = \sum_{i=1}^{2} \frac{\mu_i^2 \eta_i \omega^{\alpha_i} \sin\left(\frac{\alpha_i \pi}{2}\right)}{\mu_i^2 + 2\mu_i \eta_i \omega^{\alpha_i} \cos\left(\frac{\alpha_i \pi}{2}\right) + \eta_i^2 \omega^{2\alpha_i}} \tag{14}$$

$$\eta = \frac{G_2}{G_1} \tag{15}$$

Where G_1, G_2, and η denote the storage modulus, loss modulus and loss factor of viscoelastic materials.

There is an equivalent relationship between high temperature and low frequency for most viscoelastic materials when the temperature is from the glass transition temperature Tg to Tg^+ 100°C, which can be described by the temperature-frequency equivalent theory (Xu et al., 2014, 2015, 2016; Xu Y. S. et al., 2019), as shown in Equation (16)

$$\begin{aligned} G_1(\omega, T) &= G_1(\alpha_T \omega, T_0) \\ \eta(\omega, T) &= \eta(\alpha_T \omega, T_0) \end{aligned} \tag{16}$$

where T_0 is the reference temperature, and α_T is the function of temperature and has the form

$$\alpha_T = 10^{-12(T - T_0)/[525 + (T - T_0)]} \tag{17}$$

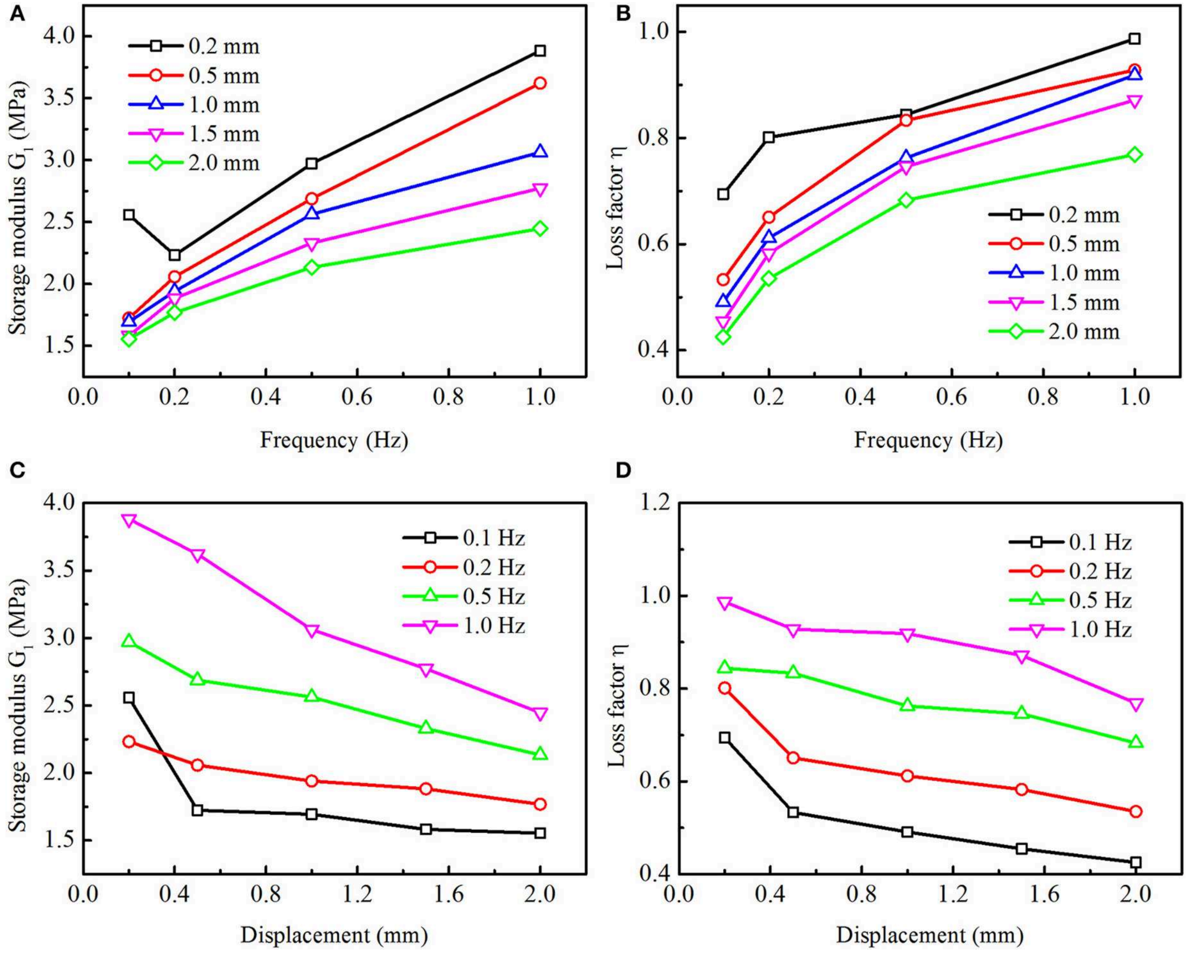

FIGURE 5 | The storage modulus and loss factor of the viscoelastic damper with different test conditions. **(A–D)** Storage modulus, loss factor, storage modulus, and loss factor, respectively.

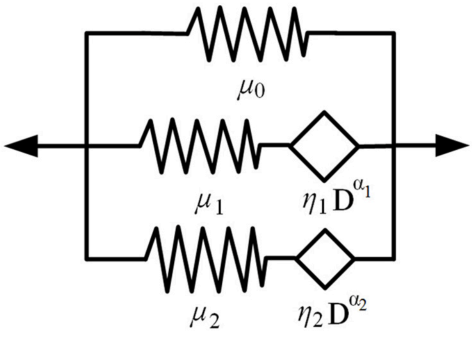

FIGURE 6 | The seven-parameter fractional derivative model.

when this theory is used to describe the dynamic properties of the viscoelastic damper with different temperatures, the dynamic parameters of the viscoelastic damper in Equations (13)–(15) can be changed as

$$G_1 = \mu_0 + \sum_{i=1}^{2} \frac{\mu_i^2 \eta_i (\alpha_T \omega)^{\alpha_i} \cos\left(\frac{\alpha_i \pi}{2}\right) + \mu_i \eta_i^2 (\alpha_T \omega)^{2\alpha_i}}{\mu_i^2 + 2\mu_i \eta_i (\alpha_T \omega)^{\alpha_i} \cos\left(\frac{\alpha_i \pi}{2}\right) + \eta_i^2 (\alpha_T \omega)^{2\alpha_i}} \tag{18}$$

$$G_2 = \sum_{i=1}^{2} \frac{\mu_i^2 \eta_i (\alpha_T \omega)^{\alpha_i} \sin\left(\frac{\alpha_i \pi}{2}\right)}{\mu_i^2 + 2\mu_i \eta_i (\alpha_T \omega)^{\alpha_i} \cos\left(\frac{\alpha_i \pi}{2}\right) + \eta_i^2 (\alpha_T \omega)^{2\alpha_i}} \tag{19}$$

$$\eta = \frac{G_2}{G_1} \tag{20}$$

Equations (17)–(20) are the formulations of the modified seven-parameter fractional derivative model. The advantage of this modified model is that it is more efficient in describing the nonlinear behavior of viscoelastic materials (Müller et al., 2011), and it can reveal the influence of different temperatures and frequencies on the mechanical properties of viscoelastic materials at the same time.

MODEL APPLICATION FOR THE VISCOELASTIC DAMPER

In this section, in order to deeply investigate the influence of frequency on the dynamic properties of the viscoelastic damper at low temperature (−5°C), the abovementioned mathematical model, the modified seven-parameter fractional derivative model, and the equivalent fractional Kelvin model (Xu et al., 2015) are employed to numerically calculate the storage modulus and loss factor of the viscoelastic damper. The expression of the equivalent fractional Kelvin model has the form

$$G_1 = q_0 + q_1(\alpha_T\omega)^\gamma \cos\left(\frac{\gamma\pi}{2}\right) \tag{21}$$

$$\eta = \frac{q_1(\alpha_T\omega)^\gamma \sin\left(\frac{\gamma\pi}{2}\right)}{q_0 + q_1(\alpha_T\omega)^\gamma \cos\left(\frac{\gamma\pi}{2}\right)} \tag{22}$$

where q_0 and q_1 are the coefficients related to the viscoelastic materials, γ is the order of fractional derivative, α_T has been given in Equation (17).

Because Equations (17)–(22) in the two models could not describe the displacement amplitude influence, the impact of displacement amplitude on dynamic properties of viscoelastic dampers is ignored, and only parts of the test data (with displacement 0.2 and 1.5 mm) in **Table 2** are used to determine the parameters of the modified seven-parameter fractional derivative model and the equivalent fractional Kelvin model with the least squares method. Then for the modified seven-parameter fractional derivative model, the parameters can be obtained as, $\mu_0 = 2.8954 \times 10^5$, $\mu_1 = 4.4113 \times 10^7$, $\eta_1 = 1.5075 \times 10^6$, $\alpha_1 = 0.2054$, $\mu_2 = 2.1123 \times 10^8$, $\eta_2 = 1.0714 \times 10^6$, $\alpha_2 = 0.7104$, and $T_0 = -16.89$°C. For the equivalent fractional Kelvin model, $q_0 = 9.3111 \times 10^5$, $q_1 = 1.831 \times 10^7$, $\gamma = 0.5516$, and $T_0 = -114.15$°C. The test data with the displacement 1.0 mm (which are not used for the parameters determination) are used to verify the numerical results of the proposed model. The experimental and numerical results comparisons of the modified seven-parameter fractional derivative model and the equivalent fractional Kelvin model of the viscoelastic damper are summarized in **Table 3** and graphed in **Figure 7**.

It can be obviously seen in **Figure 7** that both the modified seven-parameter fractional derivative model and equivalent fractional Kelvin model have perfect accuracy in describing the characteristic parameters of the viscoelastic damper with different frequencies. The errors of both models for storage modulus and loss factor are <10%, but the errors of the modified seven-parameter fractional derivative model always have smaller values. For example, when the frequency is 1 Hz, the storage modulus and loss factor of the viscoelastic damper in test data are 3.0626 MPa and 0.9186; while for the numerical results from the modified seven-parameter fractional derivative model, the storage modulus and loss factor are 3.2062 MPa and 0.8836, and the errors are 4.69 and 3.52%, respectively; for equivalent fractional Kelvin model, the storage modulus and loss factor are 3.3053 MPa and 0.845, the errors are 7.83 and 8.02%, respectively.

MODEL VERIFICATION

To further verify the accuracy of the modified seven-parameter fractional derivative model with different temperatures, the experimental data (Xu et al., 2015) for 9050 A and ZN22 viscoelastic materials under different frequencies and temperatures are compared with the numerical results calculated from the modified seven-parameter fractional derivative model and the equivalent fractional Kelvin model.

Some parts of the experimental data are used to evaluate the model parameters, and the numerical results are compared with the whole test results. With the least squares method, the model parameters of 9050A materials can be determined as, $\mu_0 = 1.0563 \times 10^6$, $\mu_1 = 4.6305 \times 10^7$, η_1=6.1554, $\alpha_1 = 0.9741$, $\mu_2 = 7.5296 \times 10^8$, $\eta_2 = 4.685 \times 10^4$, $\alpha_2 = 0.3144$, and $T_0 = 153.85$°C for the modified seven-parameter fractional derivative model; and $q_0 = 1.9032 \times 10^6$, $q_1 = 229.7502$, $\gamma = 0.6888$, and $T_0 = 164.57$°C for the equivalent fractional Kelvin model. The model parameters of ZN22 materials can also be obtained as, $\mu_0 = 2.1575 \times 10^6$, $\mu_1 = 4.6317 \times 10^8$, η_1=0.0547, $\alpha_1 = 0.6682$, $\mu_2 = 3.9676 \times 10^8$, $\eta_2 = 0.0733$, $\alpha_2 = 0.6326$, and $T_0 = 272.2$°C for the modified seven-parameter fractional derivative model; and $q_0 = 2.1972 \times 10^6$, $q_1 = 0.1322$, $\gamma = 0.6575$, and $T_0 = 270.72$°C for the equivalent fractional Kelvin model. The experimental and numerical results comparisons of 9050A and Zn22 viscoelastic materials are given in **Tables 4**, **5**, and vividly graphed in **Figures 8**, **9**. **Figure 8** shows the experimental and numerical results comparisons of 9050A material.

It can be concluded from **Figure 8A** that the modified seven-parameter fractional derivative model is more accurate than the equivalent fractional Kelvin model when describing the storage modulus with different frequencies. Take 0.1 Hz as an example, the test data for storage modulus is 2.5 MPa; and the numerical results from the modified seven-parameter fractional derivative model is 2.3737 Mpa with error 5.05%; and the numerical results from the equivalent fractional Kelvin model are 2.369 Mpa with error 5.24%. It can be seen in **Figure 8B** that with the frequencies 0.2–1.0 Hz, the errors of the modified seven-parameter fractional derivative model is a little larger than the equivalent fractional Kelvin model when describing the loss factor with different frequencies, this may due to the complexity of viscoelastic materials at low temperatures, test errors, or the local distortion when determining the model parameters.

It also can be revealed from **Figures 8C,D** that the modified seven-parameter fractional derivative model is better than the equivalent fractional Kelvin model in capturing the variation trends of storage modulus and loss factor with different temperatures. Take −20°C as an example, the test data for storage modulus and loss factor are 17 MPa and 1.38; and the numerical results from the modified seven-parameter fractional derivative model are 15.8014 Mpa and 1.3002, with errors 7.05 and 5.78%; the numerical results from the equivalent fractional Kelvin model are 13.5023 Mpa and 1.6153, with errors 20.57 and 17.05%. It should be emphasized in **Figure 8D** that the numerical loss factor curve from the modified seven-parameter fractional derivative model has more consistency with the experimental loss factor

TABLE 3 | Comparison of experimental and numerical results when $d = 1.0$ mm.

Frequency *f* (Hz)	Experimental results		Modified seven-parameter fractional derivative model		Equivalent fractional Kelvin model	
	Storage modulus G_1 (MPa)	Loss factor η	Storage modulus G_1 (MPa)	Loss factor η	Storage modulus G_1 (MPa)	Loss factor η
0.1	1.6943	0.4911	1.6295	0.4977	1.597	0.4907
0.2	1.9408	0.6119	1.9371	0.5921	1.9071	0.6022
0.5	2.5625	0.7626	2.5292	0.7484	2.5489	0.7469
1.0	3.0626	0.9186	3.2062	0.8863	3.3023	0.845

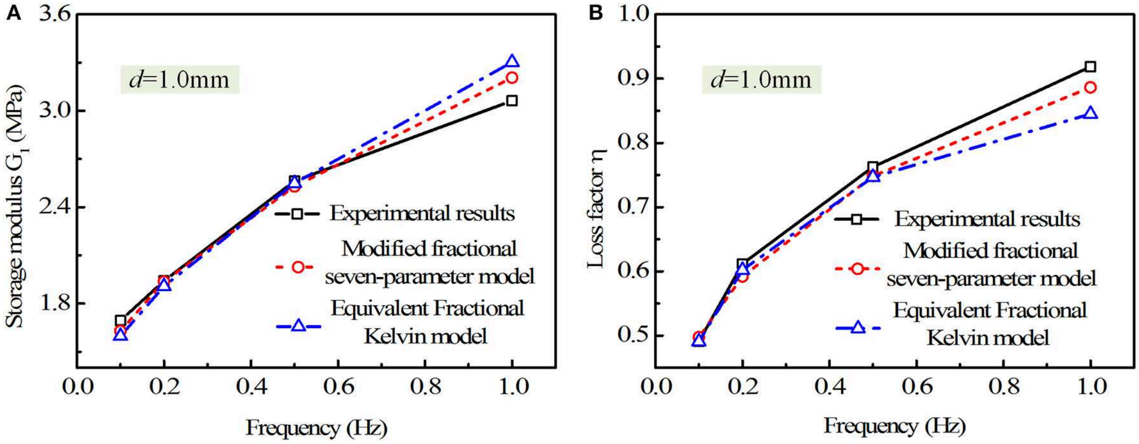

FIGURE 7 | The experimental and numerical results comparison of the viscoelastic damper when $d = 1.0$ mm. **(A,B)** Storage modulus, and loss factor, respectively.

TABLE 4 | Experimental and numerical results comparison for 9050A viscoelastic material.

Temperature *t* (°C)	Frequency *f* (Hz)	Experimental results		Modified seven-parameter fractional derivative model		Equivalent fractional Kelvin model	
		Storage modulus G_1 (MPa)	Loss factor η	Storage modulus G_1 (MPa)	Loss factor η	Storage modulus G_1 (MPa)	Loss factor η
−20	1	17	1.38	15.8014	1.3002	13.5023	1.6153
−10	1	5.8	1.39	6.2628	1.4611	6.9226	1.3634
−10	2	10	1.40	10.3450	1.4929	9.9943	1.5223
0	0.1	2.5	0.4	2.3737	0.4106	2.3690	0.3697
0	0.5	3.3	0.9	3.3091	0.7464	3.3148	0.8007
0	1	3.8	1.10	3.9911	1.0028	4.1786	1.0239
0	5	9.7	1.39	9.0002	1.5222	8.7982	1.4736
10	1	3.0	0.71	3.0625	0.6511	2.9797	0.6793
10	2	3.4	0.92	3.6285	0.8700	3.6385	0.8968
20	1	2.7	0.40	2.5096	0.4539	2.4330	0.4094

curve than that from the equivalent fractional Kelvin model, which proves the advantage of the modified seven-parameter fractional derivative model in describing the nonlinear dynamic behaviors of viscoelastic materials, especially at low temperature. The same conclusion can be obtained from **Figure 9** which compares the experimental and numerical results of ZN22 viscoelastic material.

CONCLUSIONS

In present paper, the dynamic properties tests of the viscoelastic damper are carried out at low temperature (−5°C). The influence of frequency and displacement on the dynamic properties of the viscoelastic damper are discussed. The seven-parameter fractional derivative model is modified and applied to

TABLE 5 | Experimental and numerical results comparison for Zn22 viscoelastic material.

Temperature t (°C)	Frequency f (Hz)	Experimental results		Modified seven-parameter fractional derivative model		Equivalent fractional Kelvin model	
		Storage modulus G_1 (MPa)	Loss factor η	Storage modulus G_1 (MPa)	Loss factor η	Storage modulus G_1 (MPa)	Loss factor η
15	0.5	6	1.14	6.7519	1.1116	6.6662	1.1235
15	1	9.7	1.32	9.4360	1.2457	9.2464	1.2776
15	2	14.0	1.40	13.7233	1.3362	13.3163	1.3993
20	0.1	3.1	0.5	2.9859	0.4600	3.0104	0.4527
20	0.5	4.6	0.86	4.5429	0.8657	4.5404	0.8649
20	1	5.9	1.01	5.9258	1.0425	5.8932	1.0510
20	2	8.3	1.19	8.1212	1.1926	8.0271	1.2171
25	0.5	3.1	0.6	3.4286	0.6138	3.4545	0.6099
25	1	4.3	0.72	4.1624	0.7953	4.1804	0.7950
30	1	3.6	0.58	3.2503	0.5570	3.2849	0.5549

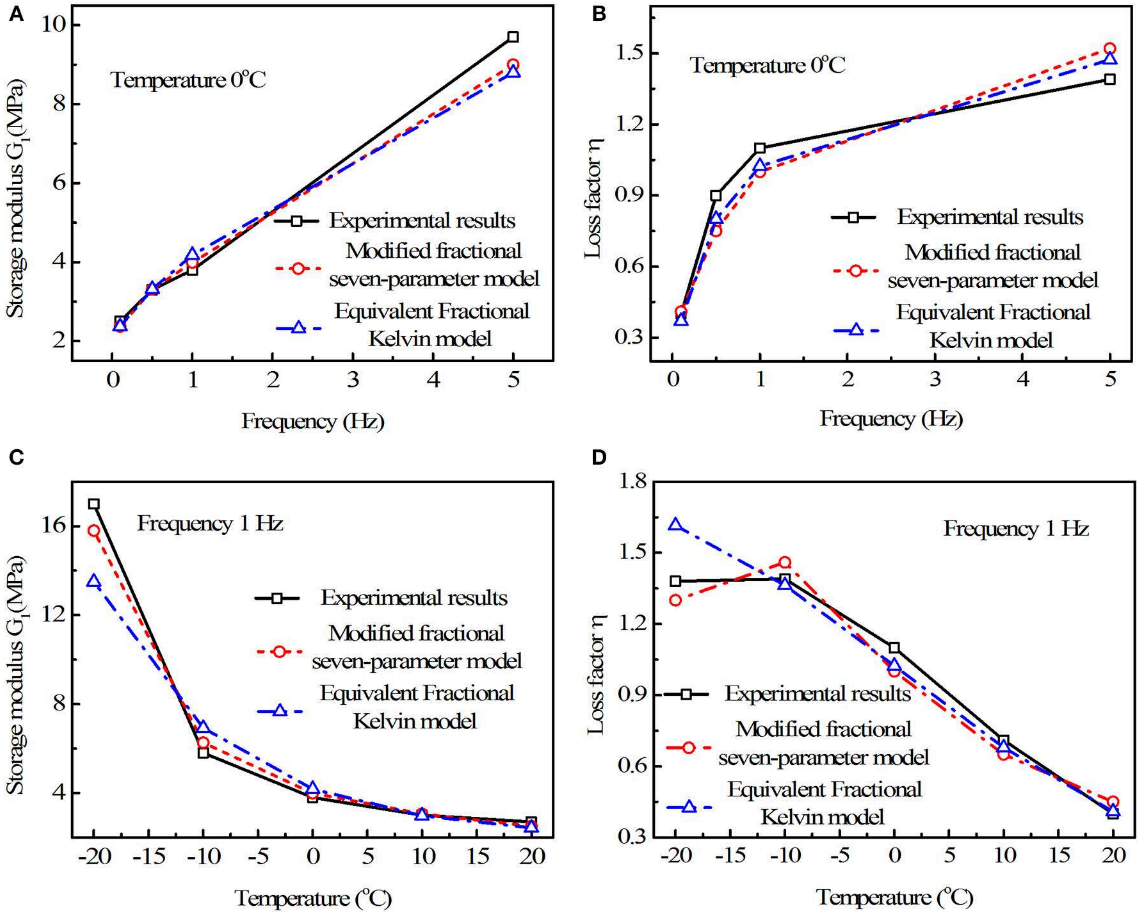

FIGURE 8 | The experimental and numerical results comparison of 9050A viscoelastic material. **(A–D)** Storage modulus, loss factor, storage modulus, and loss factor, respectively.

describe the dynamic behaviors of the viscoelastic damper. The experimental data for 9050 A and ZN22 viscoelastic materials under different frequencies and temperatures are utilized to validate the modified seven-parameter fractional derivative model. Finally, some notable conclusions can be obtained as follows:

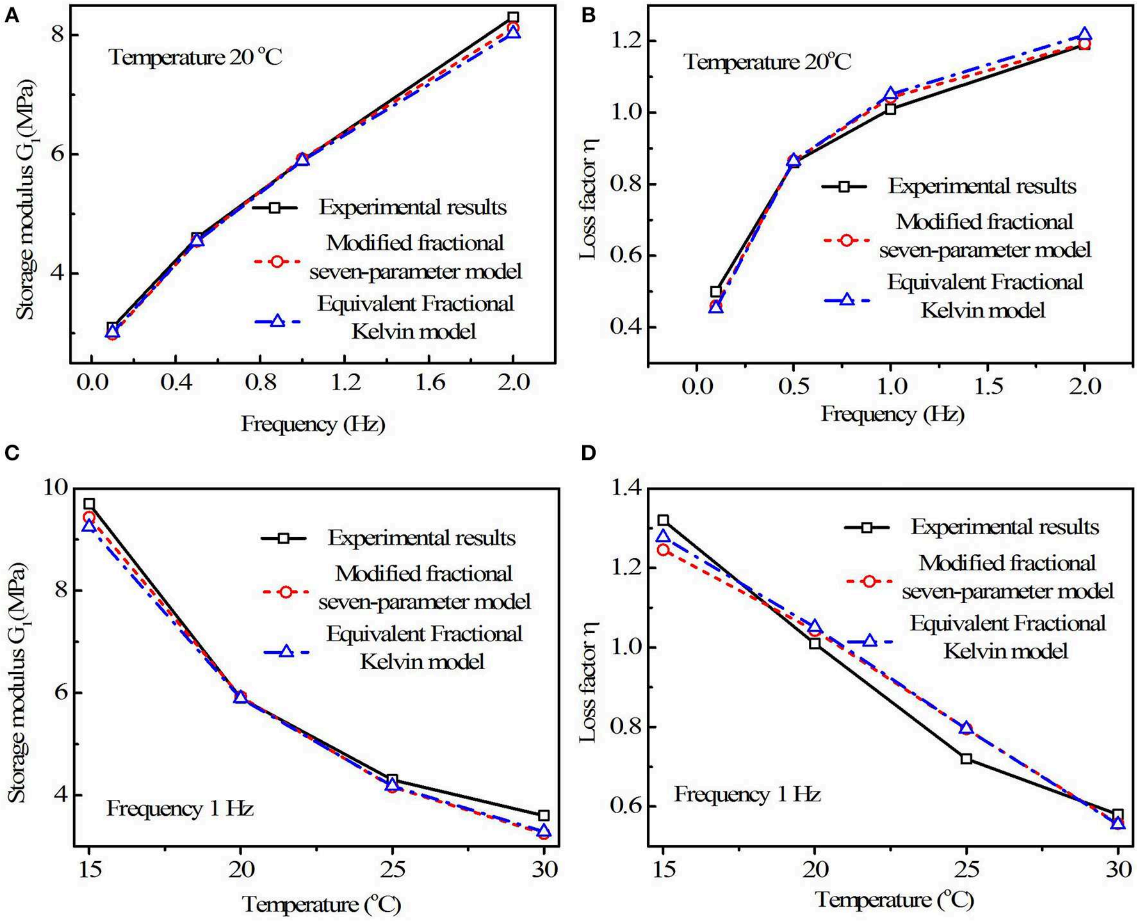

FIGURE 9 | The experimental and numerical results comparison of ZN22 viscoelastic material. **(A–D)** Storage modulus, loss factor, storage modulus, and loss factor, respectively.

(1) The viscoelastic damper has perfect energy dissipation capacity with nearly full ellipse hysteretic curves at low temperature.
(2) The loading frequency and displacement amplitude have important influence on the dynamic properties of the viscoelastic damper. The storage modulus and loss factor increase quickly with increasing frequency, while decrease when the displacement amplitude increases.
(3) The dynamic behavior of the viscoelastic damper and viscoelastic materials (9050A and ZN22) can be precisely depicted by the modified seven-parameter fractional derivative model, which can simulate the nonlinear dynamic properties of viscoelastic materials with varying frequencies and temperatures.
(4) Viscoelastic dampers can serve in a wide temperatures ranges (−20–50°C) with larger displacements. The present work only studies the viscoelastic damper at −5°C with displacements 0.2–2.0 mm. The dynamic properties and mathematical modeling of viscoelastic dampers at extreme temperatures (for example, −20 or 50°C) and large displacement amplitudes still need to be further investigated.

DATA AVAILABILITY

Publicly available datasets were analyzed in this study. This data can be found here: https://journals.sagepub.com/doi/pdf/10.1177/1077546313513604; https://journals.sagepub.com/doi/pdf/10.1177/1077546313513604/a.

AUTHOR CONTRIBUTIONS

YX and YD carried out the properties tests of the viscoelastic damper. XH formulated the mathematical model. YL and SZ conducted the application and verification of the mathematical model with viscoelastic dampers and materials. YX and YL wrote and checked the manuscript.

FUNDING

This study was financially supported by the National Key R&D Programs of China with Grant Nos. 2016YFE0200500 and 2016YFE0119700, the Jiangsu Province International

Cooperation Project with Grant No. BZ 2018058, the National Science Fund for Distinguished Young Scholars with Grant No. 51625803, the Program of Chang Jiang Scholars of Ministry of Education, National Natural Science Foundation of China with Grant No. 11572088, the Priority Academic Program Development of Jiangsu Higher Education Institutions.

REFERENCES

Bagley, R. L., and Torvik, P. J. (1983). A theoretical basis for the application of fractional calculus to viscoelasticity. *J. Rheol.* 27, 201–210. doi: 10.1122/1.549724

Caputo, M. (1974). Vibrations on an infinite viscoelastic layer with a dissipative memory. *J. Acoust. Soc. Am.* 56, 897–904. doi: 10.1121/1.1903344

Christensen, R. (1971). *Theory of Viscoelasticity: An Introduction*. New York, NY: Academic Press.

Drozdov, A. D., and Dorfmann, A. (2002). The effect of temperature on the viscoelastic response of rubbery polymers at finite strains. *Acta Mech.* 154, 189–214. doi: 10.1007/BF01170707

Koeller, R. C. (1984). Applications of fractional calculus to the theory of viscoelasticity. *J. Appl. Mech. Trans. ASME*, 51, 299–307. doi: 10.1115/1.3167616

Liu, J. G., and Xu, M. Y. (2006). Higher-order fractional constitutive equations of viscoelastic materials involving three different parameters and their relaxation and creep functions. *Mech. Time Dependent Mater.* 10, 263–279. doi: 10.1007/s11043-007-9022-9

Matsagar, V. A., and Jangid, R. S. (2005). Viscoelastic damper connected to adjacent structures involving seismic isolation. *J. Civil Eng. Manage.* 11, 309–322. doi: 10.3846/13923730.2005.9636362

Min, K. W., Kim, J., and Lee, S. H. (2004). Vibration tests of 5-storey steel frame with viscoelastic dampers. *Eng. Struct.* 26, 831–839. doi: 10.1016/j.engstruct.2004.02.004

Müller, S., Kästner, M., Brummund, J., and Ulbricht, V. (2011). A nonlinear fractional viscoelastic material model for polymers. *Comput. Mater. Sci.* 50, 2938–2949. doi: 10.1016/j.commatsci.2011.05.011

Payne, A. R. (1963). The dynamic properties of carbon black-loaded natural rubber vulcanizates Part I. *J. Appl. Polym. Sci.* 6, 57–63. doi: 10.1002/app.1962.070061906

Poojary, U. R., and Gangadharan, K. V. (2018). Integer and fractional order-based viscoelastic constitutive modeling to predict the frequency and magnetic field-induced properties of magnetorheological elastomer. *J. Vib. Acoust. Trans. ASME* 140:041007. doi: 10.1115/1.4039242

Pritz, T. (2003). Five-parameter fractional derivative model for polymeric damping materials. *J. Sound Vib.* 265, 935–952. doi: 10.1016/S0022-460X(02)01530-4

Rao, M. D. (2003). Recent applications of viscoelastic damping for noise control in automobiles and commercial airplanes. *J. Sound Vib.* 262, 457–474. doi: 10.1016/S0022-460X(03)00106-8

Rashid, A., and Nicolescu, C. M. (2008). Design and implementation of tuned viscoelastic dampers for vibration control in milling. *Int. J. Mach. Tools Manuf.* 48, 1036–1053. doi: 10.1016/j.ijmachtools.2007.12.013

Rossikhin, Y. A., and Shitikova, M. V. (1997). Applications of fractional calculus to dynamic problems of linear and nonlinear heredity mechanics of solids. *Appl. Mech. Rev. Trans. ASME* 50, 15–67. doi: 10.1115/1.3101682

Samali, B., and Kwok, K. C. S. (1995). Use of viscoelastic dampers in reducing wind-and earthquake-induced motion of building structures. *Eng. Struct.* 17, 639–654. doi: 10.1016/0141-0296(95)00034-5

Schiessel, H., Metzler, R., Blumen, A., and Nonnenmacher, T. F. (1995). Generalized viscoelastic models: their fractional equations with solutions. *J. Phys. A Math. Gen.* 28, 6567–6584. doi: 10.1088/0305-4470/28/23/012

Tsai, C. S., and Lee, H. H. (1993). Applications of viscoelastic dampers to high-rise buildings. *J. Struct. Eng. ASCE* 120, 1222–1233. doi: 10.1061/(ASCE)0733-9445(1993)119:4(1222)

Xu, Y. S., Xu, Z. D., Guo, Y. Q., Ge, T., Xu, C., and Huang, X. H. (2019). A theoretical and experimental study of viscoelastic damper based on fractional derivative approach and micro-molecular structures. *J. Vib. Acoust. Trans. ASME* 141:031010. doi: 10.1115/1.4042517

Xu, Z. D. (2007). Earthquake mitigation study on viscoelastic dampers for reinforced concrete structures. *J. Vib. Control* 13, 29–45. doi: 10.1177/1077546306068058

Xu, Z. D., Huang, X. H., Xu, F. H., and Yuan, J. (2019). Parameters optimization of vibration isolation and mitigation system for precision platforms using non-dominated sorting genetic algorithm. *Mech. Syst. Signal Process.* 128, 191–201. doi: 10.1016/j.ymssp.2019.03.031

Xu, Z. D., Liao, Y. X., Ge, T., and Xu, C. (2016). Experimental and theoretical study on viscoelastic dampers with different matrix rubbers. *J. Eng. Mech. ASCE* 142:04016051. doi: 10.1061/(ASCE)EM.1943-7889.0001101

Xu, Z. D., Shen, Y. P., and Zhao, H. T. (2003). A synthetic optimization analysis method on structures with viscoelastic dampers. *Soil Dyn. Earthq. Eng.* 23, 683–689. doi: 10.1016/j.soildyn.2003.07.003

Xu, Z. D., Wang, S. A., and Xu, C. (2014). Experimental and numerical study on long-span reticulate structure with multidimensional high-damping earthquake isolation devices. *J. Sound Vib.* 333, 3044–3057. doi: 10.1016/j.jsv.2014.02.013

Xu, Z. D., Xu, C., and Hu, J. (2015). Equivalent fractional Kelvin model and experimental study on viscoelastic damper. *J. Vib. Control* 21, 2536–2552. doi: 10.1177/1077546313513604

Xu, Z. D., Zhao, H. T., and Li, A. Q. (2004). Optimal analysis and experimental study on structures with viscoelastic dampers. *J. Sound Vib.* 273, 607–618. doi: 10.1016/S0022-460X(03)00522-4

Conflict of Interest Statement: The authors declare that the research was conducted in the absence of any commercial or financial relationships that could be construed as a potential conflict of interest.

ORIGINAL RESEARCH
published: 07 June 2019
doi: 10.3389/fmats.2019.00118

Development, Test, and Mechanical Model of the Leak-Proof Magnetorheological Damper

Jianwei Tu*, Zhao Li, Jiarui Zhang, Kui Gao, Jinpeng Liao and Jingwei Gao

Hubei Key Laboratory of Roadway Bridge & Structure Engineering, Wuhan University of Technology, Wuhan, China

As a semi-active control device, the magnetorheological (MR) damper has received much praise for its great controllability, quick response, and lower input power. However, the problem of liquid leakage arises after its long-term service, severely affecting its performance and service life. To solve this problem, this paper proposes fully vulcanizing and consolidating viscoelastic material, the cylinder barrel and the piston rod, which replaces the traditional dynamic seal with a static seal, and developing a new leak-proof MR damper. Considering that viscoelastic material has a certain energy dissipation and fluid-structure interaction with MR fluid, the correction factor of the pressure gradient is introduced to establish the mechanical model of the leak-proof MR damper which is to be tested. The testing result shows that warpage deformation of viscoelastic material weakens the damping force of the MR damper and the weakening effect increases with current intensity. Given the influence of current intensity on the correction factor, the complete mechanical model of the leak-proof MR damper is obtained on the basis of the verified model. Through the comparison between the theoretical calculation curve and the test curve, the revised mechanical model is found to well reflect the mechanical properties of the leak-proof MR damper.

Keywords: magnetorheological (MR) damper, leak-proof, viscoelastic material, mechanical model, performance test

Edited by:
Zhao-Dong Xu,
Southeast University, China

Reviewed by:
Seung-Bok Choi,
Inha University, South Korea
Yongbo Peng,
Tongji University, China
Peng Pan,
Tsinghua University, China

****Correspondence:***
Jianwei Tu
tujianwei@whut.edu.cn

Specialty section:
This article was submitted to Structural Materials, a section of the journal Frontiers in Materials

Received: *26 February 2019*
Accepted: *08 May 2019*
Published: *07 June 2019*

Citation:
Tu J, Li Z, Zhang J, Gao K, Liao J and Gao J (2019) Development, Test, and Mechanical Model of the Leak-Proof Magnetorheological Damper. Front. Mater. 6:118. doi: 10.3389/fmats.2019.00118

INTRODUCTION

Magnetorheological (MR) Fluid is a solid/liquid two-phase suspension produced by magnetizable particles dispersing in the carrier fluid. It is a new smart fluid material whose mechanical properties are adjusted remarkably by the external magnetic field. In the external magnetic field, the random disorder state of magnetizable particles is transformed into an orderly chain along the external magnetic field direction, changing MR material from homogeneously dispersed solid/liquid two-phase suspension into solid-like material. This process is fast, reversible, and controllable (Hardy, 1951; Jacob, 1951; Carlson and Spencer, 1996). Researches indicate that MR fluid is typically characterized by the shear stress, and apparent viscosity changing with the external shear rate and magnetic field intensity, and that the type, saturation magnetization, surface characteristic, size, and morphology of magnetizable particles (Jolly et al., 1999; Hato et al., 2011; Susan-Resiga and Vékás, 2014; Liu et al., 2015; Vereda et al., 2016; Mohamad et al., 2018) have a great influence on the mechanical properties of the MR material. Due to the apparent sedimentation of MR fluid, MR grease has been proposed, improving its anti-sedimentation greatly (Zhu, 2006; Hu et al., 2015). At present, the most outstanding use of MR fluid (grease) is that it is placed into a sealed container with an adjusted magnetic field to make a smart shock absorber with an adjustable damping force (Xu et al., 2013; Deng et al., 2017; Zhang et al., 2017; Christie et al., 2019), which is applied in many areas such as vibration reduction, vibration isolation, vibration absorption, and protection (Xu et al., 2000; Qu et al., 2009). For instance, there are applications in vibration control of truck seats in the auto industry (Choi et al., 2000; Sun et al., 2016), vibration control to reduce low-frequency vibration and high-frequency shock vibration of vessels in navigation field (Yao et al., 2008), vibration control to reduce the ground shock vibration of airplane landing in aviation field (Zhu et al., 2011), vibration isolation and mitigation for the precision platform of precision instrument (Xu et al., 2019).

However, the problem of liquid leakage will take place after long-term service because most magnetorheological fluid (grease) dampers are sealed with rubber seal rings. When the damper piston is moving in a reciprocating motion, friction between magnetizable particles embedded in the rubber ring and the piston rod creates vertical nicks on the rod and the carrier fluid will leak from those nicks, causing the seal failure of the damper. Some research shows that with fluid leakage, its mechanical properties will change greatly, the energy consumption area will decrease sharply, and controlling time delay will be longer, which seriously affects the vibration control effect of the MR fluid (grease) damper (Iyengar et al., 2004; Lu et al., 2011; Wang et al., 2012; Tudón-Martínez and Morales-Menendez, 2015; Jeyasenthil and Choi, 2018). Therefore, leakage shortens the service life of the MR fluid (grease) damper and restricts its application in practical projects.

To solve the problem of its leakage, Carlson (1999) has used a porous sponge material in the MR fluid damper. Under suction of capillary tubes, MR fluid is stored in the pores of the porous sponge to reduce MR fluid leakage. Kelso et al. (2003) have designed a two-tiered seal device in the damper. The first tier is at the in-out position of the piston rod, and the second is between the piston and cylinder body. The two-tiered seal can effectively prevent the damper fluid leakage. Iyengar et al. (2004) carried out the seal wear test of rod seals in a MR damper to research the wear process of the rod when the damper was working. The best sealing material is determined by wear test of fluids on sealing materials. Xu and Cao (2004) installed MRF sealing device on the inner side of cylinder barrel. The magnetic field generated by the permanent magnet is used to make the MRF form a strong liquid film, which avoids the wear and liquid leakage of the MR damper. Giorgetti et al. (2010) have designed a rotary MR damper, remarkably decreasing MR fluid sedimentation and wear of the seal device, and improving the damper durability. Tu et al. (2011) have sprayed a hard alloy coat onto the damper piston rod to improve its rigidity and delay its nicking damage, which can effectively lengthen the damper service life. Yan et al. (2013) have stored MR material with porous metallic foams in the damper to make a porous metallic foam MR damper, which can effectively reduce its leakage without a sophisticated seal. Zhou et al. (2013) used metal sealing device instead of rubber sealing to overcome the leakage problem of damper caused by aging and corrosion of rubber sealing ring. Yazid et al. (2014) have proposed a new radial hydraulic seal device, which can effectively reduce the leakage at the sealing device. Sun et al. (2016) proposes to use a rotating MR damper in seat suspension to effectively solve the shortcomings of linear dampers. The rotating MR damper can reduce not only the amount of MRF needed but also the sealing requirements. Since the O-ring cannot completely prevent hydraulic oil leakage, Delgado and San Andres (2010) have employed an end seal device with a spring contact, which has been found in testing to reduce oil leakage and air ingestion.

Most researchers propose improving the original O-ring/piston seal, and optimizing and applying a multi-tiered sealing device. Those methods can delay the fluid leakage, lengthen the service life of the MR fluid (grease) damper, but they cannot completely solve its leakage problem mainly because the dynamic seal between the O-ring and the piston will inevitably create friction damage and cause leakage. This paper proposes a static seal for the MR fluid (grease) damper. The static seal adopts viscoelastic material as the sealing material, which can produce large elastic-plastic shear deformation to ensure that viscoelastic material moves with the piston and avoids being damaged in shear deformation. This material has two properties of energy dissipation and energy storage (Christensen and Freund, 1982). When suffering external forces, its strain obviously lags behind stress, whose straining motion works over a great resistance. Some of the energy is consumed by conversion into heat and some is stored in the form of potential energy, which has a good energy dissipation action (Samali and Kwok, 1995). Viscoelastic material is extensively applied in the ship industry (Townsend et al., 2018), space industry (Cunha-Filho et al., 2016), civil engineering (Tezcan and Uluca, 2003; Xu et al., 2016) etc. Viscoelastic material is selected to be the sealing material for the leakage-proof MR damper. It is connected between the damper cylinder barrel and the piston through microwave vulcanization so that relative motion and friction will not occur between the sealing material and the piston rod in its reciprocating motion. A relative displacement is created between the piston rod and the cylinder barrel by the material's own shear deformation, forming a static seal and the viscoelastic material can absorb energy to improve the damper through its own deformation. According to this principle, a new leakage-proof MR damper is developed to radically resolve the problem of MR fluid (grease) leakage from the damper.

After applying a viscoelastic material and making the static seal device, the mechanical model of the new leakage-proof MR damper has been changed significantly and must describe the dynamic properties of both viscoelastic material and MR material. In studying the mechanical model of MR material, Stanway et al. (1987) have treated MR fluid as yield stress material and suggested the Bingham model concerning the linear relationship between shear stress and shear rate of MR fluid. Based on Bingham model, Çeşmeci and Engin (2010) have performed experiments on the linear MR fluid damper, which can predict well the outputting force of the MR fluid damper. Yang (2001) have proposed the Herschel-Bulkley model to describe the shear-thinning behaviors of MR fluid while Wen (1976) has suggested the Bouc-Wen model which is universal and is able to calculate and reflect various hysteresis curves. In studying the mechanical model of viscoelastic material, Chang et al. (1993) have suggested the Kelvin model which is formed by parallel connection of the linear spring and linear damper unit, reflecting creep and relaxation of viscoelastic material. Zhang and Soong (1992) have proposed the Maxwell model, which is formed by a series connection of the linear spring and linear damper unit. Liu (1990) has suggested the standard linear solid model, which is formed by a series connection of the spring unit and Kelvin model, reflecting both creep and relaxation of viscoelastic material and its property changes with frequency. On the basis of a standard linear solid model, Xu et al. (2010) have proposed the equivalent standard solid model with temperature-frequency equivalent theory which can accurately reflect its property changes with temperature and frequency. This paper establishes the mechanical model of a new leakage-proof MR fluid damper and tests it through the damper performance tests.

From the above research, a leakage-proof MR damper is developed to solve the leakage problem of MR damper. The leakage-proof MR damper uses viscoelastic material to vulcanize both the cylinder and piston rod, which replaces the traditional dynamic seal with a static seal. However, considering the energy-consumption of viscoelastic material and the fluid-structure interaction between viscoelastic material and magnetorheological fluid, the mechanical model of leakage-proof MR damper is changed. Based on the traditional MR damper mechanical model, the correction factor of a pressure gradient is introduced to consider the influence of viscoelastic materials on leak-proof dampers and establish the mechanical model of the leak-proof MR damper. In addition, the mechanical properties of the new MR damper also tested. It can be found that the new MR damper has good sealing performance and can fundamentally solve the leakage problem of MR damper. The mechanical model of leakage-proof MR damper can well reflect its mechanical properties.

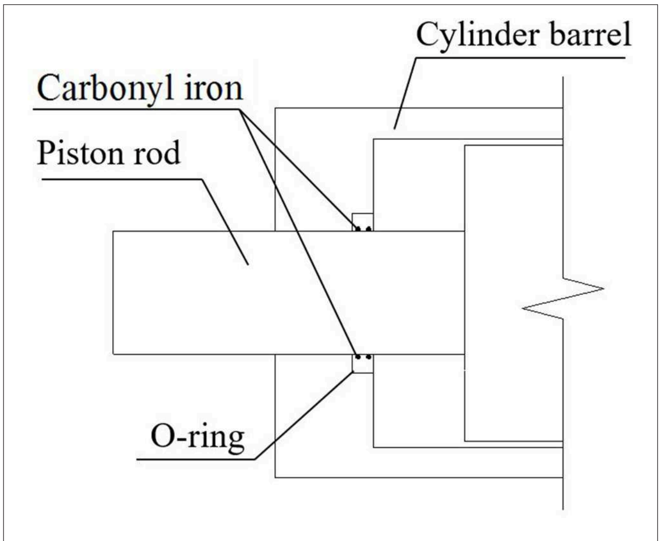

FIGURE 1 | The sealing device of a regular MR damper.

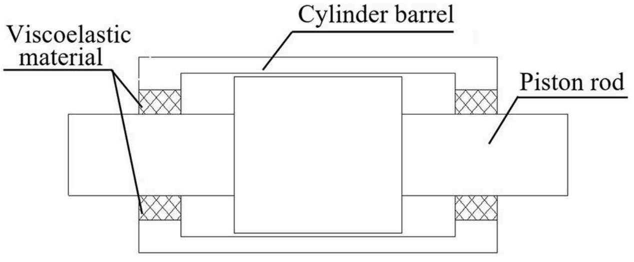

FIGURE 2 | The new leakage-proof MR damper.

THE SEALING STRUCTURE OF THE NEW LEAKAGE-PROOF MR DAMPER

When the MR damper works, its chamber is filled with MR fluid in a high-pressure condition. To prevent leakage, an O-ring made of rubber is usually devised at the port to seal the damper, as is shown in **Figure 1**. The O-ring, a regular sealing element of fluid damper, is characterized by easy manufacture, simple structure, and low cost.

As for a MR damper, magnetizable particles are embedded into the rubber O-ring by the great pressure inside the chamber, and then produce dry friction with the piston rod at the fixed position on the sealing ring. Due to the great rigidity of those particles, vertical nicks are created on the rod when it moves many times. MR fluid in the damper will leak from those nicks, seriously influencing its performance and service life. In order to solve the leakage problem of the traditional MR damper, a new leakage-proof MR damper is designed in **Figure 2**. Viscoelastic material is inserted between the cylinder barrel and the piston rod. And cylinder barrel, viscoelastic material and the piston rod are entirely connected through microwave vulcanization. The connection strength can reach the failure strength of viscoelastic materials.

When the damper operates, the reciprocating motion of the piston will cause viscoelastic material to move along, using the material's own shear deformation to make up for the displacement difference between the external cylinder barrel and the piston, as shown in **Figure 3**. In this case, no friction exists between the viscoelastic material and the piston rod, which replaces the dynamic seal with a static seal successfully. Magnetizable particles are unlikely to be embedded into the viscoelastic material to produce friction damage to the piston rod, so that the leakage problem of the traditional MR damper is radically resolved, as is shown in **Figure 4**. Besides, viscoelastic material has a stable chemical performance and strong corrosion and fatigue resistance, lengthening the damper service life and improving its engineering applicability, as shown in **Figure 5**. In the new sealing device, thickness and coherent length of viscoelastic material need designing according to reality, and a new mechanical model needs establishing to describe the mechanical properties because many changes happen to the damper.

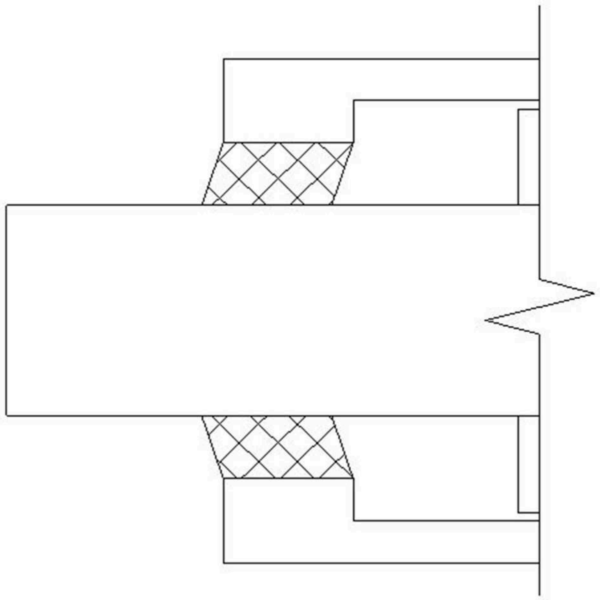

FIGURE 3 | Shear deformation of viscoelastic material.

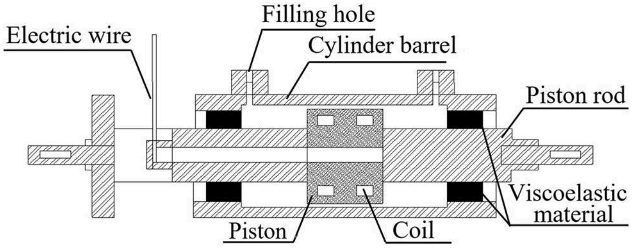

FIGURE 4 | The section diagram of the leakage-proof MR damper.

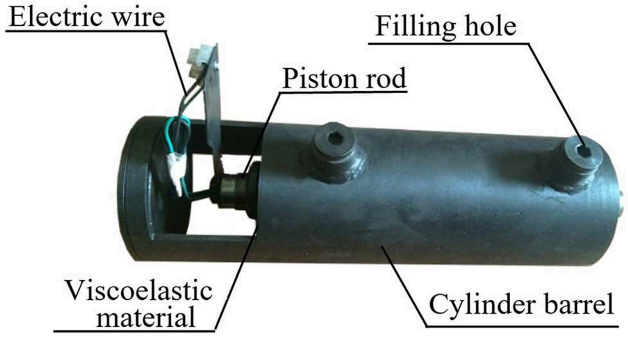

FIGURE 5 | The real diagram of the leakage-proof MR damper.

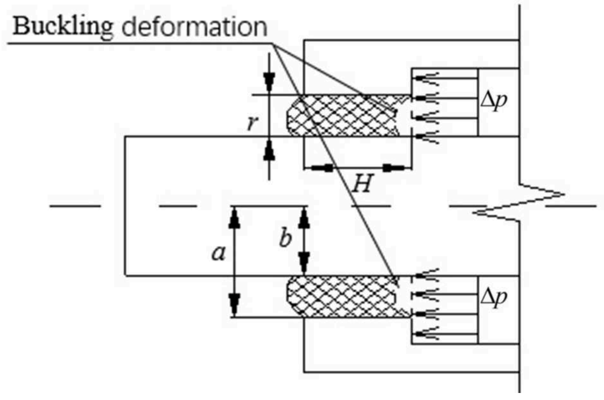

FIGURE 6 | Deformation computing model of viscoelastic material.

THE MECHANICAL MODEL OF THE NEW LEAKAGE-PROOF MR DAMPER

With viscoelastic material, the new leakage-proof MR damper is changed, compared with the traditional one in the following manner: (1) viscoelastic material itself is an energy-consume damping material. Serving as a sealing device, it will change the damping and stiffness of the device; (2) fluid-structure interaction will occur between viscoelastic material and MR fluid. On the one hand, when the MR damper works, the high pressure created by internal fluid produces warpage deformation of the viscoelastic material; on the other hand, its warpage deformation will influence the internal pressure of the damper in return. Those changes alter the damping force of the new leakage-proof MR damper. A new mechanical model must be established.

The Inner Chamber Volume Increment Caused by Warpage Deformation of Viscoelastic Material

The fluid pressure of the inner chamber produces warpage deformation of the viscoelastic material, as shown in **Figure 6**, which results in larger inner chamber capacity, smaller inner chamber pressure, and then less fluid flow through the gap channel of the damper. Fluid flow $Q_{\Delta V}$ can be obtained as:

$$Q_{\Delta V} = \frac{V-\Delta V}{t} = \left(1-\frac{\Delta V}{V}\right)\frac{V}{t} = \left(1-\frac{\Delta V}{V}\right)Q_0 \tag{1}$$

in which V is the fluid volume through the gap channel, ΔV is the inner chamber volume increment caused by viscoelastic material deformation, and Q_0 is the fluid flow through the gap channel without considering viscoelastic material deformation.

The relationship between viscoelastic material deformation ΔV and the inner chamber fluid pressure Δp is obtained by the first-order shear deformation plate theory (Wang and Ma, 2004). The dimensions of the new leakage-proof damper are shown in **Figure 6**.

Under the pressure, the corner close-form expression ψ and the deflection close-form ω of viscoelastic material can be obtained as:

$$\psi = -\frac{\Delta p}{16\Omega}r^3 + (C_1 + C_2 \ln r)r + C_3\frac{1}{r} \tag{2}$$

$$\omega = \frac{\Delta p}{64\Omega}r^4 - \frac{1}{2}(\frac{\Delta p}{2A_s} + C_1)r^2 + C_2(-\frac{r^2}{2}\ln r + \frac{r^2}{4} + \frac{2\Omega}{A_s}\ln r) \\ -C_3 \ln r + C_4 \tag{3}$$

in which $\Omega = EH^3/12(1 - v^2)$, and $A_s = k_s EH/2(1 + \mu^2)$; Δp is the pressure difference at the damper gap channel; r is the difference between inside and outside diameters of viscoelastic materials; E is the elastic modulus of viscoelastic material; H is the vulcanizing and coherent length of viscoelastic material and the piston; μ is the Poisson ratio of viscoelastic material; k_s is the shear correction factor.

The boundary conditions of viscoelastic tier are: $\Psi_a = \Psi_b = 0$, $\omega_a = \omega_b = 0$. Four unknown numbers C_1, C_2, C_3, C_4 can be obtained and substituted into Formula (3) to obtain the deflection curve. Volume increment of viscoelastic material is obtained by integrating the deflection curve. Because the fluid pressure changes with time, the deformation volume of the viscoelastic material also changes with time:

$$\Delta V(t) = 2\pi\frac{a+b}{2}\int_b^a \omega(r,t)dr = \pi(a+b)\int_b^a \omega(r,t)dr \tag{4}$$

in which a and b are the distance between the center line of the piston rod and the two bonding surface; $\omega(r,t)$ is the deflection curve of viscoelastic material.

The Correction Factor of Pressure Gradient

Because the ratio of the gap between the external cylinder barrel and the piston and the inner diameter of cylinder is very small, a parallel model (Yang, 2001) can be used to approximately simulate an axisymmetric fluid model. **Figure 7** shows the velocity profile diagram of MR fluids through parallel plates. For the different regions in **Figure 7**, the fluid velocity formulas are as follows:

$$\text{I}: \quad u_x(z) = \frac{1}{2}(-\frac{1}{\eta}\frac{dp}{dx})[h_1^2 - (h_1 - z)^2]0 \le z \le h_1 \tag{5}$$

$$\text{II}: \quad u_x(z) = \frac{1}{2}(-\frac{1}{\eta}\frac{dp}{dx})[(h - h_2)^2 - (z - h_0)^2] - v_0 h_2 \le z \le h \tag{6}$$

MR fluids in the core region "C" will flow as a whole, and the velocity of flow in the core region is $u_x(h_1) = u_x(h_2)$.

From the above formulas, the fluid flow through the damper gap can be obtained:

$$\begin{aligned} Q &= A_p v_0 = s\int_0^h u_x(z)dz \\ &= \tfrac{s}{2}(-\tfrac{1}{\eta}\tfrac{dp}{dx}){h_1}^2[h - \tfrac{1}{3}(h + h_1 - h_2)] - \tfrac{s}{3}v_0(h - h_2) \end{aligned} \tag{7}$$

in which A_p is the effective area of the piston; v_0 is the speed of the piston; s is the circumference of the piston; $u_x(z)$ is the gap fluid velocity equation; η is the viscosity of MR fluid; dp/dx is the pressure gradient; h, h_1, and h_2 are shown in **Figure 7**.

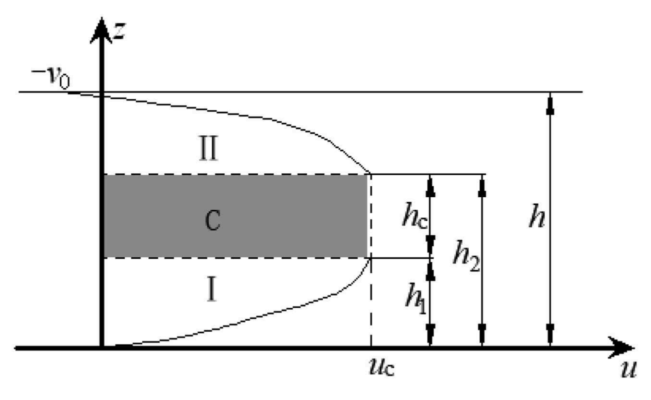

FIGURE 7 | The velocity profile diagram of MR fluids through the gap.

The gap pressure gradient is expressed from (7):

$$\frac{dp}{dx} = \frac{Q + \frac{s}{3}v_0(h - h_2)}{{h_1}^2[\frac{1}{3}(h + h_1 - h_2) - h]\frac{s}{2}\frac{1}{\eta}} \tag{8}$$

From (1) and (8), warpage deformation of viscoelastic material will influence the gap flow of MR fluid, and then influence the gap pressure gradient, while the pressure gradient will directly change the damping force of the MR damper. To consider the influence of viscoelastic material deformation on the gap pressure gradient, the correction factor of pressure gradient α is obtained:

$$\alpha = \frac{(\frac{dp}{dx})_{\Delta V}}{\frac{dp}{dx}} = \frac{Q_{\Delta V} + \frac{b}{3}v_0(h - h_2)}{Q + \frac{b}{3}v_0(h - h_2)} \tag{9}$$

in which$(\frac{dp}{dx})_{\Delta V}$ is the gap pressure gradient considering the influence of viscoelastic material deformation.

To most gap-type MR dampers, the ratio between h_2 and h can be set to be 0.7 (Spencer et al., 1998).

$$\alpha = \frac{(\frac{dp}{dx})_{\Delta V}}{\frac{dp}{dx}} = \frac{\left(1\text{-}\frac{\Delta V}{V}\right)A_p + 0.1bh}{A_p + 0.1bh} \tag{10}$$

In the movement of the damper piston, the gap pressure gradient changes at any moment, so that the correction factor of pressure gradient α also changes with time. Also, with the external current intensity increasing, the internal pressure of the damper increases, causing warpage deformation of the viscoelastic material to increase and influence the gap pressure gradient. Therefore, the correction factor of pressure gradient also considers the influence of current intensity.

The correction factor of pressure gradient of the MR damper is obtained by cycle computing of liquid-structure interaction. The computing process is: the initial pressure gradient $\Delta p(t_0)$ of the moment $t_0 = 0$ is substituted into (2) and (3) to calculate the deflection curve $\omega(r, t_0)$ of viscoelastic material, and then the deformation volume $\Delta V(t_0)$ of viscoelastic material is obtained by integrating (4); the correction factor of pressure gradient at the next moment is obtained by (10); the pressure difference $\Delta p(t_1)$ with consideration of the viscoelastic material deformation influence at the next moment is obtained by (12); the correction factor of pressure gradient α changing with time is obtained by cycle computing.

According to the capacity formula of the MR damper gap, the modified damping force produced by MR fluid with considering viscoelastic material deformation influence is obtained:

$$F_{\Delta V} = -\left(\frac{dp}{dx}\right)_{\Delta V} LA_p = -\alpha \frac{dp}{dx} LA_p = \alpha \Delta p A_p = \alpha F_{sv} \tag{11}$$

in which $F_{\Delta V}$ is the MR damping force considering the viscoelastic material deformation influence; F_{sv} is the traditional MR damping force; L is the effective length of the piston.

When the damper works, its inner chamber pressure difference changes with time, and a fluid-structure interaction exists between viscoelastic material and the inner chamber MR fluid. The inner chamber fluid pressure difference produces deformation of viscoelastic material, leading to the increase of the damper inner chamber volume, and the decrease of the gap flow and pressure difference. The decrease of the pressure difference results in the decrease of viscoelastic material deformation and then of the damper inner chamber volume, and the increase of the gap flow and of the pressure difference. Thus, a time formula related to the correction factor of pressure gradient should be established to obtain the mechanical model of the damper at work.

The internal pressure difference of the damper mostly originates from the MR damping force. The formula for the pressure difference considering the viscoelastic material deformation influence is:

$$\Delta p = F_{\Delta V}/A_P = \alpha F_{sv}/A_P \tag{12}$$

The Damping Force of the New Leakage-Proof MR Damper

The new leakage-proof MR damper is composed of two parts: one is provided by the pressure gradient created at the gap the MR fluid flows through, and the other is provided by elastic-plastic deformation of viscoelastic material. The damping force created by the pressure gradient is obtained:

$$F_{\Delta V} = -\left(\frac{dp}{dx}\right)_{\Delta V} LA_p = -\alpha \left(\frac{dp}{dx}\right)_0 LA_p = \alpha F_0 = \alpha F_{sv} \tag{13}$$

The piecewise 3-order polynomial model with high fitting accuracy is used to calculate the damping force of traditional dampers.

$$F_{sv} = \begin{cases} \sum_{i=0}^{3} a_{d1} v^i, & v \le v_3, \ \dot{v} > 0 \\ \sum_{i=0}^{3} a_{d2} v^i, & v_3 \le v \le v_1, \ \dot{v} > 0 \\ \sum_{i=0}^{3} a_{d3} v^i, & v_1 \le v, \ \dot{v} > 0 \\ \sum_{i=0}^{3} a_{u1} v^i, & v_2 \le v, \ \dot{v} < 0 \\ \sum_{i=0}^{3} a_{u2} v^i, & v_4 \le v \le v_3, \ \dot{v} < 0 \\ \sum_{i=0}^{3} a_{u3} v^i, & v \le v_4, \ \dot{v} < 0 \end{cases} \tag{14}$$

in which, a_{d1}, a_{d2}, a_{d3}, a_{u1}, a_{u2}, a_{u3} are coefficients of piecewise polynomials respectively; v_1,$v_3$are the yielding velocities of the negative acceleration section; v_2,v_4 are the yielding velocities of the positive acceleration section; v_1,v_2,v_3,v_4 are the velocity values at the turning points of the two branch curves, and they are all functions of the current.

The damping force provided by viscoelastic material is:

$$F_v = \frac{nG_1 A}{t} u + \frac{nG_1 \eta_2 A}{\omega t} v_0 \tag{15}$$

According to the standard linear solid model (Xu et al., 2010), the formula of its modulus and dissipation factor is:

$$\left.\begin{aligned} G_1 &= (q_0 + p_1 q_1 \lambda^2)/(1 + p_1^2 \lambda^2) \\ G_2 &= (q_1 - p_1 q_0)\lambda/(1 + p_1^2 \lambda^2) \\ \eta_2 &= G_2/G_1 = (q_1 - p_1 q_0)\lambda/(q_0 + p_1 q_1 \lambda^2) \end{aligned}\right\} \tag{16}$$

in which n is the number of viscoelastic material; G_1 and G_2 are storage modulus and consuming modulus respectively; u is the relative displacement of the piston; v_0 is the velocity of the piston; A is the equivalent flat area of viscoelastic material; t is the thickness of material; η_2 is the loss factor of viscoelastic material; λ is excitation frequency. The coefficients of q_0, q_1, and p_1 are determined by the properties of viscoelastic materials.

Finally, the damping force of the leakage-proof MR damper is obtained:

$$F = F_{\Delta V} + F_v \tag{17}$$

THE PERFORMANCE TEST OF THE NEW LEAKAGE-PROOF MR DAMPER

The Test Surveys

The parameters of self-made leakage-proof MR damper are shown in **Table 1**. A regular MR damper with an O-ring seal is also made, and its main parameters are the same as those of the leakage-proof MR damper, except with no viscoelastic material as the seal device. Performance tests are conducted on both dampers. There are three operating conditions: (1) the performance test for the leakage-proof MR damper without MR fluid, that is, only considering the outputting force of viscoelastic

TABLE 1 | The main parameters of the leakage-proof MR damper.

h/mm	*D*/mm	*d*/mm	*L*/mm	Viscoelastic material	
				Length/mm	Thickness/mm
2	110	40	79	30	15

h indicates the gap width of the MR damper, D indicates the inner diameter of the cylinder, d indicates the diameter of the piston, L indicates the effective length of the piston.

TABLE 2 | The operating conditions of test 1.

Frequency/Hz	Displacement amplitude/mm	Cycle index
0.1, 0.5, 1.0	4, 6, 10	20

TABLE 3 | The operating conditions of test 2 and test 3.

Frequency/Hz	Current intensity/A	Displacement amplitude/mm	Cycle index
0.1, 0.5, 1.0	0 0.5 1.0 1.5 2.0	4, 6, 10	20

TABLE 4 | Parameter identification of viscoelastic material.

Model parameters	p_1	q_0	q_1
Identification result	0.43622	0.29997	0.24157

material; (2) the performance test for the regular MR damper; (3) the performance test for the leakage-proof MR damper with MR fluid, as shown in **Tables 2–4**. The fatigue performance test was conducted for both dampers. The hydraulic servo system is used to perform the loading test to the damper, as shown in **Figure 8** and the test data for force and displacement are obtained through data acquisition system to draw the corresponding hysteresis curve.

FIGURE 8 | Diagram of the hydraulic servo loading system to the damper.

The Test Results

Figure 9 shows the hysteresis curves of the leakage-proof MR damper without MR fluid in operating conditions of 0.1, 0.5, and 1 Hz. The energy-consuming hysteresis curve of viscoelastic material is an oval. The hysteresis curve area is small but cannot be ignored, which means that the influence of viscoelastic material in the leakage-proof MR damper on its damping force cannot be ignored. With the increase of displacement amplitude, the hysteresis curve area of viscoelastic material increases, and as does its energy consumption. Besides, in the same displacement amplitude the hysteresis curve area of viscoelastic material increases with frequency, but the increase effect is not so apparent as amplitude change.

Figures 10, **11** indicate the performance test results of the regular MR damper and the leakage-proof MR damper respectively. The outputting force of either one increases with current intensity, that is, the damper has an obvious MR effect. The force-displacement hysteresis curve of the regular MR damper is almost rectangular with a slightly bulging central part, which is caused by the viscous damping force provided by damper velocity, whereas that of the leakage-proof MR damper is a parallelogram with a certain inclination. And the force-displacement hysteresis curve of the leakage-proof MR damper has a sinking central part. The reason for the different shapes between the two results is that viscoelastic material provides additional stiffness for MR damper. When the displacement of the damper is larger, the damping force provided by viscoelastic material is larger. Therefore, the force-displacement hysteretic curve of the leakage-proof MR damper is a parallelogram with a certain inclination compared with that of the regular MR damper. In addition, the inner chamber pressure gradually increases in the process of the damper returning to the equilibrium position, which results in large warping deformation of the viscoelastic material, thus continuously weakening the damper's damping force. And when the displacement of the damper is 0, the weakening effect is greatest. **Figure 11** also shows that with the increase of current intensity, the sinking degree of the hysteresis curve of the leakage-proof MR damper increases. This is because with the increase of current intensity, the inner pressure of the damper increases, warpage deformation of viscoelastic material also increases and the correction factor of pressure gradient decreases, leading to a more evident weakening effect on the damping force, which proves that it is reasonable to introduce a correction factor of pressure gradient into the mechanical model.

The same phenomenon can be reflected in the force-velocity hysteresis curve. With the maximum velocity, the curve end of the regular MR damper is a diagonal and the damping force is not weakened; while with the maximum velocity, the curve end of the leakage-proof MR damper has a descent stage, the damping force is weakened, and the force-velocity curve is a ring at the end, which means that viscoelastic material participates in energy consumption.

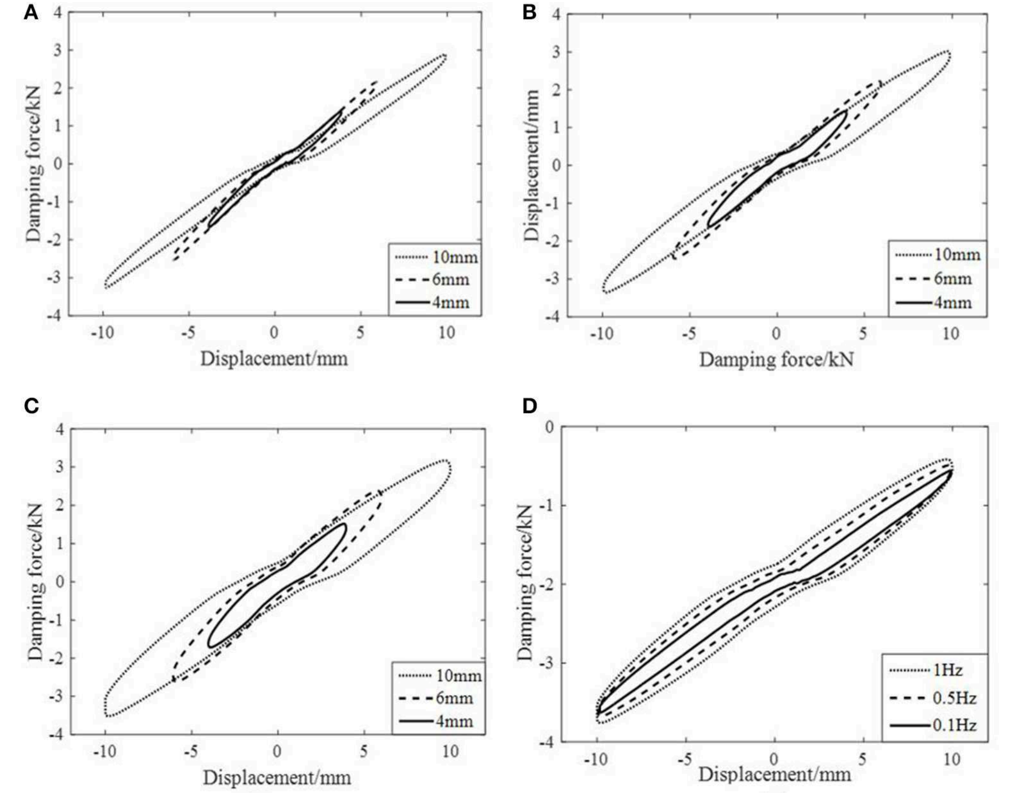

FIGURE 9 | Hysteresis curves of the empty leakage-proof MR damper with varying frequency and amplitude. **(A)** Frequency 0.1Hz. **(B)** Frequency 0.5Hz. **(C)** Frequency 1Hz. **(D)** Amplitude 10mm.

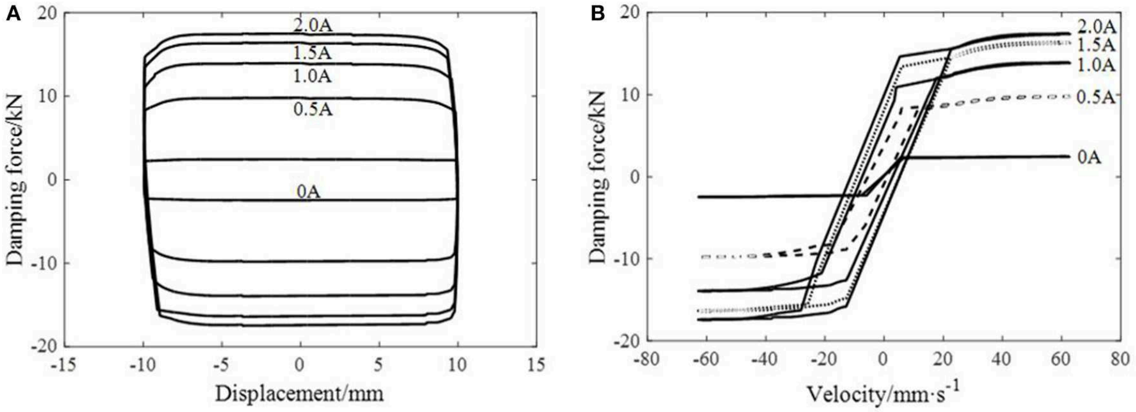

FIGURE 10 | The hysteresis curve of the regular MR damper at frequency 1 Hz and amplitude 10 mm. **(A)** The relationship curve of displacement and damping force. **(B)** The relationship curve of velocity and damping force.

The fatigue property test on the MR damper adopts the load condition of frequency 5 Hz and amplitude 2 mm to apply a current intensity of 1 A. In the loading process, the sealing position of the damper is checked once every 50,000 cycle intervals. In the beginning, both the regular MR damper and the leakage-proof one keep a favorable sealing effect; after 200,000 fatigue tests some subtle nicks are found on the piston rod of the regular MR damper, but the damper is sealed well; after 500,000 fatigue tests, evident nicks appear on the piston rod of the regular MR damper and fluid leaks from them; after 550,000–600,000 fatigue tests, MR fluid begins to leak and drop, which means its seal is invalid, as is shown in **Figure 12**. Meanwhile, viscoelastic material at the sealing position on the leakage-proof MR damper and the joint between the piston and cylinder barrel are still in good condition, even after 2,000,000 loading

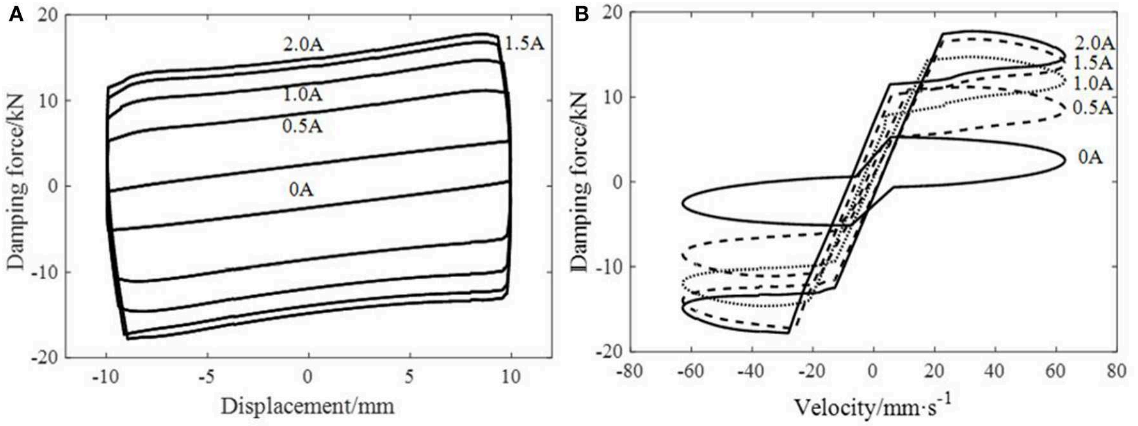

FIGURE 11 | The hysteresis curve of the leakage-proof MR damper at frequency 1 Hz and amplitude 10 mm. **(A)** The relationship curve of displacement and damping force. **(B)** The relationship curve of velocity and damping force.

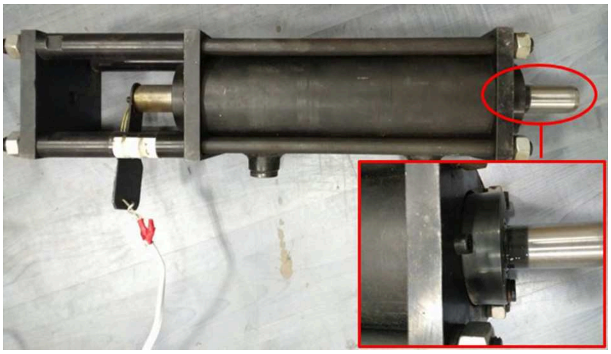

FIGURE 12 | Diagram of the regular MR damper.

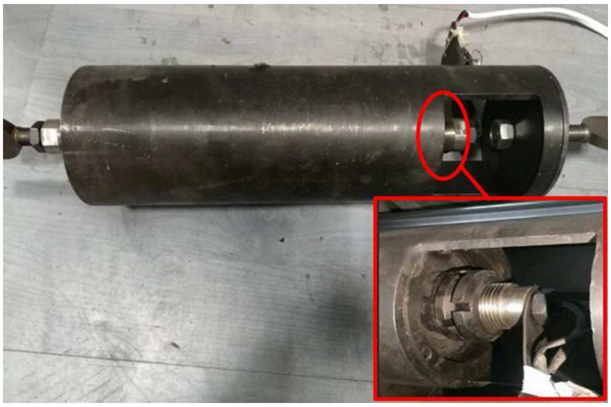

FIGURE 13 | Diagram of the leakage-proof MR damper.

cycles, as shown in **Figure 13**. The fatigue test for the MR damper indicates that the leakage-proof MR damper replaces the dynamic seal with a static seal which has a significant sealing property.

PARAMETER IDENTIFICATION OF THE MECHANICAL MODEL OF THE LEAKAGE-PROOF MR DAMPER

Constant Current Intensity Working Condition

According to the test results of the MR damper without fluid under every working condition, parameter identification in (15) can be accomplished by using the least squares method. The result is shown in **Table 4**:

From the above results, the storage modulus, consuming modulus, and loss factor can be obtained. Combining with the size parameters of viscoelastic materials, the formula for calculating the damping force of viscoelastic materials can be obtained.

$$F_v = 326.121u + 9.126v_0 \tag{18}$$

According to the performance test result of the regular MR damper, the relationship between yield velocity and current is obtained, as shown in (19–22).

$$v_1 = -0.81913 * I^3 + 3.51066 * I^2 - 4.35913 * I + 6.68888 \tag{19}$$

$$v_2 = -3.64167 * I^3 + 7.20377 * I^2 + 8.66757 * I + 5.61514 \tag{20}$$

$$v_3 = -2.46407 * I^3 + 11.4098 * I^2 - 23.224 * I - 7.75205 \tag{21}$$

$$v_4 = -4.62173 * I^3 + 17.82669 * I^2 - 20.63274 * I - 6.05764 \tag{22}$$

The least squares method is used to identify the parameters of the piecewise 3-order polynomial model. In order to ensure the accuracy of the polynomial calculation results, the relationship between the current and the coefficients of each piecewise polynomial is fitted by a second order polynomial, such as $a = b + c * I + d * I^2$.The damping force of conventional dampers can be calculated by the parameters of Equation (14). The results of parameter identification are shown in the **Table 5**.

With those identified parameters, the mechanical model of the newly-established leakage-proof MR damper is verified. For the working condition of loading frequency 1 Hz, amplitude 10 mm and current intensity 2 A the maximum outputting force of the regular MR damper is 17.4 kN, implying that the initial inner pressure of the damper is 2.11 MPa. Through the fluid-structure interaction calculation the correction factor of pressure gradient under this working condition is obtained:

$$\alpha(t) = 0.93147 - 0.1214\left|\cos(2\pi t)\right| \tag{23}$$

The damping force of the leakage-proof MR damper under this working condition is obtained from (17):

$$F = (0.93147 - 0.1214\left|\cos(2\pi t)\right|)F_{sv} + 326.121u + 9.126v_0 \tag{24}$$

Figure 14 compares the results of testing and the mechanical model under this working condition. It indicates that the theoretical result is basically coincident with the testing result. The mechanical model can reflect that the damping force is weakened when the damper is at the equilibrium position, meaning that it is appropriate to introduce the correction factor of pressure gradient when establishing the mechanical model of the leakage-proof MR damper. This model can effectively describe its mechanical properties.

Varying Current Intensity Working Condition

The tests prove that the sinking degree of the hysteresis curve of the leakage-proof MR damper is correlated to current intensity, that is, the more powerful the current intensity is, the greater sinking degree becomes in the middle of the curve. It means that the introduced correction factor of pressure gradient is also influenced by the impressed current intensity. The correction factor of pressure gradient under harmonic loads can be expressed as:

$$\alpha(I,t) = m(I) - n(I)\left|\cos(\omega t)\right| \tag{25}$$

TABLE 5 | Parametric identification of the piecewise 3-order polynomial model.

Positive acceleration section	b_{d10}	−2106.7421	c_{d10}	−2092.7288	d_{d10}	2053.6462
	b_{d11}	12.9445	c_{d11}	797.0635	d_{d11}	−125.9840
	b_{d12}	−0.0207	c_{d12}	15.9877	d_{d12}	−2.6906
	b_{d13}	−0.0014	c_{d13}	0.1066	d_{d13}	−0.0191
	b_{d20}	303.1206	c_{d20}	7705.2593	d_{d20}	−1469.1559
	b_{d21}	367.1054	c_{d21}	704.5939	d_{d21}	−254.8764
	b_{d22}	−2.2314	c_{d22}	−17.6380	d_{d22}	6.8074
	b_{d23}	−1.0225	c_{d23}	0.6041	d_{d23}	−0.1069
	b_{d30}	2299.6605	c_{d30}	8344.1253	d_{d30}	−1551.4238
	b_{d31}	13.5024	c_{d31}	385.1932	d_{d31}	−152.9216
	b_{d32}	−0.1771	c_{d32}	−7.2350	d_{d32}	3.1837
	b_{d33}	0.0009	c_{d33}	0.0464	d_{d33}	−0.0222
Negative acceleration section	b_{u10}	−2191.2561	c_{u10}	−9074.1753	d_{u10}	2328.0807
	b_{u11}	27.7848	c_{u11}	427.3314	d_{u11}	−116.2428
	b_{u12}	0.5858	c_{u12}	9.5401	c_{u12}	−2.5921
	b_{u13}	0.0042	c_{u13}	0.0693	d_{u13}	−0.0188
	b_{u20}	330.8933	c_{u20}	−3220.3091	d_{u20}	266.1578
	b_{u21}	489.8708	c_{u21}	588.1777	d_{u21}	−201.4163
	b_{u22}	−0.6123	c_{u22}	7.3300	d_{u22}	−2.4648
	b_{u23}	−2.1275	c_{u23}	2.4383	d_{u23}	−0.7646
	b_{u30}	2809.9376	c_{u30}	4532.3688	d_{u30}	−2935.9542
	b_{u31}	−14.7112	c_{u31}	618.6743	d_{u31}	−47.3269
	b_{u32}	0.2892	c_{u32}	−12.0503	d_{u32}	0.7181
	b_{u33}	−0.0015	c_{u33}	0.0790	d_{u33}	−0.0039

Subscript d indicates the positive acceleration section and u indicates the negative acceleration section; the first value of subscript (1,2,3) indicates the section of the curve; the second value 0,1,2,3 in the subscript indicates the coefficients of the constant term, the first term, the second term, and the third term of the polynomial, respectively. For example, b_{d10}, c_{d10}, and d_{d10} indicate the fitting parameter of the constant term a_{d10} in the first polynomial of the positive acceleration curve, $a_{d10} = b_{d10} + c_{d10} * I + d_{d10} * I^2$.

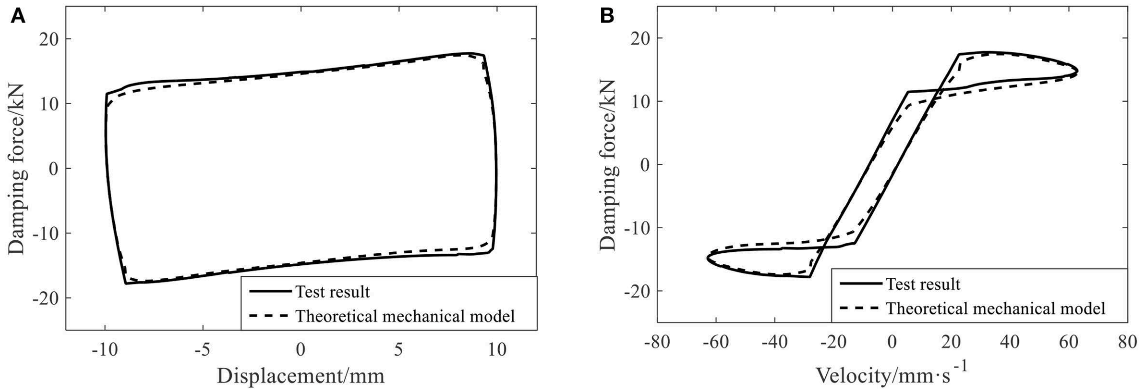

FIGURE 14 | The comparison between the theoretical mechanical model and the test result of the leakage-proof MR damper. **(A)** Hysteresis curves of displacement and damping force. **(B)** Hysteresis curves of velocity and damping force.

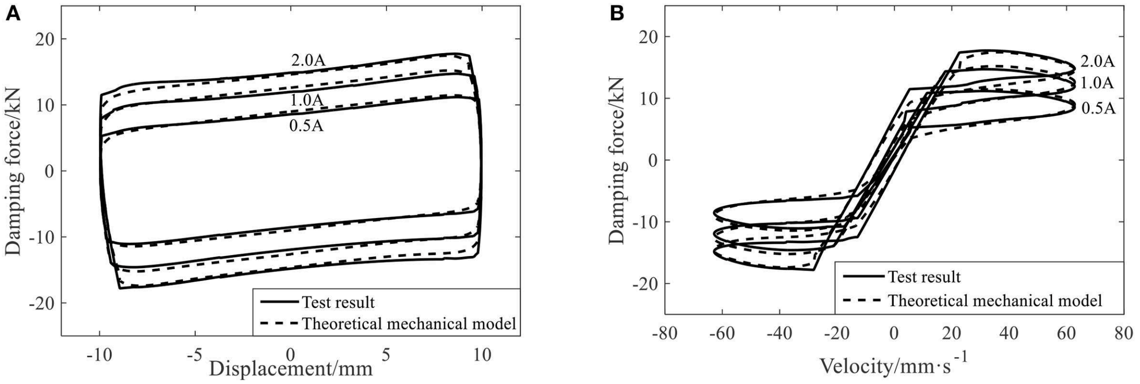

FIGURE 15 | The comparison between the theoretical mechanical model and the test result of the leakage-proof MR damper under the varying current condition. **(A)** Hysteresis curves of displacement and damping force. **(B)** Hysteresis curves of velocity and damping force.

in which $m(I)$ and $n(I)$ are parameters concerning current intensity; ω is the angular frequency of the piston.

With data from the test, it is obtained by using the least squares method:

$$\left.\begin{aligned} m(I) &= -0.00822I^3 + 0.03439I^2 - 0.07016I + 1 \\ n(I) &= 0.02442I^3 - 0.10417I^2 + 0.16353I + 0.01565 \end{aligned}\right\} \quad (26)$$

After obtaining two current intensity parameters in the correction factor, the mechanical model of the new leakage-proof MR damper can be obtained from (17):

$$F = [m(I) - n(I)\left|\cos(\omega t)\right|]F_{sv} + F_v \quad (27)$$

Figure 15 is the comparison between the mechanical model and the test result under the working condition of frequency 1 HZ and amplitude 10 mm. It shows that the hysteresis curve obtained by the mechanical model under different working conditions is basically consistent with the curve from the test result, meaning that the newly-established mechanical model of the leakage-proof MR damper can well reflect the mechanical properties of the damper under different working conditions.

CONCLUSION

In order to solve the leaking problem of the MR damper, a leakage-proof MR damper is designed and created to accomplish this task fundamentally by using a softer viscoelastic material to provide a static seal for the damper. Considering that warpage deformation occurs to viscoelastic material under the load of its internal fluid, the correction factor of pressure gradient is proposed and then the mechanical model is established for the leakage-proof MR damper. After verification, the test results show that:

(1) The external cylinder barrel is vulcanized and connected with the piston by using viscoelastic material, and the traditional dynamic seal is replaced by a static seal. The test proves that its durability is greatly improved.

(2) Compared with the regular damper, the hysteresis curve of the leakage-proof MR grease damper has a sinking part in the middle, proving that warpage deformation of the viscoelastic material can weaken the damper capacity and the weakening effect increases with the current intensity. The correction factor of pressure gradient is introduced to consider that it is reasonable for warpage deformation of viscoelastic material and current intensity to influence the damping force of the MR damper.

(3) The calculated result of the mechanical model for the new leakage-proof MR damper is basically consistent with the test results, verifying the validity of the mechanical model of the leakage-proof MR damper and reflecting its mechanical properties well.

DATA AVAILABILITY

All datasets generated for this study are included in the manuscript and/or the supplementary files.

AUTHOR CONTRIBUTIONS

JT initiated the research. ZL and JZ designed the experiments. KG, JL, and JG conducted the experiments. JT and ZL wrote the paper.

FUNDING

The research presented in this paper is supported by Natural Science Foundation of Hubei Province [grant numbers 2016CFA020]; Project of Ministry of Science and Technology [grant numbers 2018YFC0705601].

REFERENCES

Carlson, J. D. (1999). Low-cost MR fluid sponge devices. *J. Intell. Mater. Syst. Struct.* 10, 589–594. doi: 10.1106/CG4J-V704-9LPH-GEC0

Carlson, J. D., and Spencer, B. F. Jr. (1996). "Magneto-rheological fluid dampers for semi-active seismic control," in *International Conference on Motion and Vibration Control* (Chiba).

Çeşmeci, Ş., and Engin, T. (2010). Modeling and testing of a field-controllable magnetorheological fluid damper. *Int. J. Mech. Sci.* 52, 1036–1046. doi: 10.1016/j.ijmecsci.2010.04.007

Chang, K. C., Lai, M. L., Soong, T. T., Hao, D. S., and Yeh, Y. C. (1993). *Seismic Behavior and Design Guidelines for Steel Frame Structures With Added Viscoelastic Dampers*. Technical Report Nceer. Buffalo, NY: National Center for Earthquake Engineering Research, 93–0009.

Choi, S. B., Nam, M. H., and Lee, B. K. (2000). Vibration control of a MR seat damper for commercial vehicles. *J. Intell. Mater. Syst. Struct.* 11, 936–944. doi: 10.1106/AERG-3QKV-31V8-F250

Christensen, R. M., and Freund, L. B. (1982). *Theory of Viscoelasticity*. New York, NY: Academic Press.

Christie, M. D., Sun, S., Deng, L., Ning, D. H., Du, H., Zhang, S. W., et al. (2019). A variable resonance magnetorheological-fluid-based pendulum tuned mass damper for seismic vibration suppression. *Mech. Syst. Signal Process.* 116, 530–544. doi: 10.1016/j.ymssp.2018.07.007

Cunha-Filho, A. G., de Lima, A. M. G., Donadon, M. V., and Leão, L. S. (2016). Flutter suppression of plates using passive constrained viscoelastic layers. *Mech. Syst. Signal Process.* 79, 99–111. doi: 10.1016/j.ymssp.2016.02.025

Delgado, A., and San Andres, L. (2010). Identification of force coefficients in a squeeze film damper with a mechanical seal: large contact force. *J. Tribol.* 132:032201. doi: 10.1115/1.4001458

Deng, H., Wang, M., Han, G., Zhang, J., Ma, M., Zhong, X., et al. (2017). Variable stiffness mechanisms of dual parameters changing magnetorheological fluid devices. *Smart Mater. Struct.* 26:125014. doi: 10.1088/1361-665X/aa92d5

Giorgetti, A., Baldanzini, N., Biasiotto, M., and Citti, P. (2010). Design and testing of a MRF rotational damper for vehicle applications. *Smart Mater. Struct.* 19:065006. doi: 10.1088/0964-1726/19/6/065006

Hardy, E. J. R. (1951). The magnetic fluid clutch. *Electr. Eng.* 67, 1167–1167. doi: 10.1109/EE.1948.6444497

Hato, M. J., Choi, H. J., Sim, H. H., Park, B. O., and Ray, S. S. (2011). Magnetic carbonyl iron suspension with organoclay additive and its magnetorheological properties. *Colloids Surf. A* 377, 103–109. doi: 10.1016/j.colsurfa.2010.12.029

Hu, Z., Yan, H., Guo, X., Wang, X., and Wen, H. (2015). Rheological properties and stability of lithium-based magnetorheological grease with damping effect. *Acta Petrol. Sin.* 31, 166–171. doi: 10.3969/j.issn.1001-8719.2015.01.026

Iyengar, V. R., Alexandridis, A. A., Tung, S. C., and Rule, D. S. (2004). Wear testing of seals in magneto-rheological fluids©. *Tribol. Trans.* 47, 23–28. doi: 10.1080/05698190490279083

Jacob, R. (1951). *Magnetic Fluid Torque and Force Transmitting Device*. US, US2575360. Washington, DC: U.S. Patent Office.

Jeyasenthil, R., and Choi, S. B. (2018). A novel semi-active control strategy based on the quantitative feedback theory for a vehicle suspension system with magneto-rheological damper saturation. *Mechatronics* 54, 36–51. doi: 10.1016/j.mechatronics.2018.06.016

Jolly, M. R., Bender, J. W., and Carlson, J. D. (1999). Properties and applications of commercial magnetorheological fluids. *J. Intell. Mater. Syst. Struct.* 10, 5–13. doi: 10.1177/1045389X9901000102

Kelso, S. P., Denoyer, K. K., Blankinship, R. M., Potter, K., and Lindler, J. E. (2003). Experimental validation of a novel stictionless magnetorheological fluid isolator. *Smart Struct. Mater. 2003* 5052, 186–197. doi: 10.1117/12.483966

Liu, D. H. (1990). *The Technique of Viscoelastic Damping and Noise Reducing*. Beijing: Space Press.

Liu, J., Wang, X., Tang, X., Hong, R., Wang, Y., and Feng, W. (2015). Preparation and characterization of carbonyl iron/strontium hexaferrite magnetorheological fluids. *Particuology* 22, 134–144. doi: 10.1016/j.partic.2014.04.021

Lu, G., Li, Y., and Song, G. (2011). Analysis of a magneto-rheological coupler with misalignment. *Smart Mater. Struct.* 20:105028. doi: 10.1088/0964-1726/20/10/105028

Mohamad, N., Ubaidillah, Mazlan, S. A., Imaduddin, F., Choi, S. B., and Yazid, I. I. M. (2018). A comparative work on the magnetic field-dependent properties of plate-like and spherical iron particle-based magnetorheological grease. *PLoS ONE* 13:0191795. doi: 10.1371/journal.pone.0191795

Qu, W. L., Qin, S. Q., Tu, J. W., Liu, J., Zhou, Q., and Cheng, H., et al. (2009). Intelligent control for braking-induced longitudinal vibration responses of floating-type railway bridges. *Smart Mater. Struct.* 18:125003. doi: 10.1088/0964-1726/18/12/125003

Samali, B., and Kwok, K. C. S. (1995). Use of viscoelastic dampers in reducing wind and earthquake-induced motion of building structures. *Eng. Struct.* 17, 639–654. doi: 10.1016/0141-0296(95)00034-5

Spencer, B. F., Yang, G., Carlson, J. D., and Sain, M. K. (1998). "Smart dampers for seismic protection of structures: a full-scale study," in *World Conference on Proceedings* (Kyoto).

Stanway, R., Sproston, J. L., and Stevens, N. G. (1987). Non-linear modelling of an electro-rheological vibration damper. *J. Electrostat.* 20, 167–184. doi: 10.1016/0304-3886(87)90056-8

Sun, S. S., Ning, D. H., Yang, J., Du, H., Zhang, S. W., and Li, W. H. (2016). A seat suspension with a rotary magnetorheological damper for heavy duty vehicles. *Smart Mater. Struct.* 25:105032. doi: 10.1088/0964-1726/25/10/105032

Susan-Resiga, D., and Vékás, L. (2014). Yield stress and flow behavior of concentrated ferrofluid-based magnetorheological fluids: the influence of composition. *Rheologica Acta* 53, 645–653. doi: 10.1007/s00397-014-0785-z

Tezcan, S. S., and Uluca, O. (2003). Reduction of earthquake response of plane frame buildings by viscoelastic dampers. *Eng. Struct.* 25, 1755–1761. doi: 10.1016/j.engstruct.2003.07.001

Townsend, P., Suárez-Bermejo, J. C., Sanz-Horcajo, E., and Pinilla-Cea, P. (2018). Reduction of slamming damage in the hull of high-speed crafts manufactured from composite materials using viscoelastic layers. *Ocean Eng.* 159, 253–267. doi: 10.1016/j.oceaneng.2018.04.029

Tu, J. W., Liu, J., Qu, W. L., Zhou, Q., Cheng, H. B., and Cheng, X. D. (2011). Design and Fabrication of 500-kN Large-scale MR Damper. *J. Intell. Mater. Syst. Struct.* 22, 475–487. doi: 10.1177/1045389X11399942

Tudón-Martínez, J. C., and Morales-Menendez, R. (2015). Adaptive vibration control system for MR damper faults. *Shock Vibr.* 2015, 1–17. doi: 10.1155/2015/163694

Vereda, F., Segovia-Gutiérrez, J. P., de Vicente, J., and Hidalgo-Alvarez, R. (2016). Faceted particles: an approach for the enhancement of the elasticity and the yield-stress of magnetorheological fluids. *Appl. Phys. Lett.* 108:211904. doi: 10.1063/1.4952394

Wang, T. J., and Ma, L. S. (2004). Analytical solutions for axisymmetric bending of functionally graded circular/annular plates. *Acta Mech. Sin.* 36, 348–353. doi: 10.1109/SPAWDA.2013.6841128

Wang, W. R., Yan, X. Q., Sun, Z. H., and Jiang, Q. (2012). Analysis of vane hydraulic damp dynamic seal mechanism and performance influencing factors. *Adv. Mater. Res.* 530, 130–133. doi: 10.4028/www.scientific.net/AMR.530.130

Wen, Y. K. (1976). Method for random vibration of hysteretic systems. *J. Eng. Mech. Div. ASCE.* 102, 249–263.

Xu, Y. L., Qu, W. L., and Ko, J. M. (2000). Seismic response control of frame structures using magnetorheological/electrorheological dampers. *Earthq. Eng. Struct. Dyn.* 29, 557–575. doi: 10.1002/(SICI)1096-9845(200005)29:5<557::AID-EQE922>3.0.CO;2-X

Xu, Y. X., and Cao, M. (2004). Design calculation of magnetorheological damper. *J. Shanghai Jiaotong Univ.* 38, 1423–1427. doi: 10.1088/1009-0630/6/5/011

Xu, Z. D., Huang, X. H., Xu, F. H., and Yuan, J. (2019). Parameters optimization of vibration isolation and mitigation system for precision platforms using non-dominated sorting genetic algorithm. *Mech. Syst. Signal Process.* 128, 191–201. doi: 10.1016/j.ymssp.2019.03.031

Xu, Z. D., Liao, Y. X., Ge, T., and Xu, C. (2016). Experimental and theoretical study of viscoelastic dampers with different matrix rubbers. *J. Eng. Mech.* 142:04016051. doi: 10.1061/(ASCE)EM.1943-7889.0001101

Xu, Z. D., Sha, L. F., Zhang, X.-C., and Ye, H. H. (2013). Design, performance test and analysis on magnetorheological damper for earthquake mitigation. *Struct. Control Health Monitor.* 20, 956–970. doi: 10.1002/stc.1509

Xu, Z. D., Wang, D. X., and Shi, C. F. (2010). Model, tests and application design for viscoelastic dampers. *J. Vibr. Control* 17, 1359–1370. doi: 10.1177/1077546310373617

Yan, Y. X., Hui, L. X., Yu, M., Fu, J., and Dong, L. H. (2013). Dynamic response time of a metal foam magneto-rheological damper. *Smart Mater. Struct.* 22:025026. doi: 10.1039/9781849737760

Yang, G. (2001). *Large-Scale Magnetorheological Fluid Damper for Vibration Mitigation: Modeling, Testing and Control* (Dissertation). Abstracts International (B. F. Spence).

Yao, X. L., Tian, Z. D., Deng, Z. C., and Shen, Z. H. (2008). "Research on the mechanics characteristics of ship vibration reduction and impact resistance isolator based on MR," in *Vehicle Power and Propulsion Conference* (Arlington, TX: IEEE).

Yazid, I. I. M., Mazlan, S. A., Kikuchi, T., Zamzuri, H., and Imaduddin, F. (2014). Design of magnetorheological damper with a combination of shear and squeeze modes. *Mater. Design* 54, 87–95. doi: 10.1016/j.matdes.2013.07.090

Zhang, R., and Soong, T. T. (1992). Seismic design of viscoelastic dampers for structural applications. *J. Struct. Eng.* 118, 1375–1392. doi: 10.1061/(ASCE)0733-9445(1992)118:5(1375)

Zhang, X. C., Zhang, X., Zhao, Y., Zhao, J., and Xu, Z. D. (2017). Experimental and numerical studies on a composite MR damper considering magnetic saturation effect. *Eng. Struct.* 132, 576–585. doi: 10.1016/j.engstruct.2016.11.055

Zhou, Y., Zhang, M., Lu, J. N., Wang, D. Y., and Wu, C. X. (2013). Experimental study on mechanical property of viscous damper. *China Civil Eng. J.* 46, 8–15. doi: 10.15951/j.tmgcxb.2013.01.010

Zhu, C. S. (2006). Experimental investigation on the dynamic behavior of a disk-type damper based on magnetorheological grease. *J. Intell. Mater. Syst. Struct.* 17, 793–799. doi: 10.1177/1045389X06055847

Zhu, S. X., Wang, P., and Tian, J. (2011). Experimental research on aircraft landing gear drop test based on MRF damper. *Procedia Eng.* 15, 4712–4717. doi: 10.1016/j.proeng.2011.08.882

Conflict of Interest Statement: The authors declare that the research was conducted in the absence of any commercial or financial relationships that could be construed as a potential conflict of interest.

frontiers
in Materials

ORIGINAL RESEARCH
published: 03 May 2019
doi: 10.3389/fmats.2019.00100

Experimental Study on a New Damper Using Combinations of Viscoelastic Material and Low-Yield-Point Steel Plates

*Huanjun Jiang [1,2], Shurong Li [1,2] and Liusheng He [1,2]**

[1] State Key Laboratory of Disaster Reduction in Civil Engineering, Tongji University, Shanghai, China, [2] Department of Disaster Mitigation for Structures, Tongji University, Shanghai, China

To enhance the seismic resilience of coupled reinforced concrete shear walls, a new damper working in the replaceable coupling beam is proposed in present study. The new damper is a combination of metallic damper and viscoelastic (VE) damper. The metallic damper consists of an I-shaped steel beam with multiple low-yield-point steel plate webs paralleled to each other; the VE damper is composed of multiple layers of VE material bonded between multiple steel plates. Through the composite use of viscoelastic material and low-yield-point steel, the new damper is expected to work effectively against both the earthquake and the wind. To study the respective mechanical behavior of each component of the combined new damper, eight metallic dampers, two VE dampers, and one combined damper are tested under cyclic loading first. The variable parameters of the metallic damper are strength grade of web steel, web dimensions, and end stiffener configuration. It is found that the effect of the strength grade of web steel is most significant. Compared with the metallic damper using the steel web with normal strength grade, the ductility, ultimate plastic shear rotation, and cumulative plastic shear rotation of the damper using the low-yield-point steel web are much larger. The effect of web dimensions on the deformation capacity is slight. With the addition of end stiffener, plasticity concentrates thereby, which prevents the flange-to-end plate weld fracture. The VE damper exhibits extraordinary deformability. The storage modulus, shear loss modulus and loss factor of the VE material decrease with the increase of strain amplitude. The storage modulus and shear loss modulus of the VE material decrease slightly as the excitation frequency increases within the range between 0.1 and 1 Hz, and the effect of the excitation on the loss factor is not significant. At last, the combined damper, an assembly of one metallic damper component and two VE damper components, is tested, which exhibits stable hysteretic behavior and excellent deformability. The predicted yield shear strength and elastic stiffness agree well with test results.

Keywords: coupling beam, replaceable, metallic damper, viscoelastic damper, combined damper

Edited by:
Zhao-Dong Xu,
Southeast University, China

Reviewed by:
Wei Wang,
Xi'an University of Architecture and Technology, China
Yongfeng Du,
Lanzhou University of Technology, China

****Correspondence:***
Liusheng He
hls@tongji.edu.cn

Specialty section:
This article was submitted to Structural Materials, a section of the journal Frontiers in Materials

Received: *14 January 2019*
Accepted: *17 April 2019*
Published: *03 May 2019*

Citation:
Jiang H, Li S and He L (2019) Experimental Study on a New Damper Using Combinations of Viscoelastic Material and Low-Yield-Point Steel Plates. Front. Mater. 6:100. doi: 10.3389/fmats.2019.00100

INTRODUCTION

Reinforced concrete shear walls are widely used in medium- and high-rise building structures due to their large capacity of axial/lateral strength and stiffness. As commonly adopted in practice, short coupling beams are used to connect adjacent walls to have an efficient structural wall system. In case of a damaging earthquake, coupling beams as the first defense level of the coupled wall system will undergo large deformation and dissipate most energy. Therefore, coupling beams concentrate most of the damage during earthquakes, which is difficult to repair (Kam and Pampanin, 2011; Wallace, 2012). Even if the coupling beams can be repaired, the cost of time and expense is great.

To solve the problem, several researchers have proposed various types of dampers installed within the coupling beam. Most of them belong to displacement-dependent dampers which provide high initial stiffness and exhibit significant energy-dissipation capacity, such as metallic yielding dampers and friction dampers. Fortney et al. (2007) developed a new steel coupling beam with a central fuse. Test results showed that the coupling beam demonstrated good energy-dissipation capacity. Chung et al. (2009) developed a friction damper that applied in the middle of coupling beams. A non-linear time history analysis was conducted, and the analysis results showed that the seismic performance of the coupled shear wall system with friction dampers was superior to the traditional coupled shear wall system. As the metallic damper is commonly cheaper and more reliable in terms of durability, a number of studies have been focused on them in recent years (Wang et al., 2012; Ji et al., 2016; Lu X. et al., 2018a,b; Lu Z. et al., 2018a,b). However, for the I-section steel damper, the filet welds between the web and the stiffener fractured, leading to the damper failure. For the I-section steel beam with a diamond-shaped opening in the web, the stress concentrated around the opening, and corners tore with the increase of shear rotation, causing the early failure of the damper (Lu X. et al., 2018a,b; Lu Z. et al., 2018a,b). Velocity-dependent devices such as viscoelastic (VE) dampers and viscous fluid dampers can dissipate energy for all magnitudes of dynamic deformation. Therefore, VE dampers were installed in the mid-span of the coupling beams (Montgomery and Christopoulos, 2015). Non-linear dynamic analysis of tall buildings incorporating VE dampers demonstrated good performance under wind and minor earthquakes, but the improvement was not obvious under major earthquakes (Mackay-Lyons et al., 2012).

Meanwhile, different types of seismic energy absorption devices have been developed, such as viscoelastic dampers, viscous dampers, metallic dampers, tuned mass dampers, earthquake isolation devices, magnetorheological dampers, particle mass dampers, and et al (Xu et al., 2013b, 2016; Jiang et al., 2017; Lu X. et al., 2018a,b; Lu Z. et al., 2018a,b). Through the optimization of placing these devices, the structural vibration can be largely reduced (Xu et al., 2003, 2004, 2013a, 2019). Among these devices, metallic dampers are increasingly used, such as X-shaped metal dampers (Tsai et al., 1993), shape memory alloy dampers (Wang and Zhu, 2017), bucking restrained braces (Takeuchi et al., 2012; Shi et al., 2018), steel slit shear walls (Hitaka and Matsui, 2003; Kurata et al., 2015; He et al., 2016), and among others. The reasons for their popularity include low cost, stable hysteretic behavior, good reliability and so on. A certain amount of dissatisfaction on metallic dampers is the relatively large lateral deformation needed to trigger the energy dissipation and thus the efficiency in dissipating energy is usually not desirable under minor earthquakes or wind excitation. While, VE dampers are known to be effective in controlling vibrations under small ground motions. However, the stiffness they provide is limited and damping is not sufficient when experiencing strong earthquakes. Naturally, the idea comes that a proper combination of metallic dampers and VE dampers used in coupling beams might give satisfactory performance for the coupled shear wall system under both minor and strong earthquakes.

With the above background, a new combined damper installed in the mid-span of coupling beams is proposed in this paper. The new damper is a combination of the VE damper and metallic damper, so as to achieve vibration control demands under different excitation levels. A series of cyclic loading tests were carried out to gain a better understanding of the mechanical behavior of the combined damper. Comparative investigations on the failure mode, shear strength, hysteretic behavior, ductility, and energy dissipation etc. were conducted using test results.

DESCRIPTION OF NEW COMBINED DAMPER FOR REPLACEABLE COUPLING BEAMS

Figure 1A shows the schematic diagram of the replaceable coupling beam, which comprises of the new replaceable damper in the middle and non-replaceable parts at two ends of the coupling beam. In case of an earthquake, damage is expected to be concentrated on the combined damper and the non-replaceable parts remain elastic. **Figure 1B** shows the schematic drawing of the combined damper, which is the combination of one central metallic damper and two edge VE dampers. The metallic damper is an I-shaped steel beam with two steel plate webs placed in parallel, which were welded together by complete joint penetration groove welds. The VE damper consists of multiple layers of VE materials bonded between multiple steel plates.

Previous studies suggested that it was preferred to have the metallic damper yielding in shear because of its stable behavior under cyclic loading (Okazaki and Engelhardt, 2007). Meanwhile, studies also showed that for the web with stiffeners, the shear strains were observed to increase near the web stiffeners. In contrast, for web without stiffeners the distribution of strains was more uniform along the length (Dusicka et al., 2009). Therefore, to avoid web buckling, trying to have a smaller web depth-thickness ratio of the web through reducing height or increasing thickness was adopted in this study. Meanwhile, end plate stiffener was also used in one metallic damper for comparison.

TEST PROGRAM

Test Specimens

Eight metallic dampers, two VE dampers and one combined damper were designed, the dimensions of which are illustrated

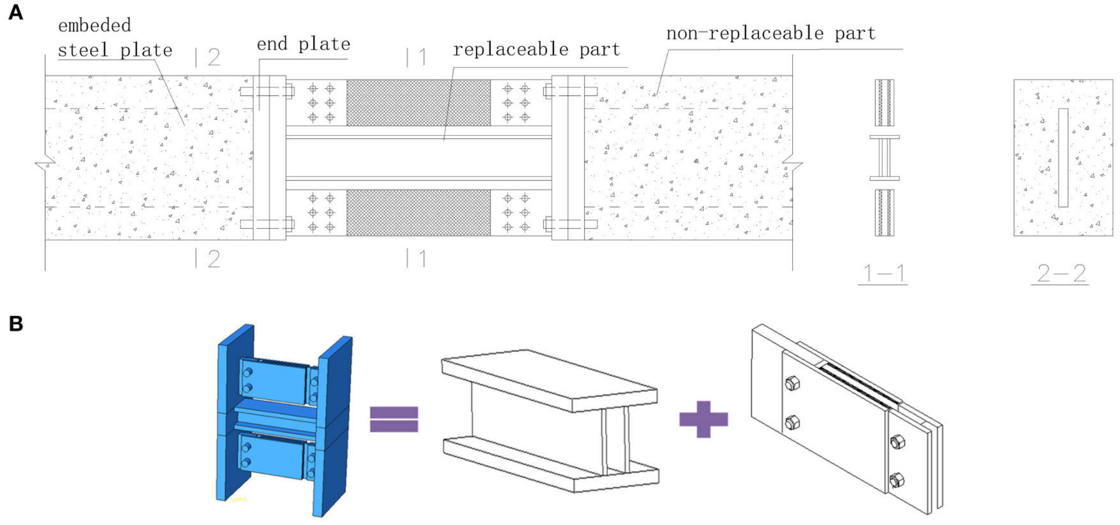

FIGURE 1 | Schematic drawing: **(A)** replaceable coupling beam; **(B)** the combined damper.

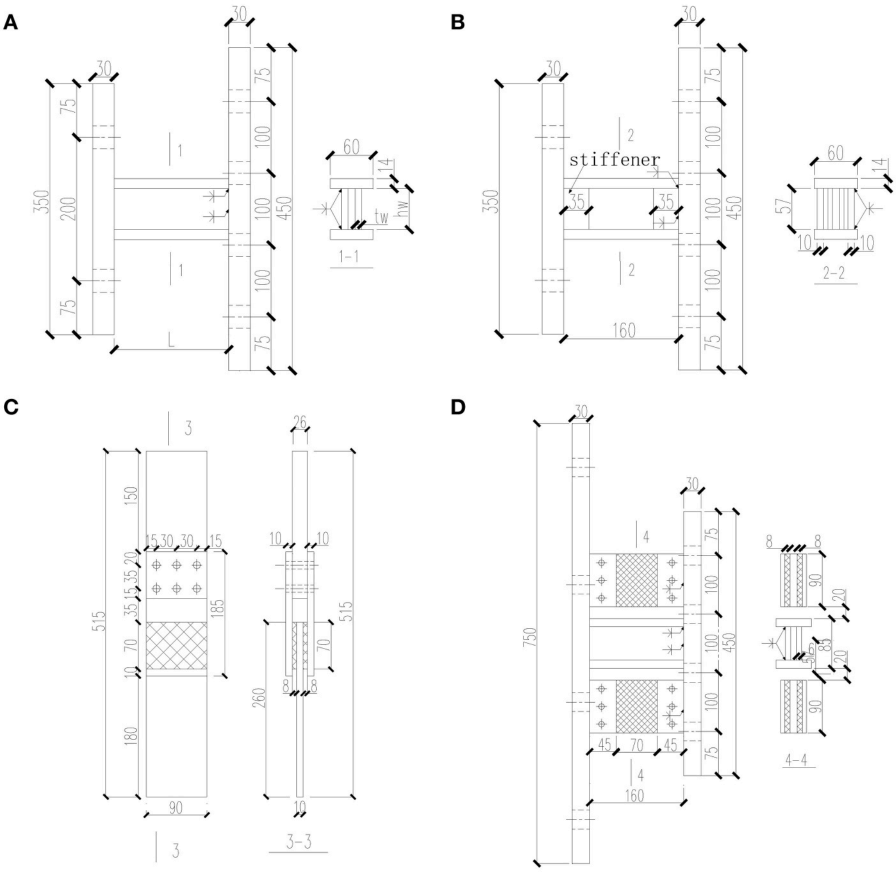

FIGURE 2 | Test specimens: **(A)** metallic dampers M1–M7; **(B)** metallic damper M8; **(C)** VE damper; **(D)** combined damper.

in **Figure 2**. For the metallic damper, the variable parameters studied are the steel grade, dimensions of the web, and end stiffener configuration. Q345 steel, one kind of Chinese standardized mild steel with the yield strength of 345 MPa, is used for flanges. For the web, three types of steel, LY160 (low yield point steel with a nominal yield stress of 160 MPa), LY225

TABLE 1 | Detailed parameters of metallic dampers.

Specimen No.	Flange width (mm)	Flange thickness (mm)	Web depth h_w (mm)	Web thickness t_w (mm)	Web number	Length *L* (mm)	Web steel	Flange steel
M1	60	14	57	6	2	160	LY225	Q345
M2	60	14	60	8	2	160	LY160	Q345
M3	60	14	57	6	2	160	Q235	Q345
M4	60	14	57	6	2	100	LY225	Q345
M5	60	14	57	6	2	200	LY225	Q345
M6	60	14	72	6	2	160	LY225	Q345
M7	60	14	45	6	2	160	LY225	Q345
M8	60	14	57	6	2	160	LY225	Q345

TABLE 2 | Mechanical properties for steel of metallic dampers.

Steel grade	Part	Yield strength (MPa)	Ultimate strength (MPa)	Elongation (%)	Elastic modulus (× 10^5MPa)
LY160-8mm	Web	207	314	52.7	1.91
LY225-6mm	Web	266	353	42.0	2.02
Q235-6mm	Web	336	470	29.7	2.08
Q345-10mm	Stiffener	382	525	26.0	2.13
Q345-14mm	Flange	464	582	24.5	2.06

(low yield point steel with a nominal yield stress of 225 MPa), and Q235 (Chinese standardized mild steel with a yield strength of 235 MPa), respectively, are adopted. To reduce the strain levels at the ends of the flange and web and prevent the failure of the end-plate welds, the approach of using end stiffeners is investigated. A metallic damper specimen (M8) with four parallel end plate stiffeners is designed. The dimensions of the end plate stiffener is 35 × 57 × 10 mm. For all the metallic damper specimens, the flanges, and webs are welded together by complete joint penetration groove welds. The detailed parameters of metallic dampers are shown in **Table 1**. Uniaxial tensile specimen tests gave the mechanical properties of the steel grade used, as listed in **Table 2**.

The VE damper consisted of two layers of 70 × 90 mm VE materials bonded between Q345 steel plates with a thickness of 10 mm. The VE material used in this study was an elastomeric one, which presented improved energy absorption capacity. For illustrative purpose, the two VE dampers were noted as V1 and V2, respectively. The thickness of the VE material for V1 was 6 and 8 mm for V2.

The combined damper was manufactured by placing two edge VE damper components and one central metallic damper component in parallel. Both ends of the three components were welded together to the 30 mm thick end plates.

Test Setup

The VE dampers were tested in a MTS uniaxial testing system (**Figure 3A**). The cyclic axial force was applied to the central VE damper through the specially designed connections. **Figure 3B** shows the setup for both the metallic damper and the combined damper. The test setup is a portal frame with four pins at each corner, with the tested dampers installed between the top loading beam and bottom foundation beam by high-strength bolts. Lateral load from the actuator is applied to the top loading beam.

Loading Protocol

For the metallic dampers and the combined damper, the lateral load was applied by displacement control with each amplitude repeated three times according to Chinese specification of testing methods for earthquake resistant building (Ministry of Construction of China, 1997). The amplitude increment was 1% rotation, defined as the ratio of lateral displacement divided by the specimen height.

The displacement controlled loading was also applied to the VE dampers. Different from the loading protocol adopted for the above dampers, the displacement in the form of sinusoidal wave was used and five cycles were repeated for each amplitude. Also, to study the effect of loading frequency on its mechanical behavior, different loading frequencies were used for certain amplitudes. **Table 3** gives the detailed loading protocol adopted. For Specimen V1, 12 loading frequencies are used at the amplitudes of 50 and 100%, and the constant frequency of 0.1 Hz is used for other amplitudes. For Specimen V2, to save the loading time, only 6 loading frequencies are used at the amplitude of 100%, and the constant frequency of 0.1 Hz is used for other amplitudes.

The loading protocol of the combined damper basically followed that of the VE damper. The loading frequency was kept constant, i.e., 0.1 Hz, for all the amplitudes.

TEST RESULTS AND DISCUSSIONS

Metallic Dampers

Failure Mode

No web or flange buckling or local instability was observed during the test, indicating that the method to avoid web buckling by adopting small depth-thickness ratio was effective. The maximum depth-thickness ratio of 12 can be used as the threshold value in designing the web. Overall, the fracture

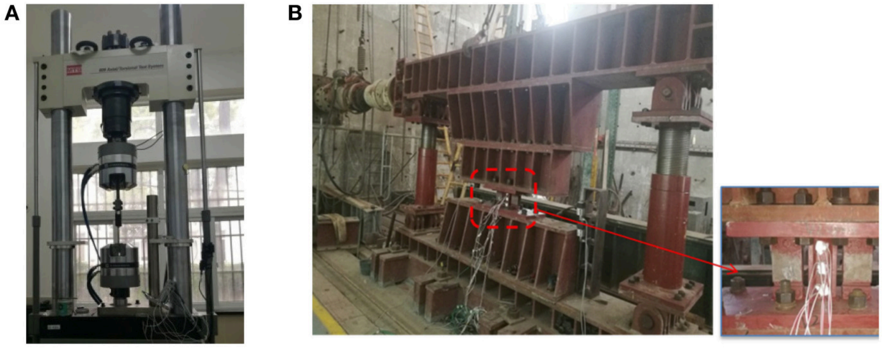

FIGURE 3 | Test setup: **(A)** VE damper; **(B)** metallic damper and combined damper.

TABLE 3 | Loading protocol of VE dampers.

Specimen No.	Loading sequence	Peak amplitude (%)	Frequency (Hz)
V1	I	25	0.1
	II	50	0.1, 0.2, 0.3, 0.4, 0.5, 0.75, 0.85, 1.0, 1.5, 2.0, 2.5, 3.0
	III	75	0.1
	IV	100	0.1, 0.2, 0.3, 0.4, 0.5, 0.75, 0.85, 1.0, 1.5, 2.0, 2.5, 3.0
	V	125, 150, 175, 200, 250, 300, 350	0.1
V2	I	25, 50, 75	0.1
	II	100	0.1, 0.3, 0.5, 1.0, 2.0, 3.0
	III	125, 150, 175, 200, 250, 300, 350	0.1

occurred in the following positions as shown in **Figure 4**: (1) flange-to-end plate weld; (2) corners of the web next to the welds; and (3) web-to-flange weld.

For Specimens M1 and M6, the fracture occurred at the flange-to-end plate weld and the corners of the web next to the welds. Cracks were first observed in the flange next to the steel plate weld. These cracks did not immediately propagate and enlarge. And the resistance did not decrease obviously until the corner of the web next to the welds fractured.

The flange-to-end plate weld fracture caused the failure of Specimens M2 and M5. No web damage was observed during the test. The main reason is that the web of Specimen M2 was made of LY160 steel whose ductility was better than that of LY225 steel and Q235 steel. As for Specimen M5, its length of 200 mm was the largest among all the specimens, which was more dominated by flexual behavior. The more obvious effect of diagonal tension at large shear deformation gave the higher stress level at the flange-to-end plate welds. Specimens M3, M4, and M7 had a similar damage development process. Cracks were first observed in the flange-steel plate weld, followed by the web-to-flange weld fracture. In the end, the development of the web-to-flange weld fracture caused the failure.

The flange-to-end plate weld fracture was not observed in Specimen M8. As previously stated, end plate stiffeners were used in Specimen M8. With the aid of stiffeners, the stress level at the flange-to-end plate weld was largely reduced, which shifted large plasticity position toward the middle part of the damper. The effectiveness of the stiffeners in preventing the flange-to-end plate weld fracture was demonstrated. With the increases of lateral displacement, fracture occurred in the stiffener-flange welds first. Finally, the web-to-flange weld was totally torn, causing the failure of Specimen M8. The failure mode is illustrated in **Figure 4D**.

Shear Force-Shear Rotation Relationship

Figure 5 shows the hysteretic curves, with abscissa being shear rotation defined as the ratio between the lateral displacement and the specimen height. The metallic dampers show very stable hysteretic loops and exhibit excellent deformation and energy-dissipation capability. With the increase of lateral displacement, the shear strength hardening is apparent, and there is no decline in bearing capacity until failure.

The normalized shear force-shear rotation envelope curves are illustrated in **Figure 6**. The ordinate of shear force is normalized by the yield shear strength (V_y), which is calculated as 0.6 f_yA_w, where f_y is the actual measured yield stress of the steel obtained from tensile coupon test, and A_w is the web sectional area. **Table 4** summarizes the shear strength and deformation capacity of metallic dampers. The overstrength ratio (V_{max}/V_y, with V_{max} being the maximum shear force obtained in the test) is an important parameter to design the non-replaceable part of the coupling beam. Test results in this study found that the overstrength ratio increased with the decrease of length and height of web and yield stress of web steel. The overstrength ratio ranged from 2.27 to 3.24, and the average of overstrength ratio was 2.62. Specimen M2 made of LY160 demonstrated the largest ductility and shear strength. The only difference among Specimens M1, M4, and M5 was the specimen length. The shortest M4 exhibited the largest shear strength. Among Specimens M1, M6, and M7, M7 had the smallest web depth and exhibited the largest shear strength. Compared with the reference

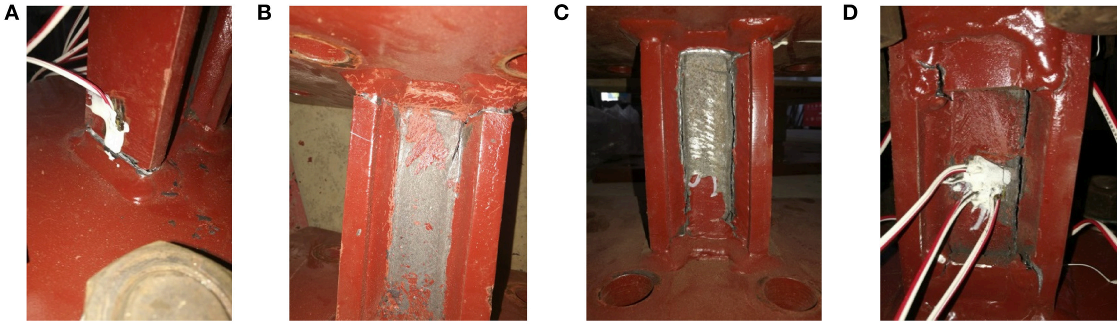

FIGURE 4 | Damage pattern of fractures: **(A)** flange-to-end plate weld; **(B)** web corners next to the welds; **(C)** web-to-flange weld; **(D)** Specimen M8.

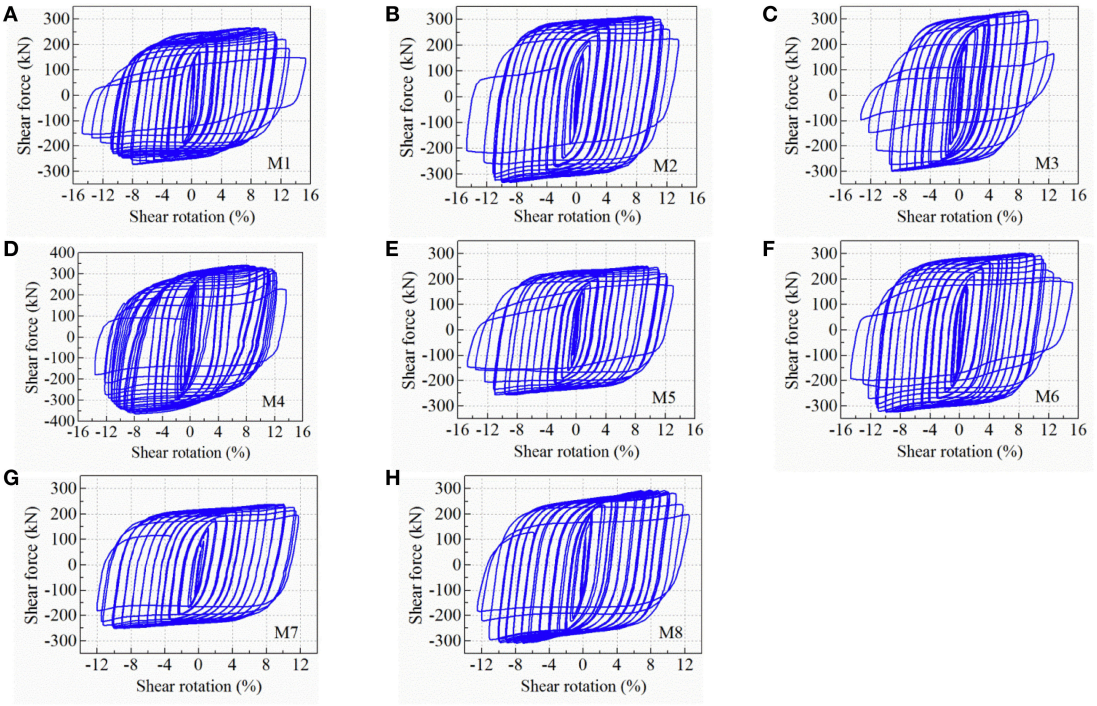

FIGURE 5 | Hysteretic curves of metallic dampers: **(A)** M1; **(B)** M2; **(C)** M3; **(D)** M4; **(E)** M5; **(F)** M6; **(G)** M7; **(H)** M8.

Specimen M1, Specimen M8 with end plate stiffener presented higher shear strength.

The ductility coefficient, defined as the ratio between the ultimate shear rotation and the yield shear rotation, is listed in **Table 4**. Compared with Specimen M3 (Q235 steel), the ductility coefficient of Specimens M1 (LY225 steel) and M2 (LY160 steel) increases by 28.1 and 67.3%, respectively. With the adoption of low-yield-point steel in the web, the ductility of the metallic damper is significantly enhanced. While the length and depth of the damper and the end stiffener have limited effect on the ductility. **Table 4** also lists the ultimate plastic shear rotation and cumulative plastic rotation. The average ultimate plastic shear rotation is 0.11, which is larger than the value of 0.08 specified in the provisions of the AISC 341-10 (ANSI/AISC, 2010). The effect of web steel grade on the deformation capacity, such as the ultimate plastic shear rotation and cumulative plastic rotation, is remarkable. The ultimate plastic shear rotation and cumulative plastic rotation increase with decrease of yield stress of the web steel. Basically, the effect of length and depth of the damper on the ultimate plastic shear rotation and cumulative plastic rotation is slight.

Energy Dissipation Capacity

The energy dissipation capacity was generally evaluated by using equivalent viscous damping coefficient C_{eq}, which is calculated according to the following formula:

$$C_{eq} = \frac{1}{2\pi} \times \frac{E_{hyst}}{E_{\max}} \tag{1}$$

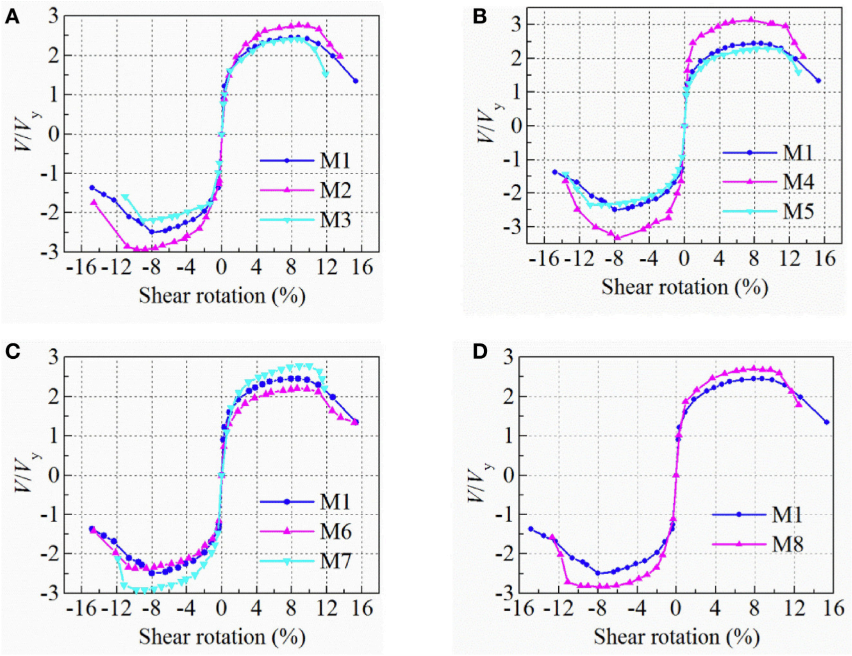

FIGURE 6 | Normalized shear force-shear rotation envelope curves: **(A)** different web steel; **(B)** different specimen length; **(C)** different web depth; **(D)** different detailing.

TABLE 4 | Shear strength and deformation capacity of metallic dampers.

Specimen No.	Yield shear strength (kN)	Maximum shear strength (kN)	Overstrength ratio	Yield shear rotation (%)	Ultimate plastic shear rotation (%)	Ductility coefficient	Cumulative plastic rotation
M1	109	269	2.46	0.26	11.03	44.40	7.31
M2	113	322	2.84	0.21	11.44	57.98	7.93
M3	138	316	2.29	0.32	11.97	34.65	5.46
M4	109	353	3.24	0.22	10.62	52.9	7.42
M5	109	253	2.32	0.32	11.60	38.13	7.75
M6	138	313	2.27	0.29	11.81	40.18	8.13
M7	86	245	2.84	0.29	11.45	39.87	7.39
M8	109	302	2.76	0.25	11.26	45.08	6.88

where E_{hyst} is the sum of the area enclosed by hysteretic loops, and $E_{\max}$ is energy absorbed by equivalent elastomers at the same displacement amplitude.

Figure 7 illustrates the calculated equivalent viscous damping coefficients of metallic dampers, using the first cycle at each shear rotation amplitude. The equivalent viscous damping coefficient rises as the shear rotation increases before the metallic damper damaged. The equivalent viscous damping coefficients are >0.5 for all specimens at the rotation beyond 0.03. For specimens with different web steel grade, the equivalent viscous damping coefficient increases as the web steel yield stress decreases (**Figure 7A**). With the decrease of length of web, the equivalent viscous damping coefficient increases slightly (**Figure 7B**). The height of the web has little effect on energy dissipation capacity (**Figure 7C**). With or without the end plate stiffener, the equivalent viscous damping coefficient is similar (**Figure 7D**).

VE Dampers

Failure Mode

There was no separation observed between the VE layer and steel plate until 300% strain for both Specimens V1 and V2. When the strain amplitude reached 350%, the VE layer separated from the steel plate and the bearing capacity dropped subsequently.

Energy Dissipation and Strain Dependency

Figure 8 shows the hysteretic loops of Specimens V1 and V2 under various strains subject to a constant frequency 0.1 Hz. It can be seen that the VE damper dissipates energy at all strain ranges. In addition, hardening behavior under relatively large strain is clearly observed for both specimens. The shear storage modulus (G'), shear loss modulus (G'') and loss factor (η) are the most important factors reflecting the properties of VE damper. These factors can be obtained from the hysteresis curves, and can

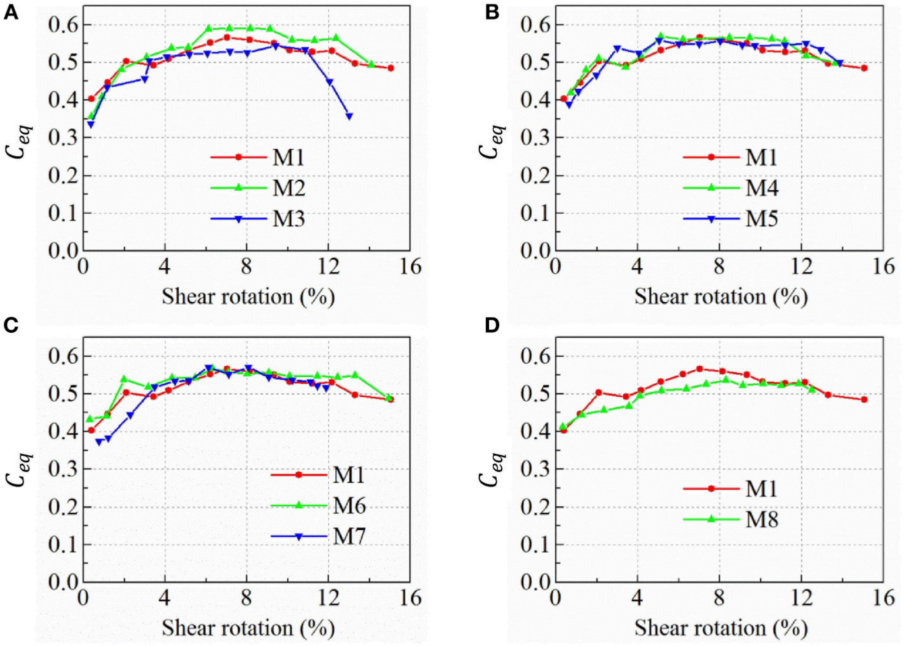

FIGURE 7 | Equivalent viscous damping coefficients of metallic dampers: **(A)** different web steel; **(B)** different specimen length; **(C)** different web depth; **(D)** different detailing.

be expressed as:

$$G' = \frac{F_1 h}{nA\mu_0} \tag{2}$$

$$G'' = \frac{F_2}{F_1}G' \tag{3}$$

$$\eta = \frac{F_2}{F_1} \tag{4}$$

where A is the VE material area, h is the thickness of the VE material, n is the layers of VE material, μ_0 is the maximum displacement, F_1 is the corresponding force at displacement μ_0, and F_2 is the corresponding force at zero displacement.

The variation of these factors with strain levels for two specimens are shown in **Figure 9**. Because of the thicker VE material layer, both the shear storage modulus and shear loss modulus of Specimen V2 are larger than that of Specimen V1. While the loss factor is quite similar for both specimens. In addition, the shear storage modulus, shear loss modulus and loss factor decrease with increase of strain. Beyond the strain of 250%, the storage shear modulus stops to decrease as hardening starts.

Frequency Dependency

As previously described, different loading frequencies were adopted for Specimen V1 at strain amplitudes of 50% and 100% and Specimen V2 at a strain amplitude of 100%. **Figure 10** illustrates the variation of the shear storage modulus, shear loss modulus, and loss factor under different frequency. It can be seen that both the shear storage modulus and shear loss modulus decrease slightly as the excitation frequency increases within the frequency range between 0.1 and 1 Hz. However, the dependency on frequency is not obvious when the frequency exceeds 1 Hz. With the increase of strain amplitude, both the shear storage modulus and shear loss modulus decrease (Specimen V1). The loss factor is not significantly dependent on both of the shear strain amplitude and the frequency.

Combined Damper

Failure Mode

The combined damper had the failure mode similar to Specimen M1. Cracks were first observed in the flange next to the steel plate weld when the rotation was 8.93%, and the bearing capacity continued to increase. The maximum shear strength reached 314 kN at the rotation of 9.92%. During the following loading cycles, cracks were observed at the coner of the web. Ultimately, the cracks tore through the entire length of the web along the flange welds, and the bearing capacity decreased. No damage of the VE damper was observed till the shear rotation of 12% when the equivalent strain of the VE material reached 240%.

Lateral Force-Displacement Relationship

Figure 11A shows the shear force vs. rotation hysteretic curves of the combined damper. With the increase of the displacement, the strength hardening is apparent. The hysteretic loop becomes S-shaped after the shear rotation of 12% because the hysteresis curve of the VE damper is S-shaped and the hardening is apparent when the strain of the VE material is >200%. The comparison of envelope curve between Specimen M1 and the combined damper is shown in **Figure 11B**. The strength and the stiffness of the combined damper are higher than that of

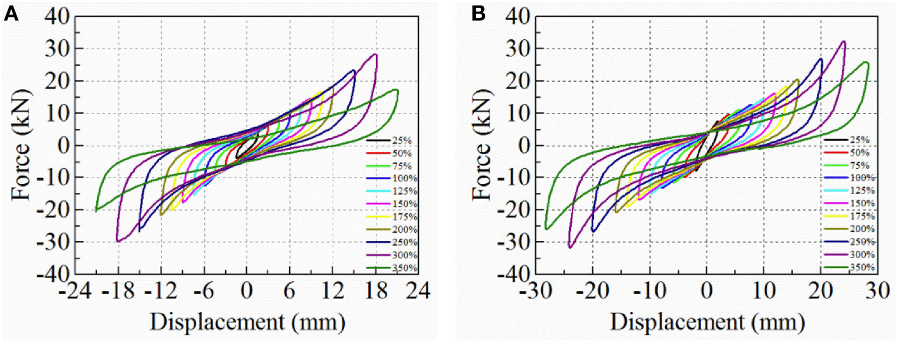

FIGURE 8 | Hysteretic curves of VE dampers: **(A)** V1; **(B)** V2.

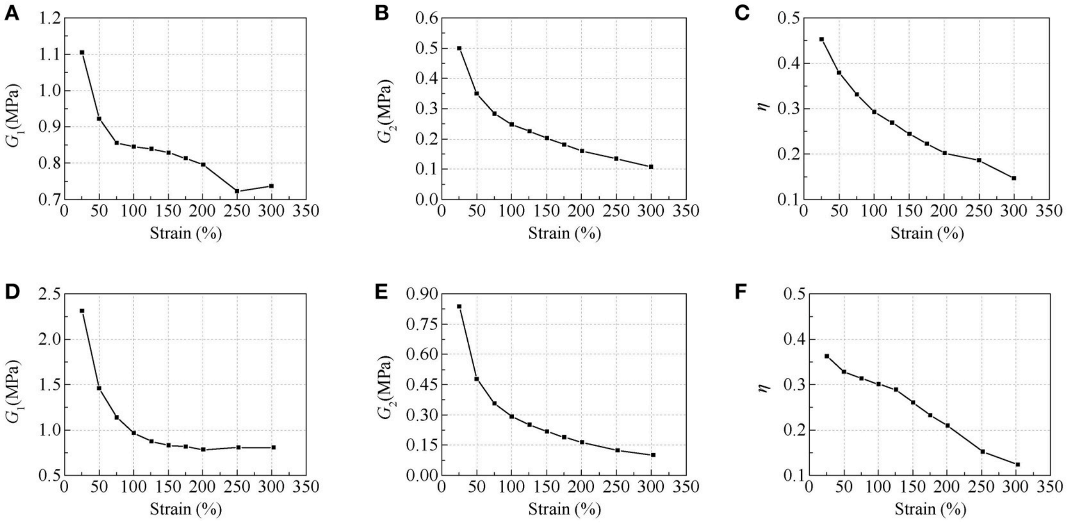

FIGURE 9 | Strain dependency: **(A)** shear storage modulus of V1; **(B)** shear loss modulus of V1; **(C)** loss factor of V1; **(D)** shear storage modulus of V2; **(E)** shear loss modulus of V2; **(F)** loss factor of V2.

metallic damper due to the contribution of VE damper. In comparison with the metallic damper, the initial stiffness of combined damper increases from 259 to 270 kN/mm, and the maximum shear strength increases from 269 to 314 kN. The VE damper contributes about 14% on the bearing capacity and 4% on the stiffness.

Energy Dissipation

It can be seen from **Figure 11B** that, basically, the combined damper experiences a greater force at the same deformation, indicating that the combined damper dissipates more energy than metallic damper. **Figure 11C** shows the ratio of the energy dissipated by the VE damper to that of the total energy in the combined damper. As indicated in the figure, the additional energy dissipation ratio is 8% at small deformation level, and then drops to 5.5% as the energy dissipated by metallic damper increases. After the metallic damper fails, the ratio increases significantly.

Estimation of Elastic Stiffness and Yield Strength

The stiffness of the metallic damper (K_{M}) and VE damper (K_{V}) can be expressed respectively as follows:

$$K_{\mathrm{M}} = \frac{1}{\frac{L^3}{12EI} + \frac{\mu L}{GA}} \tag{5}$$

$$K_{\mathrm{V}} = \frac{G' A_{\mathrm{v}}}{h} \tag{6}$$

where L is the length of the metallic damper, μ is the correction coefficients, A and A_{v} are, respectively the web cross sectional area of metallic damper and the shear area of the VE damper, I is the cross sectional moment of inertia of metallic damper, E and G are respectively the elastic modulus and shear modulus of metallic damper, and G' is shear storage modulus of the VE material.

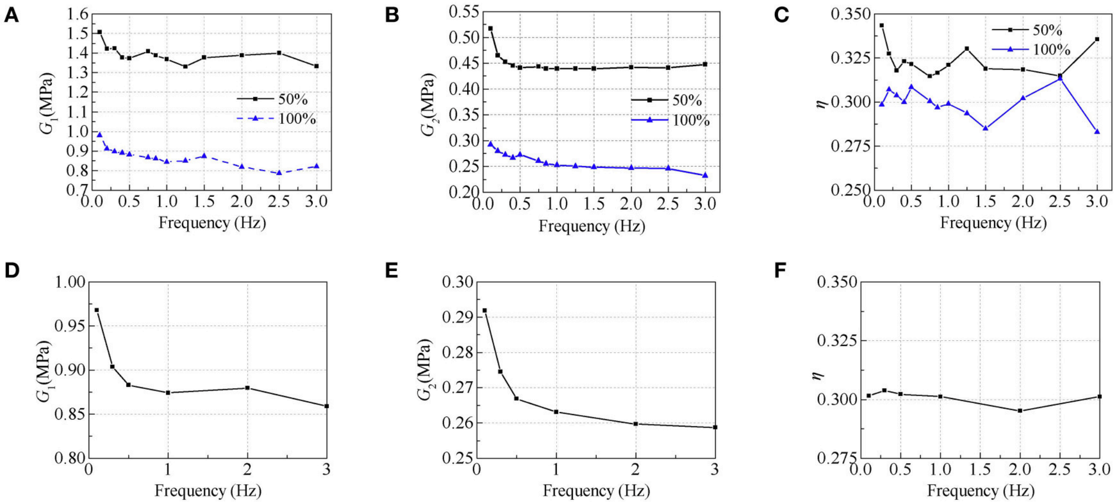

FIGURE 10 | Frequency dependency: **(A)** shear storage modulus of V1; **(B)** shear loss modulus of V1; **(C)** loss factor of V1; **(D)** shear storage modulus of V2; **(E)** shear loss modulus of V2; **(F)** loss factor of V2.

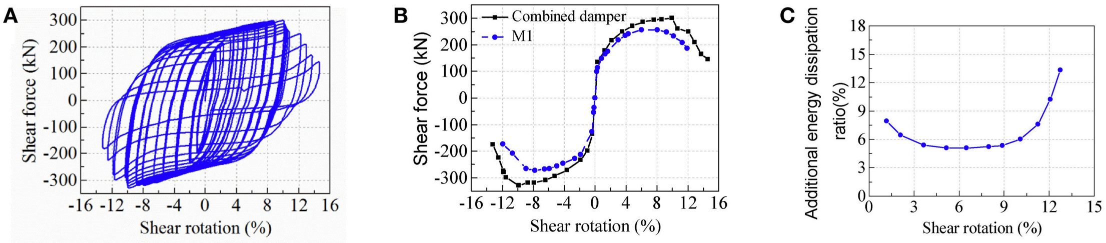

FIGURE 11 | Combined damper: **(A)** hysteretic curve; **(B)** skeleton comparison with the metallic damper M1; **(C)** energy dissipation by VE damper.

The elastic stiffness of the combined damper is then the summation of metallic damper and VE damper:

$$K = K_{\mathrm{M}} + K_{\mathrm{V}} \tag{7}$$

As previously mentioned, the yield shear strength (V_{y}) of the metallic damper was calculated as:

$$V_y = 0.6 f_y A_w \tag{8}$$

where f_{y} is the yield strength of the steel, and A_{w} is the web sectional area.

As shown in **Figure 6**, the ordinate of ±1 gives the inflection point in the shear force-rotation envelope curve, which indicates that Equation (8) is capable of capturing the yield shear strength of the metallic dampers. As there is no clear yield point in the hysteresis of the VE damper, its yield shear strength can be conservatively estimated as the shear strength at the moment when the metallic damper yields. The yield shear strength of the combined damper can be calculated as:

$$V = V_y + K_V \Delta_{\mathrm{y}} \tag{9}$$

where Δ_y is the yield displacement of metallic damper, determined as the ratio between the yield shear strength derived by Equation (8) and the stiffness derived by Equation (5).

According to Equation (7), the predicted elastic stiffness of the combined damper is 280 kN/mm with an error of 3.7% compared with the test result of 270 kN/mm. Equation (9) gives the yield shear strength of 112 kN, with an error of 7.4% compared with the test result of 122 kN. Basically, the analytical solutions predicts well both the elastic stiffness and yield shear strength.

CONCLUSIONS

A new damper, combining the viscoelastic damper and metallic damper used for replaceable coupling beams, is proposed and studied in this paper. Through a series of experimental study, the major findings are summarized as follows:

(1) No web instability was observed, indicating that unstiffened webs with depth-thickness ratio <12 was sufficient to avoid web buckling. The web end stiffeners effectively reduced the flange stress at the ends of the specimen, which prevented the failure of flange-to-end plate welds.

(2) The maximum overstrength ratio of the metallic damper reached 3.24 with an average of 2.62. The overstrength ratio increased with the decrease of the length or depth of web or the yield strength of web steel.
(3) The effect of web steel grade on the deformation and energy dissipation capacity of the metallic damper was remarkable. The metallic damper using low-yield-point steel exhibited excellent ductility and energy dissipation capacity. While the length and depth of the damper and the installation of end stiffener had limited effect.
(4) No damage occurred at the shear surface between the VE layer and steel plate until the strain of 300%, and the VE layer and steel plate started to separate at the strain of 350%.
(5) The shear storage modulus, shear loss modulus, and loss factor of the VE material decreased with the increase of strain. Both the shear storage modulus and shear loss modulus decreased slightly with the increase of loading frequency ranging from 0.1 to 1 Hz. However, the dependency on frequency was not obvious when the frequency exceeded 1 Hz. The loss factor was not significantly dependent on the loading frequency.
(6) The combined damper illustrated stable hysteretic loops and exhibited excellent deformation capability. The predicted elastic stiffness and yield shear strength agreed well with test results.

AUTHOR CONTRIBUTIONS

HJ supervised the research and revised the manuscript. SL conducted the experiments, analyzed data and wrote manuscript partially. LH reviewed and revised the manuscript. All the authors participated in discussion of the research.

FUNDING

The authors are grateful for the support from National Key Research and Development Program of China under Grant No. 2017YFC1500701 and Program of Shanghai Academic Research Leader under Grant No. 18XD1403900.

REFERENCES

ANSI/AISC (2010). *AISC 341-10, Seismic Provisions for Structural Steel Buildings*. Chicago, IL: American Institute of Steel Construction.

Chung, H. S., Moon, B. W., Lee, S. K., Park, J. H., and Min, K. W. (2009). Seismic performance of friction dampers using flexure of Rc shear wall system. *Struct. Des. Tall Spec*. 18, 807–822. doi: 10.1002/tal.524

Dusicka, P., Itani, A. M., and Buckle, I. G. (2009). Cyclic behavior of shear links of various grades of plate steel. *J. Struct. Eng*. 136, 370–378. doi: 10.1061/(ASCE)ST.1943-541X.0000131

Fortney, P. J., Shahrooz, B. M., and Rassati, G. A. (2007). Large-scale testing of a replaceable "Fuse" steel coupling beam. *J. Struct. Eng*. 133, 1801–1807. doi: 10.1061/(ASCE)0733-9445(2007)133:12(1801)

He, L., Togo, T., Hayashi, K., Kurata, M., and Nakashima, M. (2016). Cyclic behavior of multirow slit shear walls made from low-yield-point steel. *J. Struct. Eng*. 142:04016094. doi: 10.1061/(ASCE)ST.1943-541X.0001569

Hitaka, T., and Matsui, C. (2003). Experimental study on steel shear wall with slits. *J. Struct. Eng*. 129, 586–595. doi: 10.1061/(ASCE)0733-9445(2003)129:5(586)

Ji, X. D., Wang, Y. D., Ma, Q. F., and Okazaki, T. (2016). Cyclic behavior of very short steel shear links. *J. Struct. Eng*. 142:04015114. doi: 10.1061/(ASCE)ST.1943-541X.0001375

Jiang, H., Li, S., and Zhu, Y. (2017). Seismic performance of high-rise buildings with energy-dissipation outriggers. *J. Construct. Steel Res*. 134, 80–91. doi: 10.1016/j.jcsr.2017.03.013

Kam, W. Y., and Pampanin, S. (2011). The seismic performance of RC buildings in the 22 February 2011 christchurch earthquake. *Struct. Concrete* 12, 223–233. doi: 10.1002/suco.201100044

Kurata, M., He, L., and Nakashima, M. (2015). Steel slit shear walls with double-tapered links capable of condition assessment. *Earthq. Eng. Struct. Dyn*. 44, 1271–1287. doi: 10.1002/eqe.2517

Lu, X., Chen, C., Jiang, H., and Wang, S. (2018a). Shaking table tests and numerical analyses of an RC coupled wall structure with replaceable coupling beams. *Earthq. Eng. Struct. Dyn*. 47, 1882–1904. doi: 10.1002/eqe.3046

Lu, X., Chen, Y., and Jiang, H. (2018b). Earthquake resilience of reinforced concrete structural walls with replaceable "Fuses". *J. Earthq. Eng*. 22, 801–825. doi: 10.1080/13632469.2016.1264330

Lu, Z., Huang, B., Zhang, Q., and Lu, X. (2018a). Experimental and analytical study on vibration control effects of eddy-current tuned mass dampers under seismic excitations. *J. Sound Vibr*. 421, 153–165. doi: 10.1016/j.jsv.2017.10.035

Lu, Z., Huang, B., and Zhou, Y. (2018b). Theoretical study and experimental validation on the energy dissipation mechanism of particle dampers. *Struct Control Health Monit* 25:e2125. doi: 10.1002/stc.2125

Mackay-Lyons, R., Christopoulos, C., and Montgomery, M. (2012). "Enhancing the seismic performance of RC coupled wall high-rise buildings with viscoelastic coupling dampers," in *Proceedings of the 15th World Conference on Earthquake Engineering* (Lisboa).

Ministry of Construction of China (1997). *Specification of Testing Methods for Earthquake Resistant Building JGJ 101-96*, Beijing: China Architecture and Building Press (in Chinese).

Montgomery, M., and Christopoulos, C. (2015). Experimental validation of viscoelastic coupling dampers for enhanced dynamic performance of high-rise buildings. *J. Struct. Eng*. 141:04014145. doi: 10.1061/(ASCE)ST.1943-541X.0001092

Okazaki, T., and Engelhardt, M. D. (2007). Cyclic loading behavior of EBF links constructed of ASTM A992 steel. *J. Constr. Steel Res*. 63, 751–765. doi: 10.1016/j.jcsr.2006.08.004

Shi, Q.-X., Wang, F., Wang, P., and Chen, K. (2018). Experimental and numerical study of the seismic performance of an all-steel assembled Q195 low-yield buckling-restrained brace. *Eng. Struct*. 176, 481–499. doi: 10.1016/j.engstruct.2018.09.039

Takeuchi, T., Hajjar, J., Matsui, R., Nishimoto, K., and Aiken, I. (2012). Effect of local buckling core plate restraint in buckling restrained braces. *Eng. Struct*. 44, 304–311. doi: 10.1016/j.engstruct.2012.05.026

Tsai, K.-C., Chen, H.-W., Hong, C.-P., and Su, Y.-F. (1993). Design of steel triangular plate energy absorbers for seismic-resistant construction. *Earthq. Spectra* 9, 505–528. doi: 10.1193/1.1585727

Wallace, J. W. (2012). Behavior, design, and modeling of structural walls and coupling beams - Lessons from recent laboratory tests and earthquakes. *Int. J. Concr. Struct. Mater*. 6, 3–18. doi: 10.1007/s40069-012-0001-4

Wang, B., and Zhu, S. (2017). Seismic behavior of self-centering reinforced concrete wall enabled by superelastic shape memory alloy bars. *Bull. Earthq. Eng*. 16, 479–502. doi: 10.1007/s10518-017-0213-8

Wang, T., Guo, X., He, X., Duan, C., and Du, Y. (2012). Experimental study on replaceable hybrid coupling beams. *Appl. Mech. Mater*. 166–169, 1779–1784. doi: 10.4028/www.scientific.net/AMM.166-169.1779

Xu, Z., Guo, Y., and Wang, S. (2013a). Xing-Huai Huang. Optimization analysis on parameters of multi-dimensional earthquake isolation and mitigation device based on genetic algorithm. *Nonlin. Dyn*. 72, 757–765. doi: 10.1007/s11071-013-0751-9

Xu, Z., Huang, X., Xu, F., and Yuan, J. (2019). Parameters optimization of vibration isolation and mitigation system for precision platforms using non-dominated sorting genetic algorithm. *Mech. Sys. Signal Process.* 128, 191–201. doi: 10.1016/j.ymssp.2019.03.031

Xu, Z., Liao, Y., Ge, T., and Xu, C. (2016). Experimental and theoretical study on viscoelastic dampers with different matrix rubbers. *J. Eng. Mech. ASCE* 142:04016051. doi: 10.1061/(ASCE)EM.1943-7889.0001101

Xu, Z., Sha, L., and Zhang, X. (2013b). Design, performance test and analysis on magnetorheological damper for earthquake mitigation. *Struct. Control Health Monit.* 20, 956–970. doi: 10.1002/stc.1509

Xu, Z., Shen, Y., and Zhao, H. (2003). A synthetic optimization analysis method on structures with viscoelastic dampers. *Soil Dyn. Earthq. Eng.* 23, 683–689. doi: 10.1016/j.soildyn.2003.07.003

Xu, Z., Zhao, H., and Li, A. (2004). Optimal analysis and experimental study on structures with viscoelastic dampers. *J. Sound Vibr.* 273, 607–618. doi: 10.1016/S0022-460X(03)00522-4

Conflict of Interest Statement: The authors declare that the research was conducted in the absence of any commercial or financial relationships that could be construed as a potential conflict of interest.

frontiers in Materials

ORIGINAL RESEARCH
published: 09 July 2019
doi: 10.3389/fmats.2019.00135

Experimental Study on a Hybrid Coupling Beam With a Friction Damper Using Semi-steel Material

Tao Wang[1]*, *Fengli Yang*[1], *Xin Wang*[2] and *Yao Cui*[2]

[1] *Key Laboratory of Earthquake Engineering and Engineering Vibration, Institute of Engineering Mechanics, China Earthquake Administration (CEA), Harbin, China,* [2] *State Key Laboratory of Coastal and Offshore Engineering, School of Civil Engineering, Faculty of Infrastructure Engineering, Dalian University of Technology, Dalian, China*

RC coupling beams have been reported to have had serious damages during the 2008 Wenchuan earthquake. Beams are very difficult to repair once cracks occur. To improve the ductility and reparability of the traditional RC coupling beam, a damage-controllable hybrid coupling beam is proposed in this study. The hybrid coupling beam couples the wall limbs by a friction damper connected through steel beam segments. The strength and stiffness of the friction damper are carefully designed to concentrate more deformation on the damper. The friction mechanism could dissipate more energy than the traditional RC coupling beam. The uncertainties introduced by the design process and the inherent characteristics of traditional RC coupling beams or other types of dampers are significantly reduced. High-strength bolts are used for all connections so that it could be quickly replaced once any damage is observed after an earthquake. In this study, a friction damper using semi-metallic friction plates and stainless-steel shims as the contact pair was tested at different loading rates. The temperature was measured. A thermal–mechanical model was then developed to correlate the dissipated energy with the friction coefficient or friction force, which can be easily incorporated into the structural design process. Finally, the hybrid coupling beam was designed and tested quasi-statically. The force, deformation, and energy dissipation capacity were compared with the traditional RC coupling beam, which also demonstrated damage controllability by using the proposed hybrid coupling beam.

Keywords: hybrid coupling beam, friction damper, damage controllability, friction coefficient, temperature dependency

Edited by:
Yong Lu,
University of Edinburgh,
United Kingdom

Reviewed by:
Wei He,
Anhui University of Science and Technology, China
Jiafei Jiang,
Tongji University, China

***Correspondence:**
Tao Wang
wangtao@iem.ac.cn

Specialty section:
This article was submitted to Structural Materials, a section of the journal Frontiers in Materials

Received: *01 March 2019*
Accepted: *24 May 2019*
Published: *09 July 2019*

Citation:
Wang T, Yang F, Wang X and Cui Y (2019) Experimental Study on a Hybrid Coupling Beam With a Friction Damper Using Semi-Steel Material. Front. Mater. 6:135. doi: 10.3389/fmats.2019.00135

INTRODUCTION

High-rise buildings often adopt the reinforced concrete (RC) shear wall system as the lateral force resistance member. The dual seismic defense mechanism, i.e., the coupling beams and the shear walls, is particularly suitable to balance comfort living and earthquake safety. During an earthquake, the coupling beams are damaged first, and the entire structure becomes more flexible, thus preventing high-frequency dominated energy entering the structure. Therefore, the coupling beam is often expected to be ductile, as suggested by many seismic design codes (International Code Council (ICC), 2015; MOHURD, 2016a,b). However, more ductility of RC members implies more damage, because the ductility relies on the crack of concrete and yielding of steel rebars. Once the

RC coupling beam cracks, it is very difficult to repair, as reported in the 2008 Wenchuan earthquake (Wang, 2008).

The coupling beam, once combined with dampers, also called hybrid coupling beams, is appealing because of its damage controllability that is superior to traditional RC coupling beams. Recent studies (Fortney et al., 2007; Xu, 2007; Teng et al., 2010; Lu et al., 2013; Xu et al., 2016) have demonstrated that the ductility is greatly improved by use of dampers in the coupling beam. A viscoelastic coupling damper was employed by Montgomery and Christopoulos (2015) to enhance the seismic performance of high-rise buildings. The performance of two wall limbs coupled by the viscoelastic link under the wind and the earthquake loads was also validated experimentally. A self-centering damper using SMA wires for the RC coupling beam has been developed to render the system a re-centering capability, which has been demonstrated effective by experiments (Mao et al., 2012). More recently, Ji et al. (2017) proposed a short steel shear link to replace the entire RC coupling beam. Both energy dissipation capacity and quick replaceability have been verified through quasi-static cyclic tests. A 1/2 scaled four-story specimen was constructed, which was installed with low-yield steel coupling beams (Cheng et al., 2015). The connection between the steel coupling beam and the RC shear wall worked well during the entire test. However, most of the configurations mentioned above lack replacement mechansim. The dampers are found difficult to be replaced once damaged. Moreover, some metallic dampers, although connected through bolts, performed significant over-strength, making the connection damaged at large deformations.

To solve these problems, the friction damper is often employed. Theoretically, the friction damper has infinite initial stiffness, and a stable post-sliding force, which is superior to other types of dampers in the coupling beam application, as demonstrated by Ahn et al. (2013) and Ye et al. (2018). Most friction dampers are featured with a line type working in axial direction, such as the Pall friction damper (Pall and Marsh, 1982) and the Sumitomo damper (Aiken et al., 1993). They are often combined with other mechanisms to realize more sophisticated behavior, such as the self-centering damper (Filiatrault et al., 2000) and the semi-actively controlled damper (Xu and Ng, 2008). The energy can also be dissipated by the friction torqued (Mualla and Belev, 2002) or by the bolted connections (Loo et al., 2014). The key to realizing a stable friction behavior is the materials of contact pair. Several types of friction materials have been examined extensively in the past two decades, including the semi-metallic friction material, metallic alloy material, iron-based ceramic material, carbon-based composite material, and so on (Jang et al., 2004; Gurunath and Bijwe, 2007; Yun et al., 2010; Latour et al., 2014; Lee et al., 2016). These studies examined the microscopic behavior of contact surface, such as adhesion, abrasion, fatigue, corrosion, and so on, by using scanning electron microscopy. In engineering practice, it could be difficult to measure such behavior during an earthquake. Instead, displacement, velocity, and force could be obtained from the available design process. Therefore, relating friction behavior to displacement, velocity, or the dissipated energy could be very helpful for the design application.

To this end, this study proposes a friction damper using semi-metallic friction plates and stainless-steel shims as the contact pair. The dampers were tested at different loading rates, and the temperature was measured. A thermal–mechanical model was then developed to correlate the dissipated energy with the friction coefficient or friction force, which can be easily incorporated into the structural design process. Finally, the hybrid coupling beam was designed and tested quasi-statically. The force, deformation, and energy dissipation capacity were compared with the traditional RC coupling beam, and conclusions are given to provide design guidance.

MECHANICAL BEHAVIOR OF FRICTION DAMPER

Friction dampers are featured with an infinite initial stiffness and almost constant slip force, which are very appealing because the larger stiffness is helpful to resist the wind load and small or moderate earthquakes, while the constant slip force prevents unpredictable force transferred into the primary structural member due to the over-strength effect. This study developed a friction damper that works in the shear direction to adapt to the deformation of coupling beams. Although it works in the shear deformation mode, the configuration is similar to those working the axial direction.

Configuration of the Friction Damper

The proposed shear-type friction damper is configured as in **Figure 1**. It is primarily composed of five parts, i.e., one T-shaped inner steel plate pasted with one piece of 2-mm-thick stainless-steel shim on each surface, two pieces of friction plates made of semi-steel friction material commonly used as the brakes, and two pieces of L-shaped outer steel plates having two restrainers at both sides to confine the friction plates from movement. The friction material contains steel fibers, resin-based material, adhesives, rubber, and asbestos. Preliminary tests on the material showed a stable friction coefficient, high-pressure resistance, small abrasion, and low friction noise. Bolt holes are placed on the flanges of the inner and outer plates through which the damper can be connected to the main structures. Two friction pairs are formed between the friction plates and the stainless-steel shims. It should be noted that although the outer plate is also contacted with the friction plate, there is no relative movement on the interface because of the restrainers. Two high-strength bolts of Grade 10.9 penetrating all plates are used to provide the contact pressure. The diameter of the high-strength bolts is 20 mm. In order to reduce the stress relaxation, six pieces of disc springs are used as the washers for each high-strength bolt, three pieces for each side. The three pieces of disc springs work in a parallel mode. There is a slot for the bolts on the web of the inner plates and the associated stainless-steel shims, because of which, the inner plate can move smoothly in the shear direction. The dampers are usually installed after the construction of the primary structure. When installing the damper, the components are first assembled by the high-strength bolts with 10–30% of the expected load. At this moment, the height of the damper shall be smaller than

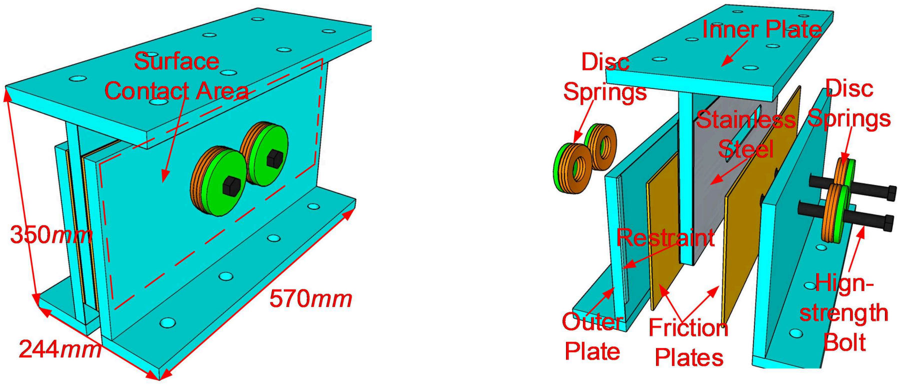

FIGURE 1 | Configuration of proposed friction damper.

the installation space. After positioning the damper, the bolts on the flanges of the inner and outer plates are securely tightened. A slight sliding in the vertical direction is allowed. Therefore, the holes in the friction plates and the slot in the inner plate shall be large enough to accommodate such slippage. Once the bolts on the flanges of the inner and outer plates are tightened, the two high-strength bolts are screwed by the torque wrench to the designed value. Two ways could be employed to achieve the design contact pressure. One is to calibrate the relationship of the pressure with respect to the torque of high-strength bolts (Cavallaro et al., 2018). The other is to relate the deformation of disc springs to the pressure, and the stiffness of the disc spring shall be verified experimentally.

Loading Setup and Measurement Scheme

In order to demonstrate the mechanical behavior of the proposed friction damper and develop an equation to predict the behavior for the design, cyclic tests were conducted. The test setup is given in **Figure 2**, where the friction damper is installed within a pin-connected loading frame. The flanges of the damper are connected to the upper and lower connectors, respectively, which are further connected to the upper and lower jigs. The upper jig is securely fixed on the bottom flange of the loading beam. To the left end of the loading beam is attached a dynamic actuator. The maximum force of the actuator is 50 tons, the stroke is 0.5 m, and the largest loading rate is 0.6 m/s. The lower jig is attached to an adapter with free adjustability in the vertical direction. With this mechanism of adapter, the high-strength bolts can be completely screwed to the design value before the installation. The adapter is fixed on the top of the foundation beam, which is securely fixed on the strong floor by eight anchor rebars with a diameter of 70 mm. The loading beam and the foundation beam are connected by two columns through four hinges. The inherent friction force provided by the loading frame can be ignored. The distance between the hinges at both ends of a column is 2.07 m. Considering the limited design stroke of the damper, 40 mm in this study, the vertical deformation introduced by the second-order effect is 0.4 mm, whose influence on the lateral behavior of the damper can be ignored.

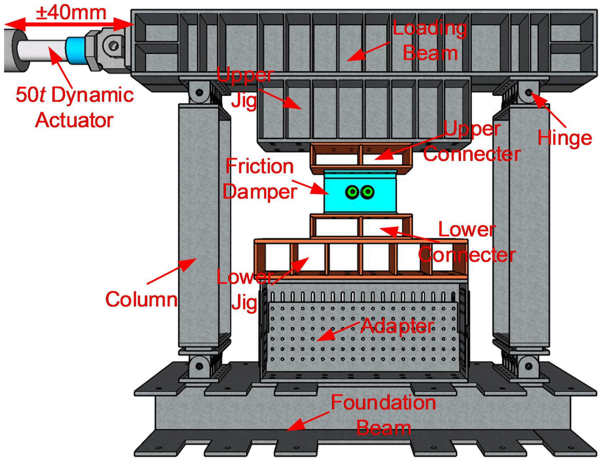

FIGURE 2 | Loading setup for the friction damper.

The loading profile adopts 100 cycles of a sine wave with an amplitude of 40 mm in the actuator. The real deformation applied on the damper might be smaller due to the deformation of the loading frame and slippage on connecting surfaces. Different loading frequencies, denoted as *f*, are adopted, i.e., 0.02, 0.1, 0.5, and 1.0 Hz. The design tensile force of M20 Grade 10.9 high-strength bolt is 155 kN. Three levels of tightening force, denoted as *P*, are designed for each high-strength bolt, i.e., 80, 120, and 140 kN. Three specimens were tested, each with different tightening forces. The loading sequence can be found in **Table 1**, where the averaged tightening force directly measured at the beginning of each test is also given.

The measurement scheme is relatively simple, as shown in **Figure 3**, where two displacement transducers are employed to measure the relative displacement between inner and outer plates, with two load cells to measure the tightening forces of high-strength bolts and one Pt100 platinum resistance thermometer to measure temperature on the contact surface. The thermometer is pasted on the back of one of the stainless-steel

TABLE 1 | Loading sequence and parameters.

Specimen no.	Load no.	Name	P_{design}/kN	P_{actual}/kN	*f*/Hz
S1	1	*P*80-*f* 0.02	80	79.5	0.02
	2	*P*80-*f* 0.1	80	82.5	0.1
	3	*P*80-*f* 0.5	80	79.0	0.5
	4	*P*80-*f* 1	80	86.0	1.0
S2	5	*P*120-*f* 0.02	120	118.0	0.02
	6	*P*120-*f* 0.1	120	97.0	0.1
	7	*P*120-*f* 0.5	120	114.5	0.5
	8	*P*120-*f* 1	120	92.0	1.0
S3	9	*P*140-*f* 0.02	140	128.5	0.02
	10	*P*140-*f* 0.1	140	144.5	0.1
	11	*P*140-*f* 0.5	140	132.5	0.5
	12	*P*140- *f*1	140	141.0	1.0

FIGURE 3 | Measurement scheme.

shims, and there is a groove cut in the web of the inner plate to host the thermometer. The force of the actuator is also synchronically measured in this measuring system.

Results

The three specimens, 12 tests in total, were loaded cyclically. Between two tests, there was a 2-h period to wait for the contact surface cooling down automatically to the room temperature.

Time Histories of Friction Forces for S2

The friction force histories, *F*, of the four tests for specimen S2 with the tightening force of 120 kN are shown in **Figures 4A–D** corresponding to the loading frequencies 0.02, 0.1, 0.5, and 1 Hz, respectively. At the smaller loading frequencies, 0.02 and 0.1 Hz, there is a small variation in the skeleton curves. After 100 cycles, the maximum force changed by 16.8 and 18.6%, respectively, for the two cases in the positive direction and 20.4 and 5.3% in the negative direction. When the loading frequency increased to 0.5 and 1 Hz, pronounced variation can be observed in the skeleton curves. For the test of 0.5 Hz, it is 50.2% in the positive direction and 49.1% in the negative direction. For the test of 1.0 Hz, they are 52.8 and 50.4% in the positive and negative directions, respectively. A similar phenomenon can be observed for the specimens S1 and S2. The reason behind this will be discussed in the section Friction Coefficient.

Hysteretic Curves

The hysteretic curves for all tests are listed in **Figure 5**, where the pictures in each row have identical frequency but different tightening forces, while those in each column have the same tightening force but different frequencies. For some tests, the connection bolts were not well fastened, and slippage occurred, such as the four tests of S3 and the test of S1 with a frequency of 0.02 Hz. From the comparison, we can also observe that the force degradation occurred if the loading frequency increased or the tightening force increased. For the tests with a loading frequency of 1 Hz, significant vibration was observed after each unloading–slipping action. One of the possible reasons is that the stuck of the contact surface was suddenly changed and the energy was released abruptly. However, details shall be examined more closely on the microscopy mechanism, which depends on the microscopic real contact area (Ar) and the compatibility of the two sliding materials (Rabinowicz, 1995; Williams, 2005; Khoo et al., 2016). When the loading direction changes, the microscopic real contact area changes, and so does the friction coefficient. Therefore, a large oscillation would occur when unloading. From these curves, the initial stiffness was also measured from each test. Generally, the initial stiffness did not change too much. The averaged initial stiffness is 286 kN/mm and the standard deviation is 11 kN/mm.

Friction Coefficient

To examine the variation of friction coefficient, the friction force corresponding to the maximum velocity or zero displacement is selected and drawn in **Figure 6**. Generally, the friction coefficients were relatively stable for the smaller loading frequencies such as 0.02 and 0.1 Hz, and significantly degraded for larger frequencies of 0.5 and 1.0 Hz. The temperature histories are also given in **Figure 6**. The degradation of friction coefficient is correlated with the increase in temperature.

Thermal–Mechanical Model

The friction coefficient is first examined at the room temperature. To avoid potential loading instability in the first cycle, the data obtained from the first three cycles are used. As shown in **Figure 7**, the friction coefficients for the 12 tests are plotted with respect to the total tightening force. The friction coefficient did not change significantly with the total tightening force. They varied between 0.361 and 0.447, and the averaged value is 0.408. Therefore, at the particular study, the contact pressure dependency can be ignored.

Several studies have regressed the friction coefficient with respect to the pressure, temperature, and the dissipated energy (Kato, 2001; Latour et al., 2014). It is found that the dissipated energy, to some extent, can reflect such micro-mechanism of contact surfaces as progressive wearing and material degradation. The correlation of the friction coefficient with the velocity and the dissipated energy is very appealing

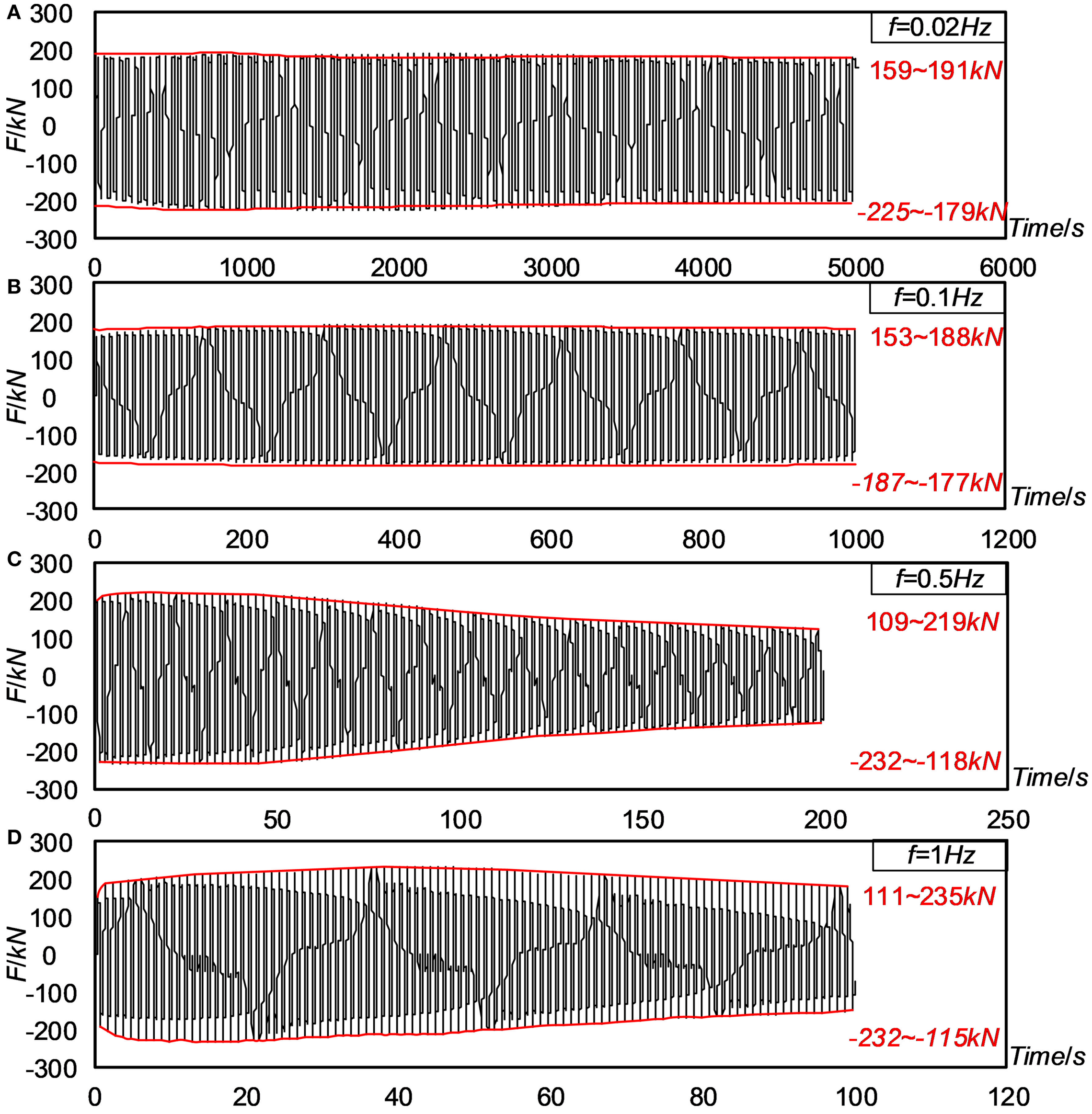

FIGURE 4 | Time histories of friction forces for S2.

because these variables can be easily obtained from the dynamic time history analysis and thus can be directly used in the design procedure.

The force of the friction damper, F, is first written as Equation (1) where P_0 is the nominal surface pressure force, and μ_{eff} is the effective friction coefficient, which is a function of dissipated energy, E_{accu}, and the nominal velocity, v_0, defined in Equation (2) where A is the nominal amplitude.

$$F = P_0 \mu_{eff} \tag{1}$$

$$v_0 = 2\pi f A \tag{2}$$

Since the surface pressure or the tightening force has limited influence on the friction coefficient, it is reasonable to take the results of S2 for the recursive analysis and use the results of S1 and S3 for the demonstration. As shown in **Figure 8A**, the friction coefficient can be expressed as a function of temperature, and the fitting function is adopted as Equation (3), where a, b, c, and d are fitting parameters and T is the measured temperature.

$$\mu_{eff} = ae^{bT} + ce^{dT} \tag{3}$$

Four sets of parameters [a, b, c, d] can be obtained at different loading frequencies. These parameters, again, can be fitted as the

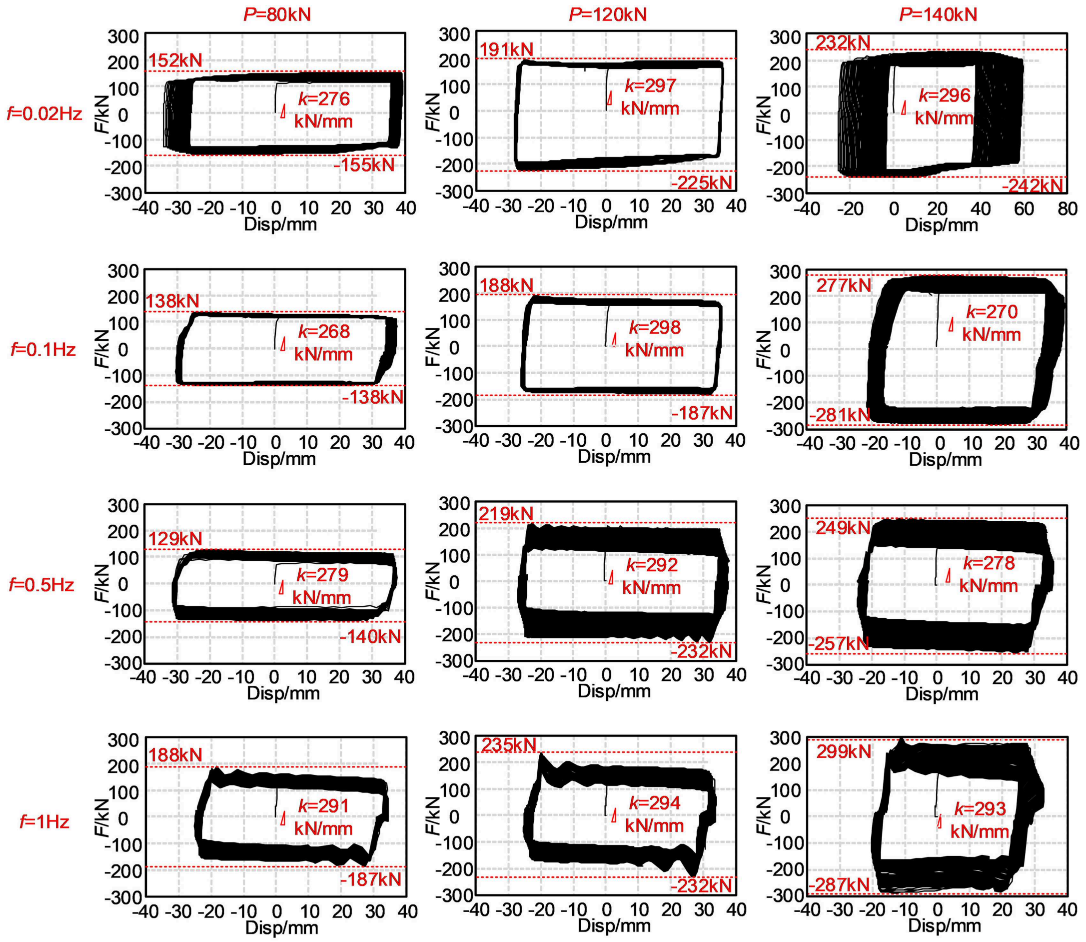

FIGURE 5 | Comparison of hysteretic curves.

functions of nominal velocity, expressed as Equations (4–7):

$$a(v_0) = p_1 v_0 + p_2 \tag{4}$$
$$b(v_0) = p_3 v_0 + p_4 \tag{5}$$
$$c = 2.0 \tag{6}$$
$$d = -0.14 \tag{7}$$

where $p_1 = 0.002518$, $p_2 = 0.3979$, $p_3 = -0.00001$, and $p_4 = 0.000255$. According to the thermodyanmics, the increase of temperature ΔT is related to the energy G, as shown in **Figure 8B**. Similar as the above procedure, Equation (8) can be recursed as:

$$G(\Delta T) = k\Delta T + l \tag{8}$$

k and l can be also expressed as the functions of the nominal velocity, as Equations (9, 10):

$$k(v_0) = q_1 \ln(v_0) + q_2 \tag{9}$$
$$l(v_0) = q_3 \ln(v_0) + q_4 \tag{10}$$

where $q_1 = 0.01329$, $q_2 = -0.00555$, $q_3 = -4.984$, and $q_4 = 12.19$. Note that the units used during the above regression procedure are kilojoule, centigrade, millimeter, and second.

To demonstrate the effectiveness of the proposed thermo-mechanical model, the above equations are applied for the cases with different tightening forces; the results are shown in **Figure 9**, and the fitting curve agrees well with the measured data for the S1 case, with all differences <5%. For S3, however, the difference is much larger. The maximum difference is 31%. The reason is that the tightening force was too big for the friction plate, and the plate was damaged during the test. The recommended pressure design value by the "Manual of design and construction for passive-controlled structure" (The Japan Society of Seismic Isolation, 2008) is 5–15 MPa. In the following hybrid coupling beam, the pressure was pre-loaded to 5 MPa.

HYBRID COUPLING BEAM INSTALLED WITH FRICTION DAMPER

Design of Specimens

The effectiveness of the friction damper is examined experimentally by a substructure test of the coupling beam.

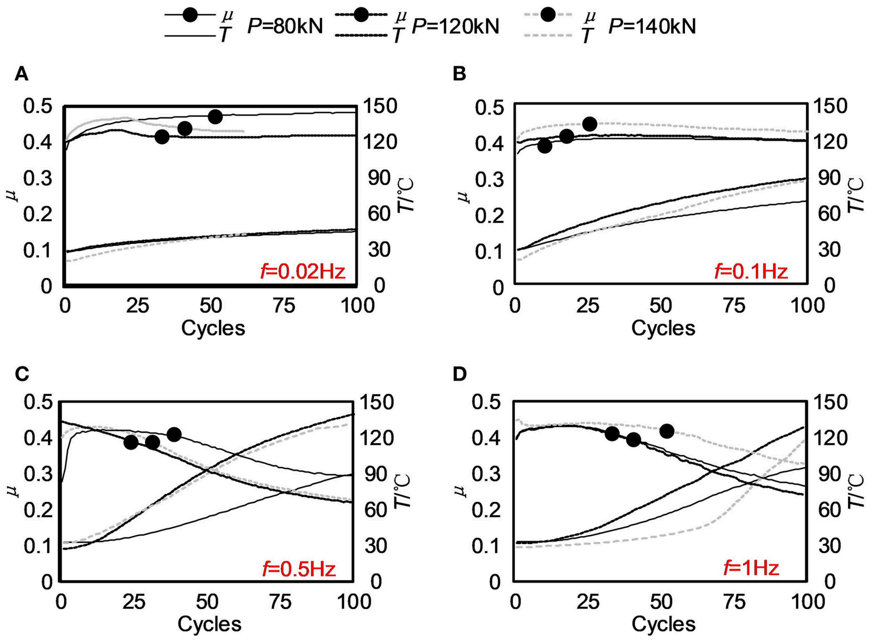

FIGURE 6 | Variation of friction coefficients: **(A)** $f = 0.02$ Hz; **(B)** $f = 0.1$ Hz; **(C)** $f = 0.5$ Hz; **(D)** $f = 1$ Hz.

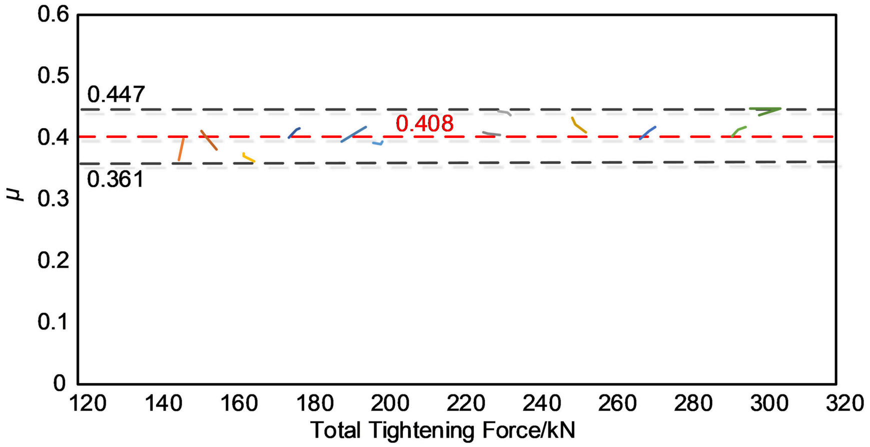

FIGURE 7 | Variation of friction coefficient with respect to total tightening force.

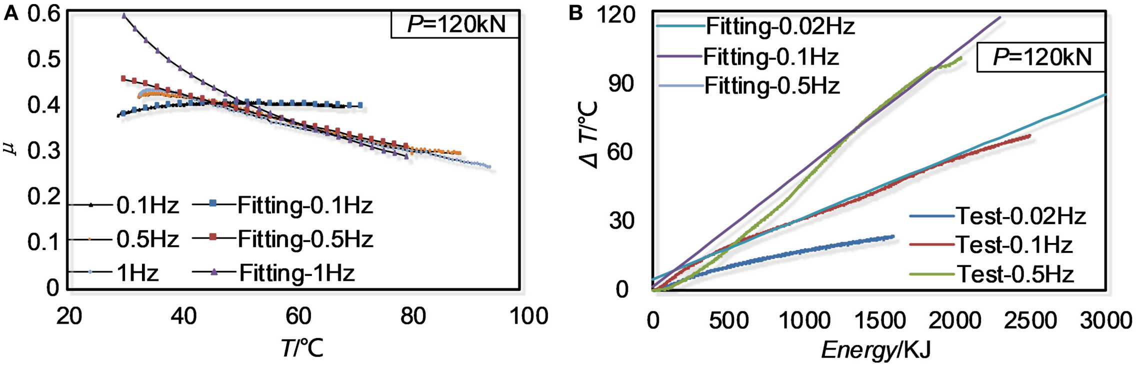

FIGURE 8 | Regression of friction coefficient using S2 data: **(A)** Friction coefficient related temperature; **(B)** Temperature incremental related to accumulated energy.

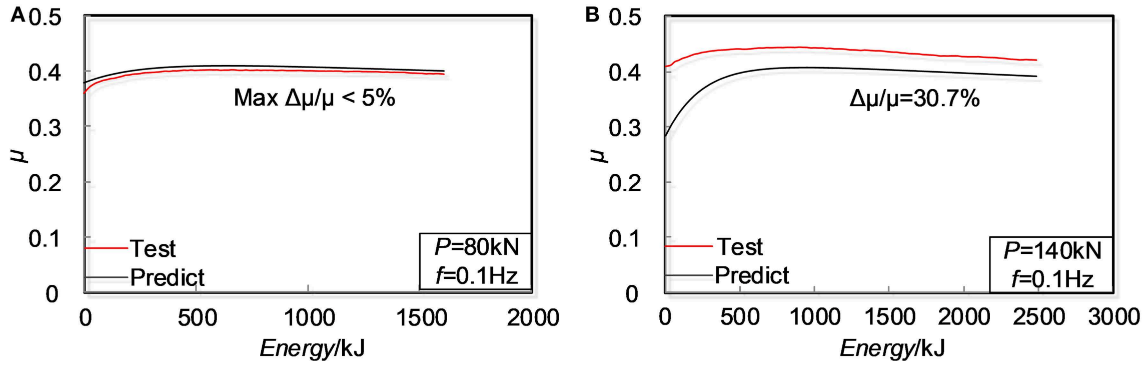

FIGURE 9 | Validation of recursive formula: **(A)** S1 at loading frequency of 0.1 Hz; **(B)** S3 at loading frequency of 0.1 Hz.

Two 2/3 scaled coupling beam specimens were designed: one being a traditional RC coupling beam and the other being a hybrid coupling beam with similar dimensions, as shown in **Figures 10A,B**, respectively. The span-to-height ratio of the RC specimen is 2, and the thickness of the slab is 70 mm. The scaled coupling beam is 240 mm thick and 675 mm high, with a span of 1,350 mm. The demands of the shear force and bending moment for the scaled model are 425.8 and 134.8 kN, respectively. The design satisfied the concrete design code and the seismic design code of China (MOHURD, 2016a,b). All longitudinal rebars in the coupling beam, boundary elements, wall limbs, slab, diagonal strut, and connection beams were HRB400, while the rest were HRB335. The concrete was C30. When fabricating the specimen, each diagonal strut was replaced by a pair of rebars because of the limited space of the scaled model, and the cover thickness was chosen as 20 mm. The anchorage length was not scaled to avoid bond slippage failure, which was 600 mm. The stiffness was calculated as 420 kN/mm.

The RC part of the hybrid coupling beam has the same design as the RC coupling beam. The friction damper was placed at the mid-span of the beam. The flanges of the friction damper were modified as the wide flange steel beams and connected the connecting beams with the same cross-section of W570 × 240 × 20 × 20 mm. Grade 10.9 high-strength bolts with a diameter of 20 mm were used to connect the damper to the connecting beams at both flanges and the web. It was supposed that a rigid connection could be realized. The steel connecting beam was welded to an end plate with a thickness of 30 mm. The end plate was embedded into the RC wall through with a 25-mm-thick steel plate to sustain the shear force and five pairs of anchorage rebars to take the bending moment. The anchorage rebars were 25 mm in diameter and 740 mm in length. The damper slip force was taken as 80% of the design value of the RC coupling beam to avoid concrete damage introduced by uncertainties of friction behavior. The connecting beam and the bolt connection were designed using 1.4 times of the damper slip force and the associated bending moment, considering the difference between static and dynamic friction coefficients. The anchor design took 2.0 times the slip force of the damper. All the steel used for the hybrid coupling beam were Q345. The design satisfied the design code of steel structures of China (MOHURD, 2017). It should be noted that the friction damper would concentrate more deformation within a much smaller span than the RC coupling beam. To avoid serious slab damage, the RC slab was separated from the steel coupling beam, and the 35-mm gap was inserted between them. However, to maintain the same architectural requirement of space, the total height of the hybrid coupling beam including the slab was not changed, and the calculated

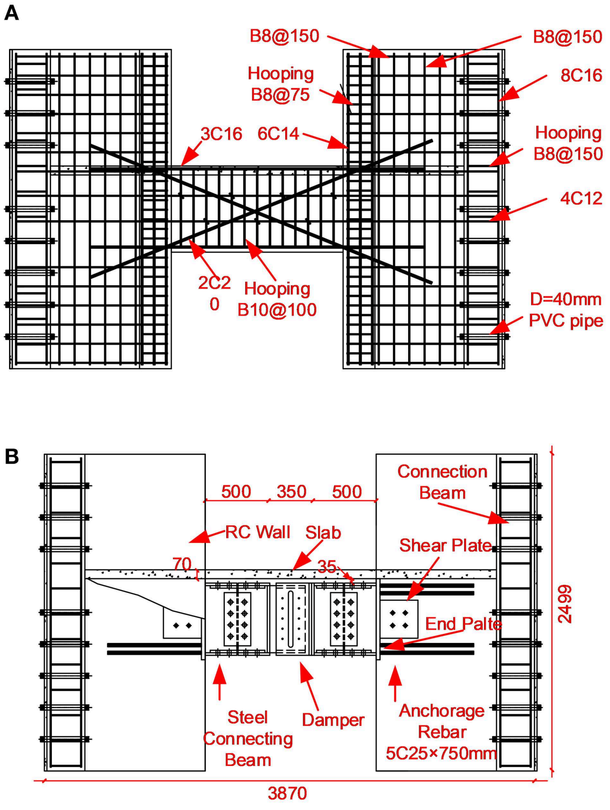

FIGURE 10 | Design of specimen: **(A)** RC coupling beam; **(B)** Hybrid coupling beam.

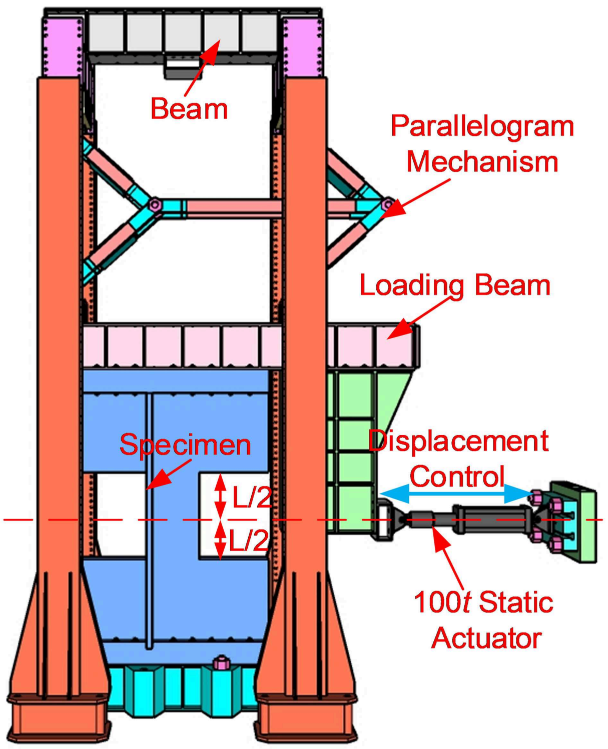

FIGURE 11 | Loading setup.

stiffness was similar to the RC coupling beam, with the difference being <5%.

Loading Setup and Measurement Scheme

The loading frame as shown in **Figure 11** was used to load the coupling beams. There are four columns and one set of beams to form the loading frame. The specimen was turned 90° for the convenience of loading, and it was securely fastened to the foundation beam, which was further fixed on the strong floor. On the top of the specimen an L-shaped loading beam was attached. The specimen was connected to the foundation beam and the loading beam by high-strength bolts, and the holes of concrete part were filled by high-strength CSV cement. This was specially designed to reduce the potential slippage of the specimen. The right bottom end of the L-shaped loading beam was attached to a 100-ton static actuator. The actuator was displacement controlled following a typical steadily increasing load profile. Several amplitudes were selected as 1/2,000, 1/1,000, 1/800, 1/500, 1/200, 1/120, 1/75, 1/50, and 1/30 of the span of the coupling beam. Two cycles were conducted at each amplitude. On the top of the loading beam, there is a parallelogram mechanism to restrain the rotation on the top of the specimen. Note that the center line of the actuator is through the mid-span of the coupling beam. This will reduce the overturning moment of the entire specimen and the idealized shear-type loading can be achieved.

Similar measurement schemes were adopted for both specimens, as shown in **Figure 12**. Horizontally, there were six displacement transducers to measure the relative deformations of the overall coupling beam, the connecting beams, and the friction damper. Vertically, there are two displacement transducers to measure the relative rotation between the wall limbs. Diagonally, there are two pairs of diagonal transducers to measure the shear deformation of steel connecting beams and the RC coupling beam. For the hybrid coupling beam, the bending deformations of steel connecting beams were also measured. Together with the transducers, the actuator force was also synchronically measured by using the same data acquisition system.

Discussion of Experimental Results

The RC coupling beam was loaded to an amplitude of 1/30. When loading in the negative direction of the first cycle, the lateral force dropped quickly from 659 to 400 kN. Because a large crack occurred in the RC wall, the loading was stopped. The hybrid coupling beam was also loaded to an amplitude of 1/30. Different from the RC coupling beam, the hybrid coupling beam survived after two cycle loadings, and the bearing force was observed to be quite stable. The loading was stopped because it almost reached the stroke of the actuator.

The hysteretic curves are shown in **Figures 13A,B** for the RC coupling beam and the hybrid coupling beam, respectively. The peak forces of the RC coupling beam are 648 and −659 kN, respectively, in the positive and negative directions. However, the design force was 426 kN. The over-strength ratio is about 1.5, which cannot be predicted without real loading. The hybrid coupling beam performed very stably. The maximum forces are 348 and −298 kN in the positive and negative direction, respectively. Due to the asymmetry of the loading device, the forces in the positive and negative directions are inconsistent, and the curve is asymmetrical. Considering the design value, 341 kN, the maximum difference is 12.6%. The hysteretic curve of the friction damper is also given in **Figure 13B**. It can be observed that most energy was dissipated by the damper.

As plotted in **Figure 14**, the deformation of coupling beam ($D_2 - D_1$) is compared with the deformation of damper ($D_5 - D_4$). At an amplitude smaller than 1/120, the friction damper almost did not move. At this stage, a large stiffness is helpful to limit the horizontal deformation of a building. With the loading increasing, at an amplitude of 1/120, the damper took larger than 50% of the overall deformation, and it took more than 80% deformation at an amplitude of 1/30. On the one hand, the damper dissipated more energy and the lateral response would be reduced. On the other hand, the deformation of the primary structure decreased, and the damage would be mitigated. As shown in **Figure 15**, the RC coupling beam suffered significant damage in the coupling beam and the wall. The longest crack was over 1 m and the maximum width was larger than 20 mm. It is very difficult to repair. The RC part of the hybrid coupling beam, however, was damaged slightly. The width of the largest crack was <0.2 mm. Upon unloading, the crack closed. It almost did not have any effect and was thus deemed repair-free or seismic-resilient.

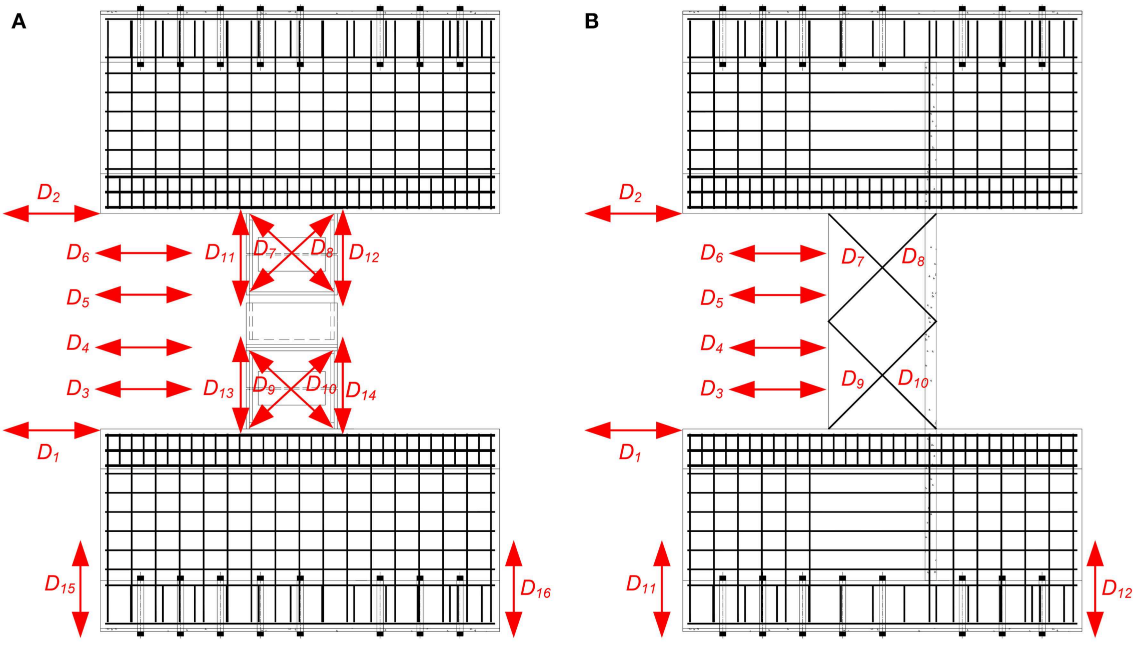

FIGURE 12 | Measurement scheme: **(A)** RC coupling beam; **(B)** Hybrid coupling beam.

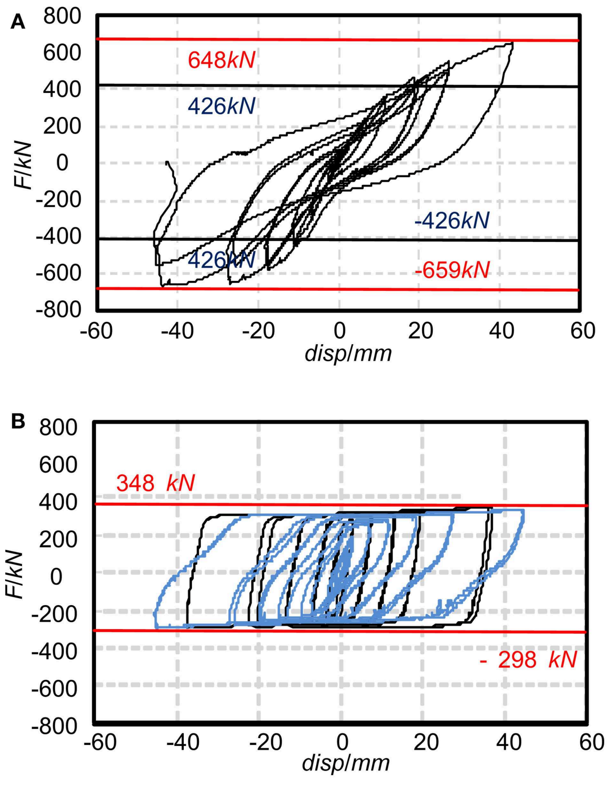

FIGURE 13 | Hysteretic curves: **(A)** RC coupling beam; **(B)** Hybrid coupling beam.

CONCLUSIONS

This study proposed a hybrid coupling beam installed in a friction damper using semi-steel friction material. Damage controllability and energy dissipation capacity are significantly improved. To comprehensively demonstrate its effectiveness, a set of experiments on the damper and the hybrid coupling beam were conducted quasi-statically and cyclically. The major findings are as follows:

(1) Significant temperature-dependent behavior was observed on the friction damper. Although at the smaller loading rate, the damper behaved quite stable, force degradation was observed at the faster loading. When the loading rate is slow, the heat generated by the friction radiates quickly to the surrounding environment, and the temperature will not significantly increase. However, if the loading rate is very high, the heat accumulates in the damper, and the physical characteristics of the contact surface change, then the friction coefficient drops.

(2) A practical thermo-mechanical model was regressed from the test data. The nominal surface pressure was used, and the friction coefficient was related to the energy and speed that can be obtained directly from the time history analysis. However, the physical meaning of some parameters is not clear and was calibrated with limited data. The accuracy shall be further improved. Moreover, the parameters are dependent on the configuration of the damper. Before any application, it is necessary to calibrate them through the test.

(3) The proposed hybrid coupling beam is configured with steel connecting beams, embedded steel plates, and a friction damper. All connection parts shall be designed considering the

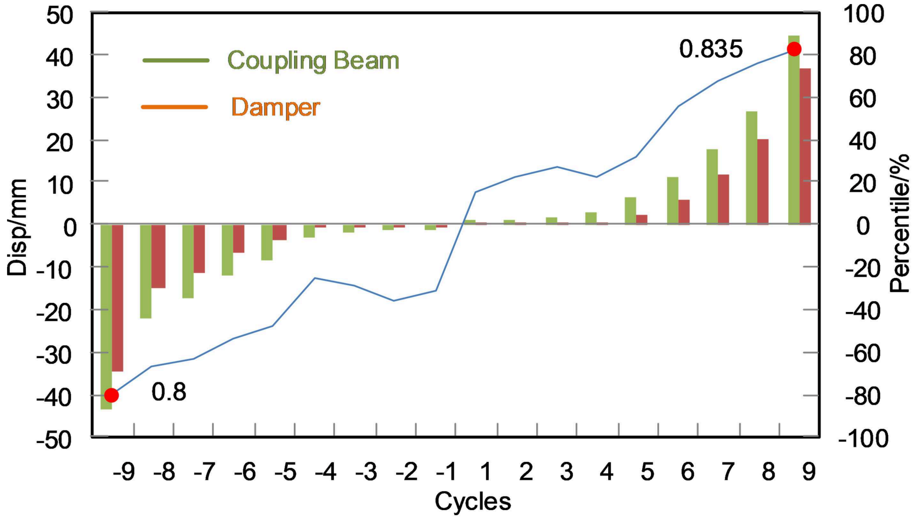

FIGURE 14 | Proportional deformation of dampers over the total lateral deformation.

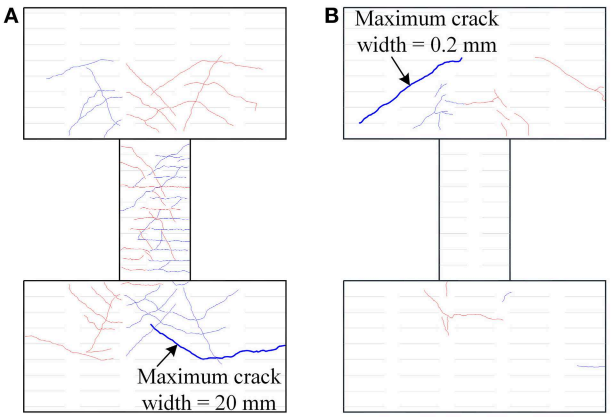

FIGURE 15 | Comparison of crack patterns: **(A)** RC coupling beam; **(B)** Hybrid coupling beam.

over-strength introduced by the friction coefficient variation. In this study, the connections worked well without any premature failure. The proposed hybrid coupling beam using a friction damper performed a larger energy dissipation capacity and better damage controllability than the traditional RC coupling beam.

The experimental results are reported in this study together with the thermo-mechanical model developed for the friction damper. However, this is a preliminary study. More studies are required to provide a theoretical basis for the thermo-mechanical model that needs to be further extensively examined. Moreover, the application of the thermo-mechanical model in the numerical analysis shall be elaborated, and the design procedures need to be developed. These issues will be resolved in future studies.

DATA AVAILABILITY

The raw data supporting the conclusions of this manuscript will be made available by the authors, without undue reservation, to any qualified researcher.

AUTHOR CONTRIBUTIONS

TW developed the hybrid coupling beam and set up the test program. FY conducted the two tests on hybrid coupling beam. XW conducted the tests on dampers. YC developed the thermo mechanical model of the damper.

FUNDING

This work was supported by the National Key Research and Development Program of China (2017YFC1500701), the Scientific Research Fund of Institute of Engineering Mechanics, CEA (2017A02), and the National Natural Science Foundation of China (51378478 and 51678538).

REFERENCES

Ahn, T. S., Kim, Y. J., and Kim, S. D. (2013). Large-scale testing of coupled shear wall structures with damping devices. *Adv. Struct. Eng.* 16, 1943–1955. doi: 10.1260/1369-4332.16.11.1943

Aiken, I. D., Nims, D. K., Whittaker, A. S., and Kelly, J. M. (1993). Testing of passive energy dissipation system. *Earthquake Spectra* 9, 335–370. doi: 10.1193/1.1585720

Cavallaro, F. G., Latour, M., Francavilla, B. A., Piluso, V., and Rizzano, G. (2018). Standardized friction damper blot assemblies time-related relaxation and installed tension variability. *J. Constr. Steel Res.* 141, 145–155. doi: 10.1016/j.jcsr.2017.10.029

Cheng, M. Y., Fikri, R., and Chen, C. C. (2015). Experimental study of reinforced concrete and hybrid coupled shear wall systems. *Eng. Struct.* 82, 214–225. doi: 10.1016/j.engstruct.2014.10.039

Filiatrault, A., Tremblay, R., and Kar, R. (2000). Performance evaluation of friction spring seismic damper. *J. Struct. Eng. ASCE* 126, 491–499. doi: 10.1061/(ASCE)0733-9445(2000)126:4(491)

Fortney, P. J., Shahrooz, B. M., and Rassati, G. A. (2007). Large-scale testing of a replaceable "fuse" steel coupling beam. *J. Struct. Eng. ASCE* 133, 1801–1807. doi: 10.1061/(ASCE)0733-9445(2007)133:12(1801)

Gurunath, P. V., and Bijwe, J. (2007). Friction and wear studies on brake-pad materials based on newly developed resin. *Wear* 263, 1212–1219. doi: 10.1016/j.wear.2006.12.050

International Code Council (ICC) (2015). *International Building Code*. US.

Jang, H., Ko, K., Kim, S. J., Basch, S. J., and Fash, J. W. (2004). The effect of metal fibers on the friction performance of automotive brake friction materials. *Wear* 256, 406–414. doi: 10.1016/S0043-1648(03)00445-9

Ji, X. D., Wang, Y., Ma, Q., and Okazaki, T. (2017). Cyclic behavior of replaceable steel coupling beams. *J. Struct. Eng. ASCE* 143, 231–241. doi: 10.1061/(ASCE)ST.1943-541X.0001661

Kato, N. (2001). Effect of frictional heating on pre-seismic sliding: A numerical simulation using a rate-, state- and temperature-dependent friction law. *Geophys. J. Int.* 147, 183–188. doi: 10.1046/j.0956-540x.2001.01531.x

Khoo, H. H., Clifton, C., Butterworth, J., MacRae, G., and Ferguson, G. (2016). Influence of steel shim hardness on the Sliding Hinge Joint performance. *J. Constr. Steel Res.* 72, 119–129. doi: 10.1016/j.jcsr.2011.11.009

Latour, M., Piluso, V., and Rizzano, G. (2014). Experimental analysis on friction materials for supplemental damping devices. *Constr. Build. Mater.* 65, 159–176. doi: 10.1016/j.conbuildmat.2014.04.092

Lee, C. H., Ryu, J., Oh, J., Yoo, C. H., and Ju, Y. K. (2016). Friction between a new low-steel composite material and milled steel for SAFE dampers. *Eng. Struct.* 122, 279–295. doi: 10.1016/j.engstruct.2016.04.056

Loo, Y. W., Quenneville, P., and Chouw, N. (2014). A new type of symmetric slip-friction connector. *J. Constr. Steel Res.* 94, 11–22. doi: 10.1016/j.jcsr.2013.11.005

Lu, X. L., Chen, Y., and Jiang, H. J. (2013). Experimental study on seismic behavior of "Fuse" of replaceable coupling beam. *Nat. Sci.* 41, 1318–1325. doi: 10.3969/j.issn.0253-374x.2013.09.007

Mao, C. X., Wang, Z. Y., and Zhang, L. Q. (2012). "Seismic performance of RC frame-shear wall structure with novel shape memory alloy dampers in coupling beams," in *15 WCEE, Paper ID: 4988*, Lisbon. doi: 10.1117/12.917304

Ministry of Housing and Urban-Rural Development of the People's Republic of China (MOHURD) (2016a). *Code for Seismic Design of Buildings (GB 50011-2016)*. Beijing: China Architecture and Building Press.

Ministry of Housing and Urban-Rural Development of the People's Republic of China (MOHURD) (2016b). *Code for Design of Concrete Structures (GB 50010-2016)*. Beijing: China Architecture and Building Press.

Ministry of Housing and Urban-Rural Development of the People's Republic of China (MOHURD) (2017). *Code for Design of Steel Structures (GB 50017-2016)*. Beijing: China Architecture and Building Press.

Montgomery, M. S., and Christopoulos, C. (2015). Experimental validation of viscoelastic coupling dampers for enhanced dynamic performance of high-rise buildings. *J. Struct. Eng. ASCE* 141:04014145. doi: 10.1061/(ASCE)ST.1943-541X.0001092

Mualla, H. I., and Belev, B. (2002). Performance of steel frames with a new friction damper device under earthquake excitation. *Eng. Struct.* 24, 365–371. doi: 10.1016/S0141-0296(01)00102-X

Pall, A. S., and Marsh, C. (1982). Response of friction damped braced frames. *ASCE J. Struct. Div.* 108, 1313–1323.

Rabinowicz, E. (1995). *Friction and Wear of Materials*. 2nd ed. New York, NY: Wiley.

Teng, J., Ma, B. T., Li, W. H., Zhang, H., and Cao, D. X. (2010). Pseudo-static test for coupling beam damper of coupled shear wall structure. *J. Build. Struct.* 31, 92–100. doi: 10.14006/j.jzjgxb.2010.12.012

The Japan Society of Seismic Isolation (2008). *Manual of Design and Construction for Passive-Controlled Structure*. Tokyo, 527-—530.

Wang, Y. Y. (2008). Lessons learnt from building damages in the Wenchuan earthquake: seismic concept design of buildings. *J. Build. Struct.* 29, 20–25.

Williams, J. A. (2005). *Engineering Tribology*. New York, NY: Cambridge University Press. doi: 10.1017/CBO9780511805905

Xu, Y. L., and Ng, C. L. (2008). Seismic protection of a building complex using variable friction damper: experimental investigation. *J. Eng. Mech. ASCE* 134, 637–649. doi: 10.1061/(ASCE)0733-9399(2008)134:8(637)

Xu, Z. D. (2007). Earthquake mitigation study on viscoelastic dampers for reinforced concrete structures. *J. Vib. Control* 13, 29–45. doi: 10.1177/1077546306068058

Xu, Z. D., Liao, Y. X., Ge, T., and Xu, C. (2016). Experimental and theoretical study on viscoelastic dampers with different matrix rubbers. *J. Eng. Mech. ASCE* 142:04016051. doi: 10.1061/(ASCE)EM.1943-7889.0001101

Ye, L. H., Qu, Z., He, S. W., Zhu, W. C., and Hou, H. T. (2018). Experimental study on uniaxial mechanical properties of brake pad-type friction damper. *China Civil Eng. J.* 51, 70–75. doi: 10.15951/j.tmgcxb.2018.07.008

Yun, R. P., Filip, P., and Lu, Y. F. (2010). Performance and evaluation of eco-friendly brake friction materials. *Tribol. Int.* 43, 2010–2019. doi: 10.1016/j.triboint.2010.05.001

Conflict of Interest Statement: The authors declare that the research was conducted in the absence of any commercial or financial relationships that could be construed as a potential conflict of interest.

frontiers
in Materials

ORIGINAL RESEARCH
published: 05 March 2019
doi: 10.3389/fmats.2019.00033

Mechanical Model of a Hybrid Non-linear Viscoelastic Material Damping Device With Its Verifications

Ying Zhou, Peng Chen and Shunming Gong*

State Key Laboratory of Disaster Reduction in Civil Engineering, Tongji University, Shanghai, China

This paper proposes a new viscoelastic (VE) material damping device with hybrid non-linear properties. Compared with traditional linear material dampers, the new non-linear VE material damping device is characterized by its better energy dissipation and deformation capability. The series performance tests of the VE device are conducted, based on which the sources and variation law of material non-linearities are analyzed. Five aspects of material non-linearities are summarized, including the shape change of hysteresis loop caused by phase difference, the initial stiffness caused by large loading rate, the softening effect caused by high temperature and fatigue, and the softening and stiffening effect under large strain deformation. A mechanic model for this device is proposed which considers multiple non-linear effects of the material. For the verifications of the proposed mechanic model, a shaking table test on a steel frame equipped with the new VE devices is designed and performed. Based on the proposed mathematic mechanic model, the numerical mechanic model is implemented in the OpenSees software. The accuracy of the mechanic model is firstly verified by comparing the performance tests data with the simulation results. Then the numerical model is also used to calculate the time history response of the shake table tested steel frame under earthquake loading. It is concluded that the mechanic model can well-depict several non-linear material behaviors of the new VE device, and the corresponding numerical model created in the open source calculation platform is reliable to be used to calculate non-linear time history response of a structure equipped with the new VE material damping devices.

Keywords: viscoelastic material, hybrid non-linearity, mechanic model, non-linear analysis, shake table test

Edited by:
Zhao-Dong Xu,
Southeast University, China

Reviewed by:
Peng Pan,
Tsinghua University, China
Ionut Ovidiu Toma,
Gheorghe Asachi Technical University of Iasi, Romania

****Correspondence:***
Ying Zhou
yingzhou@tongji.edu.cn

Specialty section:
This article was submitted to Structural Materials, a section of the journal Frontiers in Materials

Received: *24 November 2018*
Accepted: *14 February 2019*
Published: *05 March 2019*

Citation:
Zhou Y, Chen P and Gong S (2019) Mechanical Model of a Hybrid Non-linear Viscoelastic Material Damping Device With Its Verifications. Front. Mater. 6:33. doi: 10.3389/fmats.2019.00033

INTRODUCTION

The viscoelastic (VE) damper is one of the most popular passive energy dissipation devices for building structures under earthquake and wind disasters. In 1969, the VE damper was firstly used in the New York World Trade Center for wind-induced vibration control (Mahmoodi et al., 1987). After that, the VE dampers began to be used in the seismic design for buildings. In 1993, the VE dampers were used in seismic design for a 13-story steel frame retrofit project (Crosby et al., 1994). Since then, increasing research attentions have been paid on this topic, the VE damping devices have been investigated for vibration control of different types of structures including concrete building, steel building, prefab building, wood structure, bridge, base isolated structures, etc. (Samali and Kwok, 1995; Soong and Spencer, 2002; Xu et al., 2003a, 2011, 2013; Molinera et al., 2012; Wu et al., 2015; Gong et al., 2017).

With the fast development of viscoelastic damping material, VE damping devices with better energy dissipation and deformation capacity have been proposed. The better performance devices are always characterized by complex non-linear properties. By the stress-strain relation, the VE dampers can be categorized into four types: the linear, softening, hardening, and hybrid non-linear type (Gong and Zhou, 2017). For the linear type device, the mechanic properties are strain independent if the temperature influence is not included (Lai et al., 1996). The stiffness of the softening and hardening type devices will decrease and increase, respectively, with larger strain. In addition to these, this paper reveals a new type of VE damping device containing both softening and hardening effects which are defined as hybrid non-linearity.

Many previous studies have been investigating the working performance of the VE damping devices. Chang et al. (1992, 1995) and Lai et al. (1995) conducted extensive performance tests and a small scaled shake table test on a five-story steel frame with the linear VE dampers. The results prove that the VE damping devices can have a significant earthquake control effect and the mechanic behavior of the device can be well-represented using effective linear stiffness and effective damping. Xu et al. (2003b, 2004) and Xu (2009) experimentally investigated the effect of the VE dampers on a reinforced concrete building. It is concluded that the earthquake mitigation effect is significant, especially for the floor acceleration and displacement reduction. Another conclusion is that the control effect for higher frequency input is superior to lower frequency.

For non-linear VE damping devices, the investigations are fundamentally based on tests and also focus on the mechanic models which can depict the complex mechanic behavior of non-linear VE dampers. Aiken et al. (1993) studied on softening VE dampers, and the frequency dependent property of the VE dampers is summarized based on the tests. Yokota et al. (1992) conducted a comparison study between models with and without non-linear VE damping devices. It is concluded that the seismic mitigation effect for floor displacement is significant but the effect on floor shear force reduction is limited and the main seismic reduction effect comes from the additional damping. Xu et al. (2016) proposed an equivalent higher-order fractional derivative model which takes into account the temperature effects and frequency-dependent character of the non-linear VE devices with different matrix rubbers. Ghaemmaghami and Kwon (2018) proposed an extended recursive parameter model to simulate the frequency-, strain- and temperature-dependent properties of non-linear VE damper and the simulation results can better depict the experiment behavior compared with traditional Kelvin-Voigt model. The investigations on the hardening type device are limited. (Dall'Asta and Ragni, 2006) conducted performance tests on a type of high damping rubber material,

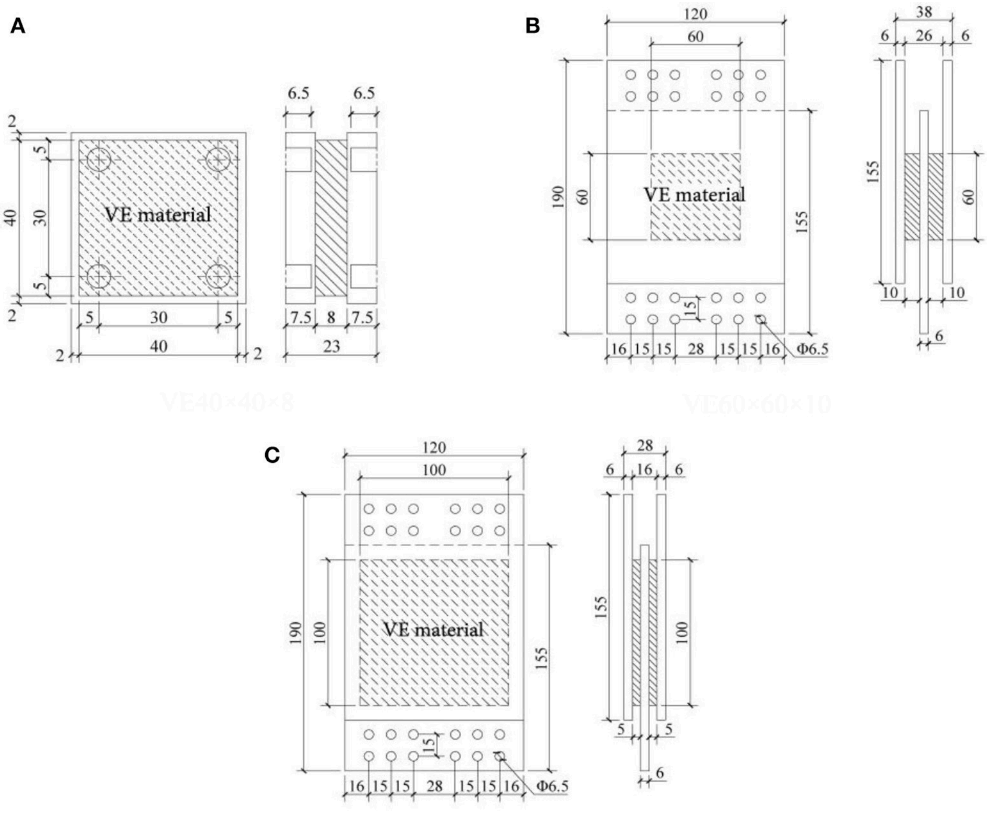

FIGURE 1 | Diagram of the different type of test specimens of **(A)** type "VE40 × 40 × 8," **(B)** type "VE60 × 60 × 10" and **(C)** type "VE100 × 100 × 5".

and the material shows a significant stiffen character. Pant et al. (2018) performed a full-scale test of a viscoelastic damper, and the accuracy of four different macroscopic numerical models are discussed. Results reveal that different models are suitable for modeling VE damping devices under different loading conditions.

According to the above literature review, we still lack enough knowledge of the non-linear sources and laws of non-linearities. Many experiment phenomenon cannot have convincible explanations, and few mechanic models can accurately depict the mechanic behavior of VE damping device with multiple non-linear mechanic behaviors or hybrid non-linearities coexisting in VE damping devices.

This paper introduces a VE damping device using new viscoelastic material. The main components of the material are natural rubber, damping agent, and antioxygen. The new damping device is characterized by its hybrid non-linearities which can have a better energy dissipation and deformation capacity, and it is supposed to have a better seismic reduction effect compared with linear type devices. Based on the analysis of the different sources of non-linearities, a new mathematic mechanic model which considers multiple non-linear behaviors is proposed. The results of performance tests are compared with the theoretical curves to validate the model. Then, a shake table test on a steel frame with new VE damping devices is conducted, and a discrete numerical model is created in an open source computing platform to calculate the time history response of the tested model. By comparing the shake table test and numerical simulation results, the remarkable seismic control effect of the new VE damping device is proved, and also the accuracy of the mechanic model is verified.

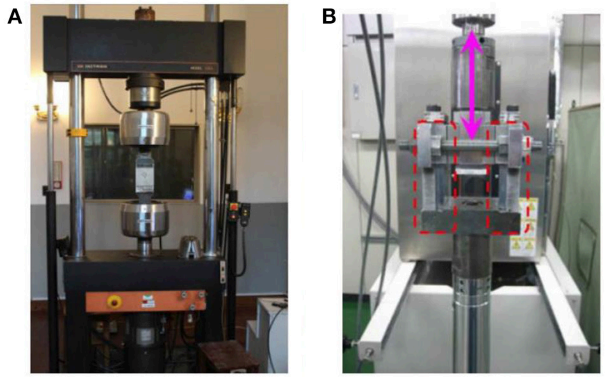

FIGURE 2 | Testing facilities of **(A)** performance tests and **(B)** performance tests under different temperatures.

PERFORMANCE TESTS

Three different types of hybrid non-linear VE dampers are tested, numbered as “VE40 × 40 × 8,” “VE100 × 100 × 5,” and “VE60 × 60 × 10.” The size and configuration of the three different types of specimens are shown in **Figure 1**. The performance tests were performed at the State Key Laboratory of Disaster Reduction in Civil Engineering of Tongji University. The testing facilities are shown in **Figure 2A**. The “INSTRON” tension-compression loading device is used to perform harmonic displacement-control loading process. The range of loading frequency is 0.1–6.0 Hz, and the strain deformation is 50–400%. The temperature related performance tests were conducted at General Building Research Corporation of Japan. The testing picture is shown in **Figure 2B**. The variation of temperature is between −20 and 60°C. The loading scheme is listed in **Table 1**. A single specimen of different damper sizes are used for each test case.

Figure 3 presents typical hysteresis curves from the performance tests. Based on the hysteresis results, significant characters are concluded as (a) The stiffness and damping of the VE damper decrease with the increase of deformation, but the stiffness begins to increase under larger strain (≥200%); (b) The device presents a large initial stiffness for the loading process of the first cycle; (c) The performance of the damper significantly deteriorate with more loading cycles. After the hysteresis loading of 30 cycles, the damper remains intact and effective; (d) The mechanic behavior of the damper is nearly independent of the loading frequency; (e) The maximum stress of the damper is

TABLE 1 | The loading scheme of the mechanic performance test.

Contents	Frequency (Hz)	Strain amplitude (%)	Cycles	Damper size
Different strain amplitude	0.1	50, 100, 110, 120, 130, 140, 150, 180, 200, 250, 300	5	VE60 × 60 × 10 VE100 × 100 × 5
Different loading frequencies	0.25, 0.50, 0.75, 0.85, 1.00, 1.50, 2.00, 2.50, 3.00, 3.50, 4.00, 4.50, 5.00, 6.00	100	5	VE60 × 60 × 10 VE100 × 100 × 5
Ultimate test	0.1	400	5	VE100 × 100 × 5
Fatigue test	0.1	100	30	VE60 × 60 × 10
Temperature relevant test (−20/0/20/30/40/60°C)	0.1	100	5	VE40 × 40 × 8

dependent on the environment temperature, based on the fitting of test results, the relation expression is given as

$$\tau_0(\theta) = 0.2823{+}0.8574\mathrm{e}^{-0.0313\theta} \tag{1}$$

τ_0 is the maximum stress in damper, θ is the temperature (°C). The variations of the damper behavior under different temperatures are shown in **Table 2**.

SOURCES AND LAWS OF NON-LINEARITIES

The non-linear behaviors of the new VE damping device are obvious and comprehensive which is affected by many factors. Based on the performance tests, five sources of material non-linearity are summarized as phase different, initial stiffness, softening under repeated loading, softening under great strain, and stiffening under considerable strain.

Non-linearity Caused by the Variation of Phase Difference

For viscoelastic damping devices, the phase difference exists between the strain and the stress which essentially creates the hysteresis loops of the stress-strain relation. Under harmonic displacement control loading, the strain deformation of the VE damper $\gamma(t) = \gamma_o \sin \omega t$, and the stress response$\tau(t) = \tau_0 \sin(\omega t + \delta)$. The stress-strain relation meets the elliptic equation. However, for linear type VE damper, the phase difference δ is a constant value. In contrast, for this new non-linear VE damping device, the phase difference $\delta(t)$ varies with time which can cause the shape change of the hysteresis loop.

A more complicated stress response is observed for the non-linear VE damper. The phase difference of the non-linear damper in one period (the duration of one single harmonic loading period) under different strain amplitude is presented in **Figure 4**. It clearly shows that the phase difference periodically changes with time. The basic reasons are the ultra-harmonic response caused by the stiffness non-linearity. Another

TABLE 2 | Mechanic parameters of the VE damping device under different temperatures.

Temperatures (°C)	Maximum stress τ_0(MPa)	Effective viscous damping ratio (%)
−20	1.894	31.7
0	1.106	33.1
10	0.917	34.5
20	0.746	34.5
30	0.638	34.5
40	0.547	34.2
60	0.386	34.0

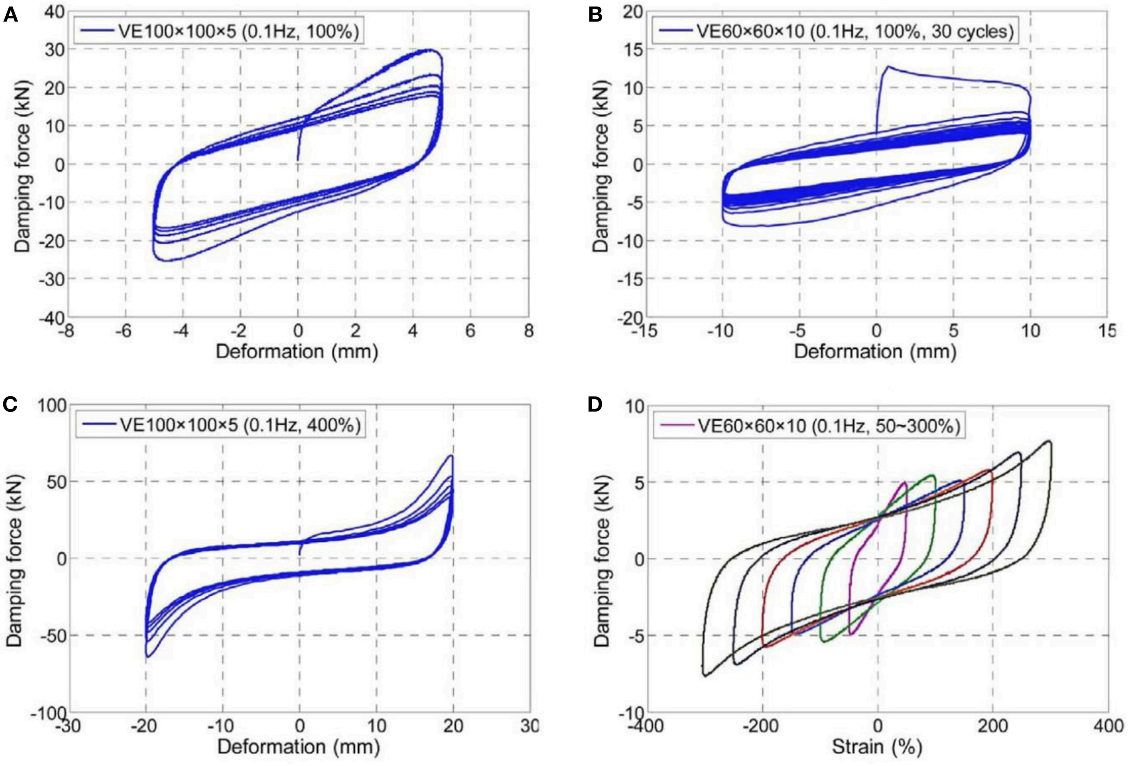

FIGURE 3 | Performance test results of **(A)** typical hysteresis curve, **(B)** fatigue test, **(C)** ultimate strain test, and **(D)** different strain amplitude tests.

interesting observation is that the phase variation amplitude is strain related. The phase change is more drastic under high strain situation (strain amplitude exceeds 200%). The reason is that when the strain goes large, the stiffening effect becomes significant, which would cause more strong ultra-harmonic components in the response.

Initial Stiffness

Figure 3B shows that there is a large initial stiffness in the first cycle due to the sudden increase of the loading frequency (from static to dynamic excitation). If the additional VE devices are not well-designed, the dampers will not generate hysteretic deformation which means the dampers provide only stiffness but no additional damping under this situation. The control effect will be limited if the dampers are not activated. Nevertheless, the problem of the initial stiffness only occurs in the first loading cycle and can be easily overcome by appropriate design. Generally, for the seismic design of buildings, the initial stiffness of VE damper can be ignored if the dampers go through plastic deformation under seismic loading.

Softening Caused by Temperature Rise and Fatigue

The previous study (Lai et al., 1996) concluded that one primary source of non-linearity of VE dampers comes from the temperature effect in the viscoelastic material. Based on this, for the design and analysis of the structures with VE dampers, identical mechanic parameters with temperature correction are used for a large variation range of temperature. The VE material will inevitably subject to temperature rise and fatigue simultaneously under the cyclic loading.

For the new VE damping device, the fatigue tests are conducted using the "VE60 × 60 × 10" specimens. For each testing specimen, 30 loading cycles are conducted. **Figure 5** presents the degradation law of different mechanic parameters. Results present that with the increase of the loading cycles, the storage shear modulus, and the loss shear modulus will significantly drop at the first few cycles, but the decrease slows down for the after cycles. Only a slight decrease is observed for the loss factor. For the whole loading process, the effective viscous damping ratio is about 30%. The damping ratio is almost half of the loss factor which is in agreement with linear VE dampers. The definition of the three mechanic parameters are given as,

$$G' = F_1 h / nAu_0 \tag{2}$$

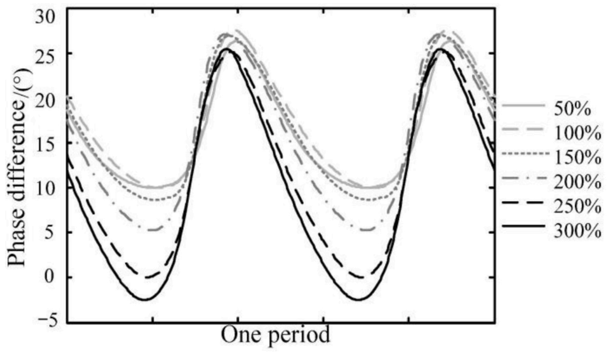

FIGURE 4 | Phase difference comparison in one period.

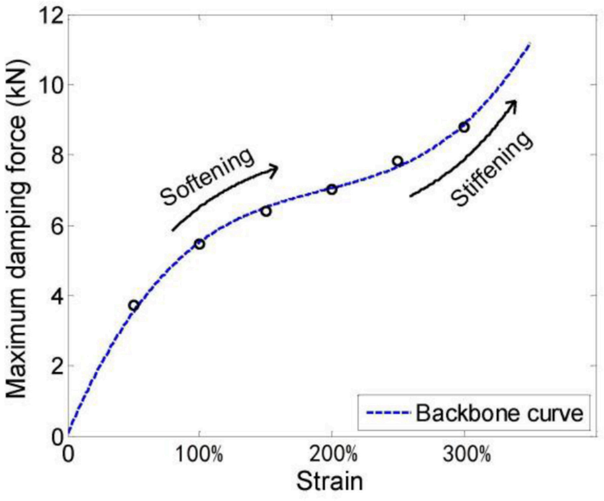

FIGURE 6 | Backbone curve.

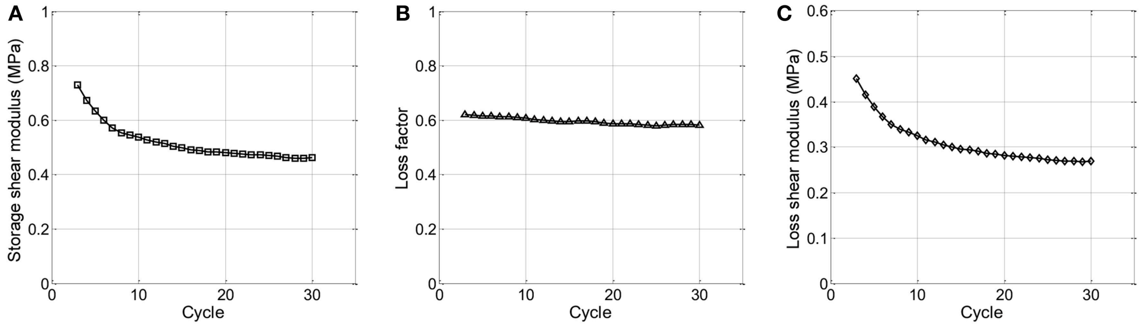

FIGURE 5 | Performance degradation law under cyclic loading on **(A)** storage shear modulus, **(B)** loss factor, and **(C)** loss shear modulus.

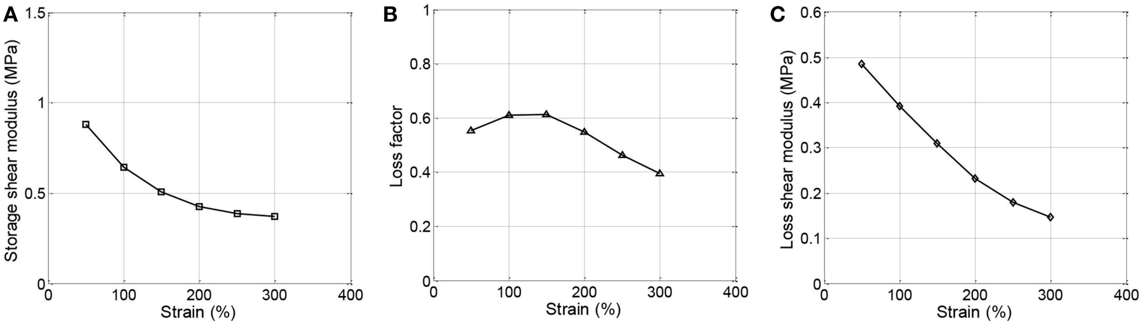

FIGURE 7 | Softening effect on the mechanic parameters of **(A)** Storage shear modulus, **(B)** loss factor, and **(C**) loss shear modulus.

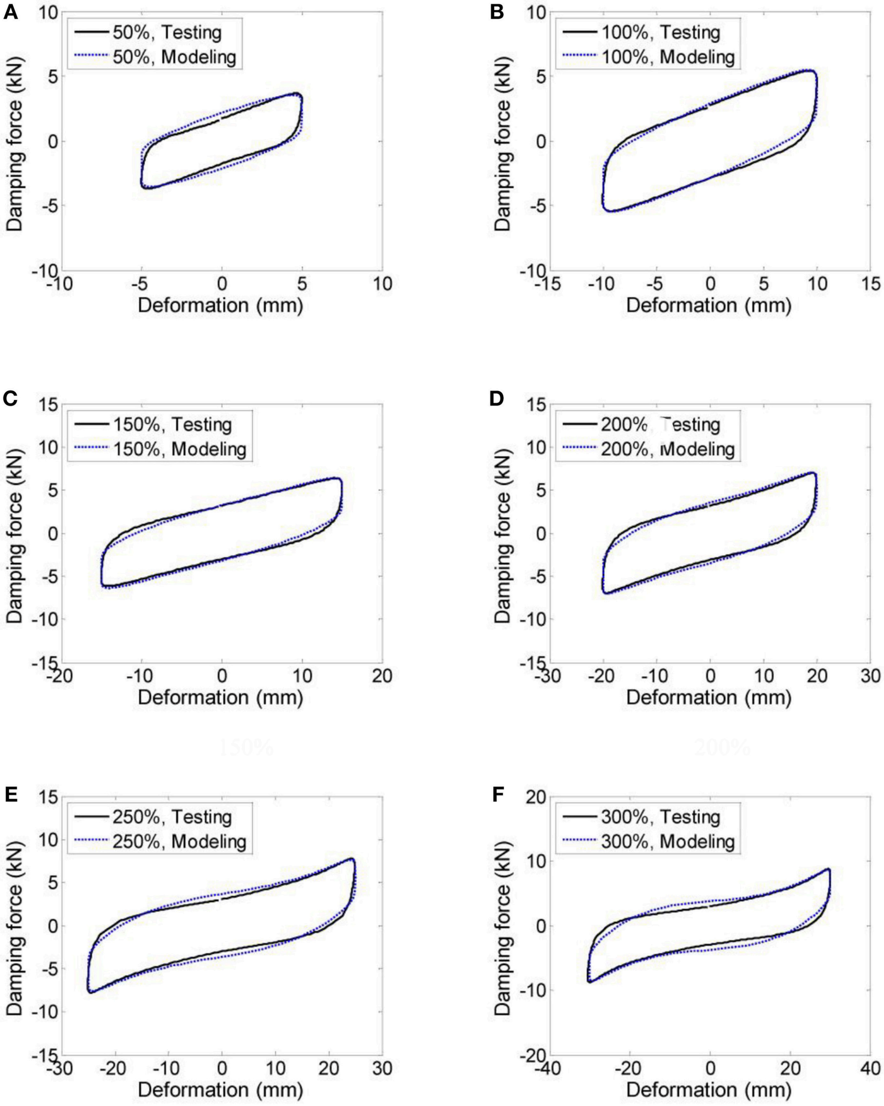

FIGURE 8 | Comparison between the mechanic model and the performance test hysteresis loop (VE60 × 60 × 10) under strain deformation of **(A)** 50%, **(B)** 100%, **(C)** 150%, **(D)** 200%, **(E)** 250%, and **(F)** 300%.

$$\eta = F_2/F_1 \tag{3}$$

$$G'' = \eta G' \tag{4}$$

where the G', η , and G'' are the storage shear modulus, loss factor and loss shear modulus. $F_1$and F_2 are the damping force correlate to the maximum shear deformation u_0 and no shear deformation, respectively. h, n, and A are the height, number of layers and area of the damping material.

Softening and Stiffening Caused by Large Strain

The softening and stiffening effect of the new VE damping device is illustrated in **Figure 6**. The maximum damping force under different strain deformation is plotted in this backbone curve. It is shown that the stiffness will decrease first with the increase of the strain, then the stiffness begins to increase as the strain goes up to about 200%.

The softening phenomenon can be explained as the rubber-like material's Mullins effect (Mullins, 1969). Mullins effect can be illustrated as an instantaneous and irreversible softening that occurs whenever the strain increases beyond its maximum historical value. After that, the equivalent stiffness of VE damper will decrease under all strains. However, there is still no accurate insight physical mechanism that can explain this effect (Diani et al., 2009). If the VE material is bolted tight with its end-plates, the damping device will show an increase in stiffness at large shear deformation. The intrinsic reason for the stiffening effect lies on the strain-induced crystallization of the filled rubber-like material at large shear strain (Kikuchi and Aiken, 1997), (Imbimbo and Kelly, 1998).

The variation of the different mechanic parameters with strain amplitude is presented in **Figure 7**. Results indicate that the storage shear modulus shows a negative exponential decrease, while the loss shear modulus undergoes linear decrease. The two trends mean that the additional damping decreases faster than the additional stiffness due to the stiffening phenomenon. The loss factor increases initially and then drop down with the increase of strain amplitude. The maximum loss factor corresponds to a strain amplitude range between about 100–150%, which also have a good agreement with the shaking table tests (Zhou et al., 2014).

MECHANIC MODEL OF THE HYBRID NON-LINEAR VE DAMPER

Many classical mechanic models have proposed to depict the mechanic behavior of VE dampers, including the Maxwell, Kelvin-Voigt, and fractional derivative models (Lewandowski and Chorążyczewski, 2010). These are the most popular models for VE dampers for the past decades. However, they are not suitable to represent the mechanic properties for this hybrid non-linear type damper. Based on the above performance test investigations, a more accurate model which considers multiple sources of non-linearity is proposed.

Three mechanic elements are set in parallel, including two non-linear stiffness elements and one non-linear viscous dashpot element. The $K_1(\tilde{u})$ is the Mullins stiffness element which considers Mullins effect, the stiffness of the element is related to the maximum strain

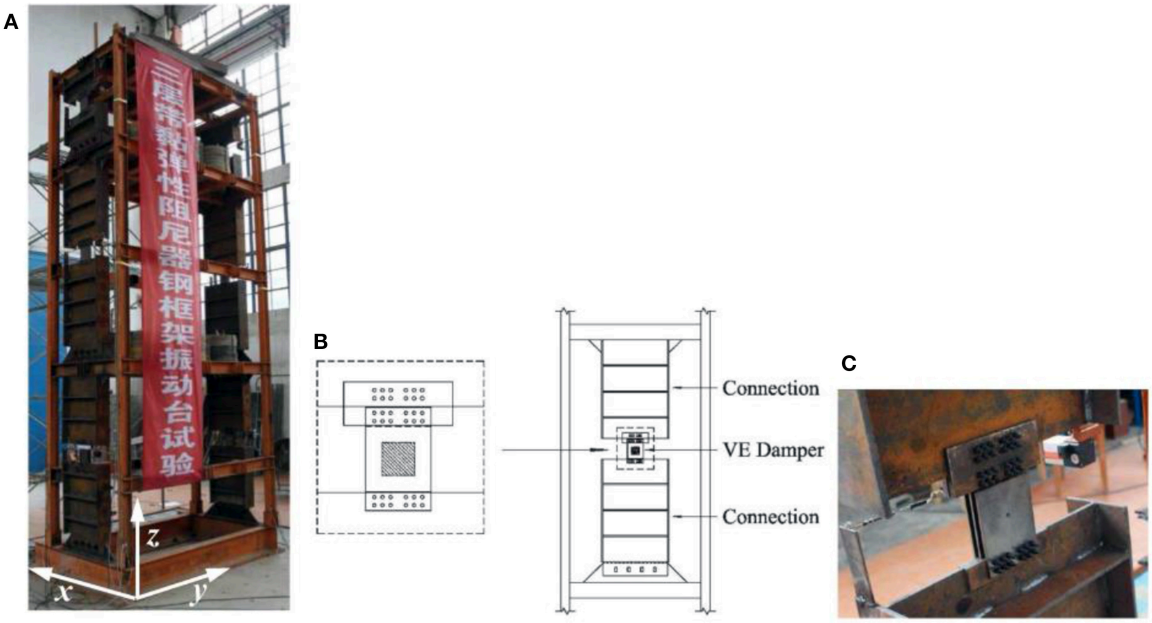

FIGURE 9 | Test structure with VE damping device, **(A)** overall model on the table, **(B)** connection detail of the VE dampers, and **(C)** picture of an installed VE damper.

amplitude $\tilde{u}$ (in absolute value). The expression of $K_1(\tilde{u})$ is given as,

$$K_1(\tilde{u}) = a_1\tilde{u}^2 + a_2\tilde{u} + a_3 \tag{5}$$

Equation (5) is a quadratic function that can depict softening effect with the increase of strain amplitude. The $K_2(u)$ non-linear stiffness element is introduced to include the stiffening effect under large shear strain in the following quadratic form,

$$K_2(u) = b_1u^2 + b_2 \tag{6}$$

The comprehensive expression for the mechanic model of the hybrid non-linear model is given as,

$$\begin{cases} F = \lambda_1\lambda_2(F_1 + F_2 + F_3) \\ F_1 = K_1(\tilde{u})u = a_1\tilde{u}^2u + a_2\tilde{u}u + a_3u \\ F_2 = K_2(u)u = b_1u^3 + b_2u \\ F_3 = C\dot{u}^\alpha = c(\dot{u}/f)^\alpha \end{cases} \tag{7}$$

where F, u, and $\dot{u}$ are the force, displacement, and velocity of the damping device; F_1, F_2, and F_3 are the forces provided by Mullins effect element, non-linear stiffness element, and the non-linear dashpot element; K_1 and K_2 are the stiffness expression of the two corresponding stiffness elements; C and α are the damping coefficient and damping exponent; f is the basic frequency of the structure; $\tilde{u}$ is the strain amplitude; a_1, a_2, a_3, b_1, b_2, C, and α are the mechanic parameters that to be identified based on

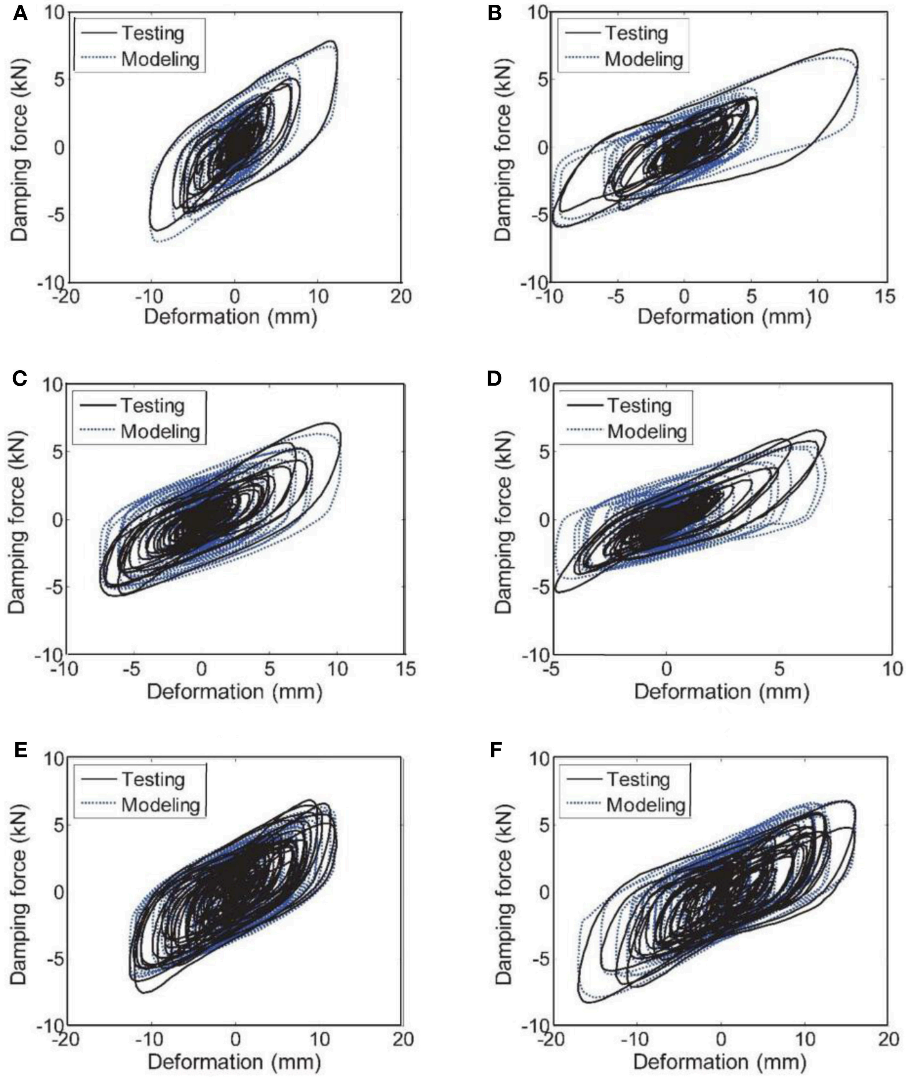

FIGURE 10 | Hysteresis curve comparison between shake table test and numerical modeling for **(A)** 1st floor-El Centro-0.3 g, **(B)** 2nd floor-El Centro-0.4 g, **(C)** 1st floor-Taft-0.3 g, **(D)** 2nd floor-Taft-0.4 g, **(E)** 1st floor-AW-0.3 g, and **(F)** 2nd floor-AW-0.4 g.

the performance tests. $\lambda_1$is the correction factor considering the influence by the ambient temperature; $\lambda_2$is the correction factor considering the heating-fatigue softening.

The mathematic expression of the proposed mechanical model is concise, and it can depict multiple non-linear behaviors of the hybrid non-linear device, such as the heating-fatigue softening, ambient temperature dependency, frequency-independency, softening, and hardening under large strain. Besides, the parameters are not case dependent, they can be identified and decided by the performance tests described before. The temperature related parameters are given as follow,

$$\begin{cases} \lambda_1 = 0.396 + 1.203e^{-0.0313\theta} \\ \lambda_2 = \frac{4.044+4.190e^{-0.222-0.109\omega_t}}{4.044+4.190e^{-0.222-0.109\omega_0}} \end{cases} \tag{8}$$

where θ is the ambient temperature; $\omega_0$is the initial accumulative dissipative energy density; $\omega_t$is the accumulative dissipated density at a given time t. Other mechanic related parameters are identified in kN-mm unit as: $a_1 = 2.60 \times 10^{-4}$; $a_2 = -2.45 \times 10^{-2}$; $a_3 = 0.50$; $b_1 = 1.91 \times 10^{-4}$; $b_2 = 5.34 \times 10^{-2}$; $C = 0.8$ and $\alpha = 0.3$.

VERIFICATIONS OF THE MECHANIC MODEL OF THE VE DAMPING DEVICE

Verifications Via Performance Tests

The proposed model is verified via the performance tests. **Figure 8** presents the comparisons between test and modeling curves under different strain amplitude. Results indicate that the hysteresis loops derived by the mechanic model agree well with the testing curves.

Design of the Shake Table Tests

A three-story steel frame with a height of 4.90 m. In the first and second stories, there are additional beams in the mid-story level in *y* direction. The "VE60 × 60 × 10" type VE dampers are installed and the ground motions are excited in the *x* direction. The shake table test is briefly illustrated in **Figure 9**. Three earthquakes are selected as the input excitations, including two natural records (El Centro and Taft records) and one artificial wave (AW) generated based on the design spectrum. More information of the shaking table test can be found in Zhou et al. (2014).

Implementation of the Numerical Model

The proposed mechanical model of VE damping device is created in a discrete numerical form in an open source finite element software—OpenSees (McKenna, 2011). The mechanical model is implemented as a uniaxial material, and VE dampers are modeled by two Node Link elements. It should be noted that the value of λ_1 is 1.0 considering the ambient temperature is 22°C. For the mechanic model, to degrade its non-linearity and achieve a better convergence performance, the value of λ_2 is taken as 0.9 and 0.7, respectively, for dampers installed in the first floor and second floor. The selection of λ_2 value also considers the difference in deformation and fatigue damage.

The tested three-story steel frame structure can be modeled as a shear-type multi-degree of freedom (MDOF) system. The concentrated mass for 1st—3rd floor are 2517, 2671, and 2606 kg. The shear stiffness for 1st to 3rd floor are 0.682, 0.367, and 2.864 kN/mm. The modal results between the numerical and physical models are also compared to verify the accuracy of the establishment of the numerical model. The first 3 order natural frequency error between the two models can be controlled within 1.5%.

Verifications Via Shake Table Tests

The numerical simulation is performed in the OpenSees platform according to the test cases, and the mechanical model is fundamentally verified by comparing the simulation results with the test data. The mechanic behaviors of the VE damping devices are shown in **Figure 10**. Typical hysteresis behaviors are compared under maximum input value of 0.3 g for the first floor

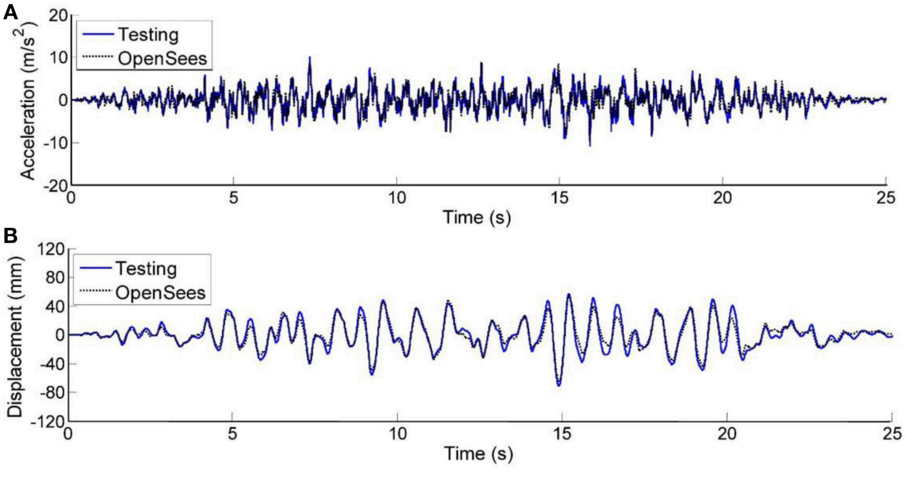

FIGURE 11 | Comparison between OpenSees and test result under AW-0.6 g wave of **(A)** acceleration time history, and **(B)** displacement time history.

and 0.4 g peak input for the second floor. It is concluded that for most cases, the test curves and the numerical modeling result can correlate well. Except for the second floor under Taft input-0.4 g, the significant connection bolt slide is the main reason for the difference.

The time history response of the relative acceleration and displacement at the top of the test model under AW input with 0.6 g peak input acceleration are shown in **Figure 11**. The time history response comparison confirms a good shape agreement between the test and numerical modeling during the integral input process. The time history comparison is not presented in detail. Instead, the maximum response of the floor acceleration and floor displacement under different input level and different earthquake waves are shown in **Figures 12**, **13**. Results indicate that, with the increase of the peak input acceleration, the numerical modeling get closer to the real

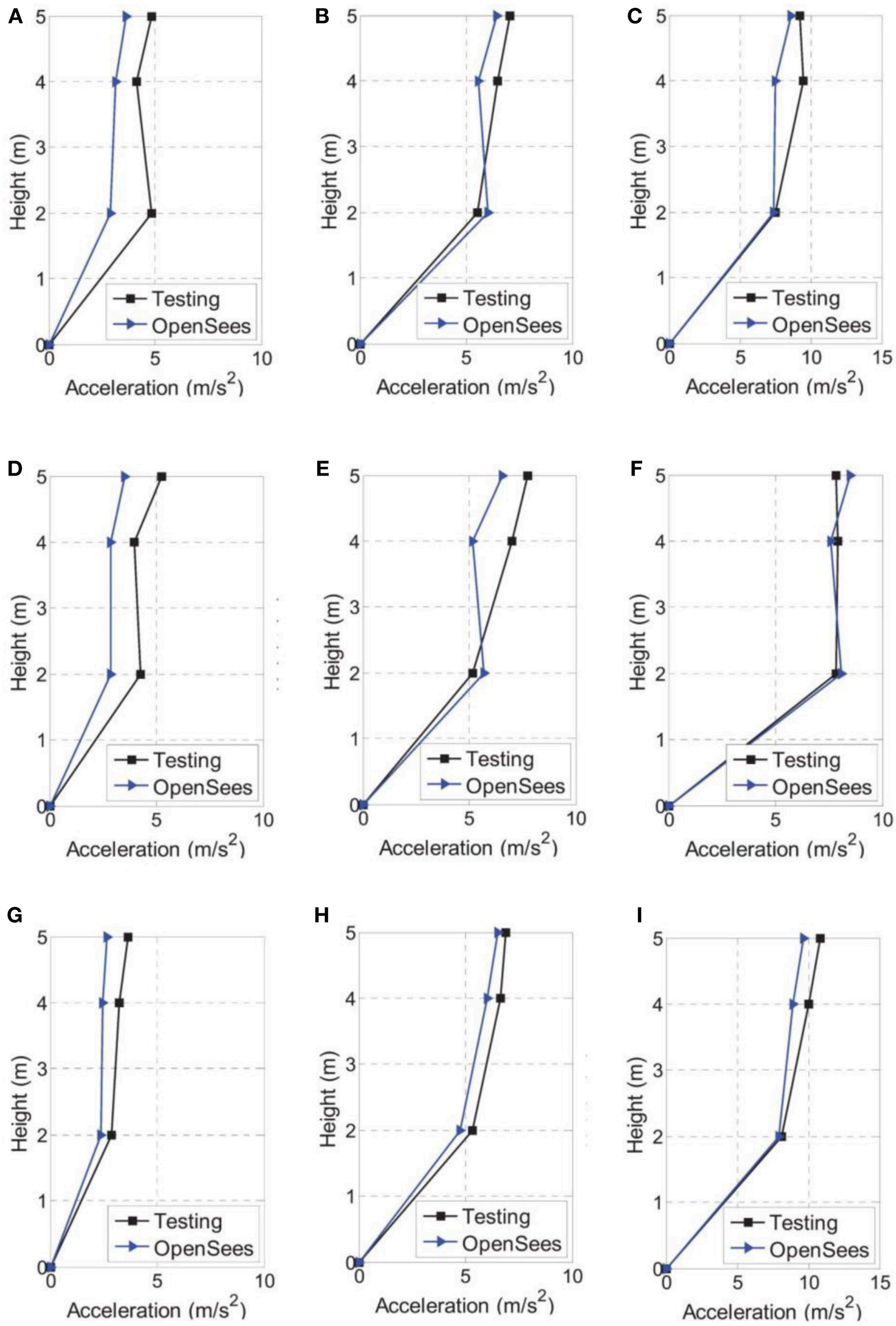

FIGURE 12 | Peak floor acceleration response comparison under input of **(A)** El Centro-0.2 g, **(B)** El Centro-0.4 g, **(C)** El Centro-0.6 g, **(D)** Taft-0.2 g, **(E)** Taft-0.4 g, **(F)** Taft-0.6 g, **(G)** AW-0.2 g, **(H)** AW-0.4 g, and **(I)** AW-0.6 g.

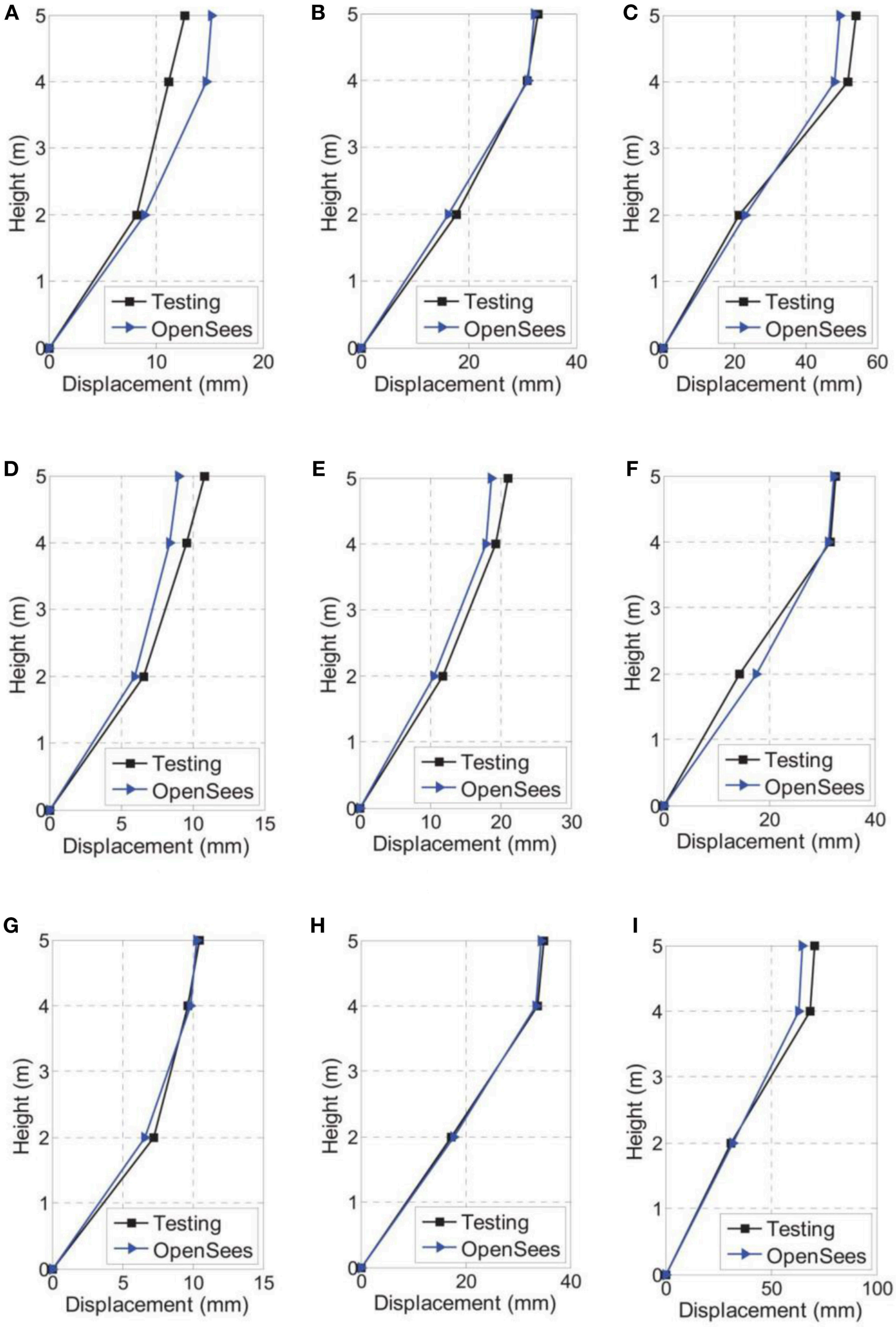

FIGURE 13 | Peak floor displacement response comparison under input of **(A)** El Centro-0.2 g, **(B)** El Centro-0.4 g, **(C)** El Centro-0.6 g, **(D)** Taft-0.2 g, **(E)** Taft-0.4 g, **(F)** Taft-0.6 g, **(G)** AW-0.2 g, **(H)** AW-0.4 g, and **(I)** AW-0.6 g.

physical tests. The reason is that the other disturbances become less significant compared to the earthquake-induced response. Another observation is that the displacement simulation result is closer to the test data compared to the acceleration simulation. In general, the simulation results closely match the test data, regarding the time history response and peak values. It is concluded that the proposed mechanic model can be used to accurately represent the mechanic property of the new VE damping device under both static and dynamic loading.

CONCLUSIONS

This paper presents a new VE damping device with hybrid non-linearity. The different sources of non-linearity are analyzed and an accurate mechanic model which can consider multi-non-linear behavior is proposed and validated via performance tests and shake table tests. The main conclusions from this study are as follows:

Five sources of non-linearity of this new VE damping device are summarized, including the non-linearity of phase difference, initial stiffness, softening caused by temperature rise and low-cycle fatigue, and the softening and hardening under large strain amplitude.

A seven-parameter mechanic model which considers the multi-non-linear behaviors is proposed based on the performance tests. The mechanic model is first verified by comparing the simulation hysteresis curves with the performance tests.

The mathematic mechanic model is implemented in a discrete numerical form in an open source calculation platform to apply the mechanic model into practical numerical calculation use. A series of shake table tests on a steel frame with the new VE dampers are performed as a comparison.

The shake table test results, regarding the VE damper hysteresis loops, time history response, and the floor peak response are compared with numerical simulation. The test results are in good agreement with the simulation results which prove the accuracy of the proposed mechanic model and the practical application of the numerical model.

AUTHOR CONTRIBUTIONS

YZ contributed conception and design of the study. YZ and SG performed the tests. PC write the first draft manuscript. YZ and PC contributed to manuscript revision, read, and approved the submitted version.

ACKNOWLEDGMENTS

The authors acknowledge the finical support from National Natural Science Foundation of China (Grant No. 51678449) and the Key innovation team program of innovation talents promotion plan by MOST of China (No. 2016RA4059).

REFERENCES

Aiken, I. D., Nims, D. K., Whittaker, A. S., and James, M. K. (1993). Testing of passive energy dissipation systems. *Earthquake Spectr.* 9, 335–370. doi: 10.1193/1.1585720

Chang, K. C., Soong, T. T., Oh, S. T., and Lai, L. (1995). Seismic behavior of steel frame with added viscoelastic dampers. *J. Struct. Eng.* 121, 1418–1426. doi: 10.1061/(ASCE)0733-9445(1995)121:10(1418)

Chang, K. C., Soong, T. T., Oh, S. T., and Lai, M. L. (1992). Effect of ambient temperature on viscoelastically damped structure. *J. Struct. Eng.* 118, 1955–1973. doi: 10.1061/(ASCE)0733-9445(1992)118:7(1955)

Crosby, P., Kelly, J., and Singh, J. P. (1994). "Utilizing visco-elastic dampers in the seismic retrofit of a thirteen story steel framed building," in *Structures Congress X. I. I. ASCE* (Atlanta, GA), 1286–1291.

Dall'Asta, A., and Ragni, L. (2006). Experimental tests and analytical model of high damping rubber dissipating devices. *Eng. Struct.* 28, 1874–1884. doi: 10.1016/j.engstruct.2006.03.025

Diani, J., Fayolle, B., and Gilormini, P. (2009). A review on the mullins effect. *Eur. Polym. J.* 45, 601–612. doi: 10.1016/j.eurpolymj.2008.11.017

Ghaemmaghami, A. R., and Kwon, O. S. (2018). Non-linear modeling of MDOF structures equipped with viscoelastic dampers with strain, temperature and frequency-dependent properties. *Eng. Struct.* 168, 903–914. doi: 10.1016/j.engstruct.2018.04.037

Gong, S., and Zhou, Y. (2017). Experimental study and numerical simulation on a new type of viscoelastic damper with strong non-linear characteristics. *Struct. Control Health Monit.* 24:e1897. doi: 10.1002/stc.1897

Gong, S., Zhou, Y., and Ge, P. (2017). Seismic analysis for tall and irregular temple buildings: a case study of strong non-linear viscoelastic dampers. *Struct. Design Tall Special Build.* 26:e1352. doi: 10.1002/tal.1352

Imbimbo, M., and Kelly, J. M. (1998). Influence of material stiffening on stability of elastomeric bearings at large displacements. *J. Eng. Mechan.* 124, 1045–1049. doi: 10.1061/(ASCE)0733-9399(1998)124:9(1045)

Kikuchi, M., and Aiken, I. D. (1997). An analytical hysteresis model for elastomeric seismic isolation bearings. *Earthquake Eng. Struct. Dynam.* 26, 215–231. doi: 10.1002/(SICI)1096-9845(199702)26:2<215::AID-EQE640>3.0.CO;2-9

Lai, M. L., Chang, K. C., Soong, T. T., Hao, D. S., and Yeh, Y. C. (1995). Full-scale viscoelastically damped steel frame. *J. Struct. Eng.* 121, 1443–1447. doi: 10.1061/(ASCE)0733-9445(1995)121:10(1443)

Lai, M. L., Lu, P., Lunsford, D. A., Kasai, K., and Chang, K. C. (1996). "Viscoelastic damper: a damper with linear or non-linear material," in *Proceedings of 11th World Conference on Earthquake Engineering* (Acapulco).

Lewandowski, R., and Chorążyczewski, B. (2010). Identification of the parameters of the Kelvin–Voigt and the Maxwell fractional models, used to modeling of viscoelastic dampers. *Comput. Struct.* 88, 1–17. doi: 10.1016/j.compstruc.2009.09.001

Mahmoodi, P., Robertson, L. E., Yontar, M., Moy, C., and Feld, L. (1987). "Performance of viscoelastic dampers in world trade center towers." in *Dynamics of Structures ASCE* (Orlando, FL), 632–644.

McKenna, F. (2011). OpenSees: a framework for earthquake engineering simulation. *Comput. Sci. Eng.* 13, 58–66. doi: 10.1109/MCSE.2011.66

Molinera, E., Muserosb, P., and Martinez-Rodrigoa, M. D. (2012). Retrofit of existing railway bridge of short to medium spans for high-speed traffic using viscoelastic dampers. *Eng. Struct.* 40, 519–528. doi: 10.1016/j.engstruct.2012.03.016

Mullins, L. (1969). Softening of rubber by deformation. *Rubber Chem. Technol.* 42, 339–362. doi: 10.5254/1.3539210

Pant, D. R., Montgomery, M., and Christopoulos, C. (2018). Full-scale testing of a viscoelastic coupling damper for high-rise building applications and comparative evaluation of different numerical models. *J. Struct. Eng.* 145:04018242. doi: 10.1061/(ASCE)ST.1943-541X.0002246

Samali, B., and Kwok, K. C. S. (1995). Use of viscoelastic dampers in reducing wind-and earthquake-induced motion of building structures. *Eng. Struct.* 17, 639–654. doi: 10.1016/0141-0296(95)00034-5

Soong, T. T., and Spencer, B. F. Jr. (2002). Supplemental energy dissipation: state-of-the-art and state-of-the-practice. *Eng. Struct.* 24, 243–259. doi: 10.1016/S0141-0296(01)00092-X

Wu, C. X., Lai, W. S., Zhou, Y., Zhang, C., and Deng, X. (2015). Experimental study on seismic behaviors of new energy-dissipative prefabricated concrete frame structure joints. *China Civil Eng. J.* 48, 23–30. doi: 10.15951/.tmgcxb.2015.09.003 (in Chinese)

Xu, Z. D. (2009). Horizontal shaking table tests on structures using innovative earthquake mitigation devices. *J. Sound Vib.* 325, 34–48. doi: 10.1016/j.jsv.2009.03.019

Xu, Z. D., Guo, Y. F., Wang, S. A., and Huang, X.-H. (2013). Optimization analysis on parameters of multi-dimensional earthquake isolation and mitigation device based on genetic algorithm. *Nonlinear Dyn.* 72, 757–765. doi: 10.1007/s11071-013-0751-9

Xu, Z. D., Huang, X. H., and Lu, L. H. (2011). Experimental study on horizontal performance of multi-dimensional earthquake isolation and mitigation devices for long-span reticulated structures. *J. Vibr. Control* 18, 941–952. doi: 10.1177/1077546311418868

Xu, Z. D., Liao, Y. X., Ge, T., and Xu, C. (2016). Experimental and theoretical study of viscoelastic dampers with different matrix rubbers.

J. Eng. Mech. 142:04016051. doi: 10.1061/(ASCE)EM.1943-7889.0001101

Xu, Z. D., Shen, Y. P., and Guo, Y. Q. (2003a). Semi-active control of structures incorporated with magnetorheological dampers using neural networks. *Smart Mater. Struct.* 12:80. doi: 10.1088/0964-1726/12/1/309

Xu, Z. D., Shen, Y. P., and Zhao, H. T. (2003b). A synthetic optimization analysis method on structures with viscoelastic dampers. *Soil Dyn. Earthquake Eng.* 23, 683–689. doi: 10.1016/j.soildyn.2003.07.003

Xu, Z. D., Zhao, H. T., and Li, A. Q. (2004). Optimal analysis and experimental study on structures with viscoelastic dampers. *J. Sound Vib.* 273, 607–618. doi: 10.1016/S0022-460X(03)00522-4

Yokota, H., Saruta, M., Nakamura, Y., Saruta, M., and Wada, A. (1992). "Structural control for seismic load using viscoelastic dampers." in *Proceedings of 10th WCEE* (Madrid).

Zhou, Y., Gong, S. M., and Lu, X. L. (2014). Study on shaking table test of a steel structure with additional viscoelastic dampers. *J. Build. Struct.* 35, 1–10. doi: 10.14006/j.jzjgxb.2014.07.001 (in Chinese)

Conflict of Interest Statement: The authors declare that the research was conducted in the absence of any commercial or financial relationships that could be construed as a potential conflict of interest.

frontiers
in Materials

ORIGINAL RESEARCH
published: 19 March 2019
doi: 10.3389/fmats.2019.00037

Study on Structures Incorporated With MR Damping Material Based on PSO Algorithm

Ying-Qing Guo[1]*, *Wen-Han Xie*[1] *and Xingjian Jing*[2]

[1] Mechanical and Electronic Engineering College, Nanjing Forestry University, Nanjing, China, [2] Department of Mechanical Engineering, The Hong Kong Polytechnic University, Hong Kong, Hong Kong

The magnetorheological (MR) damping material is a kind of smart shock absorption material, and it can be made into MR dampers for reducing the vibration or dynamic response of structures. During the vibration mitigation control of structures with MR dampers, the displacement and acceleration responses are always concerned firstly because the displacement responses determine the safety of structures and, at the same time, the acceleration responses determine the comfort level of the human body staying in structures. That means, the control currents choice of MR dampers during the vibration process is a multi-objective optimization control problem. In this paper, the particle swarm optimization (PSO) algorithm is developed to control the displacement and acceleration responses simultaneously. Numerical analysis for a five-floor steel frame structure with one MR damper installed on each floor is carried out. Simulation results of the PSO control structure are compared with those of passive control (including the ON-control and the OFF-control) structures and the uncontrolled structure. Analysis results demonstrate that the PSO algorithm can reduce the displacement responses of the structure obviously and, at the same time, it can reduce the acceleration responses of the structure to a certain extent. Furthermore, the PSO algorithm reduces the seismic responses of structures more effectively than those of passive control structures.

Keywords: magnetorheological (MR) damping material, MR damper, the particle swarm optimization (PSO) algorithm, multi-objective optimization control, building structure

Edited by:
Abid Ali Shah,
University of Science and Technology Bannu, Pakistan

Reviewed by:
Zhongwen Zhang,
Southeast University, China
Yeshou Xu,
Northwestern University, United States
Xiangcheng Zhang,
Zhengzhou University, China

***Correspondence:**
Ying-Qing Guo
gyingqing@126.com

Specialty section:
This article was submitted to Structural Materials, a section of the journal Frontiers in Materials

Received: *21 January 2019*
Accepted: *20 February 2019*
Published: *19 March 2019*

Citation:
Guo Y-Q, Xie W-H and Jing X (2019) Study on Structures Incorporated With MR Damping Material Based on PSO Algorithm. Front. Mater. 6:37. doi: 10.3389/fmats.2019.00037

INTRODUCTION

The magnetorheological (MR) damping material is a kind of smart shock absorption material, which was discovered by Jacob Rabinow at the US National Bureau of Standards in 1948 (Rabinow, 1948). The MR damping material is composed of carbonyl iron particles, a carrier liquid and some additives. Normally, it is a free-flowing liquid with a certain viscosity similar to that of motor oil. However, when subjected to a magnetic field, the liquid becomes viscoelastic solid. And the stronger the magnetic field, the harder the MR damping material becomes. That is, the yield stress of the MR damping material can be controlled very accurately by changing the intensity of the magnetic field. On the other hand, removing the magnetic field causes the solid MR damping material to once again become liquid. Furthermore, the change can occur in only a few milliseconds (Guo et al., 2017). MR dampers are developed to take advantage of these characteristics of MR damping material. Because of these properties, more and more researchers are attracted to develop MR clutches and automotive MR suspensions, etc. In the civil engineering field, MR dampers are used to reduce the dynamic responses of structures in earthquake excitation or in strong wind, cable-stayed bridges, and seismic protection.

After the MR damper is installed into the structure, its damping and stiffness will change the parameters of the structure itself and further affect the anti-vibration ability of the structure (Xu et al., 2013). However, the controllable damping and controllable stiffness of the MR damper are controlled by its control currents (or voltages), that is to say, one of the important factors determining the effect of its vibration reduction is how to effectively select control currents (or voltages) of the MR damper. Many control algorithms of control currents (or voltages) of MR dampers have been developed. A linear optimal controller based on acceleration feedback, named a semi-active clipped-optimal control strategy, was designed to adjust the control voltage of the MR damper (Dyke et al., 1996). Another acceleration feedback control method of seismic structures was used to realize vibration mitigation of structures successfully (Chung et al., 1998). An intelligent neuro-fuzzy control strategy was developed relying on the correlation between accelerations of the building (controller input) and voltage applied to the MR damper (controller output) (Schurter and Roschke, 2001). A non-clipping semi-active control method, a stochastic optimal control strategy, was proposed for randomly excited non-linear systems using semi-active MR dampers (Ying et al., 2002). An on-line real-time control method by using neural networks techniques for semi-active control of structures with MR dampers was proposed. This method considered the time-delay problem of semi-active control, which can solve distortion of the responses of structures (Xu et al., 2003). An inverse neural network model for MR dampers was established to adjust the control voltage of the MR damper to realize the semi-active control mode of structures with MR dampers (Wang and Liao, 2005). A fuzzy control algorithm with a neural network forecasting model was proposed. According to the structural dynamic response predicted by the neural network forecasting model, the fuzzy controller can update control currents of MR dampers (Guo et al., 2008). Combining with modified adaptive control, Phu et al. built an interval type 2 fuzzy model to obtain the desired damping force of a MR damper, and then realize the vibration control of a washing machine (Phu et al., 2014). A semi-active control method for a non-linear benchmark building with MR dampers included two parts. One an optimal compact Takagi-Sugeno-Kang fuzzy inverse model for the MR damper. The other is voltage regulator based on the maximum and minimum capacities of the MR damper at each time-step (Askari et al., 2016). An adaptive Fuzzy-PID controller was implemented to ensure that the MR damper performs well, even at varying frequencies (Nordin et al., 2018).

In this paper, the particle swarm optimization (PSO) algorithm is developed to control the displacement and acceleration responses simultaneously. Numerical analysis for a five-floor steel frame structure with one MR damper installed on each floor is carried out. Simulation results of the PSO control structure are compared with those of passive control (including the ON-control and the OFF-control) structures and the uncontrolled structure. Analysis results demonstrate that the PSO algorithm can reduce the displacement responses of the structure and obviously, at the same time, it can reduce the acceleration responses of the structure to a certain extent. Furthermore, the PSO algorithm reduces seismic responses of structures more effectively than those of passive control structures.

CONTROLLED STRUCTURE MODEL

MR Damper Model

In this paper, the shear-valve type of the MR damper (Xu and Guo, 2006) is used for the structural seismic mitigation control, as shown in **Figure 1**. And the Bingham model of the MR damper is proposed by Phillips (1969), which is one of the classic models and equivalent to a friction component augmented by a Newtonian viscosity component, as shown in **Figure 2** (Guo et al., 2008). The relationship between the stress and strain rate can be describe as Xu and Shen (2003)

$$\tau = \tau_y \operatorname{sgn}(\dot{\gamma}) + \eta\dot{\gamma} \tag{1}$$

$$\tau_y = A_1 e^{-I_c} + A_2 \ln(I_c + e) + A_3 I_c \tag{2}$$

where τ is the shear stress in the MR damping material; τ_y, the yielding shear stress can be adjusted by the magnitude of the external magnetic field; η is the Newtonian viscosity, which is independent of the external magnetic field; $\dot{\gamma}$ is the shear strain rate. The magnitude of the external magnetic field can be controlled by control currents, so τ_y is the function of control currents I_c as shown in Equation (2) (Xu et al., 2003). A_1, A_2, and A_3 are coefficients of the MR damping

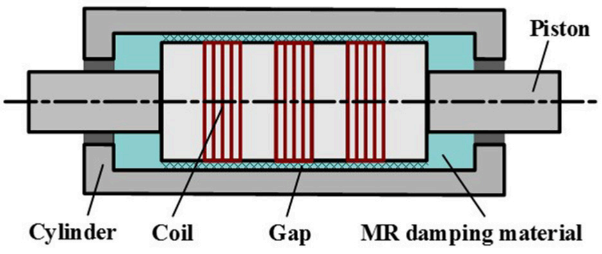

FIGURE 1 | Schematic diagram of the shear-valve type MR damper.

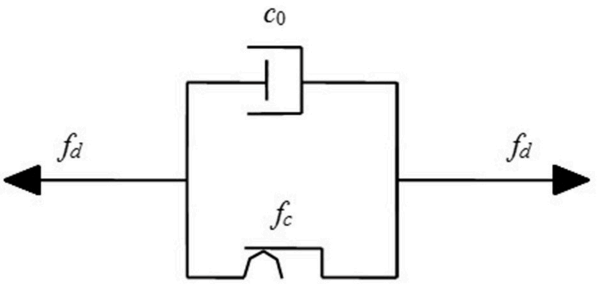

FIGURE 2 | Bingham model (Guo et al., 2008).

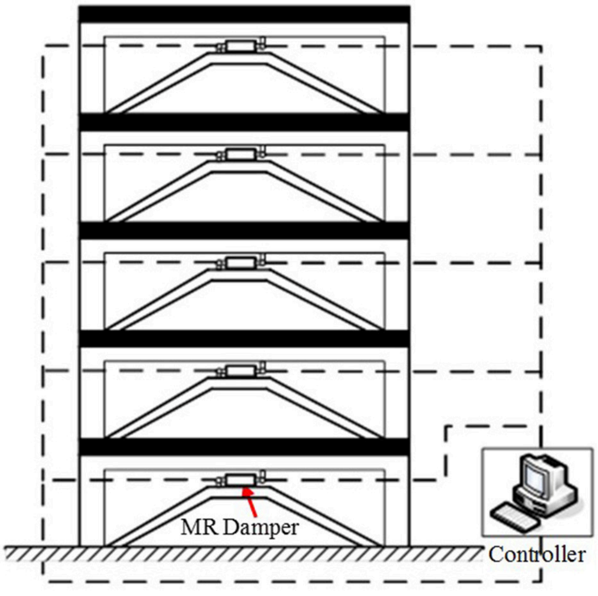

FIGURE 3 | The structure with MR dampers.

material, and e is the natural constant. Based on Equation (1) the relationship between the force and displacement of the MR damper is (Xu and Guo, 2006),

$$f_{di} = f_c \operatorname{sgn}[\dot{u}(t)] + c_0 \dot{u}(t) \tag{3}$$

where $f_c = \frac{3L_d A_p \tau_y}{h_d}$ is frictional force; $c_0 = \frac{12\eta L_d A_p^2}{\pi D h_d^3}$ is damping coefficient; L_d and A_p are the effective length and the cross-sectional area of the piston; D represents the inner diameter of the outer cylinder and h_d represents the gap between the piston and the outer cylinder, $u(t)$ represents the relative displacement of the piston to the outer cylinder.

Dynamic Equation of the Controlled Structure

In this paper, MR dampers are equipped between the chevron brace on each floor of the steel frame structure, as shown in **Figure 3**. The dynamic equation for the n-floor steel frame structure equipped MR dampers can be descripted as

$$\mathbf{M}\ddot{\mathbf{x}} + \mathbf{C}\dot{\mathbf{x}} + \mathbf{K}\mathbf{x} = -\mathbf{M}\mathbf{I}\ddot{s}_e - \mathbf{B}\mathbf{f}_d \tag{4}$$

where $\mathbf{M}$, $\mathbf{C}$, and $\mathbf{K}$ are the mass, damping, and stiffness matrixes of the steel frame structure, respectively; $\mathbf{x}$ is an n-dimensional vector to represent the displacement response of each floor of the steel frame structure relative to the ground; $\mathbf{I}$ is an n-dimensional column vector with 1 for each element; $\ddot{s}_e$ is the seismic acceleration; $\mathbf{B}$ is an n-dimensional vector to show the number of MR dampers installed on each floor of the steel frame structure; $\mathbf{f}_d$ is an n-dimensional vector of control forces generated by MR dampers at each floor.

PARTICLE SWARM OPTIMIZATION ALGORITHM

Based on the social behavior of bird flocking, fish schooling, and swarming theory, James Kennedy and Russell Eberhart proposed PSO algorithm in 1995 (Eberhart and Shi, 2001). That means, the birds in the group are abstracted into "particles" without mass and volume. Through the mutual cooperation and information sharing of these "particles," the speed of their movement is affected by the information of the historical movement status of the group and themselves. The historical optimal position affects the current motion direction and motion speed of the particles and can better coordinate the relationship between the particles themselves and the group motion, and find the optimal solution in a complex solution space.

The Original Version PSO Algorithm

In an m-dimensional problem space there is a particle swarm, and z_i is the current position of the *i-th* particle; v_i is the current velocity of the *i-th* particle; p_i is the optimal position experienced by the *i-th* particle in the particle group, which is called the optimal position of the individual; p_g is the optimal position of the all particles of the swarm that were experienced, which is called the global optimal position. Then the evolution equation of the original version PSO algorithm can be described as Eberhart and Shi (2001)

$$\begin{aligned} v_{ij}(t+1) &= v_{ij}(t) + c_1 * rand_1(\,) * (p_{ij}(t) - z_{ij}(t)) \\ &\quad + c_2 * rand_2(\,) * (p_{gj}(t) - z_{ij}(t)) \qquad (5) \\ z_{ij}(t+1) &= z_{ij}(t) + v_{ij}(t+1) \qquad (6) \end{aligned}$$

where the subscript j means the *j-th* dimension of the particle; the subscript i means the *i-th* particle in the particle swarm; t is the *t-th* generation; c_1 represents the cognitive learning coefficient which is used to adjust the step of particle that flies toward the best location of itself; c_2 represents the social learning coefficient which is used to adjust the step of a particle that flies toward the global best position; $rand_1(\,)$ and $rand_2(\,)$ are two independent random functions within the range of [0,1].

The PSO Algorithm With Constriction Factor

In order to control the flying speed of the particle effectively and let the algorithm achieve a balance between global detection and particle exploitation, that is, in order to ensure convergence of the particle swarm algorithm, in 1999, Clerc proposed the PSO algorithm with constriction factor (Clerc, 1999). In 2000, Eberhart and Shi simplified the constriction factor and enhanced its practicality (Eberhart and Shi, 2000). The velocity evolution equation of the particle swarm algorithm with constriction factor can be described as

$$\begin{aligned} v_{ij}(t+1) &= k * (v_{ij}(t) + c_1 * rand_1(\,) * (p_{ij}(t) - z_{ij}(t)) \\ &\quad + c_2 * rand_2(\,) * (p_{gj}(t) - z_{ij}(t))) \end{aligned} \tag{7}$$

$$k = \frac{2}{\left|2 - \varphi - \sqrt{\varphi^2 - 4\varphi}\right|}, \quad \text{where } \varphi = c_1 + c_2, \ \varphi > 4 \tag{8}$$

where k represents constriction factor which is a function of c_1 and c_2.

PSO ALGORITHM DESIGN OF MR INTELLIGENT STRUCTURE

In the earthquake mitigation control of an MR intelligent structure, choosing a reasonable control current for the MR damper is key to reducing seismic damage to the structure. The displacement and acceleration responses of the MR intelligent structure can reflect whether the structure will be damaged or not. In this case, the displacement, and acceleration responses control constitute a multi-objective control system in the seismic mitigation control of the MR intelligent structure. The following is a detailed description of how to use the PSO algorithm to accurately select control currents of MR dampers, and then achieve multi-objective control of the MR intelligent structure and meet the requirements of building codes.

Definition of Fitness Function

In the PSO control of an MR intelligent structure, a multi-objective optimal control algorithm is adopted, that is, structural displacement targets, and structural acceleration targets. Therefore, the fitness function, namely the objective function can be set as:

$$\text{Min } F(t): \quad F(t) = \alpha f_1(t) + \beta f_2(t) \tag{9}$$

$$f_1(t) = \frac{|x_n|}{\text{Max}x_n} \tag{10}$$

$$f_2(t) = \frac{\frac{|\ddot{x}_1|}{\text{Max}\ddot{x}_1} + \frac{|\ddot{x}_2|}{\text{Max}\ddot{x}_2} + \cdots + \frac{|\ddot{x}_n|}{\text{Max}\ddot{x}_n}}{n} \tag{11}$$

where $f_1(t)$ is the objective function of the structural displacement; $f_2(t)$ is the objective function of the structural acceleration; α and β are weighting coefficients and $\alpha + \beta = 1$; t represents the *t-th* moment; x_n represents the *n-th* floor displacement of the structure; $\ddot{x}_n$ represents the *n-th* floor acceleration of the structure; $\text{Max}x_n$ and $\text{Max}\ddot{x}_n$ are the maximum allowable displacement and acceleration response of the *n-th* floor of the structure.

It can be seen from Equation (9) that weighting coefficients α and β determine the weight relationship between the displacement target and the acceleration target in fitness function. According to the seismic requirements buildings and building codes, during the earthquake, the magnitude of the structural displacement is closely related to the safety of structures, which is the main control target. The structural acceleration is mainly to affect the safety of the internal furniture or equipment of the structure, which is the secondary control target. So, in general, $0 \le \beta < \alpha \le 1$.

In Equation (10), according to the seismic requirements buildings and building codes (China Building Code Compilation Group, 2001), $\text{Max}x_n$ can be determined. When the structure is in an elastic state, the structural maximum inter-story displacement response is $h/550$ (h is the floor height of the structure), so $\text{Max}x_n$ can be set as $h/550$ in the fitness function. When the structure is in an elastoplastic state, the structural maximum inter-story displacement is $h/50$.

Choice of PSO Algorithm

In the PSO control of the MR intelligent structure, the PSO algorithm with constriction factor proposed by Clerc (1999) was chosen, as shown in the Equation (3) and (4). The constriction factor k in the algorithm is more effective in controlling and constraining the flight speed of the particles, at the same time, enhancing the local search ability of the algorithm (Eberhart and Shi, 2000).

Termination Condition Setting of PSO Algorithm

In the PSO control of the MR intelligent structure, the termination condition of the PSO algorithms is whether the structural displacement response and the acceleration response meet the seismic requirements buildings and building codes. That is, when the displacement response and the acceleration response are less than the preset maximum value, the search for the optimal solution can be terminated, and the corresponding control current (or voltage) value of the MR damper is output. The setting of the termination conditions can not only ensure the safety of building structures but also ensure the rapid selection of the control current (or voltage) of the MR damper.

NUMERICAL ANALYSIS

Modeling and simulation analysis of a five-floor steel frame structure with one MR damper installed on each floor are carried out in MATLAB to verify the correctness and effectiveness of the designed PSO algorithm. The parameters of the five-floor steel frame structure are the each-floor mass: $\mathbf{m} = [2.60\ 2.30\ 2.30\ 2.30\ 2.30] \times 10^4$ kg; the each-floor initial stiffness: $\mathbf{k} = [2.06\ 2.32\ 2.32\ 2.32\ 2.32] \times 10^7$ N/M; the each floor height: $\mathbf{h} = [3.9\ 3.3\ 3.3\ 3.3\ 3.3]$ m. The Newtonian viscosity η is 0.9 Pa· s (Yang et al., 2002) in the Equation (1). Parameters in the Equation (2) are $A_1 = -11374$, $A_2 = 14580$, and $A_3 = 1281$. Parameters in the equation (3) are $L_d = 400$ mm, $h_d = 2$ mm, and $D = 100$ mm. Parameters of the designed PSO algorithm are: the size of particle swarm is 30, the particle dimension is 5, the weighting coefficient in fitness function $\alpha = 0.7$ and $\beta = 0.3$, the cognitive learning coefficient $c_1 = 2.8$, the social learning coefficient $c_2 = 1.3$. El-Centro seismic waves and Taft seismic waves with 200 gal acceleration amplitude are selected, and the sampling time is 0.02 s.

In the numerical analysis, El Centro seismic waves first are used for the seismic excitation of different structures, and the seismic responses of the PSO control structure are compared with those of the passive control structures and the uncontrolled structure. **Figure 4** shows the structural 5th floor responses of the PSO control and the uncontrolled structure. It can be obtained from **Figure 4** that under the PSO algorithm the structural displacement and acceleration responses of the structure both

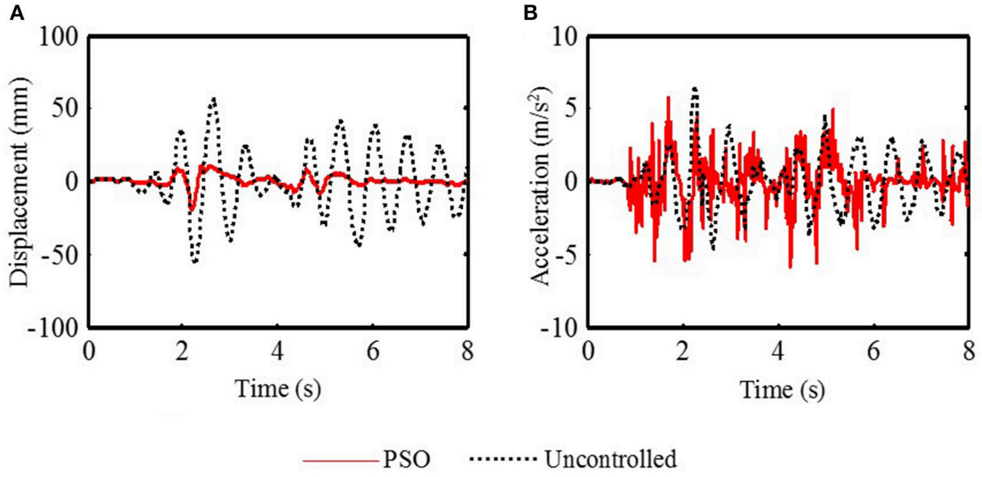

FIGURE 4 | The structural 5th floor response of the PSO control and the uncontrolled structure (El-Centrol). **(A)** The displacement response. **(B)** The acceleration response.

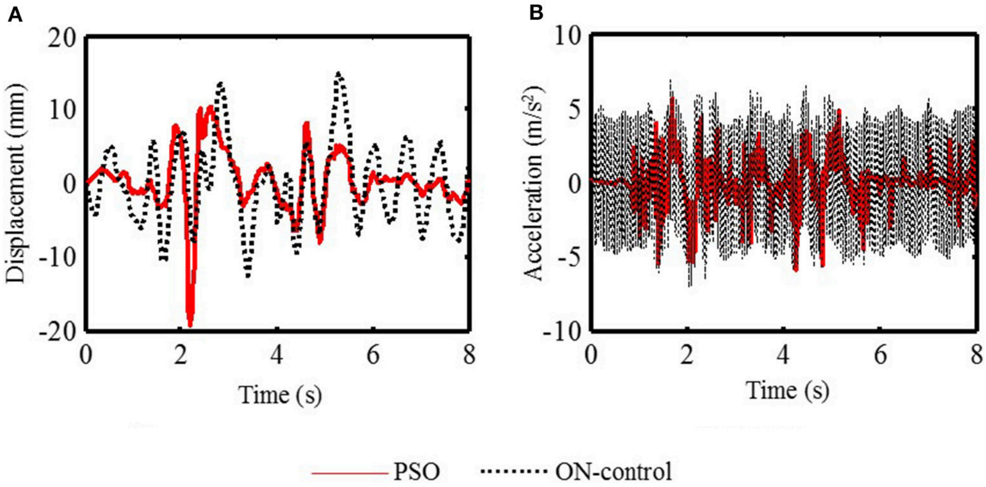

FIGURE 5 | The structural 5th floor response of the PSO control and the ON-control structure (El-Centrol). **(A)** The displacement response. **(B)** The acceleration response.

are effective. Under the PSO algorithm, the structural 5th floor maximum displacement response is 19.3 mm, which is effectively reduced by 66.43% compared to that of the uncontrolled structure, 57.5 mm. And under the PSO algorithm, the structural 5th floor maximum acceleration response, 5.90 m/s^2, is reduced by 10.58% compared to that of the uncontrolled structure, 6.60 m/s^2. That is because, in order to ensure the safety of the structure, it is necessary to increase the stiffness of the MR damper by increasing the control currents of the MR damper to reduce the structural displacement responses. It means the more stiffness increases, the more displacement response decreases. But when the stiffness is increased, the structural acceleration responses will also be affected. Moreover, the large stiffness will lead to the increase of the structural acceleration response frequency and excessive stiffness will lead to the amplification of acceleration amplitude. That is, the large stiffness is unfavorable to the control of structural acceleration responses.

To further illustrate the effectiveness of the PSO algorithm, the structural displacement and acceleration responses of the PSO control structure are compared with those of the ON-control structure and the OFF-control structure. The ON-control method and the OFF-control method belong to the passive control method. For the control current of the MR damper, when it is set as the maximum current level (2A), the control method is the ON-control method; when it is set as the minimum current level (0A), the control method is the OFF-control method. **Figure 5** shows the structural 5th floor responses of the PSO control and the ON-control structure. **Figure 6** shows

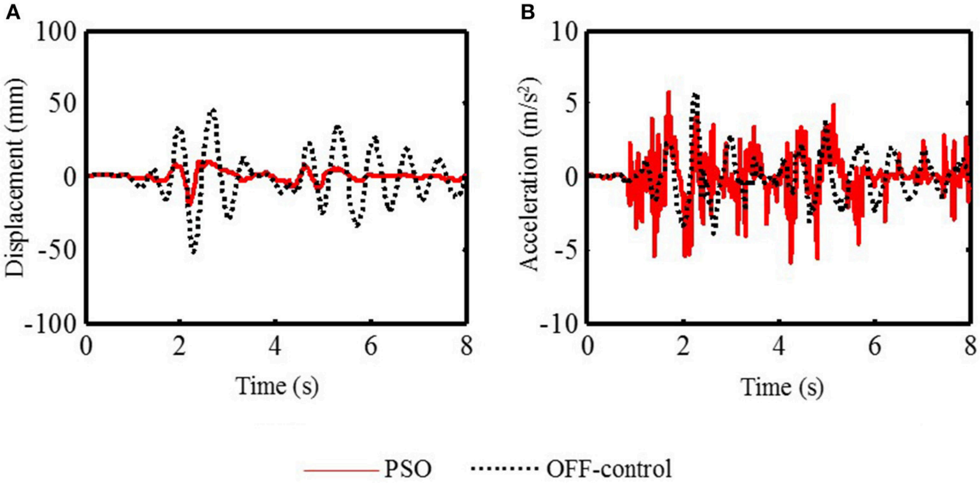

FIGURE 6 | The structural 5th floor response of the PSO control and the OFF-control structure (El-Centrol). **(A)** The displacement response. **(B)** The acceleration response.

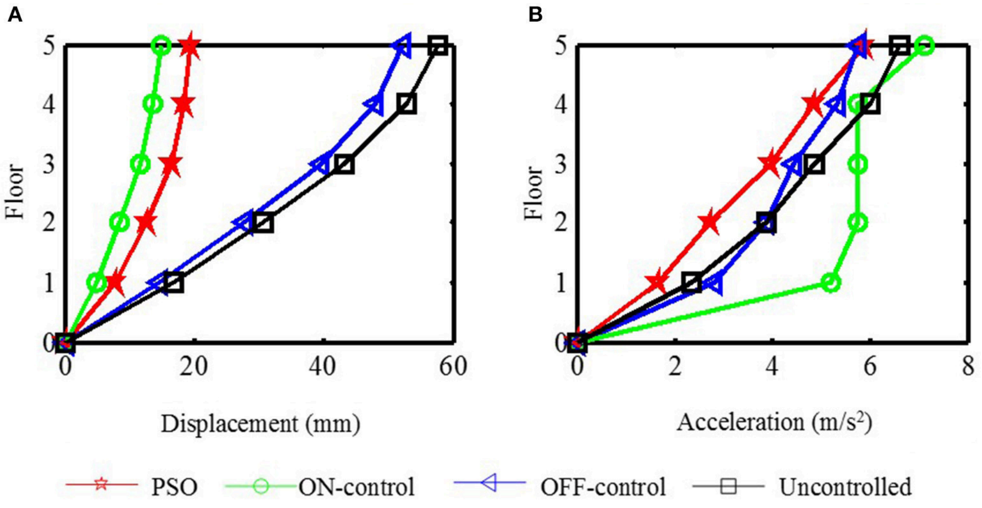

FIGURE 7 | The maximum response comparison of each floor under different control method (El-Centrol). **(A)** The maximum displacement response. **(B)** The maximum acceleration response.

TABLE 1 | The maximum displacement responses comparison of each floor (El-Centro).

Floor	Maximum displacement (mm)				Reduction rate of the PSO algorithm compared with other control algorithms (%)		
	PSO	ON	OFF	Uncontrolled	ON	OFF	Uncontrolled
1	7.8	4.9	14.6	16.8	−59.18	46.58	53.57
2	12.8	8.5	27.7	30.5	−50.58	53.79	58.03
3	16.4	11.6	39.5	43.3	−41.37	58.48	62.12
4	18.5	13.7	48.0	52.7	−35.03	61.46	64.90
5	19.3	14.8	52.2	57.5	−30.40	63.03	66.43

the structural 5th floor responses of the PSO control and the OFF-control structure.

It can be obtained from **Figure 5** that the displacement responses of the PSO control structure are inferior to those of the ON-control structure. However, the acceleration responses of the PSO control structure are far superior to those of the ON-control structure. Under the PSO algorithm, the structural 5th floor maximum displacement response is 19.3 mm, which

TABLE 2 | The maximum acceleration responses comparison of each floor (El-Centrol).

Floor	Maximum acceleration (m/s^2)				Reduction rate of the PSO algorithm compared with other control algorithms (%)		
	PSO	**ON**	**OFF**	**Uncontrolled**	**ON**	**OFF**	**Uncontrolled**
1	1.66	5.21	2.83	2.36	68.13	41.32	29.59
2	2.76	5.77	3.91	3.87	52.11	29.39	28.70
3	3.99	5.79	4.47	4.88	30.94	10.52	18.09
4	4.88	5.76	5.35	6.00	15.25	8.75	18.61
5	5.90	7.12	5.75	6.60	17.11	-2.63	10.58

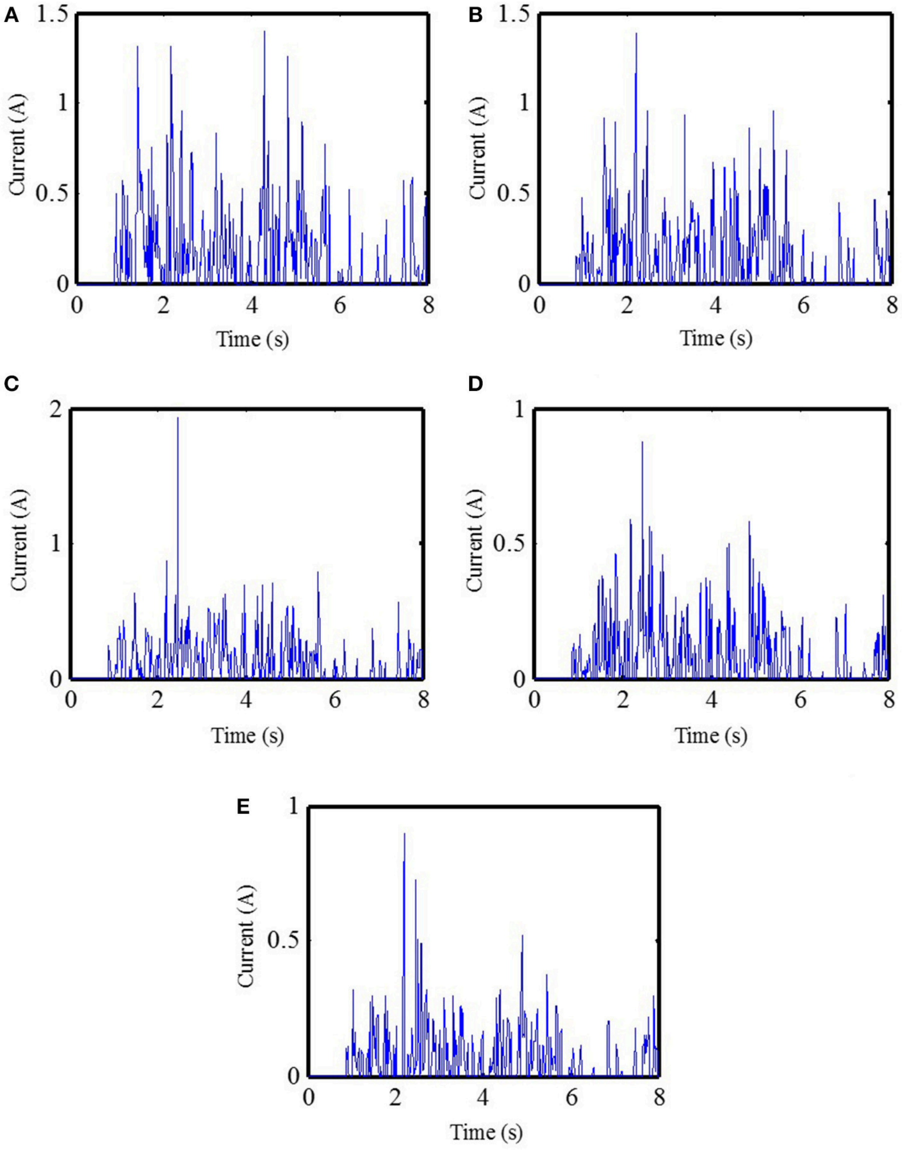

FIGURE 8 | Control currents of MR dampers of each floor of the PSO control structure (El-Centrol). **(A)** The 1st floor control currents. **(B)** The 2nd floor control currents. **(C)** The 3rd floor control currents. **(D)** The 4th floor control currents. **(E)** The 5th floor control currents.

is effectively reduced by −30.40% compared to that of the uncontrolled structure, 14.8 mm. But under the PSO algorithm, the structural 5th floor maximum acceleration response, 5.90 m/s^2, is reduced by 17.11% compared to that of the uncontrolled structure, 7.12 m/s^2. This is because under ON-control method the control currents applied to MR dampers are always the maximum current 2A, this inevitably makes the structural stiffness always very large. In this case, as mentioned above, the structural displacement responses must be significantly improved. However, the cost is that the frequency and amplitude of the structural acceleration responses are obviously amplified, which is not expected in the control process.

It can be obtained from **Figure 6** that the displacement responses of the PSO control structure are significantly better than those of the OFF-control structure but the acceleration responses of the PSO control structure are not as much as those of the ON-control structure. Under the PSO algorithm, the structural 5th floor maximum displacement response is 19.3 mm, which is effectively reduced by 63.03% compared to that of the uncontrolled structure, 52.2 mm yet under the PSO algorithm, the structural 5th floor maximum acceleration response, 5.90 m/s^2, is reduced by −2.61% compared to that of the uncontrolled structure, 5.75 m/s^2.

Figure 7 shows the maximum seismic responses of each floor under different control methods. **Table 1** lists the maximum displacement responses as a numeric comparison of each floor under different control methods. **Table 2** lists the maximum acceleration responses as a numeric comparison of each floor under different control methods. It can be seen that for the displacement responses of each floor, the PSO control algorithm is slightly inferior to ON-control method, however, its shock absorption effect has reached the seismic requirements of the buildings and building codes and the reduced amplitude of each floor relative to the uncontrolled structure is also reduced by a minimum of 53.57%. For the maximum acceleration response of each floor, the ON-control method not only fails to reduce the maximum amplitude of each floor, but also causes a large scale-up. This is mainly due to the fact that the maximum current (2A) is always given to the MR damper in each floor under ON-control method, which makes the structural stiffness increase too much. Nonetheless, the PSO algorithm reduces the maximum acceleration of each floor to a certain extent because it can define more appropriate control currents according to the fitness function, which makes sure that structural displacement responses and acceleration responses are reduced as much as possible at the same time.

Figure 8 shows control currents of MR dampers of each floor of the PSO control structure. **Figure 9** shows control currents vs. forces of the 5th floor of the PSO control structure. It can be seen in **Figure 8** that control currents applied to MR dampers at each time are completely different and most currents are <1.5A in most of the time. It can not only effectively reduce the damage to building structures caused by earthquakes, but also reduce energy waste as much as possible. It can be seen in **Figure 9** that the amplitude of damping force produced by the MR damper increases with the increase of the control current. In addition, it can be seen that there are positive and negative damping forces, and sometimes there are different damping forces under the same control current such as 0.5A, because the damping force generated by the MR damper is related not only to the control current, but also to the speed of the MR damper at the current moment. Therefore, in the case of the same current, if the direction and/or magnitude of velocity is different, the damping force generated by the MR damper is also different.

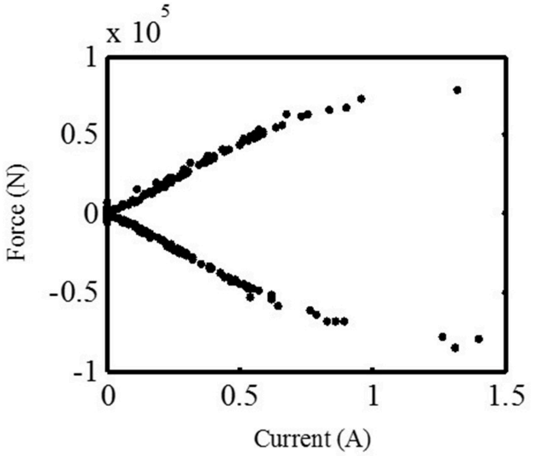

FIGURE 9 | Control currents vs. forces of the MR damper of the 5th floor PSO control structure (El-Centrol).

When the earthquake excitation is changed, is the PSO control algorithm still valid? Taft seismic waves are used as the earthquake excitation to illustrate the effectiveness the PSO control algorithm under different the earthquake excitation. **Figure 10** shows the maximum seismic responses of each floor under different control methods due to Taft earthquake. **Table 3** lists the maximum displacement responses numeric comparison of each floor under different control methods. **Table 4** lists the maximum acceleration responses numeric comparison of each floor under different control methods. It can be obtained that similar to El-Centro seismic excitation, for the displacement responses of each floor, the PSO control algorithm is slightly inferior to ON-control method, however, its shock absorption effect has reached the seismic requirements of buildings and building codes, moreover, and the reduced amplitude of each floor relative to the uncontrolled structure is also reduced by a minimum of 44.29%. For the maximum acceleration response of each floor, the PSO algorithm can reduce the maximum acceleration of each floor to a certain extent, and it works better than other methods.

CONCLUDING REMARKS

In the PSO control of the MR intelligent structure, both the structural displacement and acceleration responses are the control objectives, so a multi-objective control algorithm is required. In this paper, the PSO algorithm as a multi-objective optimal control method for the MR intelligent structure is investigated, and numerical analysis for a five-floor structure with one MR damper installed on each floor under different seismic excitation is carried out. Simulation results of the PSO control structure are compared with those of the ON-control structure, the OFF-control structure and the uncontrolled structure. The following conclusions are obtained from this study.

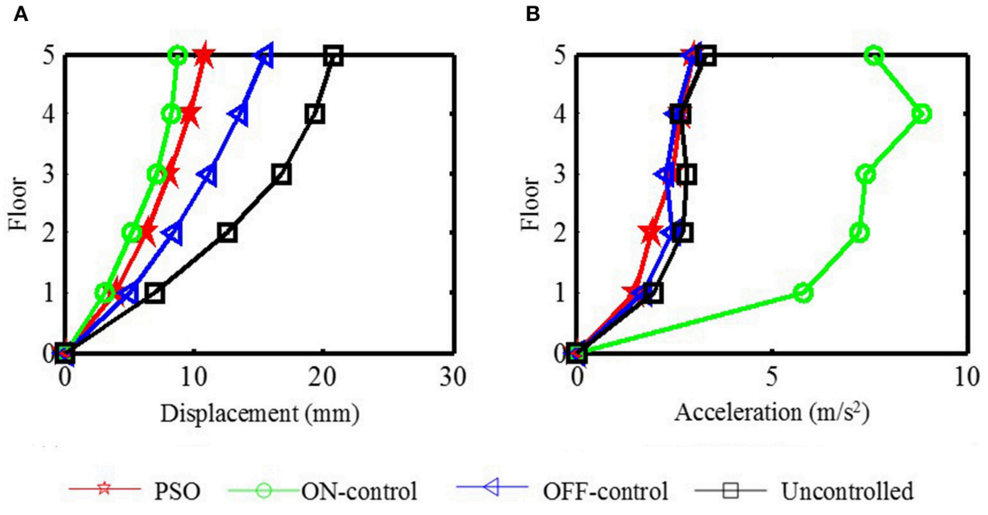

FIGURE 10 | The maximum response comparison of each floor under different control method. **(A)** The maximum displacement response. **(B)** The maximum acceleration response.

TABLE 3 | The maximum displacement responses comparison of each floor (Taft).

Floor	Maximum displacement (mm)				Reduction rate of the PSO algorithm compared with other control algorithms (%)		
	PSO	**ON**	**OFF**	**Uncontrolled**	**ON**	**OFF**	**Uncontrolled**
1	3.9	3.1	5.1	7.0	−25.80	23.52	44.29
2	6.3	5.2	8.5	12.6	−21.15	25.88	50.00
3	8.1	7.1	11.2	16.7	−14.08	27.67	51.49
4	9.7	8.3	13.6	19.3	−16.86	28.67	49.74
5	10.8	8.8	15.5	20.8	−22.72	30.32	48.07

TABLE 4 | The maximum acceleration responses comparison of each floor (Taft).

Floor	Maximum acceleration (m/s^2)				Reduction rate of the PSO algorithm compared with other control algorithms (%)		
	PSO	**ON**	**OFF**	**Uncontrolled**	**ON**	**OFF**	**Uncontrolled**
1	1.53	5.83	1.70	2.00	73.76	10.14	23.43
2	1.93	7.25	2.45	2.76	73.24	21.00	29.74
3	2.49	7.44	2.32	2.82	66.52	-7.36	11.78
4	2.66	8.87	2.58	2.68	69.94	-3.46	0.56
5	2.98	7.64	3.00	3.31	60.94	0.62	9.82

In the seismic control of structures, the magnitude of structural displacement responses is related to the safety of building structures, and the structural acceleration responses are related to the destruction of the internal appendages and furniture of the structure, and even the safety of people in it. Therefore, the weighted sum of structural displacement and acceleration is selected as the fitness function in the PSO control algorithm. The simulation results show that the selection of the fitness function is reasonable and effective.

Whether with El Centro seismic waves or Taft seismic waves as the seismic excitation, under the PSO algorithm, the structural displacement responses can be significantly reduced, meanwhile the structural acceleration responses also can be reduced to some extent, while the reduced amplitude is relatively small. This is mainly because in the seismic control of building structures, the displacement control is more important than the acceleration control, the weight of the displacement is greater than that of the acceleration in the fitness function.

ON-control method can reduce the structural displacement responses very-well and the result is better than that of the PSO method. However, since the control current is always set to the maximum, the structural stiffness is always very large, and finally the structural acceleration responses is greatly amplified.

DATA AVAILABILITY

All datasets generated for this study are included in the manuscript and/or the supplementary files.

AUTHOR CONTRIBUTIONS

Y-QG proposed the idea of this paper. Under the guidance, Y-QG and W-HX analyzed the PSO algorithm and jointly completed the writing of the article. XJ helped in proof reading of overall presentation and simulation data analysis.

FUNDING

The work was supported by National Natural Science Foundation of China with Grant Number (51878355), the National Science Fund for Distinguished Young Scholars with Grant number (51625803), the Program of Chang Jiang Scholars of Ministry of Education, Ten Thousand Talent Program of Leading Scientists and the Program of Jiangsu Province Distinguished Professor.

REFERENCES

Askari, M., Li, J., and Samali, B. (2016). Semi-active control of smart building-MR damper systems using novel TSK-Inv and max-min algorithms. *Smart Struct. Syst.* 18, 1005–1028. doi: 10.12989/sss.2016.18.5.1005

China Building Code Compilation Group (2001). *Code for Seismic Design of Buildings (GB50011-2001).* Beijing: China building industry press.

Chung, L. L., Wu, L. Y., and Jin, T. G. (1998). Acceleration feedback control of seismic structures, *Eng. Struct.* 20, 62–74. doi: 10.1016/S0141-0296(97)00060-6

Clerc, M. (1999). "The swarm and the queen: towards a deterministic and adaptive particle swarm optimization," in *Proc. I999 ICEC*, (Washington, DC), 1951–1957.

Dyke, S. J., Spencer, B. F., Sain, M. K., and Carlson, J. D. (1996). Modeling and control of magnetorheological dampers for seismic response reduction. *Smart Mater. Struct.* 5, 565–575. doi: 10.1088/0964-1726/5/5/006

Eberhart, R. C., Shi, Y. (2000). "Comparing inertia weights and constriction factors in particle swarm optimization," in *Proceedings of the IEEE Conference on Evolutionary Computation* (San Diego, CA: ICEC), 84–88.

Eberhart, R. C., Shi, Y. (2001). "Particle swarm optimization: developments, applications and resources," in *Proc. Congress on Evolutionary Computation.* IEEE service center, (Piscataway, NJ), 81–86.

Guo, Y. Q., Fei, S. M., and Xu, Z. D. (2008). Simulation analysis on intelligent structures with magnetorheological dampers. *J. Intell. Mater. Syst. Struct.* 19, 715–726. doi: 10.1177/1045389X07079650

Guo, Y. Q., Xu, Z. D., Chen, B. B., Ran, C. S., and Guo, W. Y. (2017). Preparation and experimental study of magnetorheological fluid for vibration control. *Int. J. Acoust. Vibrat.* 22, 1–7. doi: 10.20855/ijav.2017.22.2464

Nordin, N. H. D., Muthalif, A. G. A., and Razali, M. K. M. (2018). Control of transtibial prosthetic limb with magnetorheological fluid damper by using a fuzzy PID controller. *J. Low Frequency Noise Vibrat. Active Control.* 37, 1067–1078. doi: 10.1177/1461348418766171

Phillips, R. W. (1969). *Engineering Applications of Fluids with a Variable Yield Stress, Ph.D.* Thesis, university of California, Berkeley.

Phu, D. X., Shah, K., and Choi, S. B. (2014). Design of a new adaptive fuzzy controller and its implementation for the damping force control of a magnetorheological damper. *Smart Mater. Struct.* 23:065012. doi: 10.1088/0964-1726/23/6/065012

Rabinow, J. (1948). The magnetic fluid clutch. *Transac. Am. Inst. Electr. Eng.* 67, 1308–1315. doi: 10.1109/T-AIEE.1948.5059821

Schurter, K. C., and Roschke, P. N. (2001). "Neuro-fuzzy control of structures using magnetorheological dampers," in *Proceedings of the American Control Conference,* (Arlington, VA), 1097–1102. doi: 10.1109/ACC.2001.945866

Wang, D. H., and Liao, W. H. (2005). Modeling and control of magnetorheological fluid dampers using neural networks. *Smart Mater. Struct.* 14, 111–126. doi: 10.1088/0964-1726/14/1/011

Xu, Z. D., Guo, Y. Q. (2006). Fuzzy control method for earthquake mitigation structures with magnetorheological dampers. *J. Intell. Mater. Syst. Struct.* 17, 871–881. doi: 10.1177/1045389X06061044

Xu, Z. D., Sha, L. F., and Zhang, X. C. (2013). Design, performance test and analysis on magnetorheological damper for earthquake mitigation. *Struct. Control Health Monit.* 20, 956–970. doi: 10.1002/stc.1509

Xu, Z. D., Shen, Y. P. (2003). Intelligent bi-state control for the structure with magnetorheological dampers. *J. Intell. Mater. Syst. Struct.* 14, 35–42. doi: 10.1177/1045389X03014001004

Xu, Z. D., Shen, Y. P., and Guo, Y. Q. (2003). Semi-active control of structures incorporated with magnetorheological dampers using neural networks. *Smart Mater. Struct*. 12, 80–87. doi: 10.1088/0964-1726/12/1/309

Yang, G., Spencer, B. F. Jr., Carlson, J. D., Sain, M. K. (2002). Large-Scale MR fluid dampers: modeling and dynamic performance considerations, *Eng. Struct.* 24, 309–323. doi: 10.1016/S0141-0296(01)00097-9

Ying, Z. G., Ni, Y. Q., and Ko, J. M. (2002). "Non-clipping optimal control of randomly excited nonlinear systems using semi-active ER/MR dampers," in *Smart Structures and Materials: Smart Systems for Bridges, Structures, and Highways*, USA (San Diego, CA: SPIE), 209–218.

Conflict of Interest Statement: The authors declare that the research was conducted in the absence of any commercial or financial relationships that could be construed as a potential conflict of interest.

frontiers in Materials

ORIGINAL RESEARCH
published: 18 April 2019
doi: 10.3389/fmats.2019.00071

Confinement Effect of Concrete-Filled Steel Tube Columns With Infill Concrete of Different Strength Grades

*Liusheng He[1,2], Siqi Lin[3] and Huanjun Jiang[1,2]**

[1] State Key Laboratory of Disaster Reduction in Civil Engineering, Tongji University, Shanghai, China, [2] Department of Disaster Mitigation for Structures, Tongji University, Shanghai, China, [3] Department of Architecture, Kanagawa University, Yokohama, Japan

Concrete-filled steel tube (CFST) columns are increasingly used in composite construction. Under axial compression, the steel tube will sustain partial axial force and meanwhile provides the confinement to the infill concrete. The high axial strength capacity of CFST columns is largely related to the confinement provided by the steel tube. Extensive studies on CFST columns have been conducted. Nevertheless, how to quantify the efficiency of confinement effect in CFST columns using concrete with different strength grades is still missing. To address this issue, a series of compressive loading tests on CFST columns were conducted in present study. The variable parameters studied include concrete strength and diameter-to-thickness ratio of the steel tube. Six CFST stub columns in total were designed and tested under uniaxial compression. Axial strength, stress state in the steel tube, confined concrete strength and confining pressure acting on the infill concrete were carefully investigated. Test results show that the confinement factor (defined as the ratio of the nominal strength of empty steel tube to that of the unconfined concrete) is the most dominant factor influencing the confinement effect, and a larger confinement factor gives higher confinement effect. The low-strength concrete exhibits better performance of ductility and confinement compared with the high-strength concrete. The index of equivalent confining pressure was used to quantify the level of passive confinement provided by the steel tube in CFST columns. Based on the test results, a method to quickly quantify the confining pressure provided by the steel tube was proposed.

Keywords: concrete filled steel tube, confinement effect, confined concrete, active confining, passive confining

Edited by:
Zhao-Dong Xu,
Southeast University, China

Reviewed by:
Jianwei Zhang,
Beijing University of Technology, China
Dejian Shen,
Hohai University, China

Correspondence:
Huanjun Jiang
jhj73@tongji.edu.cn

Specialty section:
This article was submitted to Structural Materials, a section of the journal Frontiers in Materials

Received: *27 February 2019*
Accepted: *01 April 2019*
Published: *18 April 2019*

Citation:
He L, Lin S and Jiang H (2019) Confinement Effect of Concrete-Filled Steel Tube Columns With Infill Concrete of Different Strength Grades. Front. Mater. 6:71. doi: 10.3389/fmats.2019.00071

INTRODUCTION

Concrete-filled steel tube (CFST) columns are increasingly used in the construction of highrise buildings which require high strength and large working space especially at lower stories. As compared to reinforced concrete columns, existence of the exterior steel tube not only bears a portion of axial load but also most importantly provides confinement to the infill concrete. With the confinement provided by the steel tube, axial strength of the infill concrete can be largely enhanced. Also, the restraining effect of the infill concrete can prevent or at least delay the local buckling of the steel tube. This interaction between the infill concrete and steel tube together contributes to the high strength and good ductility.

Within the domain of researches focusing on confined concrete, there were basically two categories according to the way how the confinement was applied, active confining and passive confining. In the study of actively confined concrete, the confining pressure was either initially increased to a target value and then kept constant or increased from zero to the target value and then kept constant (Imran and Pantazopoulou, 1996; Lim and Ozbakkaloglu, 2015; Zhao et al., 2018). In active confining, a significant level of confining pressure is applied to the concrete from the very beginning. While in CFST columns, the steel tube provides confinement to the infill concrete in a passive way. At very small axial shortening, there is basically no confining pressure applied to the infill concrete because of the larger Poisson's ratio of the steel than that of concrete. The confining stress from the steel tube develops slowly even when the concrete stress reaches 80% of its unconfined compressive strength (Kinoshita et al., 1994). Also, with the increase of axial shortening, the efficiency of confinement degrades after the steel tube enters into the inelastic outward buckling. Therefore, the confinement of the passively confined concrete as in CFST columns is different from that in the actively confined concrete. Nevertheless, many compressive strength models for the confined concrete adopt the results of actively confined concrete (Mander et al., 1988; Attard and Setunge, 1996). Meanwhile, among many types, CFST columns using circular steel tubes are considered more effective in obtaining high compressive strength and ductility. In the previous study on circular CFST columns, primary research focuses include diameter-to-thickness ratio of the steel tube (Sakino et al., 2004; Han et al., 2005; Gupta et al., 2007; Abed et al., 2013), concrete strength (Giakoumelis and Lam, 2004; Yu et al., 2007; Lam and Gardner, 2008), bond behavior between steel tube and concrete (Xue et al., 2012; Liao et al., 2013; Tao et al., 2016; Chen et al., 2017), etc. Many studies conclude that the confinement effect from the exterior steel tube to the infill concrete is the key parameter in CFST columns and various means to enhance the confinement effect have been reported (Hu et al., 2011; Ho and Lai, 2013; Lai and Ho, 2015; He et al., 2018; Shen et al., 2019). The level of confinement in active confining is quite straightforward and the confining pressure can be directly adopted as a direct index in quantification. However, different from active confining, the confining pressure in CFST columns is not constant. So far, there is still less work available yet regarding the quantification of the confinement effect in CFST columns.

This paper aims to quantify the passive confinement effect in CFST columns. To address this, a series of CFST column specimens with infill concrete of different strength grades were designed and uniaxially compressed. Axial strength, stress state of steel tube and development and quantification of confinement effect were carefully investigated.

STRESS STATE OF STEEL TUBE

For CFST columns under axial compression, the axial load N is sustained by both the steel tube (σ_z) and infill concrete (σ_{cc}), as shown in **Figure 1**. The stress component σ_θ of the steel tube is the source for the lateral confining pressure σ_r applied to the infill concrete. With the existence of σ_r, the concrete compressive strength is largely enhanced. In the actively confined concrete, the confined concrete strength, f_{cc}, can be estimated by the following equation (Mander et al., 1988):

$$f_{cc} = f_c + k\sigma_r \tag{1}$$

where f_c is the compressive strength of unconfined concrete; k is a confinement coefficient, the value of which depends on the infill concrete; and σ_r is the lateral confining pressure.

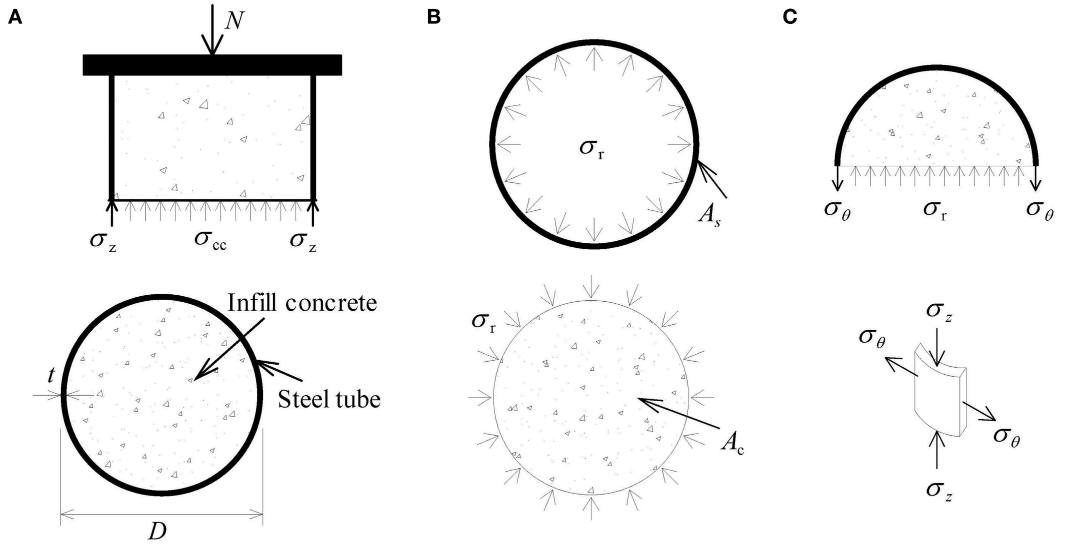

FIGURE 1 | Stress state: **(A)** axial direction; **(B)** steel tube and infill concrete; **(C)** free body diagram.

The value of the confinement coefficient k is often taken as 4.1 after the work by Richart et al. (1928). Though k should be a function of the concrete mix, its value is not much different for stronger or weaker concrete (Imran and Pantazopoulou, 1996).

In CFST columns, the lateral confining pressure can be calculated according to the force equilibrium condition of the cross section. As it can be seen from **Figure 1C**, the equilibrium of σ_r and $\sigma_{s\theta}$ gives

$$(D - 2t)\sigma_r = -2t\sigma_\theta \tag{2}$$

where D is the external diameter of the steel tube, and t is the steel tube thickness.

Once the hoop stress in the steel tube is obtained, the confining pressure provided by the steel tube to the infill concrete can be estimated.

Rewriting Equation 2 gives

$$\sigma_r = \frac{-2t}{D - 2t}\sigma_\theta \tag{3}$$

Compressive strength of the infill concrete can be obtained by subtracting the force undertook by the steel tube from the overall axial strength of the column as follows.

$$f_{cc} = \frac{N - \sigma_z A_s}{A_c} \tag{4}$$

where f_{cc} is the compressive stress of the infill concrete; N is the axial load; A_s and A_c are the cross-sectional area of steel tube and concrete, respectively; and σ_z is the axial stress in the steel tube.

For the thin-walled steel tube, the von Mises yield criterion can be applied. Under both axial stress component σ_z and the hoop stress component σ_θ, the equivalent stress σ_e can be determined as follows.

$$\sigma_e = \sqrt{{\sigma_\theta}^2 - \sigma_\theta\sigma_z + {\sigma_z}^2} \tag{5}$$

In this study, elastic-perfectly plastic model is assumed for the tube steel. By comparing the equivalent stress σ_e with the yield stress, the steel tube can be identified to being yielding or not. The stress state of the steel tube can be calculated using the strain increment method (Hu et al., 2011). In the elastic range, the stress state is calculated by the generalized Hooke law:

$$\begin{Bmatrix} d\sigma_z^i \\ d\sigma_\theta^i \end{Bmatrix} = \frac{E_s}{1 - \vartheta^2}\begin{bmatrix} 1 & \vartheta \\ \vartheta & 1 \end{bmatrix}\begin{Bmatrix} d\varepsilon_z^i \\ d\varepsilon_\theta^i \end{Bmatrix} \tag{6}$$

TABLE 1 | Summary of test specimens.

Specimen	D (mm)	t (mm)	D/t	f_c (N/mm^2)	f_s (N/mm^2)	$\lambda = \frac{f_s A_s}{f_c A_c}$	N_0 (kN)	$\frac{N_u}{N_0}$
1	165.2	3.7	44.6	29.5	366.0	1.19	1,264	1.13
2	165.2	3.7	44.6	43.5	366.0	0.81	1,538	1.09
3	165.2	3.7	44.6	58.0	366.0	0.61	1,821	1.15
4	165.2	3.7	44.6	81.6	366.0	0.43	2,283	1.10
5	230.0	2.3	100.0	32.0	360.8	0.46	1,870	1.06
6	230.0	2.3	100.0	64.0	360.8	0.23	3,147	1.04

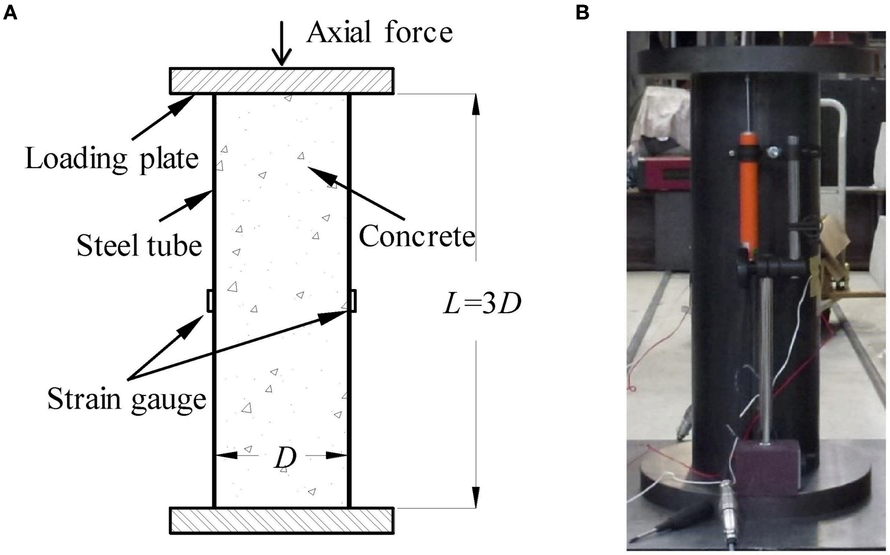

FIGURE 2 | Test setup: **(A)** diagram; **(B)** photograph in test.

where σ_z and σ_θ are the axial stress and hoop stress, respectively; ε_z and ε_θ are the axial strain and hoop strain, respectively; E_s is the elastic modulus; ϑ is Poisson's ratio of the steel tube; and i is the present strain increment number.

For the elastic-plastic range, the stress increments are calculated from strain increments by the following equation:

$$\begin{Bmatrix} d\sigma_z^i \\ d\sigma_\theta^i \end{Bmatrix} = \frac{E_s}{1-\vartheta^2}\begin{bmatrix} 1 - s_a^2/s_c & \vartheta - s_a s_b/s_c \\ \vartheta - s_a s_b/s_c & 1 - s_b^2/s_c \end{bmatrix}\begin{Bmatrix} d\varepsilon_z^i \\ d\varepsilon_\theta^i \end{Bmatrix} \quad (7)$$

$$s_a = s_x + \vartheta s_\theta \quad (8)$$

$$s_b = s_\theta + \vartheta s_x \quad (9)$$

$$s_c = s_x^2 + s_\theta^2 + 2\vartheta s_x s_\theta \quad (10)$$

$$s_x = \frac{1}{3}(2\sigma_z^{i-1} - \sigma_\theta^{i-1}) \quad (11)$$

$$s_\theta = \frac{1}{3}(2\sigma_\theta^{i-1} - \sigma_x^{i-1}) \quad (12)$$

where s_x and s_θ are the deviatoric strain and stress, respectively.

After obtaining the axial and hoop stresses of the steel tube based upon the measured axial and hoop strains at each loading step and the above equations, the confined concrete strength can be estimated according to Equation 4.

EXPERIMENTAL PROGRAM

Test Specimens

All specimens were designed to have a same length-to-diameter ratio of 3 to ensure stub column behavior. **Table 1** gives the summary of the six specimens designed. Basically, they can be divided into two groups, Specimens 1–4 are in Group 1 with a tube diameter of 165.2 mm and thickness of 3.7 mm, and Specimens 5 and 6 in Group 2 use a tube diameter of 230 mm and thickness of 2.3 mm. The concrete was commercial ready-mixed concrete with normal mixing and curing techniques. The concrete strength of Specimens in Group 1 used four grades, with cylinder (with a diameter of 100 mm and height of 200 mm) compressive strengths of 29.5, 43.5, 58.0, and 81.6 N/mm^2, respectively; Specimens in Group 2 used two grades of concrete, with cylinder compressive strengths of 32.0 and 64.0 N/mm^2, respectively. All steel tubes were cold-formed carbon steel and seam welded by machine welding. To get the basic mechanical property of the steel material, three coupons were randomly cut from the steel tube and were tested according to standard procedures (Davis, 2004). The yield strengths of the steel tube were found to be 366.0 MPa for Group 1, and 360.8 MPa for Group 2, respectively. Before casting the infill concrete, the inner surface of the steel tube was smeared with a thin layer of grease to reduce the friction between the steel tube and concrete.

Test Setup and Instrumentation

All specimens were subjected to monotonic axial compression exerted by a universal testing machine with a maximum capacity of 5,000 kN. At two end surfaces of the CFST column, two steel plates with a thickness of 50 mm were used to ensure even axial compression. Monotonic axial loading with displacement control was applied. For displacement control, axial shortening, the relative displacement between the top and bottom steel plates, was recorded and used as the actual compressive deformation. Two linear variable differential transducers (LVDTs) with a stroke of 50 mm was installed in parallel with the longitudinal axis of specimens to measure the axial shortening, as shown in **Figure 2**. To measure the strain state of the steel tubes, two bidirectional strain gauges were installed on the external surface of the steel tube at the mid-height.

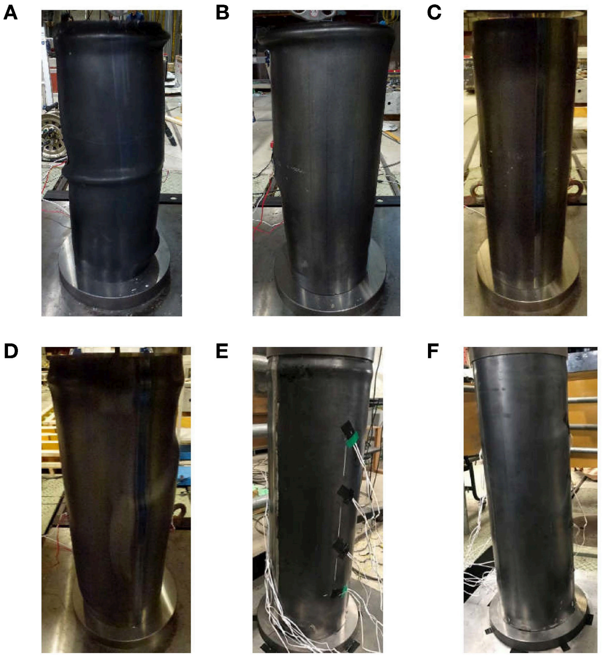

FIGURE 3 | Failure modes: **(A)** specimen 1; **(B)** specimen 2; **(C)** specimen 3; **(D)** specimen 4; **(E)** specimen 5; **(F)** specimen 6.

TEST RESULTS AND DISCUSSIONS

All specimens were centrally compressed. The compression loading was stopped when either the maximum axial shortening reached 5% of column length or axial strength dropped sharply.

General Observation

All loadings went smooth without brittle deformation observed. **Figure 3** shows the final failure mode of all six specimens. All of them experienced similar failure mode, such as the outward buckling of the steel tube at both ends at large axial shortening and continuous expansion at the mid-height. For Specimens 4 and 6 using high-strength infill concrete, cylinder compressive strength of 81.6 and 64.0 N/mm^2 respectively, exhibited clear sign of concrete crushing at the mid-height, which indicated the brittle characteristic of the high-strength concrete.

Axial Strength Capacity

In order to compare the results, the nominal axial strength of CFT columns is defined as $N_0 = f_s A_s + f_c A_c$, where f_s is steel tube yield strength; A_s is the sectional area of steel tube; f_c is

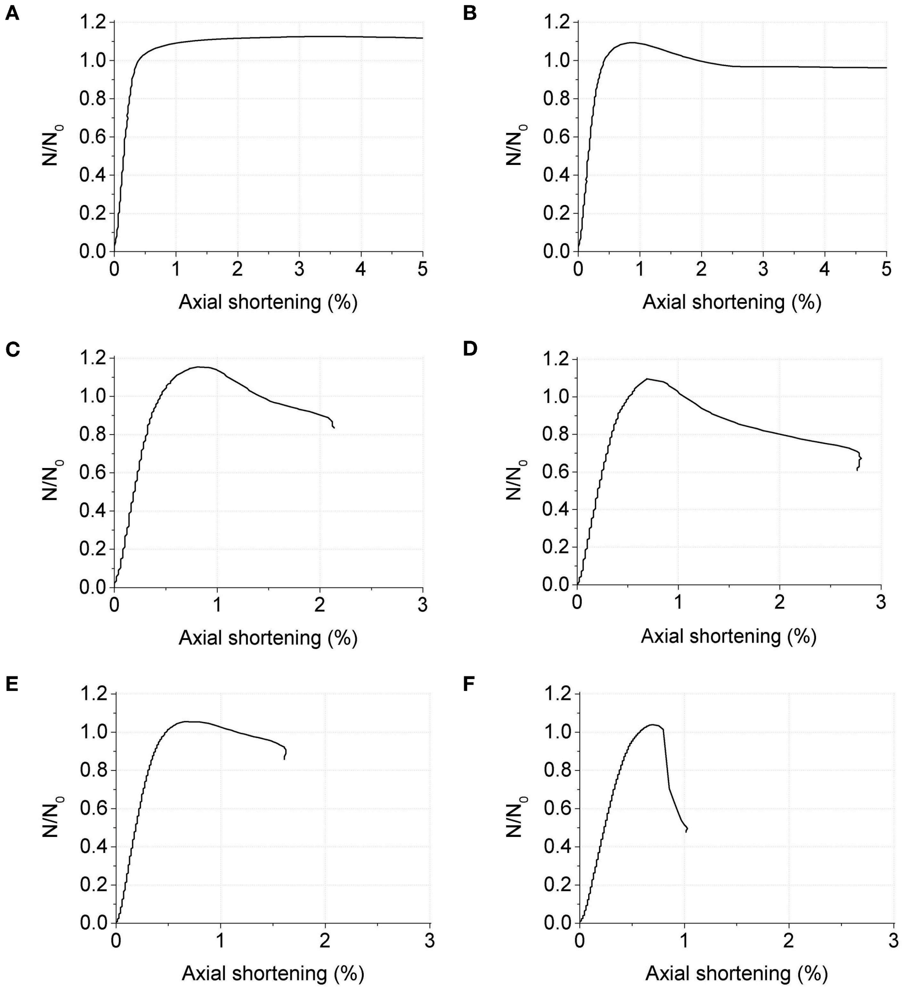

FIGURE 4 | Axial load-deformation curves: **(A)** $f_c = 29.5$, $\lambda = 1.19$; **(B)** $f_c = 43.5$, $\lambda = 0.81$; **(C)** $f_c = 58.0$, $\lambda = 0.61$; **(D)** $f_c = 81.6$, $\lambda = 0.43$; **(E)** $f_c = 32.0$, $\lambda = 0.46$; **(F)** $f_c = 64.0$, $\lambda = 0.23$.

concrete cylinder compressive strength; and A_c is the sectional area of concrete.

Figure 4 shows the measured axial load vs. compressive deformation for all specimens. The ordinate is the normalized axial strength, defined as the measured axial load N divided by the nominal axial strength N_0, and the abscissa of axial shortening is the ratio of axial displacement measured by LVDTs to the height of columns. The most obvious difference in the load-deformation curves is the post-peak behavior. Only Specimen 1 demonstrated hardening behavior while the rest specimens showed more or less softening. Specimen 6 showed the sharpest decrease of strength beyond the peak strength and its deformability was the worst with the maximum axial displacement of only about 1% of the column length. Its axial strength dropped to less than half of the peak strength almost right after reaching the peak strength. Such a sudden decrease of axial strength needs to be avoided in view of collapse resistance capacity of the building. For specimens in both Group 1 and Group 2, low-strength concrete demonstrated less post-peak strength decrease than high-strength concrete. The width-to-thickness ratio of specimens in Group 2 is much larger than that of specimens in Group 1. While there is no clear difference in the shape of axial load-deformation curve, which means the width-to-thickness of the steel tube is not the controlling parameter for the post-peak behavior. As listed in the last column of **Table 1**, there is no much difference among the maximum normalized axial strength ($\frac{N_u}{N_0}$) for all the specimens, with the value of $\frac{N_u}{N_0}$ ranging between 1.04 and 1.15.

Strain State of Steel Tube and Calculated Stress

As introduced in the section of instrumentation, both the axial and hoop strains in the steel tube were measured by electrical strain gauges. The recorded strain readings were given in **Figure 5**. The ordinate of "nominal axial stress" was the ratio of axial load divided by the whole sectional area. With the increase of axial load, both the axial and hoop strains in the steel tube increased. In the linear branch, the absolute value of axial strain

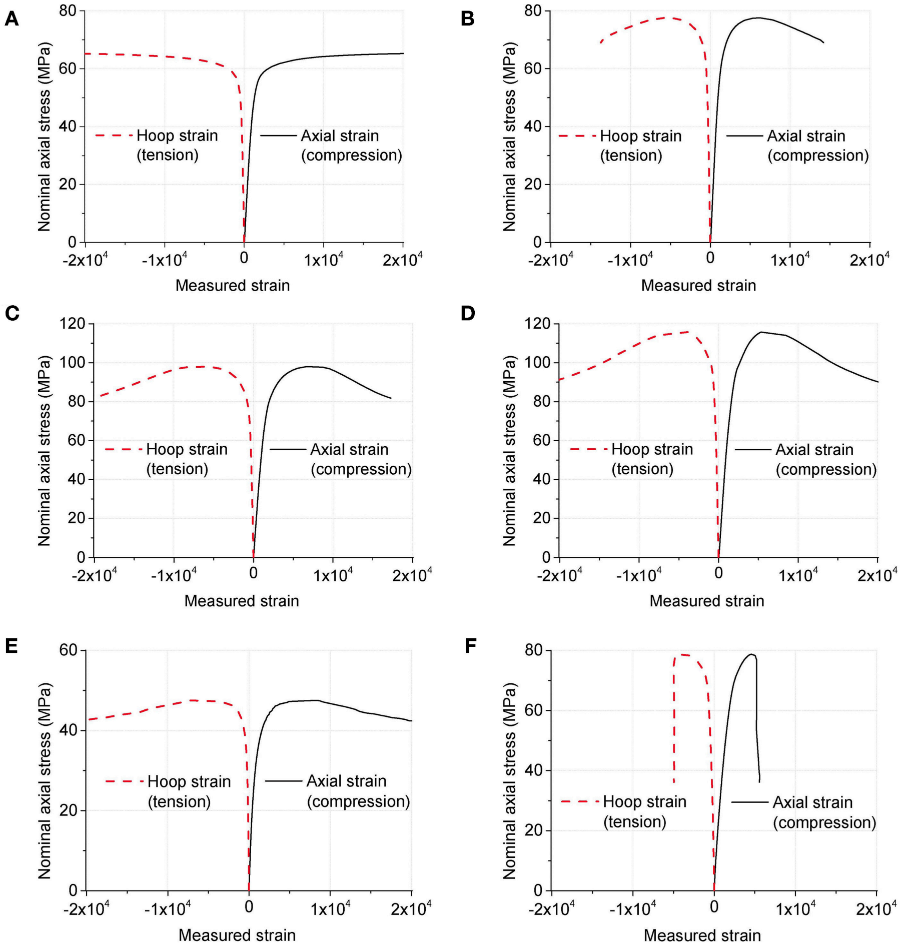

FIGURE 5 | Recorded strain data: **(A)** f_C = 29.5, λ = 1.19; **(B)** f_C = 43.5, λ = 0.81; **(C)** f_C = 58.0, λ = 0.61; **(D)** f_C = 81.6, λ = 0.43; **(E)** f_C = 32.0, λ = 0.46; **(F)** f_C = 64.0, λ = 0.23.

was about 3 times that of the hoop strain. Beyond the peak strength, Specimen 1 exhibited the most stable development of both axial strain and hoop strain, and Specimen 6 showed the most abrupt decrease of axial strain and hoop strain.

Substituting the recorded strain data into Equations 6 and 7 gives the axial stress σ_z and hoop stress σ_θ of the steel tube, as shown in **Figure 6**. It is clear that the axial stress component was much larger than the hoop stress component. For instance, at an axial shortening of 0.5%, the axial stress in the steel tube of Specimen 1 was about 4 times the hoop stress; for Specimen 6, the ratio was about 25. In view of providing confinement to the infill concrete through the hoop stress component, the steel tube is far from being fully used.

Confinement Effect

The improved compressive strength of CFST columns is ascribed to the confinement provided by the steel tube to the infill concrete. The confinement effect is usually quantified by the confinement factor λ, expressed by $\lambda = \frac{f_s A_s}{f_c A_c}$ in which A_s and A_c are the cross-sectional area of steel tube and concrete; and f_s and f_c are the strength of steel and concrete, respectively.

As described in a previous session, the maximum normalized axial strength ($\frac{N_u}{N_0}$) for specimens with different λ values was not much different for all the specimens. However, after the reaching of the maximum axial strength, the post-peak behavior was closely related to the value of λ. Specimens with a larger λ showed better ductility, which also answered the hardening or softening behavior in the axial load-deformation curves. For Specimens 4 and 5 having similar confinement factor, Specimen 5 using low strength concrete exhibited smaller decrease of axial strength. For instance, nominal axial strength deceased to 0.95 for Specimen 5 at an axial shortening of 1.5%, while 0.79 for Specimen 4 using high strength concrete. Further loading of Specimen 5 was terminated after a drift ratio of 1.6% due to the malfunction of LVDT sensor rather than the sharp decrease of strength as in other specimens. Smaller strength decrease can be expected in CFST columns using low strength concrete. Specimen 6 with the smallest value of λ demonstrated the most serious strength degradation beyond the peak strength.

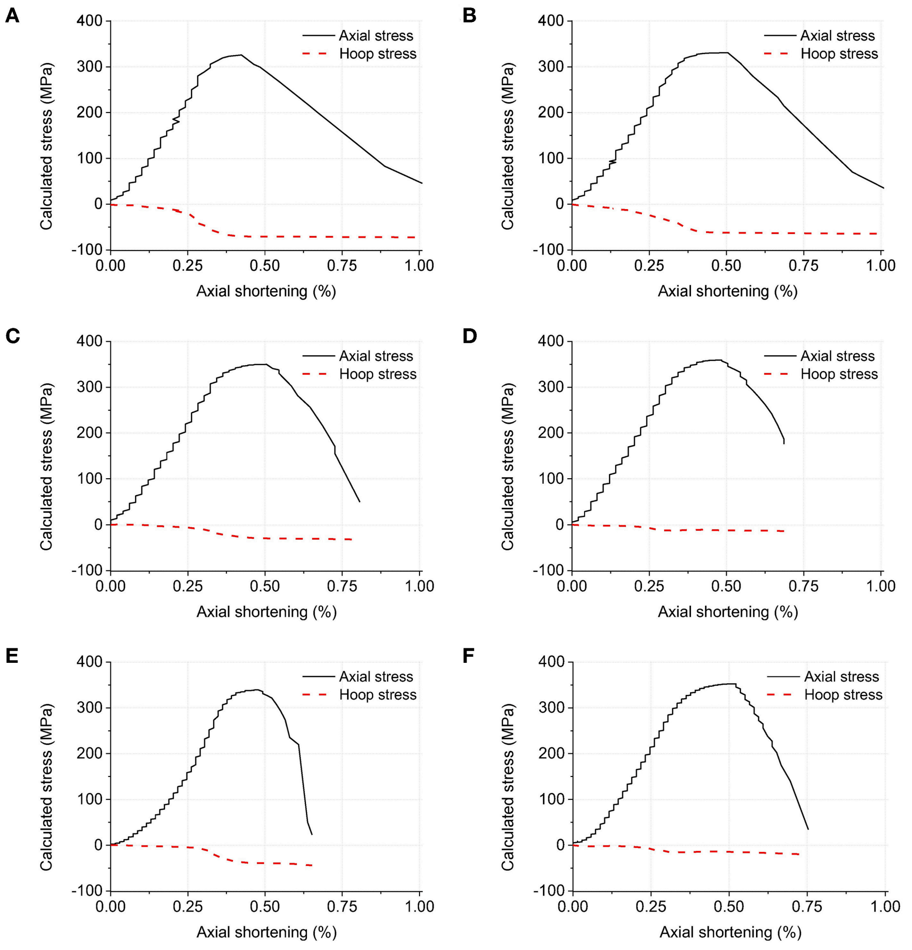

FIGURE 6 | Calculated stress data: **(A)** $f_C = 29.5$, $\lambda = 1.19$; **(B)** $f_C = 43.5$, $\lambda = 0.81$; **(C)** $f_C = 58.0$, $\lambda = 0.61$; **(D)** $f_C = 81.6$, $\lambda = 0.43$; **(E)** $f_C = 32.0$, $\lambda = 0.46$; **(F)** $f_C = 64.0$, $\lambda = 0.23$.

It is also can be seen from **Figure 6** that the value of λ influenced the ratio of axial stress to hoop stress of the steel tube. For the four specimens with the same overall dimensions in Group 1, the smaller the value of λ was, the larger the ratio became. For instance, at an axial shortening of 0.5%, the ratios were 4.2, 5.6, 12.0, and 29.0 for Specimens 1, 2, 3, and 4, respectively. The two specimens in Group 2 had the similar pattern. According to Equation 3, the hoop stress component is the source for confinement. The smaller ratio between axial stress and hoop stress meant larger hoop stress and thus larger confinement. However, the strength grade of infill concrete also had an influence on the value of confinement. For Specimens 4 and 5 having a similar value of λ, the ratio of Specimen 5 using low strength concrete was about one third of that of Specimen 4, which indicated that the confinement in CFST columns using low strength infill concrete was greater.

After obtaining the axial stress and hoop stress in the steel tube, the confining pressure applied by the exterior steel tube to the infill concrete can be calculated according to Equation 3; the confined concrete strength can be calculated according to Equation 4. **Figure 7** shows the relationship between the confined concrete strength and confining pressure, with the abscissa being the normalized confined concrete strength defined by the ratio between the confined concrete strength and unconfined concrete strength. It is clear that the confining pressure is not constant in CFST columns. The confining pressure increased from zero to a nearly constant value eventually. The confined concrete strength increased with the increase of confining pressure. The larger the value of λ is, the larger the confining pressure, which is consistent with the previous discussion.

For actively confined concrete with constant confining pressure, the relationship between the compressive strength and confining pressure can be given by the following equation (Zhao et al., 2018):

$$f_{cc} = f_c + 2.2 f_c^{0.3} \sigma_r^{0.81} \tag{13}$$

To quantify the level of confinement effect in passively confined CFST columns, Equation 13 can be adopted as an equivalent method. The level of confinement effect in CFST columns can be estimated by the equivalent confining pressure which gives the same confined concrete strength in the actively

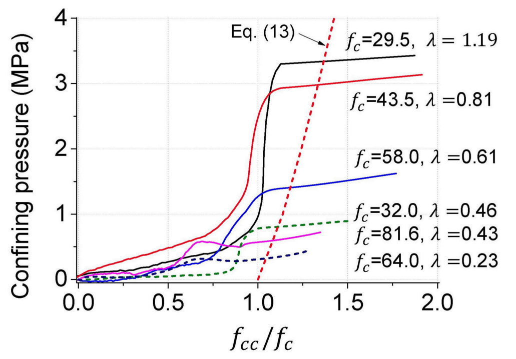

FIGURE 7 | Relationship between confined concrete strength and confining pressure.

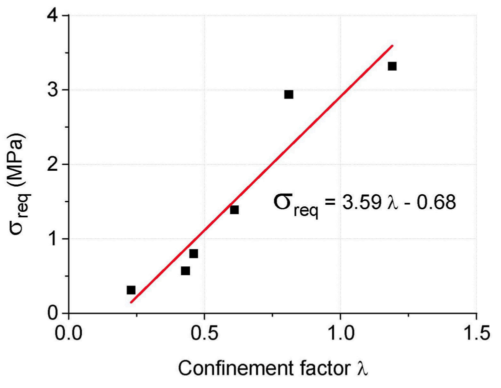

FIGURE 8 | Equivalent confining pressure.

confined concrete. Equation 13 was also plotted in **Figure 7** in dashed line. The intersections were the equivalent confining pressure for each specimen. **Figure 8** gives the relationship between the confinement factor λ and equivalent confining pressure σ_{req}. From a regression analysis, the equivalent confining pressure in CFST columns can be roughly estimated as follows.

$$\sigma_{req} = 3.59\lambda - 0.68 \tag{14}$$

The mean and coefficient of variance of the ratio of estimation according to Equation (14) to tested values are 1.0209 and 0.3255, respectively.

To this end, knowing the confinement factor of a CFST column, the level of confinement effect can be quickly estimated.

CONCLUSIONS

This study worked on the confinement effect in CFST columns and a method to quantify the equivalent confining pressure applied to the infill concrete by the steel tube was developed. The major findings are summarized as follows:

(1) The confinement factor was verified as the key parameter for the axial load carrying capacity. Basically, a larger confinement factor gave smaller post-peak axial strength decrease and larger ductility. With the similar confinement factor, the low-strength concrete exhibited less strength decrease.
(2) The confinement factor was directly related to the level of confining pressure provided by the steel tube to the infill concrete. The strength grade of infill concrete also influenced the confining pressure and CFST columns using low-strength infill concrete showed greater confining pressure.
(3) The stress state of the steel tube and the confined concrete strength were analyzed. To quantify the confinement level in CFST columns, the concept of confining pressure in actively confined concrete was adopted and an index of equivalent confining pressure was proposed. An equation capable of quickly estimating the passive confining pressure in CFST columns was proposed.

DATA AVAILABILITY

All datasets generated for this study are included in the manuscript and/or the supplementary files.

AUTHOR CONTRIBUTIONS

LH supervised the research and wrote the first draft manuscript. SL analyzed test data. HJ reviewed and revised the manuscript, and approved the submitted version. All the authors participated in discussion of the research.

FUNDING

The authors are grateful for the support from National Key Research and Development Program of China under Grant No. 2017YFC1500701 and Program of Shanghai Academic Research Leader under Grant No. 18XD1403900.

REFERENCES

Abed, F., AlHamaydeh, M., and Abdalla, S. (2013). Experimental and numerical investigations of the compressive behavior of concrete filled steel tubes (CFSTs). *J. Constr. Steel Res.* 80, 429–439. doi: 10.1016/j.jcsr.2012.10.005

Attard, M., and Setunge, S. (1996). Stress-strain relationship of confined and unconfined concrete. *ACI Mater J.* 93, 432–442.

Chen, Y., Feng, R., Shao, Y., and Zhang, X. (2017). Bond-slip behaviour of concrete-filled stainless steel circular hollow section tubes. *J. Constr. Steel Res.* 130, 248–263. doi: 10.1016/j.jcsr.2016.12.012

Davis, J. R. (2004). *Tensile Testing, Second Edition*. Novelty, OH: ASM International.

Giakoumelis, G., and Lam, D. (2004). Axial capacity of circular concrete-filled tube columns. *J. Constr. Steel Res.* 60, 1049–1068. doi: 10.1016/j.jcsr.2003.10.001

Gupta, P. K., Sarda, S. M., and Kumar, M. S. (2007). Experimental and computational study of concrete filled steel tubular columns under axial loads. *J. Constr. Steel Res.* 63, 182–193. doi: 10.1016/j.jcsr.2006.04.004

Han, L. H., Yao, G. H., and Zhao, X. L. (2005). Tests and calculations for hollow structural steel (HSS) stub columns filled with self-consolidating concrete (SCC). *J. Constr. Steel Res.* 61, 1241–1269. doi: 10.1016/j.jcsr.2005.01.004

He, L., Zhao, Y., and Lin, S. (2018). Experimental study on axially compressed circular CFST columns with improved confinement effect. *J. Constr. Steel Res.* 140, 74–81. doi: 10.1016/j.jcsr.2017.10.025

Ho, J. C. M., and Lai, M. H. (2013). Behaviour of uni-axially loaded CFST columns confined by tie bars. *J. Constr. Steel Res.* 83, 37–50. doi: 10.1016/j.jcsr.2012.12.014

Hu, Y. M., Yu, T., and Teng, J. G. (2011). FRP-confined circular concrete-filled thin steel tubes under axial compression. *J. Compos. Constr.* 15, 850–860. doi: 10.1061/(ASCE)CC.1943-5614.0000217

Imran, I., and Pantazopoulou, S. (1996). Experimental study of plain concrete under triaxial stress. *ACI Mater. J.* 93, 589–601.

Kinoshita, M., Kotsovos, M. D., and Pavlovic, M. N. (1994). Behavior of concrete under passive confinement. *J. Mater. Conc. Struct. Pavements* 502, 131–142.

Lai, M. H., and Ho, J. C. M. (2015). Effect of continuous spirals on uni-axial strength and ductility of CFST columns. *J. Constr. Steel Res.* 104, 235–249. doi: 10.1016/j.jcsr.2014.10.007

Lam, D., and Gardner, L. (2008). Structural design of stainless steel concrete filled columns. *J. Constr. Steel Res.* 64, 1275–1282. doi: 10.1016/j.jcsr.2008.04.012

Liao, F. Y., Han, L. H., and Tao, Z. (2013). Behaviour of CFST stub columns with initial concrete imperfection: analysis and calculations. *Thin Walled Struct.* 70, 57–69. doi: 10.1016/j.tws.2013.04.012

Lim, J., and Ozbakkaloglu, T. (2015). Investigation of the influence of the application path of confining pressure: tests on actively confined and FRP-confined concretes. *J. Struct. Eng.* 141:04014203. doi: 10.1061/(ASCE)ST.1943-541X.0001177

Mander, J. B., Priestley, M. J. N., and Park, R. (1988). Theoretical stress-strain model for confined concrete. *J. Struct. Eng.* 114, 1804–1826. doi: 10.1061/(ASCE)0733-9445(1988)114:8(1804)

Richart, F. E., Brandtzaeg, A., and Brown, R. L. (1928). *A Study of the Failure of Concrete Under Combined Compressive Stresses.* Bulletin No. 185, University of Illinois, Engineering Experimental Station, Urbana, Illinois.

Sakino, K., Nakahara, H., Morino, S., and Nishiyama, A. (2004). Behavior of centrally loaded concrete-filled steel-tube short columns. *J. Struct. Eng.* 130, 180–188. doi: 10.1061/(ASCE)0733-9445(2004)130:2(180)

Shen, Q., Wang, J., Wang, J., and Ding, Z. (2019). Axial compressive performance of circular CFST columns partially wrapped by carbon FRP. *J. Constr. Steel Res.* 155, 90–106. doi: 10.1016/j.jcsr.2018.12.017

Tao, Z., Song, T., Uy, B., and Han, L. (2016). Bond behavior in concrete-filled steel tubes. *J. Constr. Steel Res.* 120, 81–93. doi: 10.1016/j.jcsr.2015.12.030

Xue, J. Q., Briseghella, B., and Chen, B. C. (2012). Effects of debonding on circular CFST stub columns. *J. Constr. Steel Res.* 69, 64–76. doi: 10.1016/j.jcsr.2011.08.002

Yu, Z. W., Ding, F. X., and Cai, C. S. (2007). Experimental behavior of circular concrete-filled steel tube stub columns. *J. Constr. Steel Res.* 63, 165–174. doi: 10.1016/j.jcsr.2006.03.009

Zhao, Y., Lin, S., Lu, Z., Saito, T., and He, L. (2018). Loading paths of confined concrete in circular concrete loaded CFT stub columns subjected to axial compression. *Eng. Struct.* 156, 21–31. doi: 10.1016/j.engstruct.2017.11.010

Conflict of Interest Statement: The authors declare that the research was conducted in the absence of any commercial or financial relationships that could be construed as a potential conflict of interest.

ORIGINAL RESEARCH
published: 17 April 2019
doi: 10.3389/fmats.2019.00064

The Influence of Key Component Characteristic on the Resistance to Progressive Collapse of Composite Joint With the Concrete-Filled Steel Tubular Column and Steel Beam With Through Bolt-Extended Endplate

*Yan-Li Shi, Long Zheng and Wen-Da Wang**

School of Civil Engineering, Lanzhou University of Technology, Lanzhou, China

OPEN ACCESS

Edited by:
Zhao-Dong Xu,
Southeast University, China

Reviewed by:
Wensu Chen,
Curtin University, Australia
Lanhui Guo,
Harbin Institute of Technology, China
Rui Wang,
Taiyuan University of Technology, China

***Correspondence:**
Wen-Da Wang
wangwd@lut.cn

Specialty section:
This article was submitted to Structural Materials, a section of the journal Frontiers in Materials

Received: *03 February 2019*
Accepted: *28 March 2019*
Published: *17 April 2019*

Citation:
Shi Y-L, Zheng L and Wang W-D (2019) The Influence of Key Component Characteristic on the Resistance to Progressive Collapse of Composite Joint With the Concrete-Filled Steel Tubular Column and Steel Beam With Through Bolt-Extended Endplate. Front. Mater. 6:64. doi: 10.3389/fmats.2019.00064

In this study, a finite element (FE) analysis of a composite joint with the concrete-filled steel tubular (CFST) column and steel beam, with a through bolt-extended endplate, was carried out in a progressive collapse. The reasonable constitutive model of a steel plate, through bolt and core concrete materials under a large deformation were selected, and the comprehensive fracture criterion and damage evolution path of the ductile damage, shear damage and mixed damage modes based on the stress triaxiality, were considered in the steel constitutive structure, respectively. The accuracy of the modeling method and material constitutive, was verified by a comparison of the overall deformation processes, failure modes and resistances of joints, with both experimental and FE results. A typical composite joint, with the CFST column and steel beam with through bolt-extended endplate was designed, and four joints were derived for comparison by adjusting the diameter of the through bolt and the thickness of the extended endplate. The FE models of these five joints were established to investigate failure modes and resistance mechanisms by using the ABAQUS/Explicit module. The results showed that the failure modes of the composite joint with the CFST column and steel beam with through bolt-extended endplate, can be divided into three types: steel beam and through bolts failure, through bolts failure, and steel beam failure. The different strengths and weaknesses between the through bolt, extended endplate and steel beam affect the progressive collapse resistance of the joint directly. With the increase of the diameter of the through bolt and the thickness of the extended endplate, the failure mode of the joint gradually turns from through bolt failure to steel beam failure, and the resistance and ductility of the joint are enhanced and the anti-progressive collapse ability of the composite joint, with a CFST column and steel beam with a through bolt-extended endplate, increases.

Keywords: concrete-filled steel tubular (CFST) structures, through bolt, extended endplate, steel constitutive, core concrete constitutive, bolt constitutive, steel fracture criterion, progressive collapse

INTRODUCTION

Progressive collapse is the collapse or the disproportionate damage from the initial damage of a structure. Since the incident of Ronan Point apartment in 1958, progressive collapse captured the public's attention. After the incident of the World Trade Center buildings in 2001, studies on progressive collapse entered a climax (Adam et al., 2018). Yi et al. (2008) conducted an experimental study on progressive collapse resistance of a four-bay and three-story reinforced concrete frame and analyzed the resistance mechanism. Dinu et al. (2016) carried out a test on a 2 × 2 bay one-story steel frame under column loss, and the beam to column connection type was a bolt-extended endplate. The influence of the main and secondary beam connection was considered in the test in general. Pirmoz and Liu (2016) carried out an experimental and FE study on a three-story double-span steel frame against a progressive collapse, which uses a post-tensioned beam to column connection. Li et al. (2017) conducted a static test on the 3D reduced scale steel frame under inter column loss and analyzed the torsion effect of the main and secondary beam connection mainly. Wang et al. (2017) established FE models of CFST column to steel beam frame, using multi-scale modeling under static and dynamic loads.

As the preliminary resistance of a structural defense against a progressive collapse, the joint plays an important role in the frame structure. Recently, many researchers have carried out large-scale studies on the progressive collapse resistance of the joint. Sadek et al. (2011) conducted a comparison test of ordinary steel connections, reduced beam steel connections and ordinary concrete connections against a progressive collapse. Yang and Tan (2013) carried out static loading tests on steel beam to column joints with simple connections and semi-rigid connections and investigated the failure modes of joints with different bolt configurations. Oosterhof and Driver (2015) conducted a study on the shear beam to column connections under column removal. Wang et al. (2016) carried out an experimental and FE study on the anti-progressive collapse of three types of steel tube column to steel beam substructures. Guo et al. (2013) and Guo et al. (2015) conducted tests on the steel-concrete composite frames with rigid and semi-rigid connections, respectively. And Guo et al. (2014) and Gao et al. (2017) conducted experimental studies on the sagging moment, hogging moment, and tensile force of these two types of composite joints. Gong (2017) conducted an experimental study on the bolted-angle connections against progressive collapse, and the test results included the deformation and resistance curves of specimens. Dinu et al. (2017) conducted an anti-progressive collapse test on four specimens with a three-column double-span substructure and discussed the influence of rigid and semi-rigid connections. Xu et al. (2018a) conducted an experimental study about the resistance of a CFST column to steel beam with different bolted configurations, and the connection types covered the flush end-plate, extended the end-plate and stiffened the angle. Wang et al. (2018) performed an FE analysis of a CFST column to steel beam with a through-center construct against a progressive collapse. The characteristics, advantages, and disadvantages of the failure mode at the beam and at the column were analyzed, respectively. However, the above-mentioned research mainly focuses on steel structures and reinforced concrete structures, while there are few studies on composite structures such as CFST structures. In addition, there are few studies on the connections of through bolt-extended endplate, so it is necessary to carry out the resistance of a progressive collapse of the composite joint with the CFST column and steel beam with through bolt-extended endplate.

Indeed, the study of progressive collapse involves the fracture of metallic materials under a large deformation, including the fracture criterion and damage evolution path. Early scholars judged the damage criterion of steel based on the principle of micro-holes and micro-cracks inside the metal (McClintock, 1968; Roy et al., 1981; Atkins, 1996), and then scholars began to pay attention to the decisive influence of stress triaxiality on the damage criterion of steel (Rice and Tracey, 1969; Hancock and Mackenzie, 1976; Mirza et al., 1996; Rosa et al., 2001; Bao and Wierzbicki, 2004). The widely used fracture criterion includes VGM criterion, SMCS criterion and X-W criterion. Rice and Tracey (1969) proposed the VGM criterion, that is, the degradation mechanism of nucleation, expansion, aggregation and shrinkage of the hole. When the material stress and strain history integral amount reaches a certain value, the material is judged as damaged. Hancock and Mackenzie (1976) proposed the SMCS criterion, which instead of considering the integral form of stress triaxiality to plastic strain, assumes that the stress triaxiality remains unchanged in the damage process. Wierzbicki and Xue (2005) and Xue (2005) proposed the X-W criterion, which is mainly based on the equivalent plastic strain accumulation mechanism, that is, when the internal equivalent plastic strain accumulation reaches the critical value, the materials begin to enter the damage state. Xu and Wu (2012) and Xu et al. (2013, 2018b, 2019) carried out damage detection studies of structures and bridges based on different damage criterion and evolution processes. Indeed, the damage evaluation criterion and evolution process of steel at the degradation stage are relatively complex, moreover, the fracture criterion and damage evolution path of materials are key issues in the study of joint anti-progressive collapse. However, previous scholars did not pay much attention to these two issues, which should be considered in detail.

In this paper, the reasonable steel constitutive model was selected, and the comprehensive fracture criterion and within this model, the damage evolution path based on stress triaxiality was considered. The results of relevant tests were selected to simulate and verify the accuracy of the modeling method and material constitutive. One typical composite joint with a CFST column and steel beam with a through bolt-extended endplate named SJ-EP-TB-1 was designed, and four joints were derived for comparison, by adjusting the diameter of the through bolt and the thickness of the extended endplate. The FE models of these five joints were established to investigate the failure modes and resistance mechanisms, using the ABAQUS/Explicit module.

MATERIALS CONSTITUTIVE MODELS

This paper involves the CFST column and the stress of this type of concrete is more complicated than ordinary concrete. Due to the interaction between the steel tube and core concrete, the restraint of the steel tube on concrete, should be considered. This paper refers to the constitutive model of the compressive state of core concrete with a square section, considering the constraint effect of the steel tube proposed by Han et al. (2007).

$$y = \begin{cases} 2x - x^2 & , x \leq 1; \\ \frac{x}{\beta \cdot (x-1)^{\eta} + x} & , x > 1 \end{cases} \tag{1}$$

where, $x = \frac{\varepsilon}{\varepsilon_0}$, $y = \frac{\sigma}{\sigma_0}$, $\sigma_0 = f'_c$,

$$\varepsilon_0 = \varepsilon_c + 800\xi^{0.2} \times 10^{-6}, \varepsilon_c = \left(1300 + 12.5 f'_c\right) \times 10^{-6},$$

$$\eta = 1.6 + \frac{1.5}{x}, \beta = \frac{\left(f'_c\right)^{0.1}}{1.2\sqrt{1+\xi}}$$

In which, ε and ε_0 is the concrete compressive strain and peak compressive strain, respectively. σ and σ_0 is the concrete compressive stress and peak compressive stress, respectively. The units for stress and strain are N/mm^2 and με, respectively. f'_c is the cylinder strength of concrete. ξ is the confinement factor, and is defined as following:

$$\xi = \frac{A_S f_y}{A_C f_{ck}} \tag{2}$$

Where, A_S and A_C is the cross-sectional areas of the steel and concrete, respectively. f_y is the yield strength of steel and f_{ck} is the characteristic strength of the concrete.

In addition, the ABAQUS/Explicit module is used to analyze the progressive collapse performance of the substructure, which involves the tension and compression yield, plastic deformation and damage evolution of low-alloy steel materials. The reasonable constitutive models of steel plate and through bolt under large deformation should to be reconsidered in this paper. The comprehensive fracture criterion and damage evolution path of metal ductile damage, shear damage, and mixed damage modes based on stress triaxiality are considered in the steel constitutive structure.

The constitutive model before the degradation of steel is based on the steel plate or reinforcement model proposed by Esmaeily and Xiao (2005), which is considered as the stress and strain relationship between the elastic stage, the yield platform stage, and the strengthening stage simply. By controlling k_1, k_2, k_3, the shape at the yield platform stage and the strengthening stage in the uniaxial tensile stress-strain curve are adjusted (see **Figure 1**). The simplified stress-strain relationship is as shown in Equation (3). In the FE model of this paper, low-alloy steel plates are used for the steel beam, steel tube and extended endplate, the values are set as $k_1 = 3$, $k_2 = 300$, and $k_3 = 1.4$. And the 10.9S high strength bolts are used for through bolts, with the values set as $k_1 = 3$, $k_2 = 60$, and $k_3 = 1.3$.

$$\sigma = \begin{cases} E_s \varepsilon & , \varepsilon \leq \varepsilon_y; \\ f_y & , \varepsilon_y < \varepsilon \leq k_1 \varepsilon_y; \\ k_3 f_y + \frac{E_s(1-k_3)}{\varepsilon_y (k_2 - k_1)^2} \left(\varepsilon - k_2 \varepsilon_y\right)^2 & , k_1 \varepsilon_y < \varepsilon \leq k_2 \varepsilon_y \end{cases} \tag{3}$$

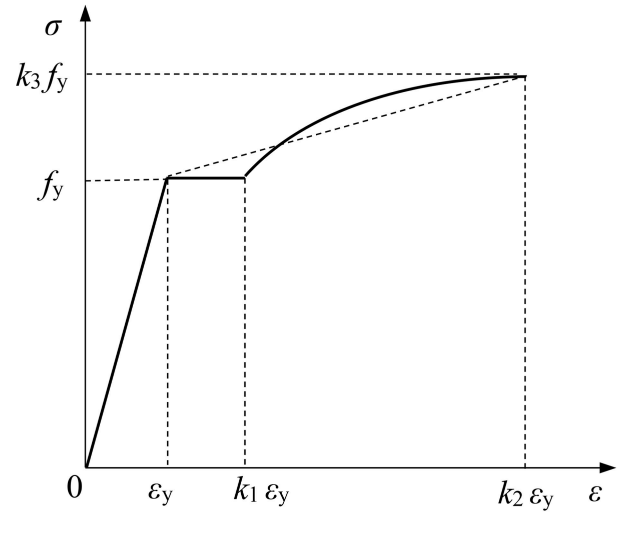

FIGURE 1 | The constitutive model before the degradation of steel.

Where,
E_s is the elastic modulus of steel,
f_y is the yield strength of steel,
ε_y is the yield strain of steel,
k_1 is the ratio of the starting strain of the strengthening stage to the yield strain,
k_2 is the ratio of the peak strain to the yield strain,
k_3 is the ratio of the peak stress to the yield strength.

According to the relevant test data of low-alloy steel in the real tensile condition (Chen et al., 2015, 2016, 2017), the stress-strain curve of steel at the strength degradation stage does not satisfy the shape characteristics of the second-order parabola, so the constitutive relationship of the fracture degradation stage of steel does not adopt the steel model proposed by Esmaeily and Xiao (2005). Moreover, the damage criterion and evolution process of steel at the degradation stage are relatively complex. Based on the X-W fracture criterion proposed by Wierzbicki and Xue (2005) and Xue (2005), the simplified equivalent plastic strain formula under the influence of stress triaxiality is proposed with reference to Yu and Jeong (2010) and Zhou et al. (2014):

$$\bar{\varepsilon}_0^{pl} = \begin{cases} \infty & , \eta \leq -1/3; \\ C_1 / (1 + 3\eta) & , -1/3 < \eta \leq 0; \\ C_1 + (C_2 - C_1)(\eta/\eta_0)^2 & , 0 < \eta \leq \eta_0; \\ C_2 \eta_0 / \eta & , \eta_0 < \eta \end{cases} \tag{4}$$

Where,
η_0 is 0.33,
C_1 is the critical plastic damage strain under pure shear condition,
C_2 is the critical plastic damage strain under uniaxial tension condition, which can be determined by the area reduction rate (A_R) after the material test is interrupted.

$$C_2 = -\ln(1 - A_R) \tag{5}$$

The conversion relationship between C_1 and C_2 can be determined by the following equations:

$$C_1 = C_2\left(\sqrt{3}/2\right)^{1/n} \tag{6}$$

$$\sigma = K(\varepsilon)^n \tag{7}$$

Where K and n are steel hardening parameters which can be derived from the true stress-strain curve, respectively.

Figure 2 shows the relationship between the stress triaxiality and critical equivalent plastic strain. It can be seen from the figure that the damage state can be judged by the value of stress triaxiality: shear damage ($-1/3 < \eta \leq 0$), mixed damage ($0 < \eta \leq \eta_0$), ductile damage ($\eta_0 < \eta$). The comprehensive fracture criterion for steel used in this paper is to simulate the damage of steel by inputting the relevant parameters of shear and ductile damage standard in the ABAQUS material module. The relevant parameters include the critical equivalent plastic strain, stress triaxiality, and strain rate. The critical equivalent plastic strain and stress triaxiality are mainly determined by Equation (4). Since the influence of the loading rate is not considered in the model, the strain rate is consistent with the loading rate of the FE model. In other words, this comprehensive fracture criterion covers the critical equivalent plastic strain of different damage modes of steel at the same strain rate.

Figure 3 shows the damage evolution path of steel. As shown by the red line in the figure, when the true strain reaches the critical equivalent plastic strain ($\bar{\varepsilon}_0^{pl}$), the steel begins to enter the damage mode. The falling section of the curve is the damage evolution path of steel and the true strain is between the critical equivalent plastic strain ($\bar{\varepsilon}_0^{pl}$) and the fracture strain ($\bar{\varepsilon}_\mathrm{f}^{pl}$). In the case of progressive collapse, the steel beam or through bolt may become damaged. The fracture process may be either a ductile fracture or brittle damage, and the partial fracture process will have a great impact on the resistance mechanism of the remaining key components. Therefore, the damage evolution path in the material constitutive is crucial.

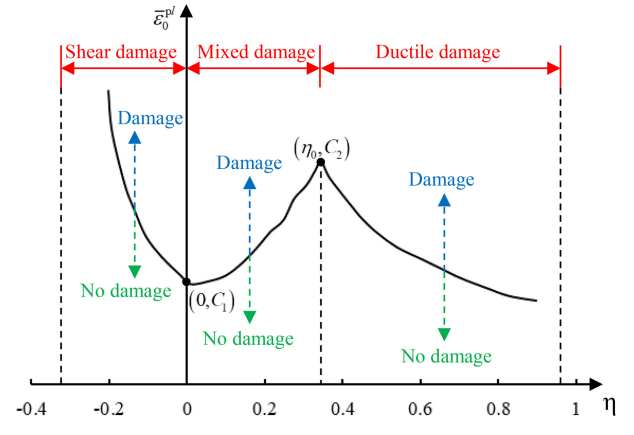

FIGURE 2 | The comprehensive fracture criterion of steel based on stress triaxiality.

The damage evolution path of steel can be controlled by the damage factor (D). When $D = 0$, the material does not damage. And when $D = 1$, the material completely fails. As shown in **Figure 3**, the residual modulus and residual stress can express the steel degradation process curve:

$$\bar{E} = (1 - D)\,E \tag{8}$$

$$\bar{\sigma} = (1 - D)\,\sigma \tag{9}$$

Where,
E is the elastic modulus,
σ is the stress at the elastic stage,
$\bar{E}$ is the residual modulus at the degradation stage,
$\bar{\sigma}$ is the residual stress at the degradation stage,
D is the damage parameter.

The ABAQUS/Explicit module provides two methods to define the damage evolution path, one is based on the fracture displacement and the other is based on the energy. In this paper, the linear displacement method is adopted, that is, the damage path evolution is realized by defining the damage displacement ($\bar{u}_\mathrm{f}^{pl}$) at $D = 1$. In order to reduce the influence of damage evolution on FE mesh size and quality, the plastic displacement ($\bar{u}^{pl}$) is defined as follows:

$$\bar{u}^{pl} = L_\mathrm{e}\bar{\varepsilon}^{pl} \tag{10}$$

Where L_e is the characteristic length of the FE mesh, which is defined by ABAQUS as the square root of the integral point area of the shell element and the cube root of the integral point volume of the solid element (Dassault Systemes Simulia Corp., 2014; ABAQUS Analysis User's Manual Version 6.14).

When the material plastic displacement ($\bar{u}^{pl}$) of one element reaches the material fracture displacement ($\bar{u}_\mathrm{f}^{pl}$), the ABAQUS/Explicit module can delete the element automatically. The material fracture displacement ($\bar{u}_\mathrm{f}^{pl}$) can be measured by a uniaxial tensile material test:

$$\bar{u}_\mathrm{f}^{pl} = e_1 \cdot d_l \tag{11}$$

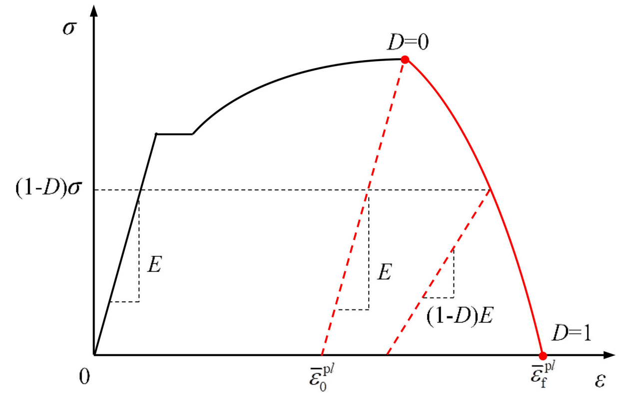

FIGURE 3 | The damage evolution path of steel.

Where e_l and d_l are the elongation and gauge length measured by the uniaxial tensile property test, respectively.

FE METHOD

The ABAQUS/Explicit module is used to analyze the resistance to progressive collapse of the composite joint with the CFST column and steel beam with through bolt-extended endplate. The rationality of this modeling method is verified by comparing the relevant static tests. Instances of one FE model include: loading plate, steel tube, core concrete, H-shaped steel beams, through bolts, extended endplates, and all of them use a C3D8R solid element. The loading plate is connected with the top of the CFST column and the steel beams on both sides are connected with the extended endplates, and the connection modes of theses use a "tie" interaction. In addition, the core concrete and the inner wall of the steel tube are set to "surface to surface" contact, with a friction penalty of 0.25. The bolt holes are reserved for the extended endplates and the steel tube, since that should be passed through by the through bolts. And the remaining contact faces are defined as "general contact" with a friction penalty of 0.45. The steel beam sections at both ends are coupled to two reference points, which are defined as hinged supports. The vertical load controlled by displacement is applied to the loading plate. Considering the influence of the loading rate on the kinetic energy of the model and the inertia of the joint in the ABAQUS/Explicit module, the smoothing loading curve is applied to the loading process. In order to ensure the reasonable development of the fracture effect in the model, the through bolts and the section of steel beam which may fracture is treated with mesh refinement, respectively (see **Figure 4**).

FE MODEL VERIFICATION

Yang and Tan (2013) carried out a test on the progressive collapse resistance of four simple connections and three semi-rigid connections. In this paper, Specimen 6 was selected for FE verification. The connection type was a high strength bolt-extended end plate. UB 254 × 146 × 37 S355 was selected for the steel beam, UC 203 × 203 × 71 S355 for the steel column, Grade 8.8 M20 steel for the high-strength bolt, and JR 436 × 200 × 12 S275 for the extended end plate, respectively. In order to obtain better simulation results, the FE model of Specimen 6 adopted the C3D8R solid element as shown in **Figure 5A**. In addition, in the FE model, the weld between the steel beam and extended end plate was weakened according to the test (Yang and Tan, 2013). During the test, the load (P) was applied to the top of column and the displacement of column (Δ) was recorded.

It can be seen from **Figure 5B** that the FE load-displacement at the top of the column curve deviates from the experimental results slightly. In the early stage of loading, the FE curve stiffness agreed well with the test curve. However, the FE model bearing capacity was slightly lower than Specimen 6 in the test at the elastic-plastic stage. When the test was loaded to 140.68 mm, Specimen 6 was damaged at the weld between the right beam and the extended end plate, and its bearing capacity reached 125.79 kN. When the fracture of weld at the right side occurs in the FE model, the bearing capacity of the joint is 122.31 kN at the displacement of 150.76 mm, which only differs by 2.77% from the experimental value. In the test, the left bolts fractured from the bottom to the top at the displacement of 284.72, 360.37, and 452.07 mm, respectively. When the bolts fractured, the bearing capacity of Specimen 6 reached 113.22, 95.36, and 67.77 kN, respectively. It is worth mentioning that the FE model also simulates the fracture of bolts three times at the displacement of 278.97, 339.62, and 384.76 mm, respectively. In addition, the bearing capacity at the fracture of bolts reached 110.64, 14.84, and 70.16 kN, respectively. It is not difficult to see that there is little difference between the simulation results and test results of the fracturing of bolts.

Figure 5C provides the failure mode comparison of the simulated and experimental Specimen 6. It was observed that by considering the fracturing properties of materials, the FE model can more accurately simulate the fracture at the weld and bolt, while the time and mode of failure do not differ much from the test results.

Dinu et al. (2017) conducted a progressive collapse test on four single-layer steel frames. In this paper, Specimen EP was selected

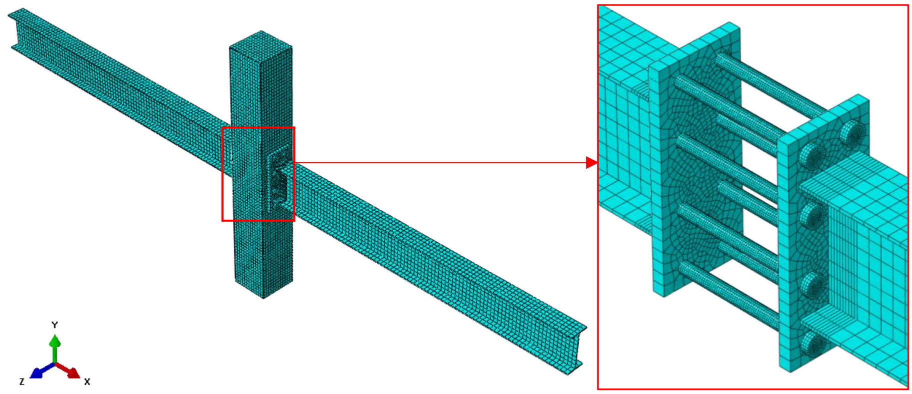

FIGURE 4 | Mesh refinement.

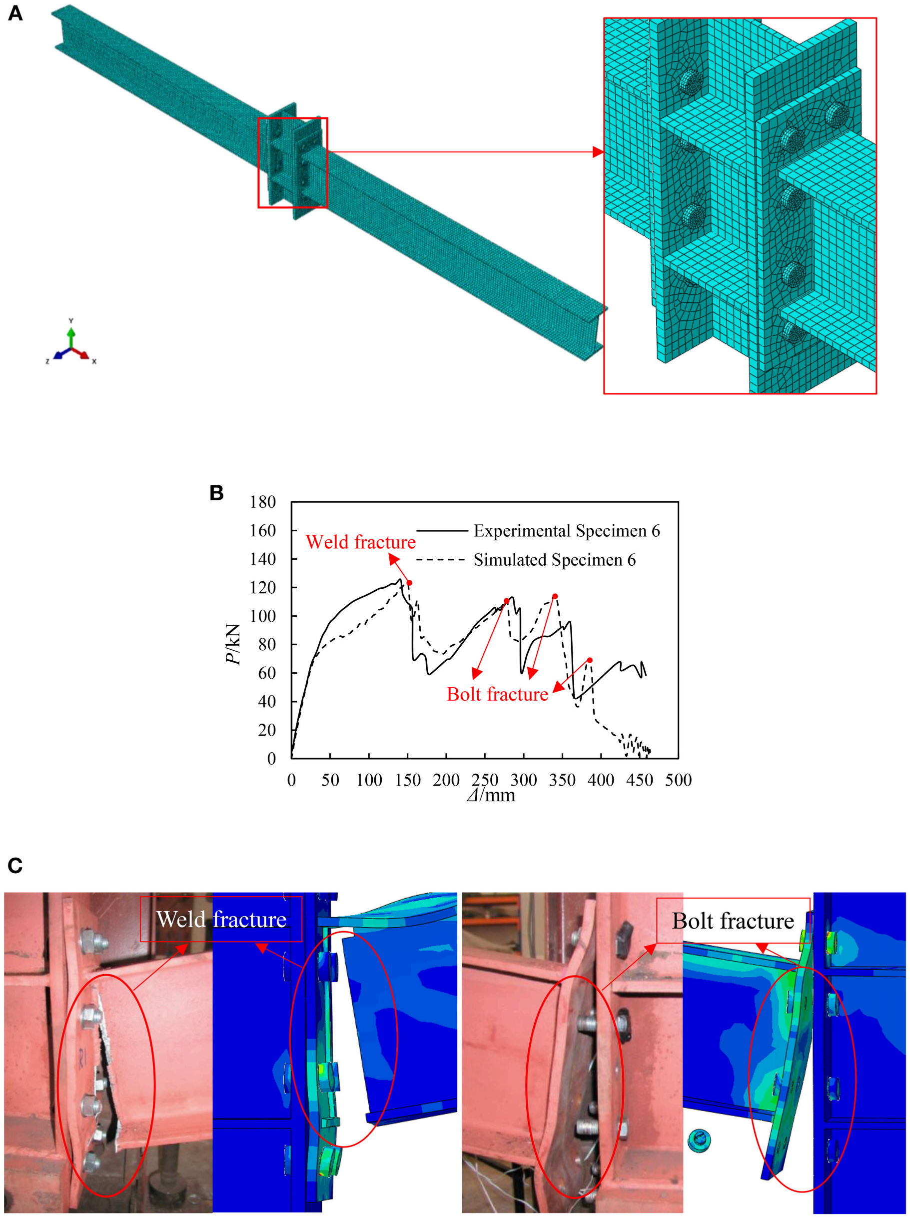

FIGURE 5 | Comparison of simulated and experimental Specimen 6. **(A)** FE model of Specimen 6. **(B)** Load-displacement at the top of column curve comparison. **(C)** Failure mode comparison.

for FE verification. The connections type was bolt-extended end plate. HEB 260 × 160 × 10 × 17.5 S275 was selected for the steel beam of this specimen, IPE 220 × 110 × 5.9 × 9.2 S275 for the steel column, and Grade 10.9S M16 for the high-strength bolt. In order to obtain better simulation results, the FE model of Specimen EP adopted the C3D8R solid element as shown in **Figure 6A**. During the test, the load (*P*) was applied to the top of the middle column and the displacement of the middle column (Δ) was recorded.

Figure 6B provides the load-displacement at the top of the middle column curve comparison of the simulated and experimental Specimen EP. The comparative result shows a good agreement between the simulated and experimental curves of Specimen EP in general. In the elastic stage, the simulated curve stiffness is slightly lower than the test curve. When the test was loaded to 195.66 mm, Specimen EP was damaged. While the failure displacement of the FE model is 192.96 mm, the difference between them is only 1.38%. Meanwhile, the ultimate bearing capacity of Specimen EP in test was 181.85 kN, which was 154.94 kN in the FE model. When Specimen EP entered the failure stage, the bolts were destroyed in sequence. However, the bearing capacity curve rose briefly and continued to oscillate since the structure did not completely lose the bearing capacity

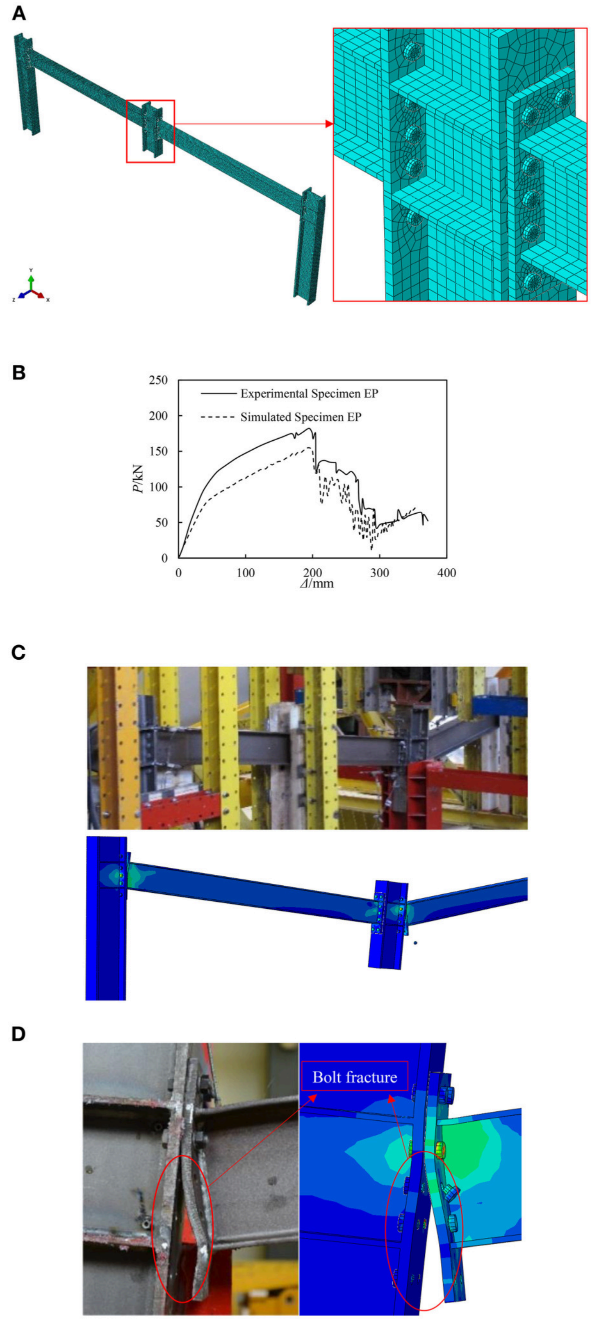

FIGURE 6 | Comparison of simulated and experimental Specimen EP. **(A)** FE model of Specimen EP. **(B)** Load-displacement at the top of middle column curve comparison. **(C)** Overall deformation comparison. **(D)** Failure mode comparison.

after parts of bolts fractured. The FE model achieves the above phenomenon completely and agrees well with the experimental results.

Figure 6C provides the overall deformation comparison of the simulated and the experimental Specimen EP. When the middle column had a large vertical displacement, the steel beam on both sides rotated around the rotating center. However, the asymmetric deformation of the joint occurred in the test. The failure of bolts occurred on one side first and then the fracture spread in this side gradually, while the other side of the joint did not damage. The FE method adopted in this paper can simulate the deformation mode accurately by considering the fracture property parameters.

Figure 6D provides the failure mode comparison of the simulated and experimental Specimen EP. During the test, the bolts on the right side of the middle column fractured when the displacement reached 195.66, 234.66, and 267.87 mm, respectively. In the FE model, the failure sequence of the bolt group and the deformation mode of the extended end plate are consistent with the test results. And the displacement of the simulated Specimen EP is similar to the test results at the bolts that are fractured. When the displacement reached 365.34 mm at the end of the test, the lower 6 bolts on the right side were damaged and the upper 4 were not damaged. The FE results are completely consistent with the experimental results.

Gao et al. (2017) conducted an experimental study on the sagging moment, hogging moment and tensile force of semi-rigid composite joints, respectively. In this paper, Specimen SJS was selected for FE verification. The connections type was a bolt-flush end plate. HN 200 × 100 × 5.5 × 8 was selected for the steel beam of this specimen, HW200 × 200 × 8 × 12 for the steel column, and Grade 10.9S M16 for the high-strength bolt. In order to obtain better simulation results, the FE model of Specimen SJS adopted the C3D8R solid element as shown in **Figure 7A**. During the test, the load was applied to the top of column and the displacement of column (Δ) was recorded. The calculation method of the bending moment (M) and rotation angle (θ) are referred to in Gao et al. (2017).

Figure 7B provides the bending moment-rotation angle curve comparison of the simulated and experimental Specimen SJS. The comparative result shows a good agreement between the simulated and experimental curves of Specimen SJS. In the elastic stage, the simulated curve stiffness is slightly higher than the experimental curve, and the simulated curve enters the elastoplastic stage later than the experimental curve. In the plastic stage, the simulated curve shows a slight downward trend, which is not reflected in the test curve. When the rotation angle of Specimen SJS was loaded to 0.82 in the test, the bending moment was 115.89 kNm. In addition, the bending moment was 104.10 kNm at the rotation angle of the simulated Specimen SJS is 0.82.

Figure 7C provides the failure mode comparison of the simulated and the experimental Specimen SJS. In the test, the lower bolts on both sides of the middle column fractured, which was realized perfectly in the FE model. Meanwhile, the flush end plates on both sides showed obvious bending phenomenon in the test, and the bending of the flush end plates of simulated Specimen SJS is similar to the test results. In brief, the FE results are completely consistent with experimental results.

JOINTS MODEL DESIGN

A typical composite joint with the CFST column and steel beam with through bolt-extended endplate was designed, named SJ-EP-TB-1, whose predictable fractured component would be the steel

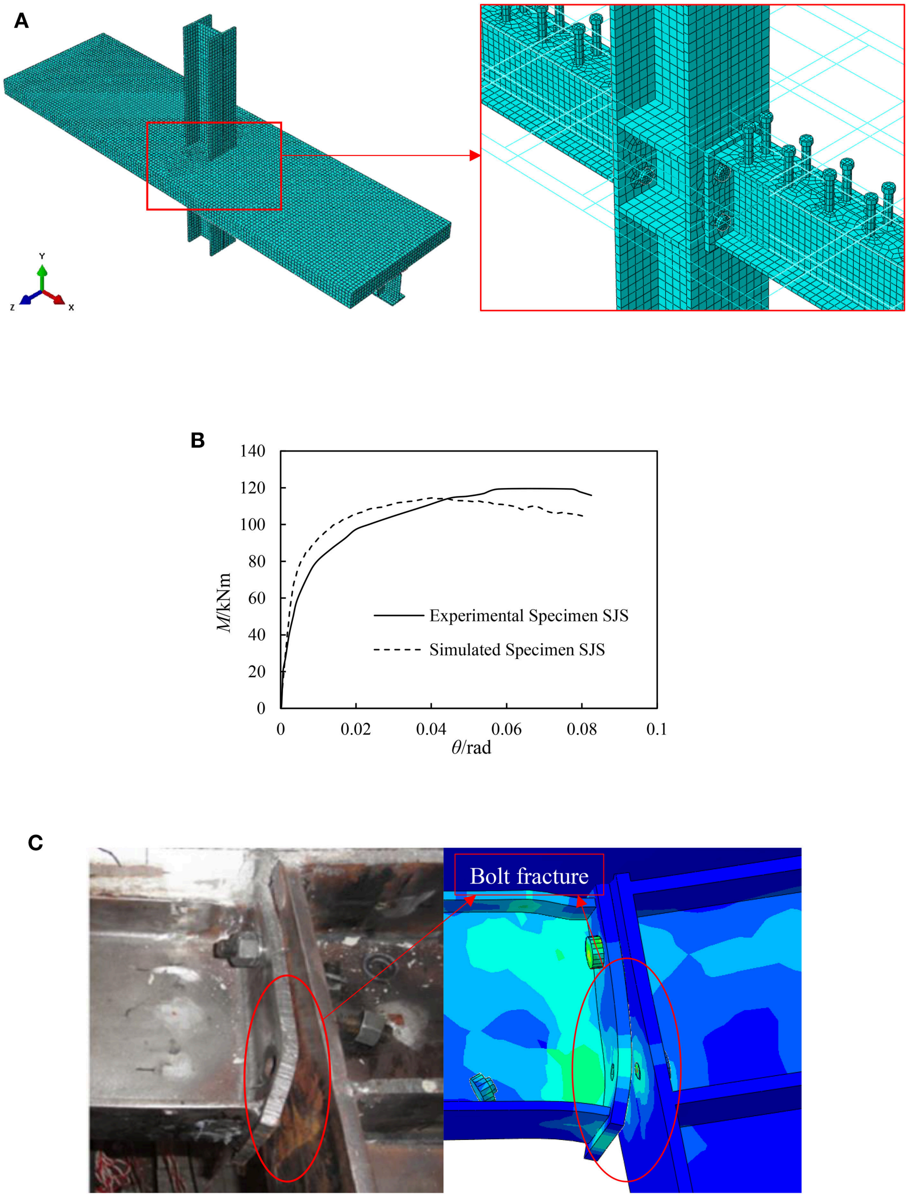

FIGURE 7 | Comparison of simulated and experimental Specimen SJS. **(A)** FE model of Specimen SJS. **(B)** Bending moment-rotation angle curve comparison. **(C)** Failure mode comparison.

beam and the through bolts. On the basis of typical joint SJ-EP-TB-1, it was proposed to control different predictable fractured components by adjusting the diameter of the through bolt and the thickness of the extended endplate. The joints whose predictable fractured component would be the through bolts, were named SJ-EP-TB-2 (by reducing the diameter of the through bolt) and SJ-EP-TB-4 (by reducing the thickness of the extended endplate), respectively. The joints whose predictable fractured component would be the steel beam, were named SJ-EP-TB-3 (by increasing the diameter of the through bolt) and SJ-EP-TB-5 (by increasing the thickness of the extended endplate), respectively. The section of the CFST column of joints is square, the span of the steel beams is 5600 mm, and the length of the CFST columns is 2000 mm. The parameters of the joints are shown in **Table 1**. The construction details of joints are shown in **Figure 8**.

THE INFLUENCE OF KEY COMPONENT CHARACTERISTIC

Table 2 provides the results of joints with different diameters of through bolts. **Figure 9** provides the resistance curve comparison. According to the comparison results, the diameter of the through bolt had a great influence on the progressive

TABLE 1 | Parameters of joints.

Joint ID	Steel beam section/mm	Column section/mm	Through bolt/mm × mm	Extended endplate/mm	Predictable fractured component
SJ-EP-TB-1	H 300 × 150 × 6 × 8	300 × 300 × 6	M 24 × 340	490 × 200 × 20	Steel beam and through bolts
SJ-EP-TB-2	H 300 × 150 × 6 × 8	300 × 300 × 6	M 20 × 340	490 × 200 × 20	Through bolts
SJ-EP-TB-3	H 300 × 150 × 6 × 8	300 × 300 × 6	M 28 × 340	490 × 200 × 20	Steel beam
SJ-EP-TB-4	H 300 × 150 × 6 × 8	300 × 300 × 6	M 24 × 324	490 × 200 × 12	Through bolts
SJ-EP-TB-5	H 300 × 150 × 6 × 8	300 × 300 × 6	M 24 × 356	490 × 200 × 28	Steel beam

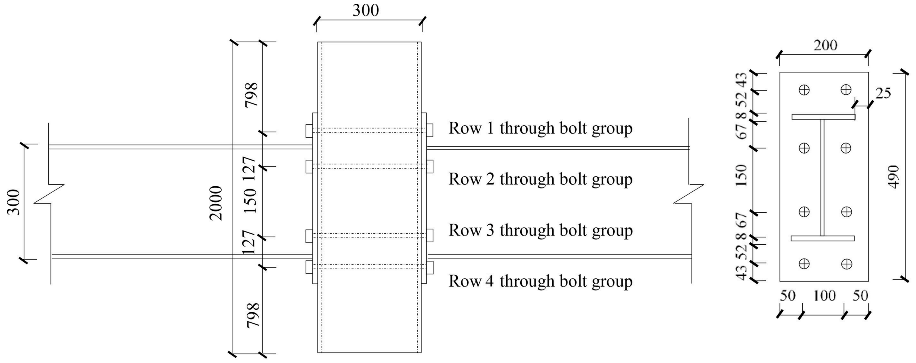

FIGURE 8 | Construction details of joints.

TABLE 2 | Results of joints with different diameter of through bolt.

Joint ID	d_{TB}/mm	Failure component	P_f/kN	Δ_{max}/mm	P_{max}/kN
SJ-EP-TB-1	24	Steel beam and through bolts	111.16	433.10	463.91
SJ-EP-TB-2	20	Through bolts	94.86	380.05	391.13
SJ-EP-TB-3	28	Steel beam	111.84	592.45	623.08

d_{TB}, Diameter of through bolt; P_f, Resistance at the end of bending mechanism; P_{max}, Maximum resistance of joint; Δ_{max}, Vertical displacement corresponding to the maximum resistance of joint.

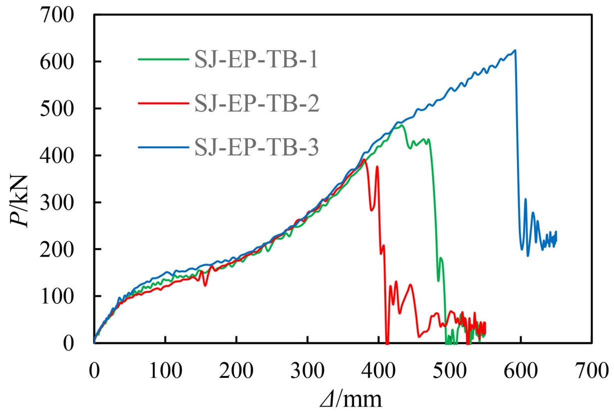

FIGURE 9 | Resistance curves comparison with a different diameter of the through bolt.

collapse resistance of the composite joint with a CFST column and the steel beam with a through bolt-extended endplate. The failure mode is usually the through bolts failure when the diameter of the through bolt is too small. However, with the increase of the diameter of the through bolt, the possibility of the through bolts fracture is reduced, that is, the failure mode is gradually transformed to the steel beam failure.

Specifically, the bolt diameters of SJ-EP-TB-2, SJ-EP-TB-1, and SJ-EP-TB-3 are 20, 24, and 28 mm, respectively. The diameter of the through bolt of SJ-EP-TB-2 is the smallest among the three, and its failure mode is the through bolts failure. At the end of bending mechanism, the resistance of the column top (P_f) is 94.86 kN. When the ultimate bearing capacity is reached, the displacement (Δ_{max}) is 380.05 mm and the maximum resistance of joint (P_{max}) is 391.13 kN. The diameter of the through bolt of SJ-EP-TB-1 is between the other two, and its failure mode is the steel beam and the through bolts failure. The top resistance at the end of the bending mechanism (P_f) is 111.16 kN, which is 17.18% higher than that of SJ-EP-TB-2. When SJ-EP-TB-1 reaches the ultimate bearing capacity, its vertical displacement (Δ_{max}) and maximum resistance (P_{max}) are 433.10 mm and 463.91 kN, respectively, which is 13.94 and 18.61% higher than that of SJ-EP-TB-2. The diameter of the through bolt of SJ-EP-TB-3 is the largest among the three, and its failure mode turns to a steel beam failure. The top resistance at the end of bending mechanism (P_f) is 111.84 kN, which is 17.18% higher than that of SJ-EP-TB-2. When SJ-EP-TB-3 reaches the ultimate bearing capacity, the vertical displacement (Δ_{max}) and maximum resistance (P_{max}) are 592.45 mm and 623.08 kN, respectively, which is 55.89 and 59.30% higher than that of SJ-EP-TB-2.

It can be seen that with the increase of the diameter of the through bolt, the failure mode of the joint gradually turns from bolt failure to steel beam failure. And the resistance at the bending mechanism, the ultimate bearing capacity and the ductility of the joint is enhanced. In summary, with the increase of the diameter of the through bolt, the anti-progressive collapse ability of the composite joint with a CFST column and steel beam with a through bolt-extended endplate obviously increases.

Table 3 provides the results of the joints with different thicknesses of the extended endplate. **Figure 10** provides the resistance curves comparison. According to the comparison results, the thickness of the extended endplate has a certain influence on the progressive collapse resistance of the composite joint with a CFST column and steel beam with a through bolt-extended endplate. The failure mode is usually the through bolts failure when the thickness of the extended endplate is too small. However, with the increase of the extended endplate thickness, the possibility of the through bolt fracture is reduced, that is, the failure mode is gradually transformed to the steel beam failure.

Specifically, the extended endplate thickness of SJ-EP-TB-4, SJ-EP-TB-1, and SJ-EP-TB-5 was 12, 20, and 28 mm, respectively. The thickness of the extended endplate of SJ-EP-TB-4 was the smallest among the three, whose failure mode was the through bolts failure. At the end of the bending mechanism, the resistance of the column top (P_f) was 79.92 kN. When the ultimate bearing capacity is reached, the displacement (Δ_{max}) is 460.20 mm and the maximum resistance of the joint (P_{max}) is 461.86 kN. The thickness of the extended endplate of SJ-EP-TB-1 is between the other two, whose failure mode is the steel beam and the through bolts failure. The top resistance at the end of the bending mechanism (P_f) was 111.16 kN, which is 39.09% higher than that of SJ-EP-TB-4. When SJ-EP-TB-1 reaches the ultimate bearing capacity, the vertical displacement (Δ_{max}) is 433.10 mm, which is 5.89% lower than that of SJ-EP-TB-4. And the maximum resistance (P_{max}) of SJ-EP-TB-1 is 463.91 kN, which is 0.44% higher than that of SJ-EP-TB-4. The thickness of the extended endplate of SJ-EP-TB-5 is the largest among the three, whose failure mode turns to a steel beam failure. The top resistance at the end of the bending mechanism (P_f) is 136.28 kN, which is 70.52% higher than that of SJ-EP-TB-4. When SJ-EP-TB-5 reaches the ultimate bearing capacity, the vertical displacement (Δ_{max}) and maximum resistance (P_{max}) is 556.40 mm and 587.46 kN, respectively, which is 20.90 and 27.19% higher than that of SJ-EP-TB-4.

It can be seen that with the increase of the thickness of the extended endplate, the failure mode of the joint turns from the bolt failure to the steel beam failure gradually. And the resistance and stiffness of the curve at the bending mechanism, the maximum resistance and the ductility of the joint are all enhanced to a certain extent. In summary, with the increase of the thickness of the extended endplate, the resistance to a progressive collapse of the composite joint with a CFST column and steel beam with a through bolt-extended endplate, increases to a certain extent.

TABLE 3 | Results of joints with different thickness of extended endplate.

Joint ID	d_{EP}/mm	Failure component	P_f/kN	P_{max}/kN	Δ_{max}/mm
SJ-EP-TB-1	20	Steel beam and through bolts	111.16	433.10	463.91
SJ-EP-TB-4	12	Through bolts	79.92	460.20	461.86
SJ-EP-TB-5	28	Steel beam	136.38	556.40	587.46

d_{EP}, Thickness of extended endplate.

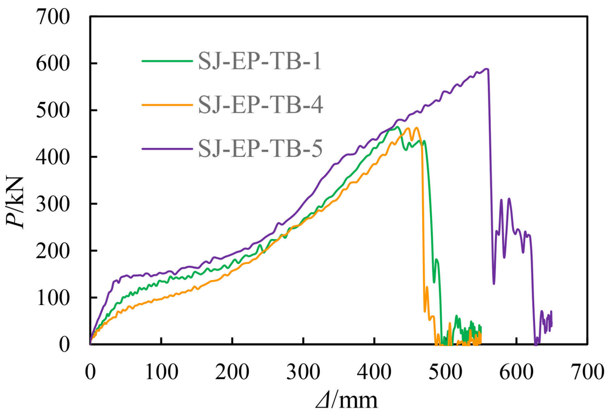

FIGURE 10 | Resistance curves comparison different thickness of extended endplate.

CONCLUSIONS

In this paper, the reasonable constitutive model of steel plate, through bolt and core concrete was selected. The accuracy of the modeling method and material constitutive was verified by the comparison between the experimental and FE results. One typical composite joint with a CFST column and steel beam with a through bolt-extended endplate named SJ-EP-TB-1 was designed, and four joints were derived for comparison, by adjusting the diameter of the through bolt and the thickness of the extended endplate. The FE models of these five joints were established to investigate failure modes and resistance mechanisms using the ABAQUS/Explicit module. The conclusions may be summarized as follows:

(1) The comprehensive fracture criterion and damage evolution path of metal ductile damage, shear damage, and mixed damage modes, based on stress triaxiality, were considered in the steel constitutive model, which were used as the basis for the study of a large deformation of joints under progressive collapse.
(2) The failure modes of the composite joint with a CFST column and steel beam with a through bolt-extended endplate can be divided into three types: steel beam and through bolts failure, through bolts failure, and steel beam failure, and the different strengths and weaknesses between

the through bolt, extended endplate and steel beam affect the progressive collapse resistance of the joint directly.

(3) With the increase of the diameter of the through bolt, the failure mode of the joint gradually turns from bolt failure to steel beam failure, and the resistance at the bending mechanism, the ultimate bearing capacity and the ductility of joint are enhanced. In summary, the anti-progressive collapse ability of the composite joint with a CFST column and steel beam with a through bolt-extended endplate increases obviously.

(4) With the increase of the thickness of the extended endplate, the failure mode of the joint gradually turns from a bolt failure to a steel beam failure, and the resistance and stiffness of the curve at the bending mechanism, the maximum resistance and the ductility of the joint are enhanced to a certain extent. In summary, the resistance to a progressive collapse of the composite joint with a CFST column and steel beam with a through bolt-extended endplate increases to a certain extent.

AUTHOR CONTRIBUTIONS

Y-LS was responsible for this research. LZ is a Ph.D. student and carried out the research work. W-DW is charge of the whole research subject.

FUNDING

This research was supported by the National Natural Science Foundation of China (No.: 51778214; 51268038) and the Universities Cooperative Innovation Team of Gansu Province (No.: 2018C-08). The financial support is highly appreciated.

REFERENCES

Adam, J. M., Parisi, F., Sagaseta, J., and Lu, X. Z. (2018). Research and practice on progressive collapse and robustness of building structures in the 21st century. *Eng. Struct.* 173, 122–149. doi: 10.1016/j.engstruct.2018.06.082

Atkins, A. G. (1996). Fracture in forming. *J. Mater. Process. Technol.* 56, 609–618. doi: 10.1016/0924-0136(95)01875-1

Bao, Y. B., and Wierzbicki, T. (2004). On fracture locus in the equivalent strain and stress triaxiality space. *Int. J. Mater. Sci.* 46, 81–98. doi: 10.1016/j.ijmecsci.2004.02.006

Chen, J. L., Li, J. W., and Li, Z. X. (2017). Experimental study strain hardening and stain rates effect of Q420 steel. *J. Tongji. Univ.* 45, 180–187. doi: 10.11908/j.issn.0253-374x.2017.02.004

Chen, J. L., Li, Z. X., Shu, W. Y., and Li, J. W. (2015). Experimental study on dynamic mechanical behavior of Q345 steel under different strain rates. *J. Tongji. Univ.* 45, 1145–1150. doi: 10.3969/j.issn.1001-0505.2015.06.022

Chen, J. L., Shu, W. Y., and Li, J. W. (2016). Experimental study on dynamic mechanical property of Q235 steel at different strain rates. *J. Tongji. Univ.* 44, 1071–1075. doi: 10.11908/j.issn.0253-374x.2016.07.014

Dassault Systemes Simulia Corp. (2014). *ABAQUS Analysis User's Manual Version 6.14*. Providence.

Dinu, F., Marginean, I., and Dubina, D. (2017). Experimental testing and numerical modelling of steel moment-frame connections under column loss. *Eng. Struct.* 151, 861–878. doi: 10.1016/j.engstruct.2017.08.068

Dinu, F., Marginean, I., Dubina, D., and Petran, I. (2016). Experimental testing and numerical analysis of 3D steel frame system under column loss. *Eng. Struct.* 113, 59–70. doi: 10.1016/j.engstruct.2016.01.022

Esmaeily, A., and Xiao, Y. (2005). Behavior of reinforced concrete columns under variable axial loads: analysis. *ACI. Struct. J.* 102, 736–744. doi: 10.14359/14669

Gao, S., Guo, L. H., Fu, F., and Zhang, Z. M. (2017). Capacity of semi-rigid composite joints in accommodating column loss. *J. Constr. Steel. Res.* 139, 288–301. doi: 10.1016/j.jcsr.2017.09.029

Gong, Y. L. (2017). Test, modeling and design of bolted-angle connections subjected to column removal. *J. Constr. Steel. Res.* 139, 315–326. doi: 10.1016/j.jcsr.2017.10.004

Guo, L. H., Gao, S., and Fu, F. (2015). Structural performance of semi-rigid composite frame under column loss. *Eng. Struct.* 95, 112–126. doi: 10.1016/j.engstruct.2015.03.049

Guo, L. H., Gao, S., Fu, F., and Wang, Y. Y. (2013). Experimental study and numerical analysis of progressive collapse resistance of composite frames. *J. Constr. Steel. Res.* 89, 236–251. doi: 10.1016/j.jcsr.2013.07.006

Guo, L. H., Gao, S., Wang, Y. Y., and Zhang, Z. M. (2014). Tests of rigid composite joints subjected to bending moment combined with tension. *J. Constr. Steel. Res.* 95, 44–55. doi: 10.1016/j.jcsr.2013.10.006

Han, L. H., Yao, G. H., and Tao, Z. (2007). Performance of concrete-filled thin-walled steel tubes under pure torsion. *Thin Wall. Struct.* 45, 24–36. doi: 10.1016/j.tws.2007.01.008

Hancock, J. W., and Mackenzie, A. C. (1976). On the mechanisms of ductile failure in high-strength steels subjected to multi-axial stress states. *J. Mech. Phys. Solids* 24, 147–160. doi: 10.1016/0022-5096(76)90024-7

Li, H. H., Cai, X. H., Zhang, L., Zhang, B. Y., and Wang, W. (2017). Progressive collapse of steel moment-resisting frame subjected to loss of interior column: experimental tests. *Eng. Struct.* 150, 203–220. doi: 10.1016/j.engstruct.2017.07.051

McClintock, F. A. (1968). A criterion of ductile fracture by the growth of holes. *J. Appl. Mech.* 35, 363–371. doi: 10.1115/1.3601204

Mirza, M. S., Barton, D. C., and Church, P. (1996). The effect of stress triaxiality and strain-rate on the fracture characteristics of ductile metals. *J. Mater. Sci.* 31, 453–461. doi: 10.1007/BF01139164

Oosterhof, S. A., and Driver, R. G. (2015). Behaviour of steel shear connections under column-removal demands. *J. Struct. Eng.* 141, 1–14. doi: 10.1061/(ASCE)ST.1943-541X.0001073

Pirmoz, A., and Liu, M. M. (2016). Finite element modeling and capacity analysis of post-tensioned steel frames against progressive collapse. *Eng. Struct.* 126, 446–456. doi: 10.1016/j.engstruct.2016.08.005

Rice, J. R., and Tracey, D. M. (1969). On the ductile enlargement of voids in triaxial stress field. *J. Mech. Phys. Solids* 17, 201–217. doi: 10.1016/0022-5096(69)90033-7

Rosa, G. L., Mirone, G., and Risitano, A. (2001). Effect of stress triaxiality corrected plastic row on ductile damage evolution in the framework of continuum damage mechanics. *Eng. Fract. Mech.* 68, 417–434. doi: 10.1016/S0013-7944(00)00109-0

Roy, G. L., Embury, J. D., Edwards, G., and Ashby, M. F. (1981). A model of ductile fracture based on the nucleation and growth of voids. *Acta Metall.* 29, 1509–1522. doi: 10.1016/0001-6160(81)90185-1

Sadek, F., Main, J. A., Lew, H. S., and Bao, Y. H. (2011). Testing and analysis of steel and concrete beam-column assemblies under a column removal scenario. *J. Struct. Eng.* 137, 881–892. doi: 10.1061/(ASCE)ST.1943-541X.0000422

Wang, W., Fang, C., Qin, X., Chen, Y., and Li, L. (2016). Performance of practical beam-to-SHS column connections against progressive collapse. *Eng. Struct.* 106, 332–347. doi: 10.1016/j.engstruct.2015.10.040

Wang, W. D., Li, H. W., and Wang, J. X. (2017). Progressive collapse analysis of concrete-filled steel tubular column to steel beam connections using multi-scale model. *Structures* 9, 123–133. doi: 10.1016/j.istruc.2016.10.004

Wang, W. D., Zheng, L., and Wei, G. Q. (2018). Resistance to progressive collapse performance analysis and assessment of CFST-steel beam joints with through-center construct. *Adv. Eng. Sci.* 50, 39–47. doi: 10.15961/j.jsuese.201800617

Wierzbicki, T., and Xue, L. (2005). *On the Effect of the Third Invariant of the Stress Deviator on Ductile Fracture*. Cambridge, MA: MIT Impact and Crashworthiness Lab.

Xu, M., Gao, S., Zhang, S. M., and Li, H. H. (2018a). Experimental study on bolted CFST-column joints with different configurations in accommodating column-loss. *J. Constr. Steel. Res.* 151, 122–131. doi: 10.1016/j.jcsr.2018.09.021

Xu, Z. D., Huang, X. H., Xu, F. H., and Yuan, J. (2019). Parameters optimization of vibration isolation and mitigation system for precision platforms using non-dominated sorting genetic algorithm. *Mech. Syst. Signal Process.* 128, 191–201. doi: 10.1016/j.ymssp.2019.03.031

Xu, Z. D., Li, S., and Zeng, X. (2018b). Distributed strain damage identification technique for long-span bridges under ambient excitation. *Int. J. Struct. Stab. Dyn.* 18:1850133. doi: 10.1142/S021945541850133X

Xu, Z. D., and Wu, K. Y. (2012). Damage detection for space truss structures based on strain mode under ambient excitation. *J. Eng. Mech.* 138, 1215–1223. doi: 10.1061/(ASCE)EM.1943-7889.0000426

Xu, Z. D., Zeng, X., and Li, S. (2013). Damage detection strategy using strain-mode residual trends for long-span bridges. *J. Comput. Civil. Eng.* 29:04014064. doi: 10.1061/(ASCE)CP.1943-5487.0000371

Xue, L. (2005). *Damage Accumulation and Fracture Initiation in Uncracked Ductile Solids Under Triaxial Loading-Part I: Pressure Sensitivity and Lode Dependence*. Cambridge, MA: MIT Impact and Crashworthiness Lab.

Yang, B., and Tan, K. H. (2013). Experimental tests of different types of bolted steel beam-columns joints under a central-column-removal scenario. *Eng. Struct.* 54, 112–130. doi: 10.1016/j.engstruct.2013.03.037

Yi, W. J., He, Q. F., Xiao, Y., and Kunnath, S. K. (2008). Experimental study on progressive collapse-resistant behavior of reinforced concrete frame structures. *ACI Struct. J.* 105, 433–439. doi: 10.1306/03250807070

Yu, H. L., and Jeong, D. Y. (2010). Application of a stress triaxiality dependent fracture criterion in the finite element analysis of unnotched Charpy specimens. *Theor. Appl. Fract. Mech.* 54, 54–62. doi: 10.1016/j.tafmec.2010.06.015

Zhou, T. H., Li, W. C., Guan, Y., and Bai, L. (2014). Damage analysis of steel frames under cyclic load based on stress triaxiality. *Eng. Mech.* 31, 146–155. doi: 10.6052/j.issn.1000-4750.2013.01.0090

Conflict of Interest Statement: The authors declare that the research was conducted in the absence of any commercial or financial relationships that could be construed as a potential conflict of interest.

frontiers
in Materials

REVIEW
published: 05 July 2019
doi: 10.3389/fmats.2019.00143

Recent Advances in Multi-Dimensional Vibration Mitigation Materials and Devices

Zhao-Dong Xu, Zheng-Han Chen, Xing-Huai Huang, Chen-Yu Zhou, Zhong-Wei Hu, Qi-Hang Yang and Pan-Pan Gai*

Key Laboratory of C&PC Structures of the Ministry of Education, Southeast University, Nanjing, China

Harmful vibrations can cause many engineering problems, such as disasters of civil engineering structures, failure of precision equipment, and the disruption of some spacecraft components. In most situations, the vibrations are usually three-dimensional excitations. Therefore, research on multi-dimensional vibration control has become a world-wide hotspot in engineering. This article presents a comprehensive assessment of recent developments of multi-dimensional vibration mitigation devices and the material applied in such devices. The vibration mitigation materials mainly include the passive vibration mitigation materials and smart vibration mitigation materials. Subsequently, the vibration mitigation devices in civil engineering, mechanical engineering, and aerospace engineering are reviewed and commented, respectively. Above all, the multi-dimensional vibration mitigation devices and materials are found to be effective for reducing multi-dimensional vibrations. However, enhancing the mitigation performance of the devices in each direction, including improving the mitigation capability of materials, is still a challenging issue.

Keywords: multi-dimensional vibration isolator, vibration control, vibration mitigation material, civil engineering, mechanical engineering, aerospace engineering

OPEN ACCESS

Edited by:
Yu-Fei Wu,
RMIT University, Australia

Reviewed by:
Zheng Lu,
Tongji University, China
Antonio Caggiano,
Darmstadt University of Technology, Germany
Yi-Qing Ni,
Hong Kong Polytechnic University, Hong Kong

****Correspondence:***
Zhao-Dong Xu
xuzhdgyq@seu.edu.cn

Specialty section:
This article was submitted to Structural Materials, a section of the journal Frontiers in Materials

Received: *15 March 2019*
Accepted: *06 June 2019*
Published: *05 July 2019*

Citation:
Xu Z-D, Chen Z-H, Huang X-H, Zhou C-Y, Hu Z-W, Yang Q-H and Gai P-P (2019) Recent Advances in Multi-Dimensional Vibration Mitigation Materials and Devices. Front. Mater. 6:143. doi: 10.3389/fmats.2019.00143

INTRODUCTION

Vibration is a cyclical reciprocating motion that exists widely in nature and engineering. When vibration exceeds a certain limit, it will cause harm to equipment, infrastructure, the environment, and the human body. Therefore, more scholars have begun to study the field of vibration isolation and mitigation, which is important for the safety, reliability, and durability of infrastructure and equipment. In this field, the vibration mitigation materials, and devices are two key factors that affect the performance of the vibration control effect.

Over the past few decades, significant contributions have been made by researchers around the world toward research on vibration mitigation materials. Many different kinds of materials are widely concerned in this field, from traditional passive vibration mitigation materials (viscoelastic materials, rubber, etc.) to smart materials (magnetorheological fluid, magnetorheological elastomers, piezoelectric ceramics, etc.). However, it is still significant to continually investigate and improve the properties of the vibration mitigation materials.

On the other hand, conventional mitigation/isolation technology of vibration usually focused on one dimension, which was far from enough. Consequently, multi-dimensional vibration isolation technology was put forward in the middle of the last century and gradually became a hotspot of research. The multi-dimensional vibration isolator was proposed by Stewart and named after himself (Stewart, 1965), and represents the beginning of research on the passive vibration isolators working in multi-dimensions. Afterwards, more optimized theories and precise models were proposed for multi-dimensional vibration isolation devices. For example, as for the description of viscoelastic dampers, the traditional models based on one dimension such as the Kelvin model, the Maxwell model, and the standard linear solid model were developed into the fractional-derivative equivalent standard solid model and the integrated mathematical model to meet the demands of multi-dimensional vibration isolation (Xu et al., 2014, 2017b). The application of these devices has been expanded in a variety of fields, such as civil engineering, mechanical engineering and aerospace engineering.

VIBRATION MITIGATION MATERIALS

Research on multi-dimensional vibration mitigation devices is committed to achieving and improving multi-directional mitigation capacity, which requires finding and developing the most suitable materials to apply to multi-dimensional vibration mitigation devices, so as to make great progress in vibration mitigation and isolation technology.

Passive Vibration Mitigation Materials

Viscous damping material usually refers to viscous fluids, which makes viscous dampers widely used in the field of vibration mitigation. The fluid damping medium commonly used in engineering is high viscosity organic material, such as hydraulic oil, silicone oil, special suspension, etc. Hydraulic oil is not suitable as a viscous medium or viscous damper due to its high freezing point and poor viscosity-temperature performance. Among the silicone oils, dimethyl silicone oil is the most suitable material for viscous medium due to its excellent high/low temperature resistance, chemical stability, shearing resistance, viscosity-temperature characteristics, and high compressibility. Many scholars have studied the viscosity, shear properties and chemical stability of methyl silicone oil. The special suspension mainly refers to magnetorheological fluid, which will be introduced later as a smart vibration mitigation material.

Viscoelastic (VE) damping material is composed of high polymer and has the characteristics of both viscous fluid and elastic solid. Many polymeric materials having long-chain molecules exhibit viscoelastic behavior, such as plastics, rubbers, acrylics, silicones, vinyls, adhesives, urethanes, epoxies, etc. Rubber is the most widely developed vibration mitigation material. In order to broaden the range of working temperature and frequency, many researchers have studied techniques such as blending (Lu et al., 2017), copolymerization (Pukkate et al., 2007; Suksawad et al., 2011; Yamazaki et al., 2011), and interpenetrating polymer networks (Manoj et al., 2002; Patri et al., 2007; Xu et al., 2016a) to improve the damping performance of VE materials. Liu et al. (2017) investigated the beneficial effect of *in-situ* polymerization blends on rubber damping properties, which proves that compared with mechanical blending, the damping temperature range is obviously expanded, meanwhile the peak and valley of the damping temperature range are greatly promoted. Qin et al. (2018) investigated gradient laminating to prepare NR/ENR composites, which proves that the layered structure can effectively improve the damping performance and the mechanical properties. Xu et al. (2016c) studied several kinds of VE materials based on different matrix rubbers, conducted experiments on VE dampers based on nitrile butadiene rubber (NBR) matrix and silicone rubber (SR) matrix. The results demonstrate that the NBR matrix VE dampers possess higher energy dissipation capacity, while the performance of the SR matrix VE dampers under various working conditions is more stable. Xu et al. (2016b) investigated the effects of the micromolecular structures and fillers on the VE properties of the VE materials and established an equivalent fractional order microstructure standard linear solid model.

Metallic materials are widely used in passive control, including alloys, metal matrix composites, and foam metals. The researchers studied the influence of heat treatment (Pulino-Sagradi et al., 1998; Murakami et al., 2006; González-Martínez et al., 2007), processing technology (Nishiyama et al., 2003), and the addition of reinforcing phase (Luo et al., 2004; Lihua et al., 2007) on the damping and mechanical properties of the alloy. Metal matrix composite material is a composite material made by adding reinforcing phase into the metal matrix, which has both good damping performance and mechanical properties. Jia (2007) investigated the damping performance of $FeAl_3$ reinforced composites and base alloy over the temperature range of 30–300°C, which proves that the $Al/FeAl_3$ composites exhibit higher damping capacity compared to Al matrix composites. Cell aluminum foams are widely used to absorb impact energy in the aero and automotive industries. Raj et al. (2009) investigated the plateau stress and energy absorption of closed-cell aluminum foam under quasi-static and dynamic compression, which shows that the plateau stress of aluminum foam improves with the increase of relative density and strain rate.

Smart Vibration Mitigation Materials

As a new type of damping material, smart materials are widely used in the field of vibration mitigation and isolation. Magnetorheological fluid (MRF) has reversible and instantaneous rheological properties, and the viscosity and yield stress change with the magnetic field intensity. The general MRF is composed of ferromagnetic particles dispersed in the carrier fluid. The density difference between particles and the carrier fluid leads to clear sedimentation, which reduces the adjustability and seismic performance of the MR device. Researchers investigated the influence of particle shape (Bell et al., 2008; De Vicente et al., 2009), size (Bondi, 1956), multi-diameter ratio (Foister, 1997; Guo et al., 2017), and material (Thomas, 1966) on the performance of magnetorheological fluids. In addition, many researchers have found that different from conventional silicon oil carrier fluids, ionic liquids (Guerrero-Sanchez et al., 2007), magnetofluids (Ginder et al., 1996), polymers (Iyengar et al., 2004) and other carrier fluids improve the properties of magnetorheological fluids. At present, it has become a hot topic to coat magnetic particles with submicron filler or polymer such as multi-walled carbon nanotubes (Guo et al., 2018), single-walled carbon nanotubes (Fang et al., 2009), graphene oxide (Xu et al., 2018b), gas-phase silica (Liu et al., 2013), etc., to improve the stability of MRF deposition.

Magnetorheological elastomers (MREs) are composed of magnetic particles dispersed in non-magnetic polymers. Compared with MRF, MREs have obvious advantages of preventing particle deposition, environmental pollution, and leakage. Stepanov et al. (2007) studied and compared the mechanical property of isotropic and anisotropic "soft" MREs in homogeneous magnetic fields of different intensities: elongation, static, and dynamic shears. Kamath et al. (1999) and Padalka et al. (2010) studied MREs composites with Fe and Co microparticles and nanowires of the same weight fraction, and the result was that the composites based on nanowire have much higher dynamic stiffness and equivalent damping coefficient values compared to the composites based on microparticles. Additionally, the properties of the aligned MRE composites filled with nanowires synthesized from typical ferromagnetic metals (Fe, Co, and Ni) were investigated. Zhu et al. (2012, 2013) and Xu et al. (2018a) investigated the magnetoviscoelasticity properties of the MREs in the condition of different magnetic fields, displacement amplitudes, and frequencies under sinusoidal loadings, then proposed a parameter model to describe MREs performances.

Shape memory alloys (SMAs) are widely used in the design of structural vibration mitigation and isolation devices due to the unique shape memory effect and superelasticity. Ferromagnetic shape memory alloys (FSMAs) as an attractive category of SMAs can change their dimensions based on the external magnetic field. Compared with traditional temperature-controlled SMAs, it has the advantages of fast response. Kainuma et al. (2006) reported the magnetic-field-induced shape recovery of a compressively deformed Ni-Co-Mn-In alloy. Stress of over 100 MPa exists in the material in a magnetic field of 70 kOe, and 3 percent deformation then almost completely recover the original shape of the alloy. Wang et al. (2008) firstly revealed that the application of a magnetic field at the martensitic transition temperature results in redistributions of local strains of martensitic variants, and investigated the effect of inhomogeneous microstructures on the magnetic-field-induced reverse transformation in the polycrystalline Ni-Co-Mn-In alloy by X-ray tomography.

Magnetostrictive materials have the property of strain with the change of magnetization state (Magnetostriction effect), thus realizing the mutual conversion of electromagnetic energy and mechanical energy. Giant magnetostrictive materials (GMM) represented by TbDyFe have become a research hotspot due to their large displacement, large output power, and fast response. Duenas and Carman (2001) studied the particle size and range of size distribution in magnetostrictive composites with low volume percentage and its influence on magnetostrictive properties. Since Guruswamy et al. (2000) found that Fe-Ga alloys have more advantages than Terfenol-D alloys, it has become a new type of promising magnetostrictive material. Many scholars have investigated the influence of the third elements (Jin et al., 2014; He et al., 2016; Meng and Jiang, 2016), heat treatment (Clark et al., 2000; Lograsso and Summers, 2006), preparation process (Yang et al., 2006; Li et al., 2008) and other factors on the magnetostrictive property of Fe-Ga alloys.

Piezoelectric ceramics produce stress/strain under the action of electric current and electric charge under stress/strain. The active control can be realized by adjusting the current level. Being environmentally friendly and lead-free, piezoelectric ceramics have gradually become one of the hotspots in the research of piezoelectric ceramics, and the main research objects are KNN, BNT, and BT ceramics. Liu and Ren (2009) reported a non-Pb piezoelectric ceramic system BaO_3-TiO_3 which shows a surprisingly high piezoelectric coefficient of $d_{33}\sim620$ Pc/N at optimal composition. This is the first time in more than 50 years that the performance of lead-free piezoelectric materials surpasses PZT piezoelectric ceramics. Leontsev and Eitel (2009) investigated dielectric, ferroelectric, and piezoelectric properties of Mn-modified (1-x) BF-xBT ceramics, which proves that the addition of Mn improves dielectric losses and increases DC resistivity by one to five orders of magnitude in bulk BF–BT.

MULTI-DIMENSIONAL VIBRATION MITIGATION/ISOLATION DEVICES APPLIED IN CIVIL ENGINEERING

Mitigation and Isolation Devices With Springs

The passive control device composed of horizontal and vertical components is the most widely used multi-dimensional mitigation and isolation device which can independently achieve isolation performance in all directions. This kind of device has strong carrying capacity under normal use, and energy dissipation capacity is provided by the springs. On the other hand, since the springs and horizontal components are usually combined in the vertical direction, the height of the device is difficult to control and the stability is relatively low. The application of springs, including air springs and metal springs, is a common vertical isolation method. Suhara et al. (2002) tested the workability of three-dimensional seismic isolation using the laminated rubber bearing and the rolling seal type air spring working in series, which demonstrates that this device combines excellent 3D seismic isolation performance with sufficient vertical load carrying capacity. Two parameters were considered in the design of the experiment, which decided the different contact of the horizontal and vertical loads. Kageyama et al. (2003) studied the feasibility of applying an isolation device using three-dimensional cable reinforcing air spring to actual nuclear power plants, which shows that the air spring enables isolation in three dimensions with a single device, achieving a cost reduction. Zhao et al. (2008) studied the valid performance of a newly multi-dimensional isolation using one main and eight auxiliary disk springs in parallel to modify the conventional rubber bearing in the vertical direction, which shows that this device can isolate three-dimensional earthquake energy remarkably. Mori et al. (2012) verified a new method to achieve three-dimensional isolation for building by exploiting a device which consists of the rubber bearing, the air spring and oil damping, which proves that both the three-direction seismic response and the rocking motion are successfully suppressed by the device. Cai et al. (2016) analyzed the influence of a

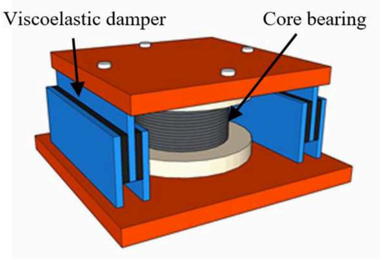

FIGURE 1 | The structural diagram of the MHEID (Xu et al., 2014).

three-dimensional isolation bearing using the combination of horizontal, vertical spring and sliding surface, "which indicates that the isolated lattice shell structures have better performance with respect to the absolute acceleration response to the axial force of components. Miyagawa et al. (2017) proposed a new combination system achieving three-dimensional seismic isolation by combing coned disc springs with rubber bearings," which mitigates vertical motion and suppresses rocking without any suppression system to provide a reasonable aseismic design for a sodium-cooled fast reactor. By combining the vertical spring with the horizontal isolation, it is possible to reduce the vertical stiffness of the device while providing a large bearing capacity, which can provide good multi-dimensional isolation performance. Furthermore, through the friction of the spring system, the seismic energy can be dissipated and the mitigation effect can be achieved.

Mitigation and Isolation Devices With High Damping Materials

Another efficient multi-dimensional mitigation and isolation method uses a high damping material such as viscous fluid and viscoelastic materials, etc. Devices with high damping materials have an excellent energy dissipation effect at the time of isolation. The structure of these devices is generally simple, therefore the stability is improved and the overturn of a superstructure under a large earthquake can be prevented effectively. Shimada et al. (2004) evaluated the performance of a three-dimensional earthquake isolation and mitigation system adopting a novel viscous damper wall, which shows that the damper wall can dissipate horizontal and vertical earthquake energy simultaneously by displacing it out of the plane direction. Xu et al. (2014) proposed an innovative multi-dimensional high-damping passive control device, named the multi-dimensional high damping earthquake isolation device (MHEID), for large-span reticulate structures, as shown in **Figure 1**. From the tests on the properties of the device, including the effect of excitation frequency and amplitude, "it is observed that the device has good capability of energy dissipation in the vertical direction and perpendicular paper direction" (Xu et al., 2012). The device has been applied on the large pipelines of Luoyang petrochemical corporation in Henan Province, China. A correction model based on the equivalent standard solid model is presented and used during the design, and excitation amplitude is taken into account.

Xu et al. (2017b) studied the excellent performance of an innovative device using viscoelastic material named MEIMD for multi-dimensional earthquake isolation and mitigation, as shown in **Figure 2**. Based on the experimental results of property tests and shaking table tests, it proves that this device has good isolation ability and damping performance both horizontally and vertically (Xu, 2009). The device has been applied on Kunming planning museum in Yunnan province, China, and effectively reduces the displacement and vertical tensile stress of the isolated layer under rare earthquakes. This study provides a new avenue for building structures to achieve multi-dimensional vibration control by adopting the viscoelastic materials with high energy dissipation capacity.

Due to the introduction of high energy-consuming materials, it not only exploits the advantages of the isolation bearing but also greatly increases the damping ratio of the whole system. Through the movement of the isolation layer and the additional damping device, it can mitigate a large amount of seismic energy to ensure safety and stability.

Other Mitigation and Isolation Devices

In addition to conceptual simplicity and moderate cost, good durability and temperature insensitivity are also basic requirements in the application of multi-dimensional vibration mitigation and devices in the field of civil engineering (Lu et al., 2018a). Shi and Huang (2013) verified the unique performance of an innovative three-dimensional seismic isolation, called periodic foundation, that was integrated with a high-density core, a soft coating and a concrete matrix, which shows that both horizontal and vertical seismic action can be greatly reduced after crossing the periodic foundation. He et al. (2014) verified the control effect of a multi-dimensional tuned mass damper named MDTMD, including tuned mass blocks, torsional blocks, and a rotation lever, which shows that the coupled responses decrease significantly by MDTMD and the vibration reduction ration is much higher compared to traditional TMD. Li et al. (2011) verified the effectiveness of a novel three-dimensional seismic isolation made up of martensitic shape memory alloy wires named 3-D SMAPRI, which proves that the 3-D isolator has effective mechanical properties as well as energy dissipation performance along both horizontal and vertical directions.

Hybrid Multi-Dimensional Mitigation and Isolation Device

The combination of various types of devices into a hybrid device is a novel multi-dimensional mitigation and isolation method with high control efficiency. One type of hybrid device is the passive hybrid multi-dimensional mitigation and isolation device. Ou and Jia (2010) validated the effectiveness of a three-dimensional isolation bearing consisting of a laminated rubber bearing and a combined coned disc spring with a vertical energy dissipation device, which shows that the 3D seismic isolation bearing is expected to be applied to the medium-to-short span bridges. Okamura et al. (2011) evaluated the effectiveness of an advanced seismic isolation system adopting thicker laminated rubber bearings and oil dampers, which confirms the possibility of isolating three-dimensional earthquake motion to protect

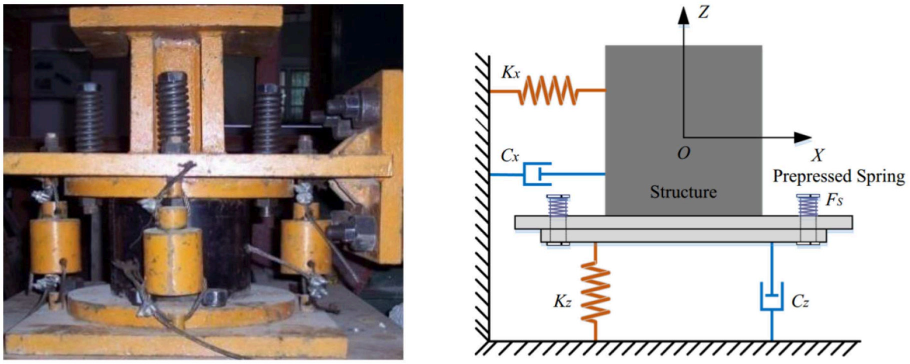

FIGURE 2 | The structural diagram and the mechanics model of MEIMD (Xu et al., 2017b).

nuclear power plants by increasing the thickness of the rubber layer of conventional rubber bearings. Yang and Niu (2012) studied the beneficial effect of a new three-dimensional isolation combining SMA strands and the disc spring with laminated rubber bearings, which indicates that the application of SMA causes clear seismic energy dissipation and reduces upper structure deformation in all directions. Jia et al. (2014) illustrated the advantages of a 3D isolation device composed of combined disk springs, rhombic steel plate damper and lead rubber bearing, which indicates that the isolator supplies appropriate vertical and horizontal stiffness and an energy dissipation mechanism to protect engineering structures in severe 3D earthquake motions. Kitayama et al. (2017) assessed the seismic performance of a three-dimensional isolator composed of a triple FP isolator in the horizontal direction and a spring-damper system in the vertical direction by incremental dynamic analysis, which is demonstrated to be a reliable way to seismically protect the electric power system. Liu et al. (2018a) analyzed the excellent property of a separation type three-dimensional isolation system with multiple guide rails to decouple horizontal and vertical motion, which indicates that the system not only displays desirable isolation but also contributes significantly to resist the overturning moment. Liu et al. (2018b) studied the property of a new multi-dimensional device using several inclined lead rubber bearings to decompose vertical seismic action, as shown in **Figure 3**. From the analysis of dynamic properties such as vertical acceleration, it is found that the seismic response is largely reduced compared with that of fixed-base structures. It is indicated that this device balances a high supporting capacity and low vertical stiffness to realize 3D isolation by optimizing the inclination angle of the lead rubber bearings.

Cimellaro et al. (2018) investigated the performance of a novel three-dimensional base isolation system adopting an adoptive passive protection system called a negative stiffness device, as shown in **Figure 4**. From the numerical analyses of the isolated frame in strong earthquake, it can be observed that the vertical acceleration in the structure is apparently decreased. This study proposes a new method to reduce the multi-direction seismic responses of superstructures by way of combining the negative stiffness device with the conventional bearing systems.

Another type of hybrid device is the intelligent hybrid multi-dimensional mitigation and isolation device. Fujita et al. (2011) studied the basic property and performance of an intelligent three-dimensional isolation system encompassing air bearings and an earthquake early warning system, which indicates that this system is suitable for earthquakes in multiple directions and complex situations, even against near-field earthquakes. MR damper is also considered to be an effective intelligent control method. Xu et al. (2003) presented an on-line real-time control method for structures with MR dampers and proposed a novel design method for MR dampers (Xu et al., 2013), both of which promote the use of MR dampers in multi-dimensional mitigation and isolation devices. Cesmeci et al. (2018) demonstrated the superiority of a new device utilizing controllable MR damper and liquid springs in series with an elastomeric bearing for the three-dimensional isolation of building structures, as shown in **Figure 5**. From the experiments which reflect the device's real-life loading condition, it proves that the device operates well under the combined axial and shearing loading without any loss in performance. This study is the first time an MR damper has been tested in combination with horizontal and vertical seismic loads. Through semi-active control, the stability of the mitigation and isolation system during normal use can be ensured, while the horizontal and vertical performance can be fully exhibited under multi-dimensional earthquakes.

The hybrid multi-dimensional mitigation and isolation device not only involves the advantages of each component, but also overcomes the deficiencies of the individual parts. Taking devices combining springs and high damping materials as an example, the springs arranged vertically isolate the earthquake efficiently, but the capability of energy dissipation is relatively weak. The addition of high damping materials enhances the energy dissipation performance during the earthquake; consequently, both the vibration isolation and vibration mitigation properties are realized in the device. Therefore, this has become the most mainstream research direction in the field of multi-dimensional mitigation and isolation device. On the other hand, these devices are currently in the theoretical research stage and are not yet applicable in practical engineering because of the immature technology.

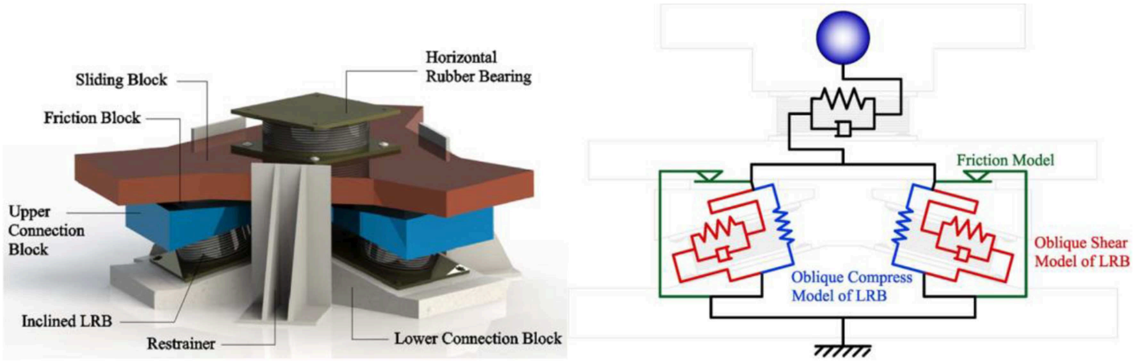

FIGURE 3 | The 3D structural diagram and the mathematical model of the inclined lead rubber bearings (Liu et al., 2018b).

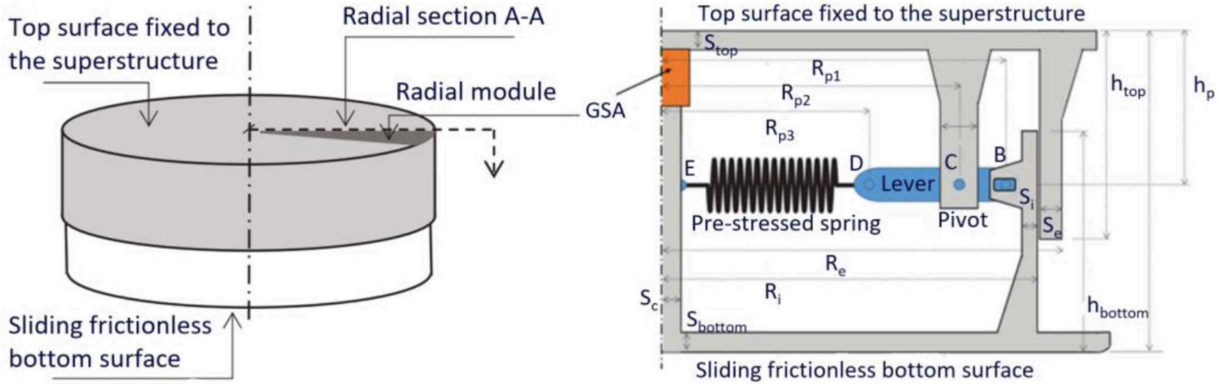

FIGURE 4 | 3D view and detailed diagram of the Negative Stiffness Devices (Cimellaro et al., 2018).

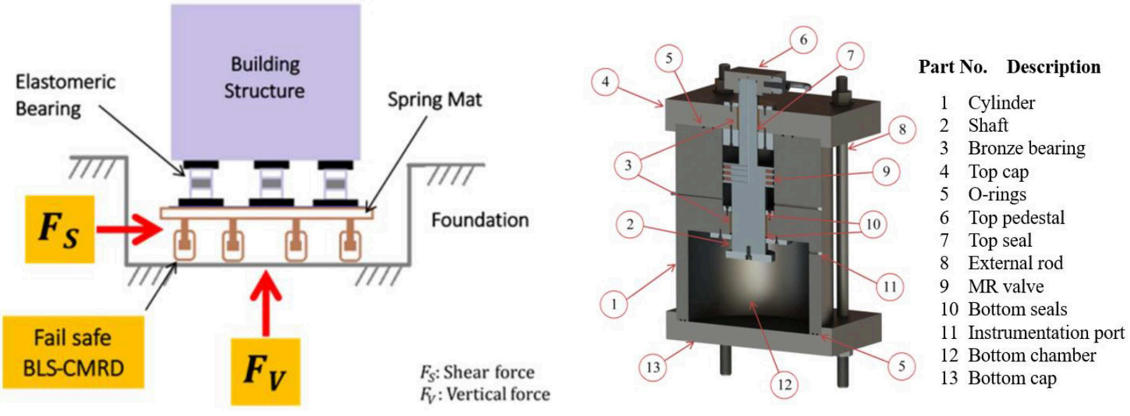

FIGURE 5 | The installation of the liquid spring–magnetorheological damper in structure and its cutout view (Cesmeci et al., 2018).

MULTI-DIMENSIONAL VIBRATION MITIGATION/ISOLATION DEVICES APPLIED IN MECHANICAL ENGINEERING

Passive Control Devices

Passive control systems add an energy mitigation device or substructure system to the appropriate portion of the structure to optimize the dynamic characteristics of the structural system. Carrella et al. (2007) investigated the static characteristics of a quasi-zero-stiffness (QZS) mechanism consisting of a vertical spring and two oblique springs, which uses a negative stiffness component and realizes low stiffness without overlarge static deflection. Hoque et al. (2011) presented a module-type 3 degree of freedom (DOF) vibration isolation system using reformative zero-power control and parallel mechanism technique, whose reliability and efficiency has been verified by the analytical and experimental studies. Kim et al. (2013) presented an optimal design of a QZS isolator consisting of flexures, a vertical spring, a horizontal spring, and a vertical gravity compensator. The isolator has strong vertical stiffness to sustain a wide range of payloads because the properties of vertical springs lead to more gravity compensation within a given stroke. Sun and Jing (2015) presented an advanced vibration isolator with 3D QZS property, as shown in **Figure 6**. The isolator applies symmetrically scissor-like structures (SLS) in the horizontal directions and a conventional spring-mass-damper system in the vertical direction with positive stiffness. Due to the non-linear stiffness and damping properties produced by the non-linearity of geometric relations within the SLSs, the isolator has noticeable performance with structural non-linearity and only passive elements.

Wu et al. (2016) studied on a novel 6-DOF passive vibration isolator which has been validated with experiments that the isolator has effective isolation behavior in all the six directions and takes the advantage of passive control on account of the combination of the Stewart platform and the X-shape structure. Zhou et al. (2017) extended the QZS vibration isolation method from one DOF to six DOFs by the method of applying a new-type QZS strut to establish a 6-DOF QZS vibration isolation platform, which possesses broader bandwidth and higher effectiveness compared with the linear counterpart. Ramesh et al. (2019) combined rigid body isolation and modal analysis principles to obtain the elastic and dissipative properties of the vibration isolator and analyzed several kinds of 3-DOF model isolation systems on the modal experiments and system characterization for validation purposes. Traditional linear energy dissipative methods and devices are greatly limited for wider application on account of the unsatisfactory properties under certain conditions, while non-linear vibration mitigation devices with broadband response and high robustness are being widely investigated and applied (Lu et al., 2018b). Non-linear stiffness is designed on the QZS vibration isolators, whose static stiffness is high while dynamic stiffness is low. The studies using passive control take advantage of non-linearity to enhance the performance of isolation, and the bandwidth of isolators has been broadened into both lower and higher frequencies.

Intelligent Control Devices

Different from passive control systems, intelligent control systems often require the input of external energy, while they have superior vibration control performance. Yoshioka et al. (2001) presented an active 6-DOF micro-vibration isolation system consisting of voice-coil linear motors and pneumatic and piezoelectric actuators with a feed-forward control link applied to the sway elements in each direction, which shows good vibration control performance in the vibration isolation table test. Liao and Wang (2003) investigated a semi-active secondary train suspension system with MR dampers which has been verified to be significantly effective in attenuating the vertical pitch and roll vibrations of the car body. Unsal et al. (2008) proposed a 6-DOF parallel platform model for which each leg is modeled as a 2-DOF system with a coil-over MR damper to adjust damping and an actuator for positioning, and it provides effective vibration isolation performance and precise positioning capability with reduced cost and reduced power requirements. Zareh et al. (2012) proposed an 11-DOF passenger car's suspension system which uses MR dampers with neuro-fuzzy (NF) control strategy as well as a novel intelligent semi-active control system. The inverse mapping model is proposed to estimate the force needed for a semi-active damper. Xu and Sun (2015) investigated the potential remarkable behavior of a multi-direction QZS vibration isolator using linear time-delayed active control, as shown in **Figure 7**. "From the research on the inherent property such as natural frequency, it can be observed that the performance of the isolator in different dimensions can be adjusted independently". "The study provides an advanced insight into the design and analysis of multi-dimensional vibration isolation devices by utilizing potential non-linear superiority of the time delay in active vibration control".

Zhou et al. (2015) demonstrated experimentally an ultra-low frequency active vibration isolation system which suppresses the vibration noise in three dimensions. The system is provided for atom gravimeters, especially for the gravimeter whose sensitivity is adversely affected by vibration couplings. The performance of multi-dimensional isolators using MR dampers is verified by the simulation and experiment and enhanced by a variety of control strategies (Xu et al., 2016d,f). In the field of mechanical engineering, the novel instruments put forward higher demands for precision and the rheological properties of the MR dampers meet the needs. For further research, it is imperative to establish a more accurate model of MR dampers to improve the control effect because of its highly non-linear nature.

Hybrid Control Devices

Aside from the passive control systems and intelligent control systems, hybrid systems combining active and passive devices are also one of the main development directions of multi-dimensional vibration isolation systems. Wang and Liu (2009) presented a hybrid control system comprising five air springs installed vertically in parallel and eight actuators installed in both vertically and horizontally, whose control performance against ground motion and direct disturbance is superior to that of the passive control system verified by the simulation. Hoque et al. (2010) presented a 6-DOF hybrid vibration isolation system composed of an active negative suspension, an active–passive positive suspension and a passive weight support mechanism, as shown in **Figure 8**. The system possesses outstanding behavior on direct disturbance suppression and payload supporting capabilities without diminishing transmissibility characteristics. Additionally, the influence of on-board generated direct disturbances of the six-axis motions in vertical and horizontal directions and ground vibrations could be isolated effectively. The mathematical model of the system has been developed and it is indicated that zero compliance to direct disturbance is provided by the system.

Li et al. (2012) proposed a novel vibration isolator possessing three translational DOFs and two rotational DOFs, which widens the range of frequency by decoupling

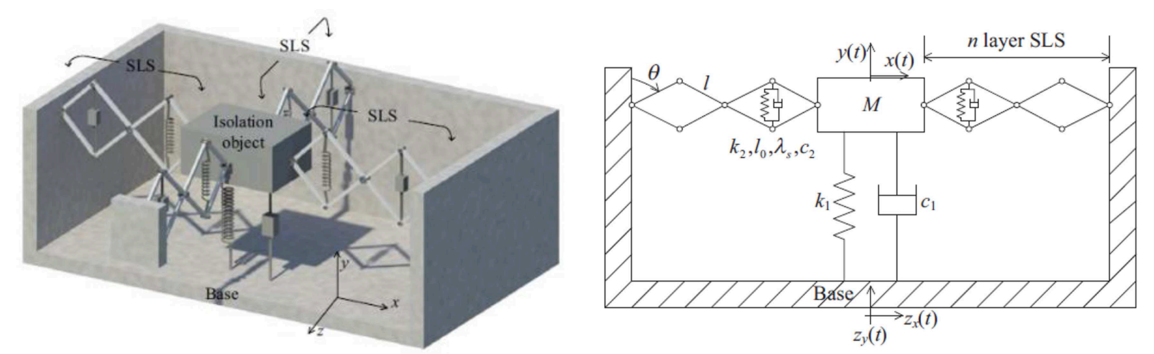

FIGURE 6 | The structural diagram of the multi-direction isolation system (Sun and Jing, 2015).

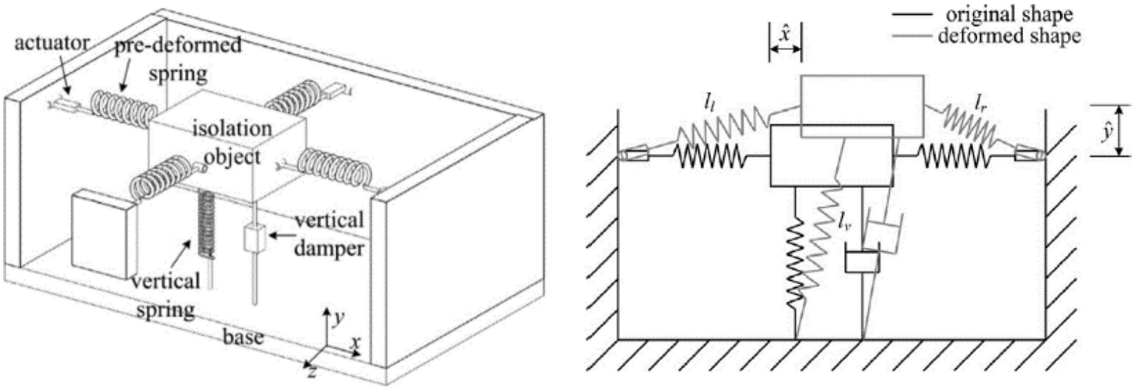

FIGURE 7 | Structural diagram of the multi-direction QZS vibration isolator (Xu and Sun, 2015).

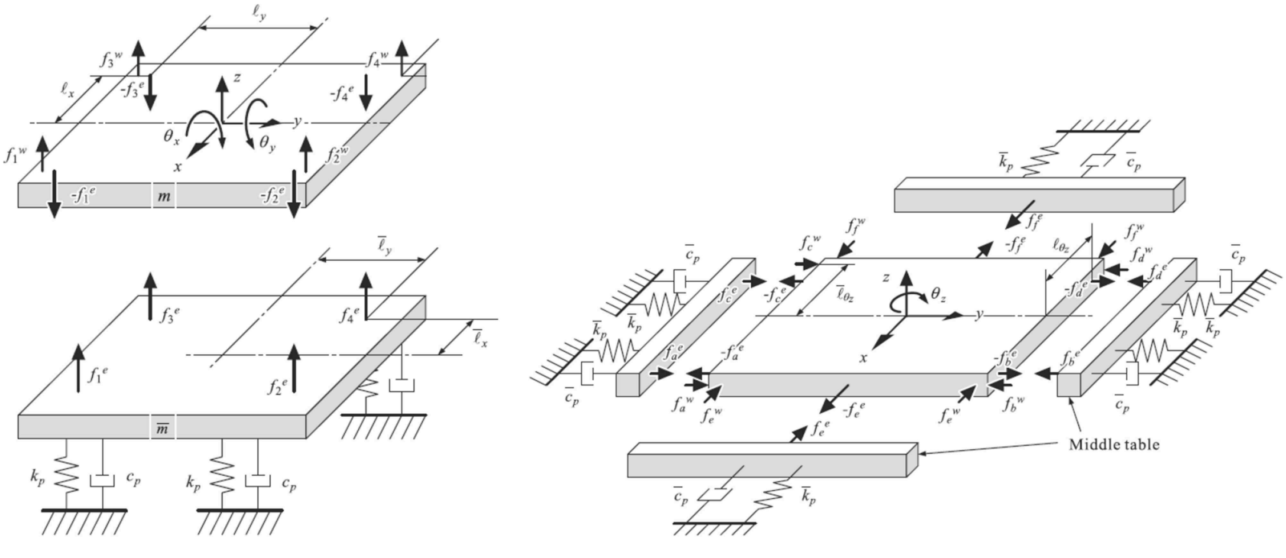

FIGURE 8 | The structural diagram of the solation table for six-axis motions (Hoque et al., 2010).

the translations and rotations of the manipulator. The systems reviewed above achieve a superior performance to passive control systems within a wide frequency range of vibrations. The dynamic characteristics of the systems are related to the control parameters as well as the physical parameters, hence, the optimal design of control and physical parameters is imperative to improve the dynamic performance of the systems.

MULTI-DIMENSIONAL VIBRATION MITIGATION/ISOLATION DEVICES APPLIED IN AEROSPACE ENGINEERING

Vibration Mitigation/Isolation of Whole-Spacecraft

Vibration control in aerospace engineering falls into two main categories—whole-spacecraft vibration isolation (WSVI) and micro-vibration control of satellites. WSVI is for the reduction of the vibration loads during launch, and it greatly reduces the risk of the spacecraft and its instruments being damaged before entering orbit. Jun et al. (2007) presented a whole-spacecraft passive isolation system with a demonstration unit integrated with all kinds of isolator components. The payload attach fitting is limited by the constrained viscoelastic layer on the outer surface, thus its damping is enhanced obviously. Li et al. (2016) designed and tested an active vibration isolator, which includes flexible piezoelectric sensors and actuators. The thin shell hypothesis and the converse piezoelectric effect are considered to obtain the modal control force during the design of the isolator.

Tang et al. (2018) designed, fabricated, and tested a novel active whole-spacecraft isolation system based on voice coil motors (VCMs), as shown in **Figure 9**. Vibration tests were conducted on the developed prototype for the verification purpose, and the experiment results indicate that the new system attenuates the resonant peak remarkably well. The study provides advanced insight into the analysis and design of whole-spacecraft isolator in active vibration control.

ESA developed an active payload adaptor to take the place of the traditional passive payload adaptors whose framework is a truss structure with 24 active struts in the load path applying piezo-ceramics as actuator (Rittweger et al., 2005). The adaptor is designed to reduce the vibration below 100 Hz to a quarter for Ariane 5, and the result is obtained in the frame of the ESA GSP program. Liu et al. (2006) proposed an octo-strut passive vibration isolation platform for whole-spacecraft vibration isolation which introduces redundancy. Liu et al. (2010) presented a novel Circular Payload Adapter Fitting (CPAF) which integrates passive and active vibration control with the piezoelectric stack actuators based on passive control. Based on the CPAF, Chi et al. (2014) designed an active vibration isolation method applying the voice coil based actuator whose voice coil motor is designed and optimized as the active control actuator. The passive isolator is simpler and more convenient than the new adapter, but the new adapter has better vibration isolation performance. The active isolator proposed by Tang is in between. Both whole-space vibration isolator and new payload adaptors have great vibration isolation performance and as a result, more sensitive equipment is able to be launched into space.

Micro-Vibration Mitigation/Isolation of Satellite

The micro-vibration of satellites in orbit is an important factor that restricts the resolution of the payload. Therefore, it is necessary to control the micro-vibration of satellites in orbit. The James Webb Space Telescope employed dual-stage passive isolation (Bronowicki, 2006). The first stage of isolation is at the disturbance source in which individual reaction wheels use the flight-proven Chandra isolator while the second stage of isolation is a full isolator positioned between the top of the spacecraft bus and the pop-up thermal isolation tower which orientates the telescope. More than one kind of damping material are added, thus, the analysis methodology is extended to fit the multiple structural partitions. Kamesh et al. (2010) proposed a passive and active space frame platform integrated with four folded continuous beams arranged in three directions.

The Air Force Research Laboratory (AFRL) Space Vehicle Directorate and Honeywell Defense and Space designed MVIS-II for miniature hybrid (passive/active) vibration isolation of sensitive optical payloads (McMickell et al., 2007), as shown in **Figure 10**. Results of the experiment based on ground lead to the expectation of better on-orbit isolation properties, and the study provides a useful insight into the design of payload isolators in vibration hybrid control.

Dai et al. (2018) proposed a bio-inspired quadrilateral shape (BIQS) structure inspired by the smooth movement of a running kangaroo to suppress the vibrations of a free-floating spacecraft suffered from periodic or impulsive forces, as shown in **Figure 11**. Numerical simulation shows that the BIQS system has superior behavior under conditions of either periodic or impulsive forces. The study provides a highly efficient passive way for vibration suppression in free-floating spacecraft.

Compared to the vibration isolation method of the James Webb Space Telescope, the integrated attitude control and vibration isolation of MVIS-II is more convenient but more expensive. Dai's design includes the idea of simulation, which is a promising research direction. In addition, hybrid control is also worth studying. For example, Xu et al. (2016e) presented a platform combining MR and VE devices, which is able to effectively isolate 0–500 Hz vibrations. Above all, with the development of high-resolution satellites, the research of micro-vibration control methods will be further deepened.

CONCLUSIONS AND PROSPECTS

Using materials of high performance, including wide temperature domain and wide frequency domain, is supposed to be an efficient way to reduce the vibration, even for high-intensity vibrations. Meanwhile, there still exists promising prospects for the coupling application of various materials and promoting them to multi-dimensional vibration mitigation and isolation devices. The research will continuously focus on optimizing the performance of existing materials and establishing accurate constitutive models for describing the behavior of materials and in the future.

In the field of civil engineering, research started late on multi-dimensional mitigation and isolation devices. Most of the traditional research focuses on a single direction or a single function, while little research is concerned about mitigation and isolation in multiple directions or multiple functions. For example, most of the current isolation systems just focus on

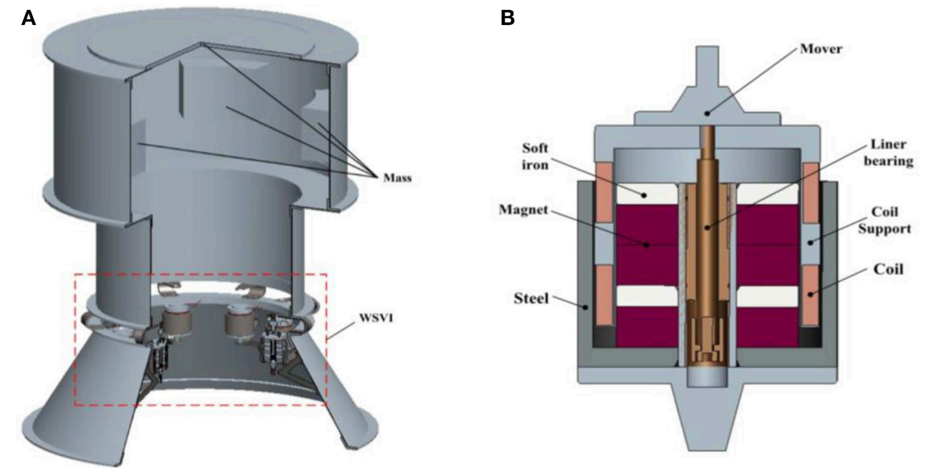

FIGURE 9 | (A) WSVI system **(B)** Structure of the electromagnetic actuator (Tang et al., 2018).

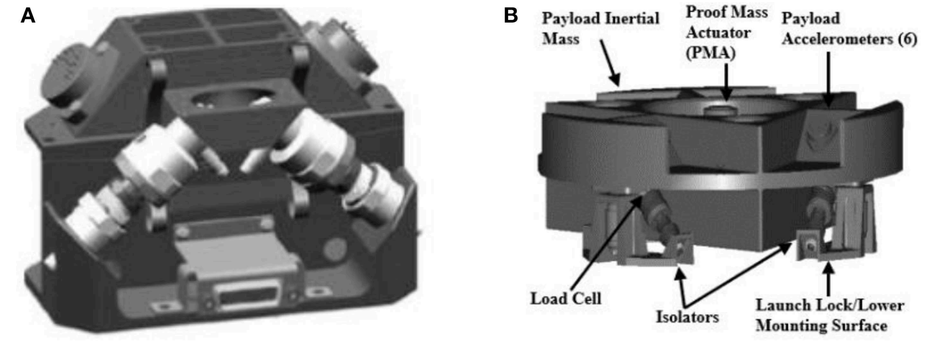

FIGURE 10 | (A) Two hybrid MVIS-II Isolators **(B)** MVIS-II original flight demonstration with integral launch lock (McMickell et al., 2007).

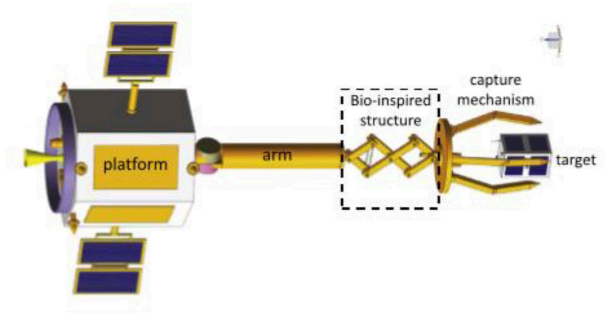

FIGURE 11 | The schematic diagram of an on-orbit capture mission (Dai et al., 2018).

horizontal or vertical isolation, while the shocking effect after the combination of horizontal and vertical motion and the uplifting action caused by the swing of superstructure are less involved. Additionally, the existing multi-dimensional mitigation and isolation devices commonly adopt different combinations of springs and a variety of dampers. Few devices utilize high damping material or smart mitigation material. Therefore, research should accelerate when it comes to the development of hybrid multi-dimensional mitigation and isolation devices and the application of high damping and smart mitigation materials.

In the field of mechanical engineering, precision for instruments and instantaneity of mitigation are in great demand. Thus, intelligent control under different directions is a promising approach for mitigating multi-dimensional vibration responses. As for semi-active vibration control devices, the accuracy of the parametric dynamic modeling is of great importance due to the inherent non-linearity. Although the research on active control devices is still a small proportion of multi-dimensional isolators, it will be promoted in further research. Furthermore, the optimal design for intelligent control devices needs to be investigated and more work should look at the problems of control algorithms.

In the field of aerospace engineering, multi-dimensional vibration control is an important means to ensure the safety of satellites and their equipment in the launch stage, while improving the accuracy of satellite payloads in orbit. Meanwhile, the vibrations during launch are generated by a variety of flight events such as engine ignition, booster separation, and acoustic excitation, and the frequency domains of each excitation are different. Thus, the vibration mitigation and isolation of wide frequency domains in multiple dimensions will be the future development priority. For whole-spacecraft vibration isolation, passive control devices have been widely used, but their performance in vibration isolation is inferior to active control devices, which are more complex and expensive. Therefore, research on semi-active control devices deserves more attention because of relatively excellent performance and simple structure. For micro-vibration control of satellites in orbit, it has great prospects to combine attitude control and the isolation of micro-vibrations generated by the attitude control unit. Additionally, current research focuses on internal vibration sources such as the attitude control unit, while vibration caused by external sources deserves more attention.

At present, research on multi-dimensional mitigation and isolation devices is relatively scarce. Moreover, research on most devices is still in the theoretical and experimental stages, and there are few examples of using these multi-dimensional isolation devices in practical engineering. The authors aim to devote themselves to researching the wide temperature domain and wide frequency domain of vibration mitigation materials, meanwhile the application of the materials and devices is also an important research direction. However, there is still a long way to go to expand different multi-dimensional mitigation and isolation devices and promote applications in practical engineering.

AUTHOR CONTRIBUTIONS

Z-DX identified the framework of the article and wrote the main content of the article. All other authors are responsible for the organization of literature and pictures.

FUNDING

This study was financially supported by the Program of Chang Jiang Scholars of Ministry of Education, National Science Fund for Distinguished Young Scholars with Grant No. 51625803, National Key R&D Programs of China with Grant Nos. 2016YFE0200500 and 2016YFE0119700, National Natural Science Foundation of China with Grant No. 11572088.

REFERENCES

Bell, R. C., Karli, J. O., Vavreck, A. N., Zimmerman, D. T., Ngatu, G. T., and Wereley, N. M. (2008). Magnetorheology of submicron diameter iron microwires dispersed in silicone oil. *Smart Mater. Struct.* 17:015028. doi: 10.1088/0964-1726/17/01/015028

Bondi, A. A. (1956). *Magnetic Fluids.* U.S. Patent No. 2,751,352. Washington, DC: U.S. Patent and Trademark Office.

Bronowicki, A. J. (2006). Vibration isolator for large space telescopes. *J Spacecraft Rockets* 43, 45–53. doi: 10.2514/1.12036

Cai, Y., Li, X., and Xue, S. (2016). Application and design of 3D seismic isolation bearing in lattice shell structure. *HKIE Transac.* 23, 200–213. doi: 10.1080/1023697X.2016.1231016

Carrella, A., Brennan, M. J., and Waters, T. P. (2007). Static analysis of a passive vibration isolator with quasi-zero stiffness characteristic. *J. Sound Vibration* 301, 678–689. doi: 10.1016/j.jsv.2006.10.011

Cesmeci, S., Gordaninejad, F., Ryan, K. L., and Eltahawy, W. (2018). A liquid spring–magnetorheological damper system under combined axial and shear loading for three-dimensional seismic isolation of structures. *J. Intell. Mater. Syst. Struct.* 29, 3517–3532. doi: 10.1177/1045389X18783090

Chi, W., Cao, D., and Huang, W. (2014). "Design of active whole-spacecraft vibration isolation based on voice-coil motor," in *Sensors and Smart Structures Technologies for Civil, Mechanical, and Aerospace Systems*, Vol. 9061. 90613X-1–90613X-7. doi: 10.1117/12.2044920

Cimellaro, G. P., Domaneschi, M., and Warn, G. (2018). Three-dimensional base isolation using vertical negative stiffness devices. *J. Earthquake Eng.* 1–29. doi: 10.1080/13632469.2018.1493004. [Epub ahead of print].

Clark, A. E., Restorff, J. B., Wun-Fogle, M., Lograsso, T. A., and Schlagel, D. L. (2000). Magnetostrictive properties of body-centered cubic Fe-Ga and Fe-Ga-Al alloys. *IEEE Transac. Magnetics* 36, 3238–3240. doi: 10.1109/20.908752

Dai, H., Jing, X., Wang, Y., Yue, X., and Yuan, J. (2018). Post-capture vibration suppression of spacecraft via a bio-inspired isolation system. *Mech. Syst. Signal Proc.* 105, 214–240. doi: 10.1016/j.ymssp.2017.12.015

De Vicente, J., Segovia-Gutiérrez, J. P., Andablo-Reyes, E., Vereda, F., and Hidalgo-Álvarez, R. (2009). Dynamic rheology of sphere-and rod-based magnetorheological fluids. *J. Chem. Phys.* 131:194902. doi: 10.1063/1.3259358

Duenas, T. A., and Carman, G. P. (2001). Particle distribution study for low-volume fraction magnetostrictive composites. *J. Appl. Phys.* 90, 2433–2439. doi: 10.1063/1.1389518

Fang, F. F., Choi, H. J., and Jhon, M. S. (2009). Magnetorheology of soft magnetic carbonyl iron suspension with single-walled carbon nanotube additive and its yield stress scaling function. *Colloids Surfaces A Physicochem. Eng. Aspects* 351, 46–51. doi: 10.1016/j.colsurfa.2009.09.032

Foister, R. T. (1997). *U. S. Magneto-Rheological Fluid.* Patent No. 5,667,715. Washington, DC: U.S. Patent and Trademark Office.

Fujita, S., Minagawa, K., Tanaka, G., and Shimosaka, H. (2011). Intelligent seismic isolation system using air bearings and earthquake early warning. *Soil Dynam. Earthquake Eng.* 31, 223–230. doi: 10.1016/j.soildyn.2010.06.006

Ginder, J. M., Davis, L. C., and Elie, L. D. (1996). Rheology of magnetorheological fluids: models and measurements. *Int. J. Modern Phys. B* 10, 3293–3303. doi: 10.1142/S0217979296001744

González-Martínez, R., Göken, J., Letzig, D., Steinhoff, K., and Kainer, K. U. (2007). Influence of aging on damping of the magnesium–aluminium–zinc series. *J. Alloys Compounds* 437, 127–132. doi: 10.1016/j.jallcom.2006.07.085

Guerrero-Sanchez, C., Lara-Ceniceros, T., Jimenez-Regalado, E., Rașa, M., and Schubert, U. S. (2007). Magnetorheological fluids based on ionic liquids. *Adv. Mater.* 19, 1740–1747. doi: 10.1002/adma.200700302

Guo, Y. Q., Sun, C. L., and Xu, Z. D. (2018). Preparation and tests of MR fluids with CI particles coated with MWNTs. *Front. Mater.* 5:50. doi: 10.3389/fmats.2018.00050

Guo, Y. Q., Xu, Z. D., Chen, B. B., Ran, C. S., and Guo, W. Y. (2017). Preparation and experimental study of magnetorheological fluids for vibration control. *Int. J. Acoust. Vibration* 22, 194–201. doi: 10.20855/ijav.2017.22.2464

Guruswamy, S., Srisukhumbowornchai, N., Clark, A. E., Restorff, J. B., and Wun-Fogle, M. (2000). Strong, ductile, and low-field-magnetostrictive alloys based on Fe-Ga. *Scripta Mater.* 43, 239–244. doi: 10.1016/S1359-6462(00)00397-3

He, H. X., Han, E. Z., and Lv, Y. W. (2014). Coupled vibration control of tuned mass damper in both horizontal and torsional direction. *Appl. Mech. Mater.* 578, 1000-1006. doi: 10.4028/www.scientific.net/AMM.578-579.1000

He, Y., Jiang, C., Wu, W., Wang, B., Duan, H., Wang, H., et al. (2016). Giant heterogeneous magnetostriction in Fe–Ga alloys: effect of trace element doping. *Acta Mater.* 109, 177–186. doi: 10.1016/j.actamat.2016.02.056

Hoque, M. E., Mizuno, T., Ishino, Y., and Takasaki, M. (2010). A six-axis hybrid vibration isolation system using active zero-power control supported by passive weight support mechanism. *J. Sound Vibration* 329, 3417–3430. doi: 10.1016/j.jsv.2010.03.003

Hoque, M. E., Mizuno, T., Ishino, Y., and Takasaki, M. (2011). A three-axis vibration isolation system using modified zero-power controller with parallel mechanism technique. *Mechatronics* 21, 1055–1062. doi: 10.1016/j.mechatronics.2011.05.002

Iyengar, V. R., Alexandridis, A. A., Tung, S. C., and Rule, D. S. (2004). Wear testing of seals in magneto-rheological fluids. *Tribol. Transac.* 47, 23–28. doi: 10.1080/05698190490279083

Jia, C. (2007). Study on damping behavior of FeAl_3 reinforced commercial purity aluminum. *Mater. Design* 28, 1711–1713. doi: 10.1061/9780784413234.057

Jia, J. F., Dong, H. H., Zhang, T., and Du, X. L. (2014). "Mechanics performance test and seismic behavior of a novel 3D isolation bearing for bridges," In *International Efforts in Lifeline Earthquake Engineering* (Chengdu), 441–448.

Jin, T., Wu, W., and Jiang, C. (2014). Improved magnetostriction of Dy-doped Fe83Ga17 melt-spun ribbons. *Scripta Mater.* 74, 100–103. doi: 10.1016/j.scriptamat.2013.11.010

Jun, Z., Hongxing, H., and Zhiyi, Z. (2007). An evaluation of the whole-spacecraft passive vibration isolation system. *Proc. Inst. Mech. Engineers Part G J. Aerospace Eng.* 221, 67–72. doi: 10.1243/09544100JAERO81

Kageyama, M., Iba, T., Umeki, K., Somaki, T., and Moro, S. (2003). "Development of three-dimensional base isolation system with cable reinforcing air spring," In *Proceedings of the 17th International Conference on Structural Mechanics in Reactor Technology* (Prague: SMiRT 17).

Kainuma, R., Imano, Y., Ito, W., Sutou, Y., Morito, H., Okamoto, S., et al. (2006). Magnetic-field-induced shape recovery by reverse phase transformation. *Nature* 439:957. doi: 10.1038/nature04493

Kamath, G. M., Wereley, N. M., and Jolly, M. R. (1999). Characterization of magnetorheological helicopter lag dampers. *J. Am. Helicopter Soc.* 44, 234–248. doi: 10.4050/JAHS.44.234

Kamesh, D., Pandiyan, R., and Ghosal, A. (2010). Modeling, design and analysis of low frequency platform for attenuating micro-vibration in spacecraft. *J. Sound Vibration* 329, 3431–3450. doi: 10.1016/j.jsv.2010.03.008

Kim, K. R., You, Y. H., and Ahn, H. J. (2013). Optimal design of a QZS isolator using flexures for a wide range of payload. *Int. J. Precision Eng. Manufacturing* 14, 911–917. doi: 10.1007/s12541-013-0120-0

Kitayama, S., Lee, D., Constantinou, M. C., and Kempner L. Jr. (2017). Probabilistic seismic assessment of seismically isolated electrical transformers considering vertical isolation and vertical ground motion. *Eng. Struct.* 152, 888–900. doi: 10.1016/j.engstruct.2017.10.009

Leontsev, S. O., and Eitel, R. E. (2009). Dielectric and piezoelectric properties in Mn-modified (1– x) BiFeO3–BaTiO3 ceramics. *J. Am. Ceramic Soc.* 92, 2957–2961. doi: 10.1111/j.1551-2916.2009.03313.x

Li, B., Zhao, W., and Deng, Z. (2012). Modeling and analysis of a multi-dimensional vibration isolator based on the parallel mechanism. *J. Manufacturing Syst.* 31, 50–58. doi: 10.1016/j.jmsy.2010.12.001

Li, H., Li, H. Y., Chen, Z. B., and Tzou, H. S. (2016). Experiments on active precision isolation with a smart conical adapter. *J. Sound Vibration* 374, 17–28. doi: 10.1016/j.jsv.2016.03.039

Li, J. H., Gao, X. X., Zhu, J., Zhang, M. C., and He, C. X. (2008). Texture and magnetostriction in rolled Fe-Ga alloy. *Acta Metallurg. Sinica* 44, 1031–1034.

Li, S., Mao, C., Li, H., and Zhao, Y. (2011). Mechanical properties and theoretical modeling of self-centering shape memory alloy pseudo-rubber. *Smart Mater. Struct.* 20:115008. doi: 10.1088/0964-1726/20/11/115008

Liao, W. H., and Wang, D. H. (2003). Semiactive vibration control of train suspension systems via magnetorheological dampers. *J. Intell. Mater. Syst. Struct.* 14, 161–172. doi: 10.1177/1045389X03014003004

Lihua, L., Xiuqin, Z., Xianfeng, L., Haowei, W., and Naiheng, M. (2007). Effect of silicon on damping capacities of pure magnesium and magnesium alloys. *Mater. Lett.* 61, 231–234. doi: 10.1016/j.matlet.2006.04.038

Liu, F., Fang, B., and Huang, W. H. (2010). "Vibration control of flexible satellites using a new isolator," In *2010 3rd International Symposium on Systems and Control in Aeronautics and Astronautics* Harbin: IEEE, 593–597.

Liu, K., Lv, Q., and Hua, J. (2017). Study on damping properties of HVBR/EVM blends prepared by *in situ* polymerization. *Polymer Test.* 60, 321–325. doi: 10.1016/j.polymertesting.2017.02.026

Liu, L. K., Zheng, G. T., and Huang, W. H. (2006). Octo-strut vibration isolation platform and its application to whole spacecraft vibration isolation. *J. Sound Vibration* 289, 726–744. doi: 10.1016/j.jsv.2005.02.040

Liu, W., and Ren, X. (2009). Large piezoelectric effect in Pb-free ceramics. *Phys. Rev. Lett.* 103:257602. doi: 10.1103/PhysRevLett.103.257602

Liu, W., Tian, K., Wei, L., He, W., and Yang, Q. (2018a). Earthquake response and isolation effect analysis for separation type three-dimensional isolated structure. *Bull. Earthquake Eng.* 16, 6335–6364. doi: 10.1007/s10518-018-0417-6

Liu, W., Xu, H., He, W., and Yang, Q. (2018b). Static test and seismic dynamic response of an innovative 3D seismic isolation system. *J. Struct. Eng. ASCE* 144:04018212. doi: 10.1061/(ASCE)ST.1943-541X.0002195

Liu, Y. D., Lee, J., Choi, S. B., and Choi, H. J. (2013). Silica-coated carbonyl iron microsphere based magnetorheological fluid and its damping force characteristics. *Smart Mater. Struct.* 22:065022. doi: 10.1088/0964-1726/22/6/065022

Lograsso, T. A., and Summers, E. M. (2006). Detection and quantification of D03 chemical order in Fe–Ga alloys using high resolution X-ray diffraction. *Mater. Sci. Eng. A* 416, 240–245. doi: 10.1016/j.msea.2005.10.035

Lu, X., Huang, R., Li, H., Long, J., and Jiang, Z. (2017). Preparation of an elastomer with broad damping temperature range based on EPDM/ENR blend. *J. Elastomers Plastics* 49, 758–773. doi: 10.1177/0095244317698737

Lu, Z., Wang, Z., Masri, S. F., and Lu, X. (2018a). Particle impact dampers: past, present, and future. *Struct. Control Health Monitor.* 25:e2058. doi: 10.1002/stc.2058

Lu, Z., Wang, Z., Zhou, Y., and Lu, X. (2018b). Nonlinear dissipative devices in structural vibration control: a review. *J. Sound Vibration* 423, 18–49. doi: 10.1016/j.jsv.2018.02.052

Luo, B. H., Bai, Z. H., and Xie, Y. Q. (2004). The effects of trace Sc and Zr on microstructure and internal friction of Zn–Al eutectoid alloy. *Mater. Sci. Eng. A* 370, 172–176. doi: 10.1016/j.msea.2002.12.007

Manoj, N. R., Chandrasekhar, L., Patri, M., Chakraborty, B. C., and Deb, P. C. (2002). Vibration damping materials based on interpenetrating polymer networks of carboxylated nitrile rubber and poly (methyl methacrylate). *Polymers Adv. Technol.* 13, 644–648. doi: 10.1002/pat.324

McMickell, M. B., Kreider, T., Hansen, E., Davis, T., and Gonzalez, M. (2007). "Optical payload isolation using the miniature vibration isolation system (MVIS-II)," in *Industrial and Commercial Applications of Smart Structures Technologies 2007,* eds L. P. Davis, B. K. Henderson, and M. B. McMickell (San Diego, CA: International Society for Optics and Photonics), 652703.

Meng, C., and Jiang, C. (2016). Magnetostriction of a Fe83Ga17 single crystal slightly doped with Tb. *Scrip. Mater.* 114, 9–12. doi: 10.1016/j.scriptamat.2015.11.022

Miyagawa, T., Watakabe, T., Yamamoto, T., Fukasawa, T., and Okamura, S. (2017). "Research and development of three dimensional seismic isolation system utilized coned-disc-springs with rubber bearings," in *ASME 2017 Pressure Vessels and Piping Conference* (Waikoloa: American Society of Mechanical Engineers), V008T08A043.

Mori, S., Suhara, I., Saruta, M., Okada, K., Tomizawa, T., Tsuyuki, Y., et al. (2012). "Simulation analysis of free vibration test in a building "Chisuikan" using three-dimensional seismic base isolation system," in *15th World Conference on Earthquake Engineering* (Lisbon).

Murakami, T., Inoue, T., Shimura, H., Nakano, M., and Sasaki, S. (2006). Damping and tribological properties of Fe–Si–C cast iron prepared using various heat treatments. *Mater. Sci. Eng. A* 432, 113–119. doi: 10.1016/j.msea.2006.06.090

Nishiyama, K., Matsui, R., Ikeda, Y., Niwa, S., and Sakaguchi, T. (2003). Damping properties of a sintered Mg–Cu–Mn alloy. *J. Alloys Comp.* 355, 22–25. doi: 10.1016/S0925-8388(03)00256-1

Okamura, S., Kamishima, Y., Negishi, K., Sakamoto, Y., Kitamura, S., and Kotake, S. (2011). Seismic isolation design for JSFR. *J. Nucl. Sci. Technol.* 48, 688–692. doi: 10.1080/18811248.2011.9711750

Ou, J. P., and Jia, J. F. (2010). "Seismic performance of a novel 3D isolation system on continuous bridges," in *Active and Passive Smart Structures and Integrated Systems 2010, 7643* (San Diego, CA: International Society for Optics and Photonics), 764304. doi: 10.1117/12.847506

Padalka, O., Song, H. J., Wereley, N. M., Filer, I. I., J. A., and Bell, R. C. (2010). Stiffness and damping in Fe, Co, and Ni nanowire-based magnetorheological elastomeric composites. *IEEE Trans. Magn.* 46, 2275–2277. doi: 10.1109/TMAG.2010.2044759

Patri, M., Reddy, C. V., Narasimhan, C., and Samui, A. B. (2007). Sequential interpenetrating polymer network based on styrene butadiene rubber and polyalkyl methacrylates. *J. Appl. Polymer Sci.* 103, 1120–1126. doi: 10.1002/app.24338

Pukkate, N., Kitai, T., Yamamoto, Y., Kawazura, T., Sakdapipanich, J., and Kawahara, S. (2007). Nano-matrix structure formed by graft-copolymerization of styrene onto natural rubber. *Eur. Polymer J.* 43, 3208–3214. doi: 10.1016/j.eurpolymj.2007.04.037

Pulino-Sagradi, D., Sagradi, M., Karimi, A., and Martin, J. L. (1998). Damping capacity of Fe-Cr-X high-damping alloys and its dependence on magnetic domain structure. *Scrip. Mater.* 39. doi: 10.1016/S1359-6462(98)00157-2

Qin, R., Huang, R., and Lu, X. (2018). Use of gradient laminating to prepare NR/ENR composites with excellent damping performance. *Mater. Design* 149, 43–50. doi: 10.1016/j.matdes.2018.03.063

Raj, R. E., Parameswaran, V., and Daniel, B. S. S. (2009). Comparison of quasi-static and dynamic compression behavior of closed-cell aluminum foam. *Mater. Sci. Eng. A* 526, 11–15. doi: 10.1016/j.msea.2009.07.017

Ramesh, R. S., Fredette, L., and Singh, R. (2019). Identification of multi-dimensional elastic and dissipative properties of elastomeric vibration isolators. *Mech. Syst. Signal Proc.* 118, 696–715. doi: 10.1016/j.ymssp.2018.09.009

Rittweger, A., Beig, H. G., Konstanzer, P., and Bureo Dacal, R. (2005). Feasibility demonstration of an active payload adapter for Ariane 5. *In Spacecraft Structures, Materials and Mechanical Testing* 2005, 581.

Shi, Z., and Huang, J. (2013). Feasibility of reducing three-dimensional wave energy by introducing periodic foundations. *Soil Dynam. Earthquake Eng.* 50, 204–212. doi: 10.1016/j.soildyn.2013.03.009

Shimada, T., Fujiwaka, T., and Moro, S. (2004). "Study on three-dimensional seismic isolation system for next-generation nuclear power plant: hydraulic three-dimensional base isolation system," in *Proceedings of Pressure Vessels and Piping Conference* (San Diego, CA: ASME) 486, 35–42. doi: 10.1115/PVP2004-2931

Stepanov, G. V., Abramchuk, S. S., Grishin, D. A., Nikitin, L. V., Kramarenko, E. Y., and Khokhlov, A. R. (2007). Effect of a homogeneous magnetic field on the viscoelastic behavior of magnetic elastomers. *Polymer* 48, 488–495. doi: 10.1016/j.polymer.2006.11.044

Stewart, D. (1965). A platform with six degrees of freedom. *Proc. Instit. Mech. Eng.* 180, 371–386.

Suhara, J., Tamura, T., Okada, Y., and Umeki, K. (2002). "Development of three dimensional seismic isolation device with laminated rubber bearing and rolling seal type air spring," in *ASME 2002 Pressure Vessels and Piping Conference* (Vancouver, BC: American Society of Mechanical Engineers), 43–48. doi: 10.1115/PVP2002-1430

Suksawad, P., Yamamoto, Y., and Kawahara, S. (2011). Preparation of thermoplastic elastomer from natural rubber grafted with polystyrene. *Eur. Polymer J.* 47, 330–337. doi: 10.1016/j.eurpolymj.2010.11.018

Sun, X., and Jing, X. (2015). Multi-direction vibration isolation with quasi-zero stiffness by employing geometrical nonlinearity. *Mech. Syst. Signal Proc.* 62, 149–163. doi: 10.1016/j.ymssp.2015.01.026

Tang, J., Cao, D., Ren, F., and Li, H. (2018). Design and experimental study of a VCM-based whole-spacecraft vibration isolation system. *J. Aerospace Eng. ASCE* 31:04018045. doi: 10.1061/(ASCE)AS.1943-5525.0000871

Thomas, J. R. (1966). Preparation and magnetic properties of colloidal cobalt particles. *J. Appl. Phys.* 37, 2914–2915. doi: 10.1063/1.1782154

Unsal, M., Niezrecki, C., and Crane, I. I. I., C. D. (2008). Multi-axis semi-active vibration control using magnetorheological technology. *J. Intel. Mater. Syst. Struct.* 19, 1463–1470. doi: 10.1177/1045389X07088287

Wang, Y., and Liu, H. J. (2009). Six degree-of-freedom microvibration hybrid control system for high technology facilities. *Int. J. Struct. Stab. Dynam.* 9, 437–460. doi: 10.1142/S0219455409003168

Wang, Y. D., Huang, E. W., Ren, Y., Nie, Z. H., Wang, G., Liu, Y. D., et al. (2008). *In situ* high-energy X-ray studies of magnetic-field-induced phase transition in a ferromagnetic shape memory Ni–Co–Mn–In alloy. *Acta Mater.* 56, 913–923. doi: 10.1016/j.actamat.2007.10.045

Wu, Z., Jing, X., Sun, B., and Li, F. (2016). A 6DOF passive vibration isolator using X-shape supporting structures. *J. Sound Vibrat.* 380, 90–111. doi: 10.1016/j.jsv.2016.06.004

Xu, C., Xu, Z. D., Ge, T., and Liao, Y. X. (2016b). Modeling and experimentation of a viscoelastic microvibration damper based on a chain network model. *J. Mech. Mater. Struct.* 11, 413–432. doi: 10.2140/jomms.2016.11.413

Xu, J., and Sun, X. (2015). A multi-directional vibration isolator based on Quasi-Zero-Stiffness structure and time-delayed active control. *Int. J. Mech. Sci.* 100, 126–135. doi: 10.1016/j.ijmecsci.2015.06.015

Xu, K., Chen, R., Wang, C., Sun, Y., Zhang, J., Liu, Y., et al. (2016a). Organomontmorillonite-modified soybean oil-based polyurethane/epoxy resin interpenetrating polymer networks (IPNs). *J. Therm. Anal. Calorim.* 126, 1253–1260. doi: 10.1007/s10973-016-5795-x

Xu, Z. D. (2009). Horizontal shaking table tests on structures using innovative earthquake mitigation devices. *J. Sound Vibrat.* 325, 34–48. doi: 10.1016/j.jsv.2009.03.019

Xu, Z. D., Gai, P. P., Zhao, H. Y., Huang, X. H., and Lu, L. Y. (2017b). Experimental and theoretical study on a building structure controlled by multi-dimensional earthquake isolation and mitigation devices. *Nonlinear Dynam.* 89, 723–740. doi: 10.1007/s11071-017-3482-5

Xu, Z. D., Liao, Y. X., Ge, T., and Xu, C. (2016c). Experimental and theoretical study of viscoelastic dampers with different matrix rubbers. *J. Eng. Mech. ASCE*, 142:04016051. doi: 10.1061/(ASCE)EM.1943-7889.0001101

Xu, Z. D., Sha, L. F., Zhang, X. C., and Ye, H. H. (2013). Design, performance test and analysis on magnetorheological damper for earthquake mitigation. *Struct. Control Health Monit.* 20, 956–970. doi: 10.1002/stc.1509

Xu, Z. D., Shen, Y. P., and Guo, Y. Q. (2003). Semi-active control of structures incorporated with magnetorheological dampers using neural networks. *Smart Mater. Struct.* 12:80. doi: 10.1088/0964-1726/12/1/309

Xu, Z. D., Suo, S., and Lu, Y. (2016d). Vibration control of platform structures with magnetorheological elastomer isolators based on an improved SAVS law. *Smart Mater. Struct.* 25:065002. doi: 10.1088/0964-1726/25/6/065002

Xu, Z. D., Suo, S., Zhu, J. T., and Guo, Y. Q. (2018a). Performance tests and modeling on high damping magnetorheological elastomers based on bromobutyl rubber. *J. Intel. Mater. Syst. Struct.* 29, 1025–1037. doi: 10.1177/1045389X17730909

Xu, Z. D., Tu, Q., and Guo, Y. F. (2012). Experimental study on vertical performance of multidimensional earthquake isolation and mitigation devices for long-span reticulated structures. *J. Vibrat. Control* 18, 1971–1985. doi: 10.1177/1077546311429338

Xu, Z. D., Wang, S. A., and Xu, C. (2014). Experimental and numerical study on long-span reticulate structure with multidimensional high-damping earthquake isolation devices. *J. Sound Vibrat.* 333, 3044–3057. doi: 10.1016/j.jsv.2014.02.013

Xu, Z. D., Xu, F. H., and Chen, X. (2016e). Intelligent vibration isolation and mitigation of a platform by using MR and VE devices. *J. Aerospace Eng. ASCE*, 29:04016010. doi: 10.1061/(ASCE)AS.1943-5525.0000604

Xu, Z. D., Xu, F. H., and Chen, X. (2016f). Vibration suppression on a platform by using vibration isolation and mitigation devices. *Nonlinear Dynam.* 83, 1341–1353. doi: 10.1007/s11071-015-2407-4

Xu, Z. D., Xu, M., and Sun, C. L. (2018b). Performance tests and microchain model validation of a novel kind of MR fluid with GO-coated iron particles. *J. Mater. Civil Eng. ASCE*, 30:04018072. doi: 10.1061/(ASCE)MT.1943-5533.0002253

Yamazaki, H., Takeda, M., Kohno, Y., Ando, H., Urayama, K., and Takigawa, T. (2011). Dynamic viscoelasticity of poly (butyl acrylate) elastomers containing dangling chains with controlled lengths. *Macromolecules* 44, 8829–8834. doi: 10.1021/ma201941v

Yang, C., Yang, G., Liu, F., Chen, Y., Liu, N., Chen, D., et al. (2006). Metastable phase formation in eutectic solidification of highly undercooled Fe83B17 alloy melt. *Physica B Condensed Matter* 373, 136–141. doi: 10.1016/j.physb.2005.11.112

Yang, S. Y., and Niu, J. (2012). "Numerical analysis on isolation effect of the SMA-disc spring three-dimensional composite bearings," in *Advanced Materials Research,* eds H. Li, Y. F. Liu, M. Guo, R. Zhang, and Jing Du (Trans Tech Publications), 374, 2245–2249. doi: 10.4028/www.scientific.net/AMR.374-377.2245

Yoshioka, H., Takahashi, Y., Katayama, K., Imazawa, T., and Murai, N. (2001). An active microvibration isolation system for hi-tech manufacturing facilities. *J. Vibrat. Acoust.* 123, 269–275. doi: 10.1115/1.1350566

Zareh, S. H., Sarrafan, A., Khayyat, A. A. A., and Zabihollah, A. (2012). Intelligent semi-active vibration control of eleven degrees of freedom suspension system using magnetorheological dampers. *J. Mechan. Sci. Technol.* 26, 323–334. doi: 10.1007/s12206-011-1007-6

Zhao, Y., Su, J., Zhou, X., and Sui, Y. (2008). Shaking table test and numerical analysis of vertical-isolated building model with combined disk spring bearing. *J. Build. Struct.* 29, 99–106.

Zhou, J., Xiao, Q., Xu, D., Ouyang, H., and Li, Y. (2017). A novel quasi-zero-stiffness strut and its applications in six-degree-of-freedom vibration isolation platform. *J. Sound Vibrat.* 394, 59–74. doi: 10.1016/j.jsv.2017.01.021

Zhou, M. K., Xiong, X., Chen, L. L., Cui, J. F., Duan, X. C., and Hu, Z. K. (2015). Note: A three-dimension active vibration isolator for precision atom gravimeters. *Rev. Sci. Instr.* 86:046108. doi: 10.1063/1.4919292

Zhu, J. T., Xu, Z. D., and Guo, Y. Q. (2012). Magnetoviscoelasticity parametric model of an MR elastomer vibration mitigation device. *Smart Mater. Struct.* 21:075034. doi: 10.1088/0964-1726/21/7/075034

Zhu, J. T., Xu, Z. D., and Guo, Y. Q. (2013). Experimental and modeling study on magnetorheological elastomers with different matrices. *J. Mater. Civil Eng. ASCE*, 25, 1762–1771. doi: 10.1061/(ASCE)MT.1943-5533.0000727

Conflict of Interest Statement: The authors declare that the research was conducted in the absence of any commercial or financial relationships that could be construed as a potential conflict of interest.

Advantages of publishing in Frontiers

OPEN ACCESS
Articles are free to read
for greatest visibility
and readership

FAST PUBLICATION
Around 90 days
from submission
to decision

HIGH QUALITY PEER-REVIEW
Rigorous, collaborative,
and constructive
peer-review

TRANSPARENT PEER-REVIEW
Editors and reviewers
acknowledged by name
on published articles

Frontiers
Avenue du Tribunal-Fédéral 34
1005 Lausanne | Switzerland

Visit us: www.frontiersin.org
Contact us: info@frontiersin.org | +41 21 510 17 00

REPRODUCIBILITY OF RESEARCH
Support open data
and methods to enhance
research reproducibility

DIGITAL PUBLISHING
Articles designed
for optimal readership
across devices

FOLLOW US
@frontiersin

IMPACT METRICS
Advanced article metrics
track visibility across
digital media

EXTENSIVE PROMOTION
Marketing
and promotion
of impactful research

LOOP RESEARCH NETWORK
Our network
increases your
article's readership